Aqueous alteration on early Mars: New insights from the aqueous geochemistry and secondary mineralogy of meteorite ALH 84001

Thesis

Aqueous alteration on early Mars

New insights from the aqueous geochemistry and secondary mineralogy of meteorite ALH 84001

by
Mohit Melwani Daswani, MSc.

A thesis submitted for the degree of
Doctor of Philosophy (PhD)

Department of Physical Sciences
Open University

DATE OF SUBMISSION : 17 APRIL 2015
DATE OF AWARD : 23 JUNE 2015

16th April 2015

Abstract

In the wake of the discovery of clay minerals in Gale crater (an ancient martian crater) by NASA's *Curiosity* rover, and numerous remote and *in situ* detections of hydrous minerals on the early surfaces of Mars, the absence of clays in the oldest martian meteorite, ALH 84001, remains conspicuous. ALH 84001 is an orthopyroxenite that contains carbonate minerals which were formed on Mars – probably as a result of low temperature, near-surface aqueous alteration of the rock – but it does not contain clays.

This body of work comprises a number of studies and different analytical techniques used to understand and constrain the composition of early martian fluids that lead to the alteration of the meteorite when it was emplaced near the surface of Mars ~ 3.9 Ga ago. Petrological and mineralogical studies; carbon, nitrogen and noble gas stepped-combustion analyses; geochemical modelling under different conditions; and aqueous alteration experiments were all carried out here for this purpose. A young martian meteorite, shergottite NWA 6234, was also investigated in the context of this work to understand whether aqueous alteration persisted in time.

Compositional clues described here point to varying degrees of aqueous alteration in ALH 84001, and possibly even in a shock melt vein in NWA 6234. The results of the extensive geochemical modelling strongly suggest that the fluid that altered ALH 84001 was near-neutral (pH ≈ 7), low temperature (~ 20 °C), and that the atmospheric CO_2 pressure required to produce the carbonates was under 1 bar. The fluid was probably transient, and evaporated after precipitating the ubiquitous carbonates. A suite of other secondary products are predicted to have formed neighbouring ALH 84001, a few of which

have been detected on Mars (such as clays), yet others are more surprising (such as talc and zeolites, and a possible pathway to the abiotic production of methane).

Acknowledgements

I apologise for this fairly long list; it follows no particular order. The fact that there are so many named here does not dilute my gratefulness for their contribution(s). And I apologise if I have missed anyone out – if you feel I have, it was unintentional!

I thank my 妹妹, Nuri, and my parents, Nirmala and Chandru, for their love, support and patience. Also, the cats.

This work would not have been possible without the guidance of my supervisors, Susanne Schwenzer, Ian Wright and Monica Grady, and the technical help from Pete Landsberg, Jessica Barnes, Andy Tindle, Diane Johnson, Mark Reed, Jim Palandri, Feargus Abernethy, James Mortimer, Sasha Verchovsky, Mabs Gilmour, Michelle Higgins, Kay Green, John Faithfull, John Watson, Sam Hammond, Natalie Starkey, Ian Franchi, Chris Hall, Caroline Smith, David Smith, Anton Kearsley, John Spratt, Jill Clarke, Andreas Morlok, Manish Patel and Tim Ringrose. Discussions with Allan Treiman, Justin Filiberto, Mikhail Zolotov, David Catling and John Bridges, and my mini-viva assessors, Matt Balme and David Rothery, helped shape this thesis. I thank Sarah Sherlock, Nicolas Mangold and John Murray for being my examiners, and Axel Hagermann for being the panel chair (thanks for the stroopwafels!). Karen Guyler, Beverley Bishop and Andy Lloyd provided assistance with admin, printing and the like.

The Science and Technology Facilities Council provided financial support for this PhD project. I am grateful to the Royal Astronomical Society, Geochemistry Research Group, UK Space Agency, Mineralogical Society of Great Britain and Ireland, and Lunar and Planetary Institute for providing financial support and awards so I could attend and present at conferences.

Assorted family also supported me, hosted me, fed me or gave me a call every so often to find out whether I was still on planet Earth: Rosie Daswani; the Melwanis: Vishal, Reena, Romina, Ramesh and Sapna, and Arjan; the Nathurmals: Valmik, Sonali, Sneha, Neetu and Arjan; Geeta Mirpuri, Sanju Lakhani and Arvin Lakhani.

Some good friends have given me (whether they know it or not) a lot of emotional support/came to visit/hosted me/were subjected to my rants: Jaume Borras, Natàlia Pou Gascón, Charlene Tan, KayKey Teo, Dan Dawson, Adam Stevens, Jean-David Bodenan, Beth Steer, Kathryn McDermott, Ed Allanwood, Bharath Sukumaran, Ben Rozitis, Andreas Morlok, Jess Barnes, Diego Antela, James Mortimer, Feargus Abernethy, Romain Tartèse, Josh Snape, Martine Harvey, Calum MacCormick, Erika Kaufmann, Sabrina Gärtner, Debora Oswald, Rhiannon Gwyn, Laura Bridgestock, Laia Barrufet, Stephan Doember, Jon Dawson, Karen Dawson, Becca Wolsey, Sam Rolfe, Gemma Muros, Anna Novgorodova, Goran Gruden, Ling Qin, Martin Reyes, Nathan Tift, Rob Burgess, Melese Tesfaye, Toni Alcaraz, Alex Barrett, Dan Weatherill, Joe Rushton, Helen Davidge, Euan Monaghan, Phillipa Smith, Rob Piper, Becca Thomas, Mario Cabeza Ferriz, Carlos Colom Montes, Stephen Wolters, Aniol Olmedo, Andri Foppa, Mario Caviezel, Bruno Albalat, Carlos Berrens, Ester Comellas, Gerard Montaner, Roy Adkin, Tom Barrett, Tim Tomkinson, David Martí Pete, Jon Mason, Imma Vicent, Julian Clausin, Silvia Clausin, Alastair Lockie, Jimmi Garvin, Janet Williams, Matt Soman, Ben Dryer, Neil Murray, USSAC, the DPS house band, the Cellar Bar regulars, the Wednesday RPG group, the Pub Wednesday regulars ("Do you know what we should do?"), the Big Rockers, and the GEM family.

Contents

List of figures

List of tables

1 Introduction

The role and presence of water on early Mars has for a long time been an intensely debated topic. Whether the surface conditions allowed for water to remain liquid for sustained lengths of time or only for punctuated episodes during the Noachian period (> 3.7 Ga ago) has been particularly contentious. A growing body of evidence, from alteration minerals in martian meteorites to direct analyses of soils by rovers on the surface of Mars, points to water having existed in various states and compositions. What follows in this chapter is a review of essential current literature on the role and state of water on ancient Mars. Furthermore, based on the body of literature, a series of research problems, questions and objectives are laid out at the end of the chapter which motivate and justify the research carried out throughout this thesis.

1.1 Initial inventory of water on Mars

Dynamic models of planetary accretion estimate that the terrestrial planets were accreted around ~ 30 to 100 Ma after the formation of the Solar System (O'Brien et al., 2006; Raymond et al., 2009). Interpretation of hafnium-tungsten (Hf-W) isotope chronometry for the most part agrees with this view (Allègre et al., 2008, 1995), except for Mars (Dauphas and Pourmand, 2011; Nimmo and Kleine, 2007). Mars is exceptional for having too small a mass compared to what the models predict (Raymond et al., 2009), and for accreting from planetesimals to planetary embryo, and finally into a planet in a few million years – which is comparable to the growth rate of the asteroids in the asteroid belt (Dauphas and Pourmand, 2011; Yin et al., 2002).

Earth acquired most of its water through the collision of several planetary embryos from the asteroid belt, and a significantly smaller fraction of water (up to 10 %) was delivered by comets as a late veneer (Morbidelli et al., 2000), however, the origin of water on Mars is thought to have followed the opposite pattern (Lunine et al., 2003). Lunine et al. (2003) analysed the deuterium/hydrogen (D/H, or $^{2}H/^{1}H$) isotopic record in hydrous magmatic minerals in martian meteorites and calculated a high primitive D/H ratio of water on Mars (1.2 to 1.6 times the Vienna Standard Mean Ocean Water value (VSMOW)[i]; Lunine et al. (2003); where the calculated D/H abundance ratio of VSMOW on Earth is 155.76 ± 0.05 ppm). Comparing this value to D/H measurements of possible primitive sources of water (carbonaceous chondrite meteorites, and long-period (Oort-cloud) and short-period (Kuiper Belt) comets) and combining dynamical models of planetary accretion and material delivery from comets and asteroids revealed that even accounting for its size, Mars was relatively dry when it accreted compared to Earth, and acquired most of its water as a late veneer of comets and asteroids from beyond 2.5 AU (Lunine et al., 2003). The water content finally incorporated into Mars was calculated at 0.06 to 0.27 oceans (Lunine et al., 2003; Raymond et al., 2007, 2006) (where an 'ocean' is equivalent to the amount of surface water on the Earth, ~ 1.5×10^{21} kg (Lécuyer et al., 1998)[ii]).

In light of the 'Grand Tack' model of terrestrial planet formation (Walsh et al., 2012, 2011), which provides a comprehensive explanation for the formation of the terrestrial planets (including the small size of Mars and the water mass of Earth), dependent on the extension of the protoplanetary disk and migration of the gas giant planets, it is likely that the

[i] The Vienna Standard Mean Ocean Water values are the adopted standards to report the relative deviation of e.g., $^{2}H/^{1}H$ and $^{18}O/^{16}O$ in a sample from the standard (e.g., Gat et al., 2001).

[ii] Or Water Equivalent to a Global layer (WEG) of ~ 600 to 2700 m, assuming a flat surface and a radius of 3389.5 km for Mars.

calculations for water delivered to all terrestrial planets and their sources will need to be revised. This problem is not addressed in this thesis directly, but a scope for future work to attempt to solve it is presented in the conclusions (Chapter 6), making use of the results from this thesis.

1.2 Hydrous geomorphology on the early surface

The surface of Mars was extensively affected by water from formation until the early Hesperian period, ~ 3.7 Ga ago (Figure 1-1), after which it underwent regional episodes of active hydrological activity. Examples of geomorphological evidence of aqueous activity of the surface during the Noachian to the early Hesperian include:

- valley networks (e.g., Carr and Head, 2010; Fassett and Head, 2011).
- Outflow channels, sometimes with related chaotic terrains, thought to have formed from large, rare floods (e.g., Rodriguez et al., 2005; Zegers et al., 2010).
- Deltas, lakes, and possibly an ocean from observed paleoshorelines and synthetic aperture radar (SAR) readings (Clifford and Parker, 2001; Di Achille and Hynek, 2010; Parker et al., 2010) using the Mars Advanced Radar for Subsurface and Ionosphere Sounding instrument (MARSIS; Picardi et al., 2004) on the Mars Express (MEx; Chicarro et al., 2004) orbiter. These proposed large bodies of water appear to date up to the late Hesperian/early Amazonian ~ 3.0 Ga ago (Clifford and Parker, 2001; Di Achille and Hynek, 2010; Parker et al., 2010).

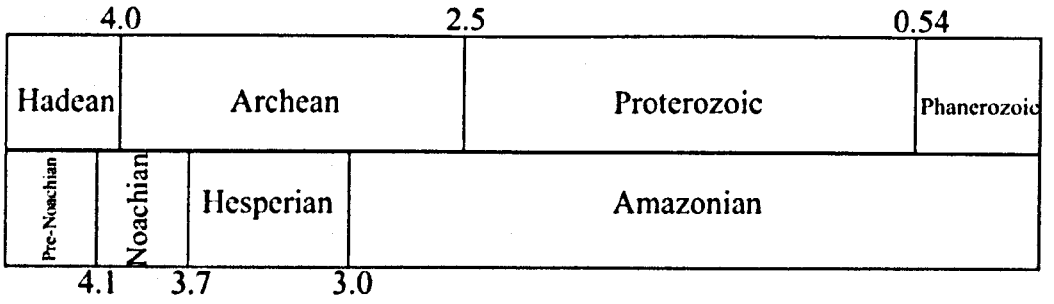

Figure 1-1. Comparison of geological eons on Earth (above) and Mars (below), after Carr and Head (2010). Numbers are Ga before present.

Punctuated examples of limited, late aqueous activity have been described (e.g., Amazonian outflow channels (e.g., Berman and Hartmann, 2002) valley networks (Fassett and Head, 2008) and gullies (e.g., Balme et al., 2006; Malin et al., 2006). Linear and sinuous gullies are currently active on Mars (Reiss et al., 2010) and have been ascribed to aqueous activity (melting H_2O ice, e.g., Mangold et al., 2010; Reiss et al., 2010), but have also been described as features formed by CO_2 ice blocks mobilised by melting and favourable slope inclines (Diniega et al., 2013). Recurring slope lineae are also modern small flow features probably formed by liquid water (McEwen et al., 2011). They appear seasonally, when temperatures might allow frozen brines to melt (Chevrier and Rivera-Valentin, 2012; McEwen et al., 2014, 2011) and seemingly recharge over time (Chevrier and Rivera-Valentin, 2012; Grimm et al., 2014).

Most recently, sedimentological features have been observed by the Curiosity rover in the late Noachian/early Hesperian Gale crater. Sedimentary conglomerates composed of moderately sorted, rounded pebbles cemented together at Bradbury Rise are inferred to be fluvial and to have been transported for several kilometres (Williams et al., 2013). Several metres of fine-grained stratified sedimentary rocks at Yellowknife Bay are inferred to have been deposited under lacustrine conditions that were stable for at least 10 to 100 ka (Grotzinger et al., 2014) (see also compositional and mineralogical evidence for

depositional and diagenetic aqueous processes at Yellowknife Bay, Section 1.3.1). A mixture of detrital and authigenic components in those rocks has been dated as age of 4.21 ± 0.35 Ga with in situ K-Ar systematics by the SAM instrument on *Curiosity* (Farley et al., 2014).

This thesis particularly focuses on the aqueous activity that occurred during the Noachian period and the Late Heavy Bombardment (LHB)[iii] ~4.1 to ~3.7 Ga ago due to the perceived abundance of aqueous processes occurring then.

Noachian geomorphological features of undoubtable hydrous origin include widely spread and well developed branching valley networks on ancient terrains (particularly in the Southern Highlands; Fassett and Head, 2008) identified by high resolution orbital imagery on Mars Global Surveyor, Mars Express and Mars Reconnaissance Orbiter (see Table 1-1 for relevant orbital instruments and missions). The presence of these features suggests erosion by liquid water driven by an active hydrological cycle, i.e., regulated by copious precipitation (e.g., Craddock and Howard, 2002). As precipitation was necessary to recharge the valley networks, so too were a denser atmosphere and higher average temperatures than today in order to maintain water in liquid state (at least transiently; Forget et al., 2013; Wordsworth et al., 2013).

Calculations of the amount of surface water needed to form the Noachian geomorphological features and extrapolated to the whole planet estimate a lower limit of ~500 m of Water Equivalent to a Global layer (WEG) remaining in the crust since the Noachian (Baker, 2001; Carr and Wänke, 1992), much of which may be stored in

[iii] The LHB is widely understood from observed crater densities and dynamic models to have been caused by an increase in the number of impactors striking the terrestrial planets after their formation, likely due to the perturbation of the orbits of planetesimals in the outer solar system and the asteroid belt as the giant gas planets migrated outwards, away from the Sun (Gomes et al., 2005).

phyllosilicate minerals, e.g., ~ 400 m WEG in serpentine (Chassefière and Leblanc, 2011; see Section 1.3.1), and a small amount (~ 35 m) as ice in permafrost and in the polar regions (Christensen, 2006).

Table 1-1. Relevant orbital instrumentation used in the last decade for the scientific study of Mars. Shaded rows are VNIR spectrometers used for surface composition analyses, and plain rows are high resolution orbital imagers used for geomorphological studies.

Mission		Instrument		
Name	Acronym	Name	Acronym	Reference
Mars Global Surveyor	MGS	Mars Orbiter Camera	MOC	(Malin and Edgett, 2001)
		Thermal Emission Spectrometer	TES	(Christensen et al., 2001)
Mars Reconnaissance Orbiter	MRO	High Resolution Imaging Science Experiment	HiRISE	(McEwen et al., 2007)
		Context Camera	CTX	(Malin et al., 2007)
		Compact Reconnaissance Imaging Spectrometer for Mars	CRISM	(Murchie et al., 2007)
Mars Express	MEx	High Resolution Stereo Camera	HRSC	(Neukum and Jaumann, 2004)
		Observatoire pour la Minéralogie, l'Eau, les Glaces et l'Activité	OMEGA	(Bibring et al., 2004)
2001 Mars Odyssey	Odyssey	Thermal Emission Imaging System	THEMIS	(Christensen et al., 2004)

1.3 Early aqueous activity inferred from the composition of the surface

1.3.1 Direct observations

Orbital imagery from the visible to near-infrared (VNIR) spectrometers (see Table 1-1 for relevant instruments and missions) has been used to determine the composition of minerals related to aqueous activity on the surface of Mars at a range of spatial scales. So too have the in-situ analytical instruments on the rovers (see

Table 1-2 for relevant instruments and missions) Mars Exploration Rovers (MER) *Spirit* and *Opportunity* and Mars Science Laboratory (MSL) Curiosity. The following sections detail detections of particular relevance to Noachian surface aqueous processes. A Mars Orbital Laser Altimeter map showing the locations and outcrops discussed in the text is included in Appendix A for reference.

Table 1-2. Relevant instruments for the study of aqueous processes and mineral compositions on recent rovers on Mars.

Mission Name	Acronym	Instrument Name	Acronym	Reference
Mars Exploration Rover (A: *Spirit*, B: *Opportunity*)	MER	Alpha Particle X-ray Spectrometer	APXS	Athena instrument payload (Squyres et al., 2003)
		Miniature Thermal Emission Spectrometer	Mini-TES	
		Miniaturised Mössbauer Spectrometer	MIMOS II	
		Panoramic Camera	PanCam	
Mars Science Laboratory (*Curiosity*)	MSL	Sample Analysis at Mars Instrument Suite	SAM	Sample Acquisition, Processing and Handling subsystem (SA/SPaH; Anderson et al., 2012)
		Chemistry and Mineralogy	CheMin	
		Alpha Particle X-ray Spectrometer	APXS	
		Mars Hand Lens Imager	MAHLI	
		Mast Cameras	MastCam	
		Chemistry and MicroImaging instruments	ChemCam	

1.3.1.1 Phyllosilicates

An extensive distribution of phyllosilicate minerals is found in the ancient Southern highlands and along the N.-S. dichotomy[iv]. Many of these deposits have been excavated by

[iv] The N.-S. dichotomy is a central feature of Mars which visibly divides North and South hemispheres into the Northern lowlands and the Southern highlands. The origin of the N.-S. dichotomy is uncertain, but

subsequent impacts and erosion (which may be subaerial or subaqueous) and are often associated with crater walls, central peaks and ejecta (Mustard et al., 2008; Poulet et al., 2005). The sizable presence of Fe/Mg-smectite-rich (most likely nontronite and chamosite) units and localised Al-rich phyllosilicates (most likely montmorillonite) in Nili Fossae, Mawrth Vallis, Terra Meridiani are interpreted as the weathering of mafic precursor rocks (Bibring et al., 2006; Poulet et al., 2005). Mustard et al. (2008) argue that the presence of these phyllosilicates indicate that they formed under 'moderate to alkaline pH' (a *specific* pH was not reported). The predominance of these phyllosilicate-rich rocks throughout the early and mid-Noachian terrains has led to this period of early martian history being sometimes dubbed as the 'Phyllosian' (Bibring et al., 2006), although there are concerns about this term and its implications, especially as other minerals such as sulfates were present in the Noachian (Wray et al., 2010), and phyllosilicates are also clearly detected in Hesperian lacustrine environments (Vaniman et al., 2014). The complex geological history of Mars means that clays are unlikely to have formed in a single global event.

Other phyllosilicates identified by remote sensing, particularly at Nili Fossae, include kaolinite, chlorite and K-Al-bearing phyllosilicates (probably illite or muscovite), and also hydrated silica or glass (possibly opal or volcanic glass; Mustard et al., 2008). Kaolinite seems to be restricted to a few locations of limited extent (under 200 m^2), where enhanced hydrothermal activity may have occurred (Mustard et al., 2008). At Mawrth Vallis, however, kaolinite together with hydrated silica appears to form large units overlying montmorillonite and hydrated silica units, themselves overlying large Fe-Mg smectite units (McKeown et al., 2009). These large packages could have formed from volcanic ash

---

current models suggest a giant impact or multiple impacts in the Pre-Noachian, followed by volcanic resurfacing and crustal relaxation in the Northern hemisphere lead to it (e.g., Watters et al., 2007). The Southern highlands are noticeably older as crater numbers, sizes and densities attest.

altered by hydrothermal fluids, or by being deposited in a large body of water such as a lake or sea (McKeown et al., 2009). Signatures for Fe^{3+}-rich smectites were detected by *Opportunity* in layered veneers at Matijevic Hill, which pre-dates the Noachian-aged Endeavour crater, and were interpreted to be formed as surface layers or from neutralising mildly acidic (pH > 5) fluids (Arvidson et al., 2014; cf. the alkaline conditions mentioned above and proposed by Mustard et al., 2008). In certain locations on Matijevic Hill (Espérance), substantial aqueous alteration by reducing fluids is interpreted by the probable presence of Al-rich smectites and siliceous phases and the loss of iron (Arvidson et al., 2014).

Although also associated with craters, Fe/Mg phyllosilicates have been detected in sedimentary fans and deltas in the Holden, Eberswalde and Jezero craters, but it is unknown whether these were transported or formed in situ (Mustard et al., 2008). Smectites with high Al/Si ratios (most likely montorillonite) were also detected at Columbia Hills in Gusev crater as a result of extensive aqueous alteration, and although they do not appear to have been transported, the actual mode of origin (whether they are related to lacustrine or hydrothermal processes) is unknown (Clark et al., 2007). Clearly lacustrine sediments were identified at Yellowknife Bay in Gale crater (Grotzinger et al., 2014), comprised of mudstones, probably containing Fe-saponite and associated magnetite from the low-temperature alteration of Fe-forsterite rocks < 60 °C, dating from the Noachian to well into the Hesperian (Farley et al., 2014; Vaniman et al., 2014).

1.3.1.2 Sulfates

Mg-bearing sulfates (possibly kieserite) and hydrated Ca-bearing sulfates (gypsum) (Poulet et al., 2005) have also been observed on the surface of Mars. Gypsum veins in impact breccias and sandstones cemented with sulfate have been identified by Opportunity at

Copper Hill and Matijevic Hill at Endeavour crater, and are interpreted to have been deposited by low temperature (< 40 to 60 °C), pH neutral (possibly 6 – 7, although a specific number is not reported), dilute fluids (Squyres et al., 2012), although acidic hydrothermal activity (linked to the formation of the crater) may have played a role in their precipitation (Arvidson et al., 2014). Gypsum, bassanite and anhydrite veins were also found by Curiosity at Yellowknife Bay in Gale crater, but are likely to have originated as late diagenetic features (Vaniman et al., 2014), possibly into the Hesperian.

Layered hydrated sulfate deposits are also thought to occur within Valles Marineris and appear to be abundant in late Noachian to late Hesperian terrains, possibly as a consequence of the formation of the Tharsis bulge, and prompting this period to be named 'Theiikian' (Bibring et al., 2006). Again, like the 'Phyllosian', this name may not be entirely accurate: the abundance of large-scale sulfate does appear to be linked to a global change in aqueous chemistry approximately from the Noachian to the Hesperian, veering towards acidic conditions (Bibring et al., 2006). But as seen by Opportunity and Curiosity (above), sulfate deposits appear to be in the form of veins in localised Ca-sulfate deposits requiring near-neutral conditions (Arvidson et al., 2014), and also as jarosite, probably indicative of acidic conditions (McLennan et al., 2005). Moreover, bassanite has been detected in layers predating the layered phyllosilicates at Mawrth Vallis, so sulfates formed in the Noachian, too (Wray et al., 2010).

1.3.1.3 Iron oxides

Iron oxides such as crystalline grey hematite (α-Fe_2O_3) (and/or possibly maghemite, γ-Fe_2O_3) at Terra Meridiani, Valles Marineris and Aram Chaos, are thought to have formed in the presence of water. Whether the minerals were precipitated from low temperature solutions, were altered and transported sulfates, or deposited from higher temperature

hydrothermal fluids remains unclear (Bibring et al., 2006; Christensen et al., 2001), but Fe-oxides in the form of (most likely authigenic) magnetite have been detected at the John Klein and Cumberland mudstones at Yellowknife Bay in Gale crater, associated with Fe-saponites (Vaniman et al., 2014). The rarer akaganeite (β-FeO(OH,Cl)) also occurs at Yellowknife Bay, although its relation with the other phases is not well understood: it may result from the alteration of sulfides such as pyrrhotite, also present in the rocks (Vaniman et al., 2014).

1.3.1.4 Chlorides

Chlorides (Osterloo et al., 2008) are found in mid- to late-Noachian terrains (particularly the Southern highlands, e.g., in Terra Sirenum) and extending to Hesperian terrains, in topographically low areas, sinuous channels and craters. Typically, chlorides on the surface of Mars are found on 1 – 25 km^2 expanses which are thought to be the evaporitic precipitates of ponded brines, as inferred by the polygonal desiccation cracks observed.

1.3.1.5 Carbonates

Carbonates have been detected on the surface, particularly Mg-bearing carbonates in Nili Fossae (Ehlmann et al., 2008). Typically, these carbonates have been described within layers of olivine-rich rocks above Fe-Mg smectites, but below Al-bearing phyllosilicates. The genesis of these carbonates is as yet uncertain, but Ehlmann et al. (2008) contended that neutral to alkaline waters (possibly pH 7 – 9, although a specific pH is not reported) were involved in their formation. Fe-Mg carbonates are present in the Comanche outcrop in the Columbia Hills at Gusev Crater in concentrations of 16 – 34 wt. %, and by comparison to the martian meteorite Allan Hills 84001 (ALH 84001, see Section 1.4).

While global mineralogical maps derived from remote sensing observations provide insight on large-scale processes and climatic conditions, arguably, it is the local analyses by the rovers as mobile laboratories that have provided a more detailed understanding of the composition and role of early martian water, especially because compositional and geomorphological differences throughout Mars reflect in characteristic variations in degree of alteration (i.e., at different water/rock ratios).

1.4 Martian meteorite Allan Hills 84001

Martian meteorite Allan Hills 84001 (ALH 84001) is a ~4.1 Ga old (Lapen et al., 2010) igneous orthopyroxenite cumulate and the oldest known martian meteorite to date. The main mass (~1.9 kg) was collected in 1984 by the Antarctic Search for Meteorites programme (ANSMET) in the vicinity of the Allan Hills in Antarctica. Analyses of the ^{14}C activity of the bulk rock and the calculated production rate of ^{14}C by the bulk rock have been used to estimate the terrestrial residence age of the meteorite (~ 13 ka; Jull et al., 1995). Furthermore, Nyquist et al. (2001) interpret the cosmic ray exposure age from the ^{3}He, ^{21}Ne, ^{38}Ar and ^{81}Kr produced by cosmic rays as ~ 15 ± 0.8 Ma.

1.4.1 Description

The main mass is composed of ~ 97 % orthopyroxene ($En_{70}Wo_3$), ~ 1 % Fe^{3+}-rich chromite, ~ 1% maskelynite ($An_{31}Ab_{63}$), minor amounts of phosphates (apatite, merrilite and whitlockite; e.g., Mittlefehldt, 1994; Treiman, 1998, 1995), olivine inclusions (Fo_{65}; Shearer et al., 1999), augite ($En_{45}Wo_{43}$; Treiman, 1995), feldspathic and silica glass (Greenwood and McSween, Jr., 2001), periclase (Barber and Scott, 2002), and only trace

amounts of phyllosilicates (Brearley, 2000; Shearer et al., 1999). Salts (Ca-sulfate, Mg-sulfate and NaCl), SiO_2 and possibly amorphous carbon-rich material from contamination by exposure to the atmosphere in Antarctica have also been described on the fusion crust (Wentworth et al., 1998; Wentworth and Gooding, 1995).

A zoned carbonate alteration assemblage exists in ALH 84001, forming 1 – 3 % volume of the meteorite (Gleason et al., 1997; Mittlefehldt, 1994), and occurs in interstices, replacing maskelynite and orthopyroxene (Gleason et al., 1997; Kring et al., 1998; Mittlefehldt, 1994; Treiman, 1995), and can be divided into at least two distinct groups: 'rosette'-type spheroid zoned concretions (Figure 1-2), and massive ankeritic 'slab'-like domains (Corrigan and Harvey, 2004; Eiler et al., 2002b). Most rosettes measure 50 to 200 μm in diameter and are composed of orange-coloured cores of ankerite/magnesiosiderite solid solution (~$(Fe_{0.2}Mg_{0.6}Ca_{0.2})CO_3$), overlain by a 5 to 10 μm–thick black rim of siderite (with substantial heterogeneously admixed nanocrystalline magnetite), itself coated by a 10 to 15 μm white magnesite rim (Eiler et al., 2002b; McKay et al., 1996). Another important compositional distinction (regarding the origin of the carbonates, see Section 1.4.2) was made between the different carbonate morphologies concerning their Mn content: the ankeritic slabs are both richer in Ca and Mn (4 – 8 mol %) and nearly constant Mn/Ca, whereas the rosettes have lower contents of both Ca and Mn and variable but generally lower Mn/Ca (Corrigan and Harvey, 2004; Eiler et al., 2002b). Sulfide grains (mainly pyrite, but possibly also pyrrhotite and greigite) occur next to primary chromite grains, within the siderite rims and possibly as trace constituents in the carbonates (Eiler et al., 2002b; Greenwood et al., 2000; McKay et al., 1996; Mittlefehldt, 1994; Treiman, 1995). ZnS and Fe-sulfate accessories were also found enclosed within or near the carbonates (though the latter mineral was later put into doubt; Wentworth et al., 1998). More recently, hematite and graphite have been identified within the carbonates, and hematite and rutile

associated with macromolecular carbon (MMC) hosted in the orthopyroxene (Steele et al., 2012a, 2012b, 2007). The origin of the hematite is uncertain (Steele et al., 2007). The slab carbonates are not bound by rims of magnesite or magnetite (Corrigan and Harvey, 2004; Eiler et al., 2002b), and in some surfaces, rings of magnetite are not associated with carbonates (Steele et al., 2007). Most likely, carbonates were once present inside these rings of magnetite, but it is unclear whether they dissolved or vaporised in some posterior event (Steele et al., 2007), and why this happened to some carbonates and not all. Figure 1-2 depicts my own observation in the ALH 84001 aliquot available to study for this thesis, of a partially 'retreating' carbonate core, were part of the magnetite-rich rim is left behind. The carbonates have been dated to 3.92 ± 0.04 Ga based on ^{40}Ar-^{39}Ar, Rb-Sr and U-Th-Pb dating (Nyquist et al., 2001). They were, therefore, formed in a secondary process after the crystallisation of the magmatic parent, which has been dated as 4.51 ± 0.11 Ga with ^{40}Ar-^{39}Ar, Rb-Sr and Sm-Nd (Nyquist et al., 2001), though this age has been revised to 4.091 ± 0.030 Ga by Lapen et al. (2010), who argued that ^{176}Lu-^{176}Hf measurements are more reliable than the $^{146,147}Sm$-$^{142,143}Nd$ system for ALH 84001 because the phosphate phases disturb the apparent age of the latter system (resulting in ages older than the Solar System). The magnetite nanocrystals, together with polycyclic aromatic hydrocarbons (PAHs), sulfides, and fossil-like structures within the carbonate rosettes were interpreted as possibly biogenic (similar to an origin by magnetotactic bacteria on Earth; McKay et al., 1996; Thomas-Keprta et al., 2009, 2000), but these structures have since been explained abiogenically (e.g.,, Golden et al., 2001, 2000; Steele et al., 2012a, 2012b, 2007; Treiman and Essene, 2011; Treiman et al., 2002). This thesis focuses largely on the origin of these features, beginning with the hypothesis that they are abiogenic.

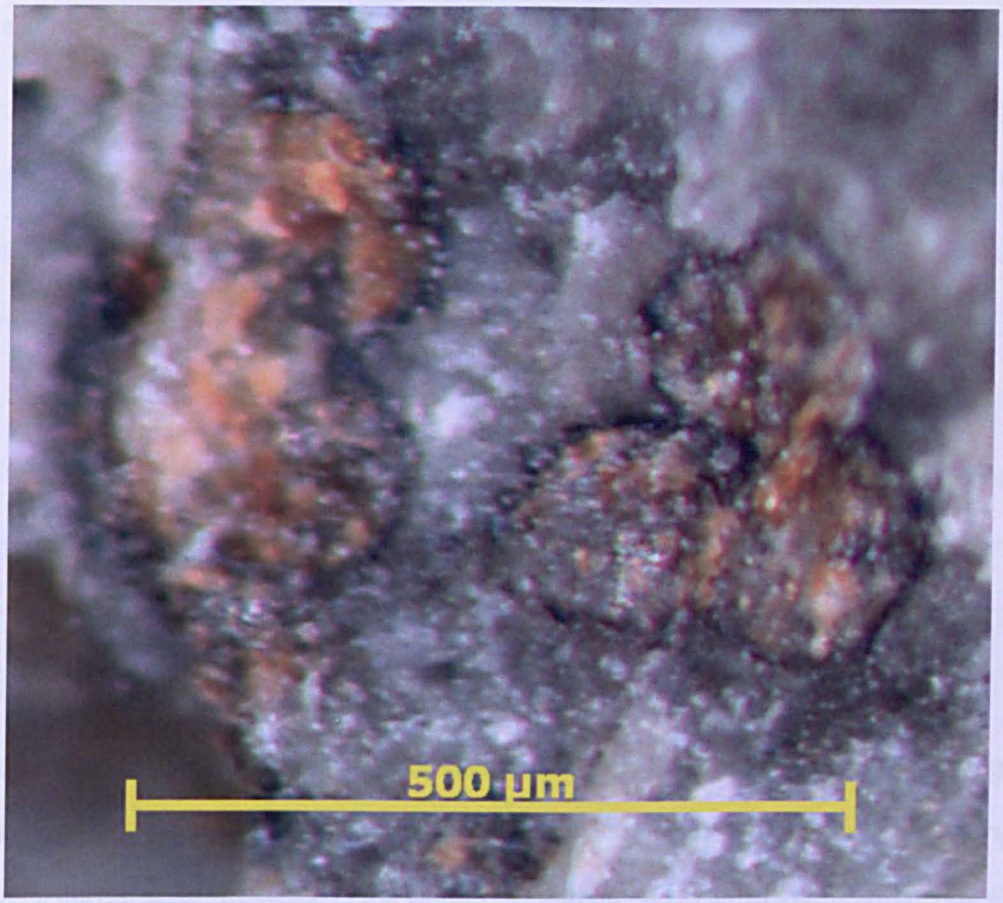

Figure 1-2: Carbonate rosettes typical in ALH 84001 observed under optical microscope, with orange ankerite cores and a single black siderite-magnetite-rich rim. Note the three fused rosettes on the right. The left-most of the fused rosettes is missing part of the ankerite core, revealing the orthopyroxene/maskelynite beneath, and leaving behind the black siderite-magnetite-rich rim. It is unknown whether the 'retreat' of the core is due to dissolution/vaporisation after formation, or whether it is simply due to handling. See Section 1.4.2 for a review of possible formation mechanisms.

1.4.2 Abiogenic formation of the carbonates

A large range of P-T conditions and formation environments have been invoked to explain the abiotic formation of the alteration assemblage, which are summarised in this section. Figure 1-3 shows the range of formation temperatures described in the literature.

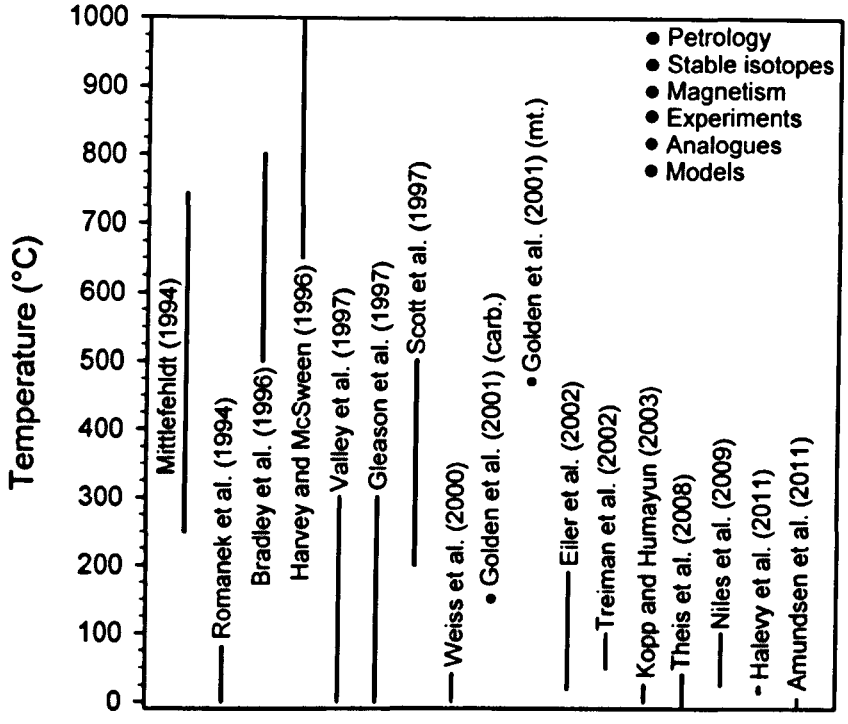

Figure 1-3. Range of temperatures at which the carbonates in ALH 84001 have been considered to have formed, from a variety of techniques and studies. 'Carb.' refers to the carbonates, and 'mt.' refers to magnetite, where different formation conditions are given by the same authors.

1.4.2.1 Petrology, and mineral equilibria and stability

Initial petrographic and petrologic observations, along with assessments of mineral equilibria (thermometry of the $CaCO_3$-$MgCO_3$-$FeCO_3$ system) indicated that the carbonate rosettes must have nucleated and grown at up to ~700 °C by upwelling cooling hydrothermal fluids rich in CO_2 and poor in H_2O (Mittlefehldt, 1994; Harvey and McSween, 1996; but cf. work by the same authors, Mcsween and Harvey, 1998, where a reappraisal of the data led to it being interpreted as a low temperature, alkaline lacustrine environment undergoing evaporation). Shock melting of pre-existing carbonates as a result of an impact has also been proposed as a mechanism (Scott et al., 1997), given that ALH 84001 demonstrates evidence of being shocked (possibly up to five times; Treiman, 1998). Impact appears to have melted and mobilised the plagioclase (rather than

transforming it to maskelynite), and produced differing carbonate globule forms and shapes in the crushed and uncrushed zones of the meteorite (Scott et al., 1997). From this, Scott et al. (1997) inferred that the carbonates crystallised from an impact melt from a pre-existing carbonate, which was heated and mobilised by high pressure (> 10 GPa). This high pressure scenario appears to be compatible with the scarcity of phyllosilicates, which should be abundant in an aqueous alteration scenario.

Additionally, Bradley et al. (1996) observed the morphologies of the magnetite nanocrystals (elongated 'whiskers' and platelets) by transmission electron microscopy (TEM) and interpreted (at least some of) them as having being formed at 500 – 800 °C by condensation from a vapour phase or precipitation from a supersaturated fluid. The recent detection of graphite with Raman spectroscopy and TEM, associated with the magnetite, also points to a relatively high temperature origin (at least 350 °C) of the carbonates if they formed in the same event (Steele et al., 2012a).

Contrary to the observations by Scott et al. (1997) on mobilised plagioclase, Gleason et al. (1997) and Kring et al. (1998) note that the maskelynite was probably replaced by the carbonates in dissolution-precipitation reactions based on textural and compositional analyses of these phases. They favour a scenario where shock pressures greater than 31 GPa produced the maskelynite, and later mildly to strongly basic hydrothermal solutions (pH = 7 – 12, T = < 350 °C) dissolved the maskelynite and rapidly replaced it with radially growing carbonates in up to 1 million years, but not long or hot enough to devitrify the remaining maskelynite. In this scenario, the hypothetical fluid would progressively be more enriched in K, Na and Al (Gleason et al., 1997; Treiman, 1995). What seems overlooked in these models, where carbonate growth is mediated by maskelynite dissolution, is the elevated Mn content in the slab-like carbonates (up to 8 mol %; Corrigan and Harvey, 2004; Eiler et al., 2002). Maskelynite is not a phase bearing high Mn-

concentration in ALH 84001 (Gleason et al., 1997; cf. terrestrial plagioclase containing only trace amounts of MnO in analyses from Wedepohl, 1969, p. 25–D–12) so a percolating fluid would need to have contained substantial Mn in solution. As textural evidence for dissolution of the (more Mn-rich) orthopyroxene is scarce (or non-existent), the Mn content in the carbonates seems likely to have come from the dissolution of Mn-bearing phases, but not from the phases in the meteorite per se. The question of the Mn content in the carbonates and the meteorite is revisited in more detail in the thermochemical modelling chapter (Chapter 4) and the conclusion (Chapter 6).

Studies on the diffusivities of Mg in calcite and Ca in magnesite demonstrated that zoned carbonates would homogenise at temperatures > 400 °C, annealing chemical variations on the scale of ~ 1 μm between 100 and 1000 years (Kent et al., 2001). From this, Kent et al. (2001) extrapolate their data to lower temperatures and contend that the carbonates in ALH 84001 were unlikely to have experienced temperatures below ~200 to 400 °C; however, the diffusion rates of Fe and iron-bearing carbonates were disregarded in their study. Nevertheless, the stability of siderite and the inorganic synthesis of Fe-Ca-Mg carbonates at low temperatures were studied by numerous other authors (notably Hollingbery and Hull, 2010; Koziol, 2004; Romanek et al., 2009) and are further explored in Chapter 4 (thermochemical modelling).

Insights into the magnetic field properties of the meteorite further expounded the low P-T conditions (< 40 °C) it must have experienced prior to ejection (Weiss et al., 2000).

1.4.2.2 Isotope systematics and thermometry

High temperature explanations (e.g., Harvey and McSween, 1996; Mittlefehldt, 1994; Scott et al., 1997) assumed formation of the carbonates under equilibrium conditions, resulting in their use of major element and mineral equilibria thermometry in order to

determine their formation temperature. However, the carbonates are very unlikely to have formed under chemical and isotopic equilibrium conditions, as evidenced by the core to rim variability in stable carbon and oxygen isotopes across the carbonates (e.g., Niles et al., 2005; Romanek et al., 1994a, 1994b; Valley et al., 1997). A changing composition of CO_2-charged fluids and equilibrium conditions of formation as carbonates precipitated could also account for the zoning (Gleason et al., 1997; Treiman, 1995). Carbon and oxygen stable isotope analyses, Sr/Ca carbonate thermometry, and $^{12}C^{16}O^{16}O$ – $^{13}C^{18}O^{16}O$ "clumped isotope" thermometry of the carbonates, revealed that relatively low temperature (14 – 190 °C) fluids were responsible for producing the carbonates (Eiler et al., 2002b; Halevy et al., 2011; Romanek et al., 1994a). Specifically, the higher $\delta^{18}O_{SMOW}$ in the carbonates compared to the host rock is indicative of an external source for the carbonates, particularly from a permeating fluid (Romanek et al., 1994a). The large range in high $\delta^{18}O$ (0 – +22.6 ‰; Eiler et al., 2002; Romanek et al., 1994a; Valley et al., 1997) and $\delta^{13}C_{PDB}$[v] (+27 – +64 ‰; Grady et al., 1994; Halevy et al., 2011; Jull et al., 1997; Niles et al., 2005; Romanek et al., 1994a; Valley et al., 1997) suggests high variability of $\delta^{18}O$ and $\delta^{13}C$ within the carbonates themselves, and that the carbonates did not experience equilibrium with the host rock or compositional and isotopic homogenisation, as would occur at high temperatures (e.g., Hoefs, 2009, p. 15) typical in metamorphic carbonates (e.g., Sheppard and Schwarcz, 1970). Moreover, a series of reactions would be observed at higher temperature equilibrium (e.g., 4 enstatite + 1 CO_2 = 1 anthophyllite + 1 magnesite at ≈ 500 °C; Johannes, 1969). The compositional and isotopic variability suggests that the fluid responsible for the carbonate formation was either in contact with the martian atmosphere (Romanek et al., 1994a) and/or came from a high pH spring environment (Mcsween and Harvey, 1998; Niles et al., 2005; but cf. Niles et al., 2009, where a high pH environment is

[v] Pee Dee Belemnite standard (PDB), for the deviation in $^{13}C/^{12}C$.

unsuitable for the precipitation of these carbonates). However, rosettes and carbonates show differences in texture, major and minor element compositions, and $\delta^{18}O$, and presumably have different origins (Eiler et al., 2002b). Whereas the rosettes are clearly in disequilibrium relative to the surrounding silicate host (and itself), the slabs are similar in $\delta^{18}O$ (+5.5 ± 2.2 ‰) and major element ratios (e.g., Fe/Mg ~ 0.4) to the orthopyroxene ($\delta^{18}O$ +4.9 ± 1.2 ‰, Fe/Mg ~ 0.38; Eiler et al., 2002). As such, it has been proposed that the rosettes are aqueous precipitates consistent with low temperature diagenetic or evaporitic processes, and the slabs are shocked rosettes (over 15 kbar and up to 20 kbar, 300 – 700 °C; Eiler et al., 2002). If this occurred, it is unclear why not all rosettes were converted to slab-like carbonates and why there is no evidence of decarbonation in at least some carbonates – unless the graphitic and macromolecular carbon described by Steele et al. (2012b) is the result of decarbonation and not a vapour phase or fluid condensation as they described.

Sulfur stable isotopes exhibit seemingly inconsistent trends in the sulfides of ALH 84001, which may be due to different origins for the different sulfides: sulfides (probably pyrite) in the rims of carbonates appear to have $\delta^{34}S$ values of −9.7 to −4.6 ‰, while sulfides with positive $\delta^{34}S$ values (+2 to +8 ‰) exist elsewhere in the meteorite (Boctor et al., 1998; Greenwood et al., 2000, 1997; Shearer et al., 1996). Greenwood et al. (2000) ascribed the negative $\delta^{34}S$ to hydrothermal (possibly post-impact as opposed to post-magmatic) activity, which formed the sulfides, whereas other sulfides could be primary.

Other stable isotope studies report $\delta^{56}Fe$ = +0.62 ± 0.11 ‰ and $\delta^{57}Fe$ = +0.83 ± 0.15 ‰ for the bulk carbonates, which, used with the partition coefficients for silicate-carbonate fractionation of Fe, determines the isotopic fractionation between the carbonates and silicates in ALH 84001 ($\Delta^{56}Fe$ = +0.6 ‰; Theis et al., 2008). A temperature of precipitation was derived from this fractionation (-10 ± 30 °C; Theis et al., 2008). This, of

course, assumes that the Fe reservoir from which the carbonates were formed was the same as the Fe reservoir the silicates were crystallised from. However, this is considered unlikely, given for example the enhanced ratios of $^{87}Rb/^{86}Sr$ and $^{87}Sr/^{86}Sr$ detected in the carbonates, interpreted as evidence that the fluid that deposited the carbonates leached pre-existing phyllosilicates (possibly celadonite or smectite; Beard et al., 2013).

1.4.2.3 Terrestrial analogues for ALH 84001

Terrestrial analogue rocks (or 'analogues') here denote rocks that demonstrate similar compositions, petrology and petrography as martian meteorites, and consequently, are presumed to have formed in similar conditions. In analogue studies specifically looking to understand the carbonate formations in ALH 84001, Treiman et al. (2002) compared the rosettes to very similar non-biological formations in lherzolite xenoliths from northern Spitsbergen, Svalbard (Norway). These formations probably deposited from a single event, i.e., from cooling primary mantle CO_2-rich fluids at ≥ 50 °C. Some features compare well morphologically to the rosettes, though they differ slightly compositionally (Steele et al., 2007; Treiman et al., 2002). Hematite and MMC were later identified in the carbonates of the Svalbard xenoliths, as in ALH 84001 (Steele et al., 2007). The MMC was probably formed in the same process, with cooling hydrothermal fluids (Steele et al., 2007). Amundsen et al. (2011) also discussed a possible cryogenic origin for the zoned carbonates in both ALH 84001 and Spitsbergen by determining the composition of the neighbouring blue ice. They speculate that melting ice with high Mg/Ca ratio could have mixed with mantle derived fluids to form the carbonates, and low $\delta^{18}O$ values in the Svalbard carbonates could be more representative of freezing than hydrothermal deposition (Amundsen et al., 2011).

Chemically and mineralogically zoned carbonates similar to the rosettes have also been described in the alkaline (pH ~ 9.7) Lake Van, Turkey (Kazmierczak and Kempe, 2003). The origin of these carbonates is uncertain, with conflicting biological and abiological moderated models proposed. However, groundwater rich in divalent cations (i.e., Fe^{2+}, Mn^{2+}, Mg^{2+}, Ca^{2+}) percolating through crystalline rocks into an alkaline lake (pH 9 – 10) at < 25 °C appears to be a plausible mechanism for them, including the microstructures interpreted as possible fossils (Kazmierczak and Kempe, 2003; Kempe and Kazmierczak, 1997).

1.4.2.4 Experimental alteration studies

In experimental studies, Golden et al. (2000) abiotically produced zoned carbonate globules similar to the rosettes in ALH 84001 at 150 °C and even amorphous carbonate spheres at 25 °C in under 96 hours. Golden et al. (2001) expanded on prior work to form magnetite and Fe-sulfides as well at 470 °C. The solution used in the experiment contained high CO_2 content as well as $CaCl_2$, $FeCl_2$, $MgCl_2$, $NaHCO_3$, and elemental sulfur.

Baker et al. (2000) found that aqueous alteration of a martian analogue basalt in a flow-through reactor was able to form calcite, ankerite and magnesite at 23 °C, 1 – 2 bar CO_2 pressure and a water-to-rock ratio (W/R) of ~ 200, while avoiding the precipitation of hydrous silicates, although the morphology of the rosettes was not replicated, and the composition of the analogue basalt differed somewhat from ALH 84001.

Experimental studies are further expanded on in Chapter 5 (environmental chamber experiments).

1.4.2.5 Thermodynamic and thermochemical modelling

Finally, thermochemical reaction modelling has been used to constrain the carbonate formation process and P-T-X[vi] conditions. The observation of ZnS enclosed within carbonate in ALH 84001 (and the assumption that it precipitated with it) has led to the calculation that the alteration fluid had a pH > 7.8 and formed the carbonates under reducing conditions (Eh[vii] < −0.1 V) at < 300 °C ('but still warmer than those of SNC[viii]-type solutions'; Wentworth and Gooding, 1995). Although low temperature (10 – 25 °C) evaporites are well characterised in the nakhlite group of martian meteorites (e.g., Bridges and Grady, 2000, 1999; Bridges et al., 2001), it has since been reasonably well established that temperatures experienced by the SNCs for some of their secondary alteration formation were relatively high temperature (90 – 300 °C), probably driven by post-impact (e.g., Bridges and Schwenzer, 2012; Changela and Bridges, 2010; Schwenzer and Kring, 2013, 2009) and/or magmatic (> 700 °C; Filiberto et al., 2014) hydrothermal systems.

On the other end of the temperature spectrum, Kopp and Humayun (2003) contended that the rims of the carbonate rosettes were possibly formed as a result of Antarctic alteration, based on kinetic thermochemical modelling. They observed that partial dissolution of the carbonates and reprecipitation as rims under modern martian and terrestrial CO_2 pressures (8 mbar and 0.35 mbar respectively) was feasible at < 25 °C in < 50 years. They justified the high $\delta^{18}O$ measured in the rims (e.g., Eiler et al., 2002) as typical for Antarctic carbonates based on alteration of carbonates in other meteorites (Grady et al., 1989) despite isotopically lighter meteoric waters in Allan Hills (Fireman and Norris, 1982). It is

[vi] P = pressure, T = temperature, X = composition.

[vii] Eh = reduction potential, the tendency an aqueous solution has to gain electrons (to be reduced), measured in volts.

[viii] The Shergottite—Nakhlite—Chassignite suite of martian meteorites; an older designation of martian meteorites.

worth noting that this model considered only the dissolution and precipitation rates of pure siderite and magnesite as endmembers, and no carbonate solid solutions were studied. Moreover, the CO_2 pressure varied after initial equilibrium with the solution (i.e., a closed-system model), and the carbonates have been dated at 3.92 ± 0.04 Ga (Nyquist et al., 2001), while the terrestrial residence age is ~ 13 ka (Jull et al., 1995).

Niles et al. (2009) proposed a model contrary to the one described by Kopp and Humayun (2003), which used thermochemical equilibrium conditions to form the carbonates in martian conditions relying on water-rock interaction between a fluid and ALH 84001 or surrounding rocks of identical composition. They constrained the chemistry of the fluid required to deposit the carbonates to have a Mg/Ca ratio > 5.3 and an Fe/Ca > 1, and a pH = 5 – 7 (contrary to the proposed high pH environment in Niles et al. (2005)), temperatures ideally between 50 – 100 °C and with elevated (open) CO_2 fugacities (0.1 – 1 bar). The mechanism they proposed was an upwelling CO_2-rich fluid encountering ALH 84001, depositing the carbonates and depressurising (or evaporating) into a hypothetical dry, low-pressure early martian atmosphere. They contended that the elevated $\delta^{18}O$ and $\delta^{13}C$ in the carbonates would be maintained (contrary to their expected depletion in evaporitic environments on Earth) if H_2O pressure in the atmosphere was low. Several caveats exist with this model (see Chapter 4) including an assumption of equilibrium conditions for the formation of the carbonates (see e.g., Valley et al., 1997) and the formation of phyllosilicates and oxides under low temperature conditions (mineral types that are not actually found in ALH 84001). An explanation for the slab carbonates was also not addressed.

Van Berk et al. (2011) varied CO_2 partial pressures in their thermodynamic model, thereby controlling the extent of water-orthopyroxenite interactions. Furthermore, they considered equilibrium and disequilibrium conditions in order to simulate a possible mechanism for

the development of zonation in the rosettes. They found that equilibrium conditions worked best to explain the observed carbonate zonation (from magnesiosiderite to magnesite), coupled with a progressive decrease of CO_2 pressure at a constant temperature (5 °C or 75 °C), pH < 7 and a water/rock ratio (W/R) = 438 mol mol^{-1}[ix]. They conclude that a setting in which ALH 84001 must have been in when the carbonates formed in the Noachian was at the most 500 m deep[x], 'adequate surface temperatures and thermal gradients' existed, and CO_2 degassed from a CO_2-rich aquifer in which ALH 84001 was submerged. A number of problems can be identified in this model, including the limited W/R considered (only three: 43.8, 438 and 4380 mol mol^{-1}), the disequilibrium scenario not producing more realistic results, the production of Ca-rich montmorillonite in the model and discounting the Mn content in carbonates, which is relatively elevated in the slab carbonates (up to 8 mol %; e.g., Eiler et al., 2002) and would affect the solubility of endmembers and carbonate solid solutions. On the other hand, the characterisation of CO_2 pressures is well documented in this model.

Thermochemical modelling features strongly in this thesis, and further information and critiques of models in the literature may be found in Chapter 4.

1.5 Shergottites

While samples of ALH 84001 were being sourced, an opportunity was presented to investigate a newly discovered martian shergottite find (Northwest Africa 6234). Though unlikely to belong to the early martian crust (see below), characterising the mineralogy and

[ix] i.e., Calculated as ~ 70 kg water/1 kg rock, if the host orthopyroxenite rock is 97 mol % orthopyroxene, 0.6 mol % olivine, 0.2 mol % maskelynite, 0.5 mol % pyrite and 1.2 mol % apatite, as considered by van Berk et al. (2011) — MMD.

[x] Even though their model does not account for total pressure — MMD.

examining the sample for possible evidence of aqueous alteration – martian or otherwise – was considered important. For this reason, it is appropriate to contextualise the shergottites. The shergottites are the most numerous group of martian meteorites[xi]. Shergottites are also the youngest martian meteorites, generally thought from K-Ar, Rb-Sr, Re-Os, Sm-Nd, Lu-Hf and U-Pb radiometric isotope systematics to have crystallised between ~ 150 – 575 Ma ago (Bloch and Ganguly, 2014; Debaille et al., 2008; Nyquist et al., 2001), an interpretation challenged by the whole-rock Pb-Pb date (> 4.0 Ga; Bouvier et al., 2009, 2005) and the possibility of age resetting by shock (El Goresy et al., 2013). Nevertheless, Pb-Pb systematics are more susceptible to modification by shock, thermal and aqueous alteration and contamination effects compared to Sm-Nd and Rb-Sr (Gaffney et al., 2011), lending credence to the fact that the Pb-Pb radiometric age may be the disturbed systematic in the shergottites.

The shergottites may be classified, in the first instance, according to their petrology and lithology, into three separate groups: basaltic, lherzolitic, and olivine-phyric (Goodrich, 2002; McSween, 1994; Nyquist et al., 2001). Basalts (such as the type name Shergotty) are basaltic or diabasic Fe-zoned clinopyroxene (pigeonite and augite) and maskelynite-rich rocks, as well as Ti-magnetite and ilmenite (Goodrich, 2002; Nyquist et al., 2001). Lherzolites (e.g., Allan Hills A77005 and Northwest Africa 2646) are cumulates composed of 40 – 60 vol. % olivine grains in large orthopyroxene crystals, poikilitic pigeonite, and low plagioclase content (< 10 vol. %; Nyquist et al., 2001). Olivine-phyric shergottites (e.g., Tissint and NWA 6234), though similar in whole-rock composition to the basalts, are distinct for having porphyritic olivine crystals, chromite, and low augite contents in a fine-

[xi] 107 meteorites including pairs, or 57 out of 70 unique martian specimens as of October 2014, see http://www.imca.cc/mars/martian-meteorites-list.htm and http://www.lpi.usra.edu/meteor/index.php compiled from the Meteoritical Society's Meteoritical Bulletins for an up to date list.

grained pigeonite and plagioclase (now maskelynite) groundmass, and chromite instead of Ti-magnetite and ilmenite (Bridges and Warren, 2006; Goodrich, 2002).

Another classification of the shergottites, based on the light rare earth element (LREE) patterns observed in them, distinguishes between highly depleted, moderately depleted and slightly depleted shergottites, with respect to incompatible elements in CI chondrites (Bridges and Warren, 2006). This classification does not correlate precisely with the petrological/lithological classification already mentioned, although most basaltic shergottites are slightly depleted, lherzolites tend to be moderately depleted and olivine-phyric shergottites are generally highly depleted. Instead, the LREEs (particularly the La to Lu ratio) appear to correlate with the calculated oxygen fugacity conditions for their source regions, indicating mantle heterogeneities (Bridges and Warren, 2006; Herd et al., 2002; Herd, 2003).

Secondary alteration products have been observed in shergottites, but distinguishing between terrestrial contaminants and martian phases is not as straightforward as it is for the nakhlite group of martian meteorites and ALH 84001 (Bridges et al., 2001). Near-surface secondary alteration which has been proposed to be probably martian includes:

$CaCO_3$ and sulfate (possibly gypsum, $CaSO_4 \cdot H_2O$) in Elephant Moraine 79001 (EET 79001; (Gooding et al., 1988), probably precipitated in an evaporative environment (Bridges et al., 2001) and/or were shock implanted after weathering of the host rock (Gooding et al., 1988). Substantial P and Mg measured in the $CaCO_3$ (> 0.08 P atoms per formula unit (apfu) and > 0.2 Mg apfu) may be attributed to intergrown phosphate (Gooding et al., 1988), although its origin is uncertain. Additionally, Na-Ca-smectite, illite (K-Na-Ca mica) and Fe-oxihydroxides occurring in the meteorite were purported to be martian (Gooding, 1992).

Ca-sulfate in Shergotty, similar to occurrences in EET 79001 (Wentworth et al., 2005). A report of halite and some form of phyllosilicate in Shergotty also exists (Wentworth et al., 2005, 2000), but compositional data and evidence pointing to a martian origin is tenuous.

Additionally, perchlorate (ClO_4^-), chlorate (ClO_3^-) and nitrate (NO_3^-) were found in EET 79001 hosted in a salt-rich inclusion (Kounaves et al., 2014). A possible mechanism for the formation and deposition of ClO_4^- in EET 79001 has been proposed whereby Cl-minerals (e.g., halite, often associated to the involvement of water in terrestrial environments) are photo-oxidised by UV radiation (Kounaves et al., 2014).

Hydrous amphiboles were also found in melt inclusions hosted in pigeonite in Shergotty, Zagami and Lewis Cliff (LEW) 88516, indicating that the magma from which the inclusions formed had some water (> 0.2 weight %; Treiman, 1998, 1985), but as such, the amphiboles do not represent near-surface alteration purposes.

In summary, secondary aqueous alteration in the shergottites appears to be limited and ambiguous in comparison to the more obvious carbonates in ALH 84001 (see Section 1.4) and smectite-carbonate and Fe-oxihydroxide veins in the nakhlites (e.g., Bridges et al., 2001; Bridges and Grady, 2000, 1999; Changela and Bridges, 2010; Hicks et al., 2014; Treiman, 2005; Treiman et al., 1993).

1.5.1 Northwest Africa 6234[xii]

A sample of Northwest Africa (NWA) 6234 was made available for investigation by an international consortium designed to maximise the results from studying a small, 3.31 g sample purchased from Marmet Meteorites (Filiberto et al., 2011).

NWA 6234 appears to be paired with NWA 2990, NWA 5960 and NWA 6710, all of which are meteorite finds. Based on REE abundances, mineralogy and lithology, they are classified as an intermediate olivine-phyric shergottite (Filiberto et al., 2012; Irving et al., 2011). The cores of the olivine crystals within appear to be in equilibrium with the Mg content of the bulk meteorite, signifying that NWA 6234 may represent a magma composition not derived from an extreme mantle partial melt, and instead, may represent a primitive melt (Gross et al., 2012).

The NWA 6234 sample available for study (Figure 1-4) appears to be unaltered, fine-grained (probably from rapid cooling) and with a black glassy shock-melt vein (Filiberto et al., 2012; Gross et al., 2012). The aim was to study the mineralogy, compositional variations (particularly zoning) within the minerals, and especially to analyse the glassy shock vein which cuts across the sample (Figure 1-4) in order to aid subsequent Ar-Ar analytics (not reported in this thesis) and investigate possible evidence of alteration.

[xii] Note that work carried out to characterise the mineralogy of Northwest Africa 6234 as part of this thesis was subsequently used for a conference abstract (Gross et al., 2012) and in the peer-reviewed paper by Gross et al. (2013).

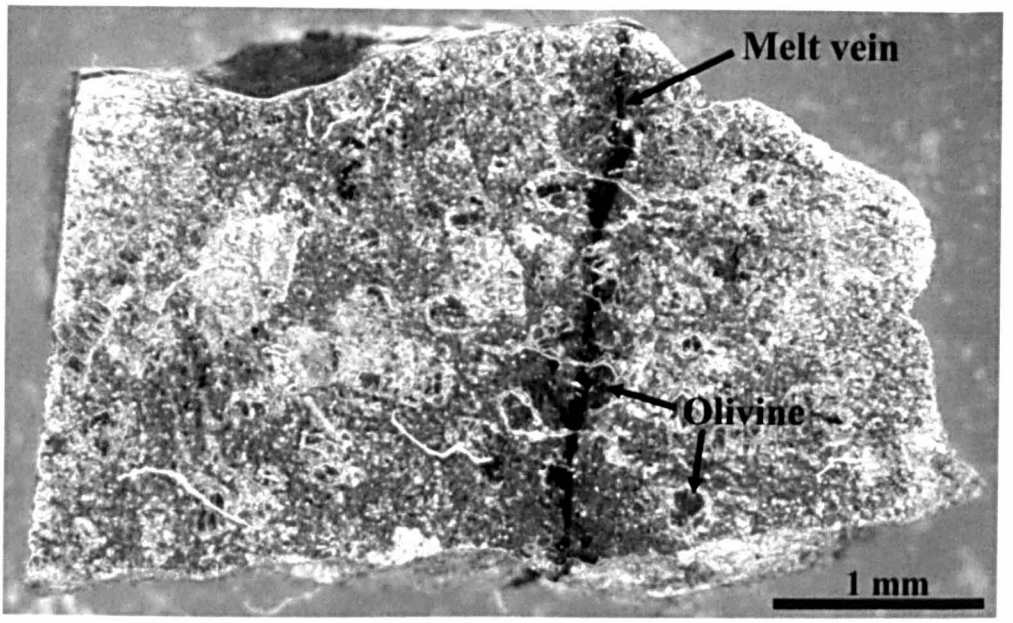

Figure 1-4. Optical microscope image of the polished NWA 6234 sample studied here.

1.6 Research questions and objectives

In a broad sense, this project aims to constrain our understanding of the role, quantity and composition of water during early times on Mars, i.e., prior to, or contemporaneous with the Late Heavy Bombardment. Specifically, in order to carry out this study, the meteorite ALH 84001 serves as a proxy for early rocks on Mars. Studying the minor alteration components will help characterise aqueous alteration in the early martian crust. As we have seen in the background review above, the nature of aqueous alteration on Mars is not entirely understood. The Noachian phyllosilicates on the surface are not entirely substituted by sulfates in the Hesperian, and other processes occurring both on local and larger scales have led to other alteration products. The alteration history of ALH 84001 is still perplexing, too. Being the only meteorite sample entirely belonging to Noachian Mars identified with certainty, ALH 84001 is our only insight into the earliest martian aqueous

processes available to analytical techniques on Earth[xiii]. Yet, with the relative scarcity of carbonates identified on the surface of Mars, and conversely, the absence of Fe-Mg phyllosilicates in the meteorite, is ALH 84001 really representative of early martian alteration processes? The work carried out in this thesis intends to answer the following research questions:

- What evidence does meteorite ALH84001 contain of aqueous processes and the presence of water on early Mars?
- Assuming that aqueous processes formed the alteration assemblage (carbonates, possible phyllosilicates, possible sulfates, etc.), what was the nature of these aqueous processes? What mechanism(s) of alteration was responsible for the assemblage, and what pressure, temperature and compositional characteristics did it have?
- What is the role of this possible aqueous system on Mars, and how does it work? Was it widespread or local? What influence did it have (if any) on a local, regional or global scale? Was it linked to the early martian atmosphere or hydrosphere?

The specific research objectives that will be followed in order to answer the questions are as follows:

- To characterise the chemistry and mineralogy of phases formed or influenced by hydrous processes in ALH 84001, in order to help constrain their formation conditions and environment.

[xiii] The meteorite NWA 7034 and its pairs were brought to public attention in 2013 (Agee et al., 2013), after the start of this study. Though dating to the early Amazonian (~ 2.1 Ga old; Agee et al., 2013), this basaltic breccia contains ~ 4.4 Ga old zircons (Humayun et al., 2013) and is the most water-rich martian meteorite to date (Agee et al., 2013).

- To construct viable thermodynamic models of the geochemical system that may have resulted in the possible signature of aqueous processes in ALH 84001. The precipitation-dissolution and mineral-fluid interaction of phyllosilicates will be investigated in particular, given their association to hydrous weathering on Noachian terrains, and the apparent absence of noticeable amounts of these in ALH 84001.
- To test the thermodynamic models experimentally, by working with analogue materials and attempting to reproduce the features of ALH 84001, in order to validate the models.
- To relate any new knowledge gained from the models and tests to published knowledge of possible workings of the martian lithosphere-atmosphere-hydrosphere interaction, and to constrain the geological settings in which they may have occurred.

1.7 Justification of research: Why water on early Mars?

As seen above, the early aqueous history of Mars is difficult to study. The complexity lies largely in the fact that there is no alternative but to interpret the conditions of early Mars somewhat indirectly, relying heavily on remote sensing of the degraded ancient terrains of Mars. Rovers and probes directly observe the martian surface on the ground, but these are not necessarily in the locations of most relevance (i.e., not on the most ancient terrains). Another way to make progress is back on Earth using thermochemical modelling, and studies of martian meteorites and relevant terrestrial analogue materials. Yet, the importance of the subject is generally axiomatic: the early history of Mars coincides with the early history of the terrestrial planets, and thus if life arose on Earth, it could have done

so on Mars too. Liquid water is a fundamental condition for the reactions in pre-biotic and biotic chemistry, so establishing how pervasive water was is especially important. Moreover, the Earth has largely recycled its ancient crust because of active tectonics. Ancient martian terrains offer valuable insight into what the early crust of the Earth might have looked like, since tectonic activity seems to have been limited on Mars. As mentioned in Section 1.4, ALH 84001 has not been free of contention for the possible biogenic origin of some of its features and the aqueous alteration it was subjected to. As such, continuing to research this meteorite will contribute to its documentation and literature as well, and its conditions of formation and alteration will be further constrained.

Another point which became progressively topical as research was carried out was the understanding of thermochemical conditions of carbonate formation, particularly with regards to carbon (particularly CO_2) sequestration from the atmosphere.

2 Analytical methods and samples

The following chapter is a description of the analytical methods used throughout this thesis, and of the samples analysed. Characterisation of the petrography of the rock samples (both meteoritic and terrestrial) and detailed compositional analyses were carried out with the variety of techniques detailed below, but additional analytical techniques (high precision mass spectrometry of carbon, nitrogen, and noble gases; Raman spectroscopy; as well as different analytical settings for the wave dispersive spectroscopy/electron probe microanalyser (WDS/EPMA; from here on, EPMA) were incorporated as work on the project progressed and a need for different analyses emerged. The rationale and details for the selection of these techniques are further described below, and links to the results are given where appropriate.

Thermochemical reaction modelling, which features heavily in this project, is detailed in Chapter 4 as it is a method which combines analytical and theoretical aspects in order to obtain results, and often necessitates an iterative process of refinement whereby the results of one model are introduced as initial data points for a subsequent model.

Experiments to produce secondary minerals and alter terrestrial analogues for martian rocks, although requiring analyses (pre- and post-alteration) with a suite of instruments are detailed in Chapter 5, as it is the experimental aspect of the technique that produced the results.

2.1 Samples and preparation

2.1.1 ALH 84001

A description of ALH 84001 can be found in Chapter 1 (Section 1.4)

Aliquot ALH84001,126 (~ 5 mg) had previously been fragmented for the work carried out in Tomkinson (2012). The remainder (Figure 2-1) not used in the aforementioned study was used in the investigations described in this thesis (Figure 2-2). This mass was fragmented (not pulverised) here using a sterilised pestle and mortar into irregularly shaped chips in order to prepare three thick sections for energy dispersive spectroscopy/scanning electron microscopy (EDS/SEM; from here on, SEM), EPMA and Raman spectroscopy. These sections were prepared by setting the chips in Buehler EPOXICURE epoxy blocks which were subsequently polished to achieve a flat surface. Polishing was accomplished using isopropyl alcohol (IPA) and silicon carbide abrasive (~ 8.4 μm particle size). Water was avoided in the preparation process to minimise the risk of physical and chemical reaction with the rock, which might have led to the possible formation of hydrated and contaminant phases.

The thick sections were coated with carbon (~ 30 nm) using a manual coater in order to ensure a conductive surface and to avoid charging the samples under the EPMA's electron beam.

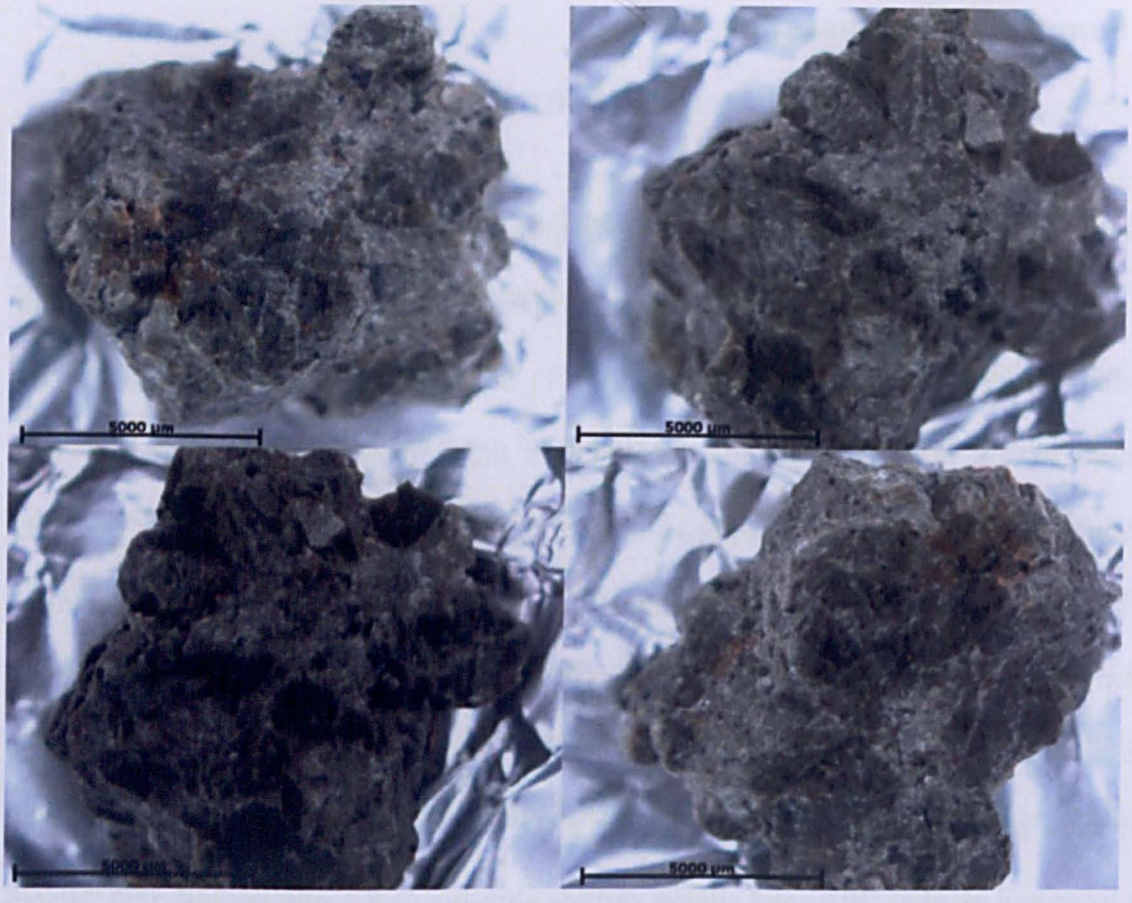

Figure 2-1. Full sample of ALH 84001 available for this study, prior to further fragmentation and preparation. Images were captured under a binocular microscope. Scale bar is 5 mm.

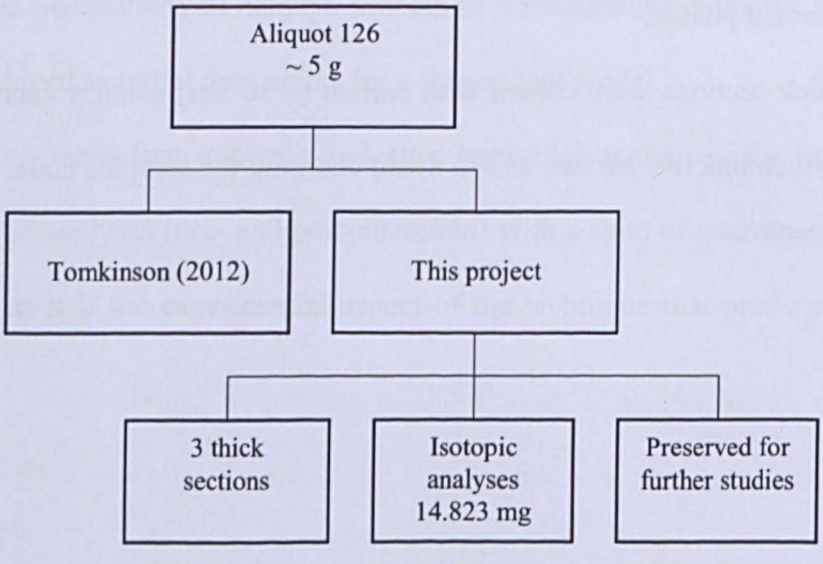

Figure 2-2. Genealogy diagram of the ALH 84001 samples used in this study.

The thick sections consisted of:

a. *ALH-section-A*: containing three medium-sized fragments of ALH 84001 (Figure 2-3), with a total surface of exposed sample of ~ 2.72 mm^2.

b. *ALH-section-B*: containing a single large fragment of ALH 84001 (Figure 2-4), with a total sample surface of ~ 3.51 mm^2.

c. *ALH-section-C*: containing 28 very small fragments of ALH 84001 (Figure 2-5), with a total sample surface of ~ 2.26 mm^2. The thick section appears to have more fragments when viewed from above, but this is due to the irregular shapes and surfaces of the fragments.

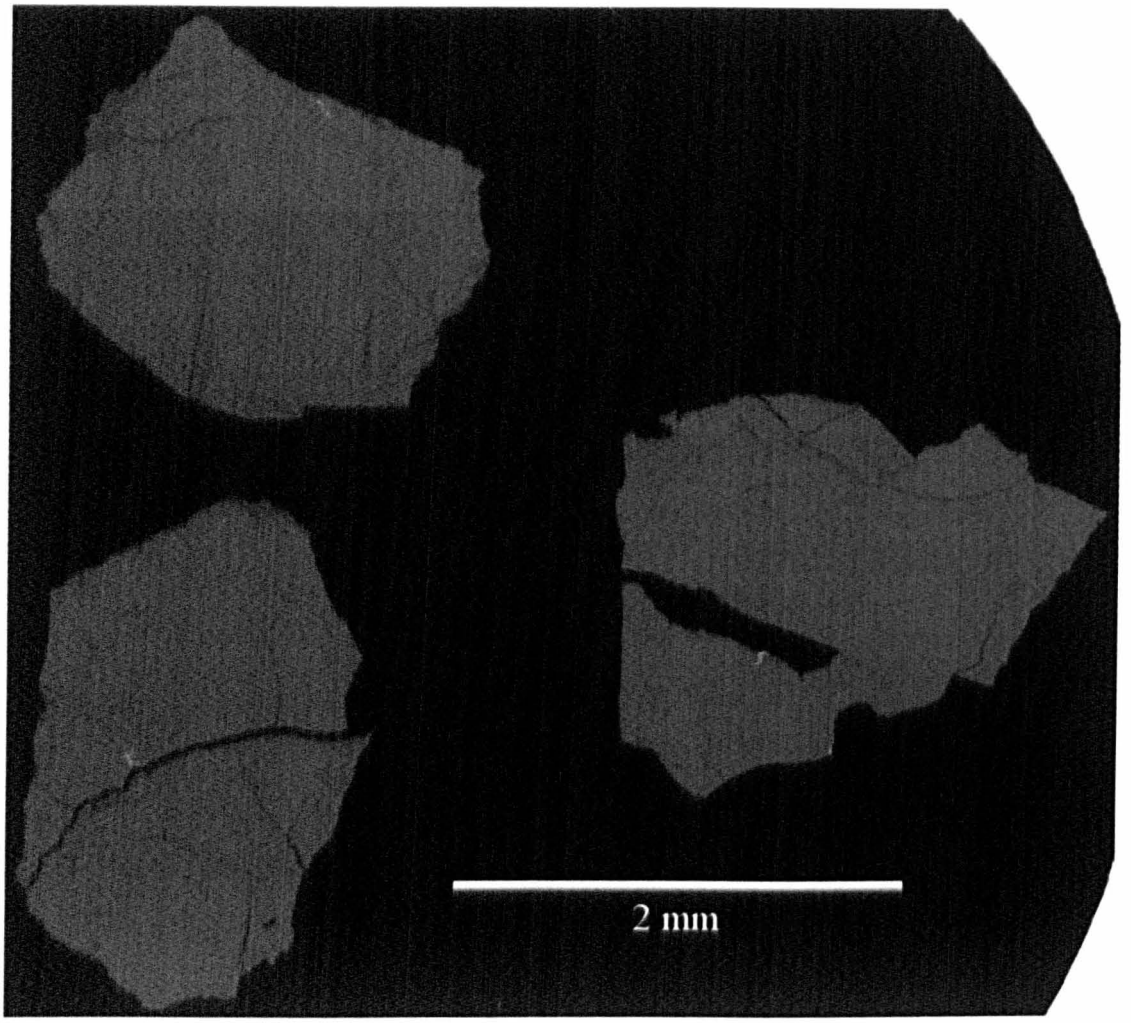

Figure 2-3. SEM BSE image of sample *ALH-section-A*.

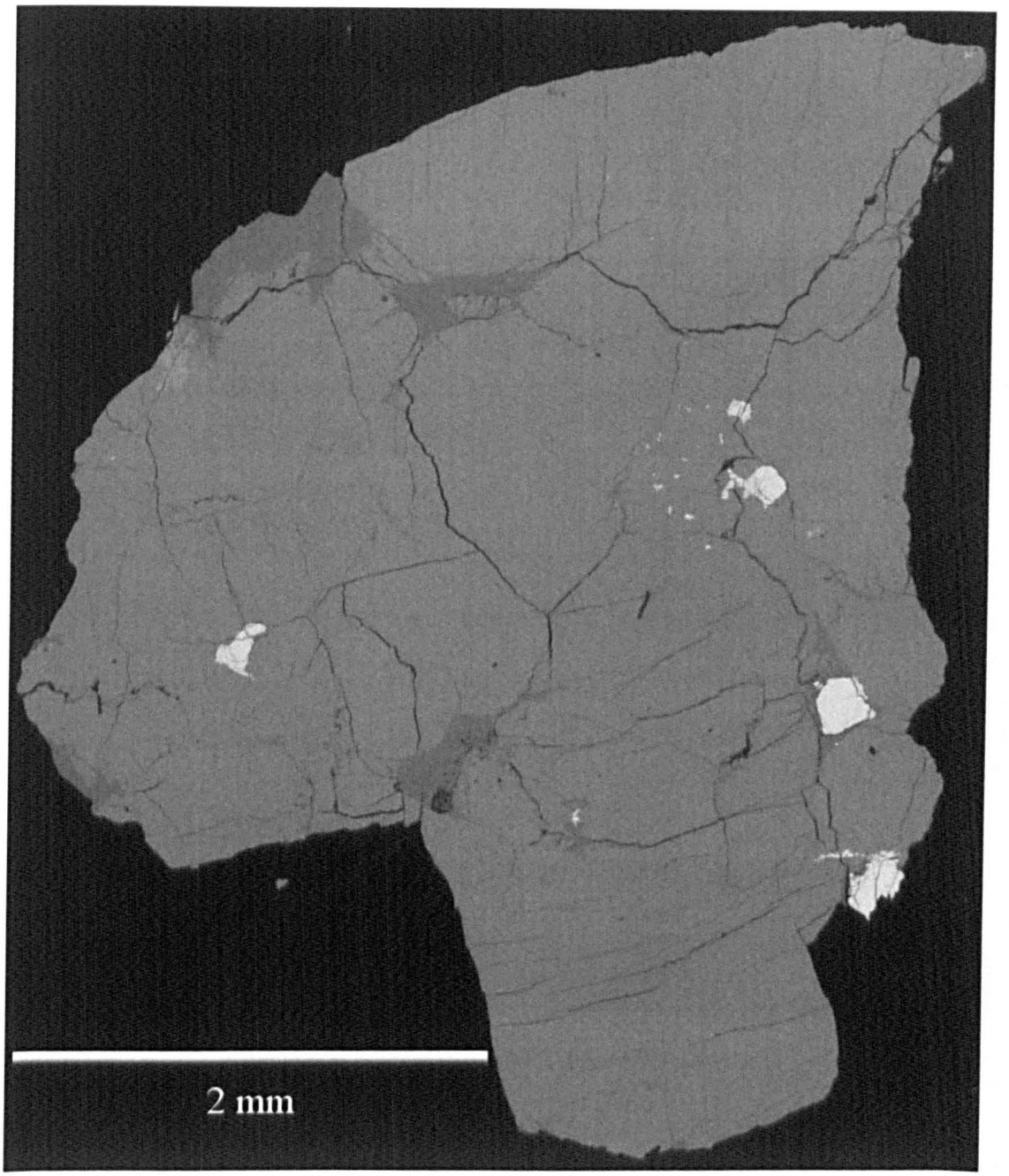

Figure 2-4. SEM BSE image of sample *ALH-section-B*.

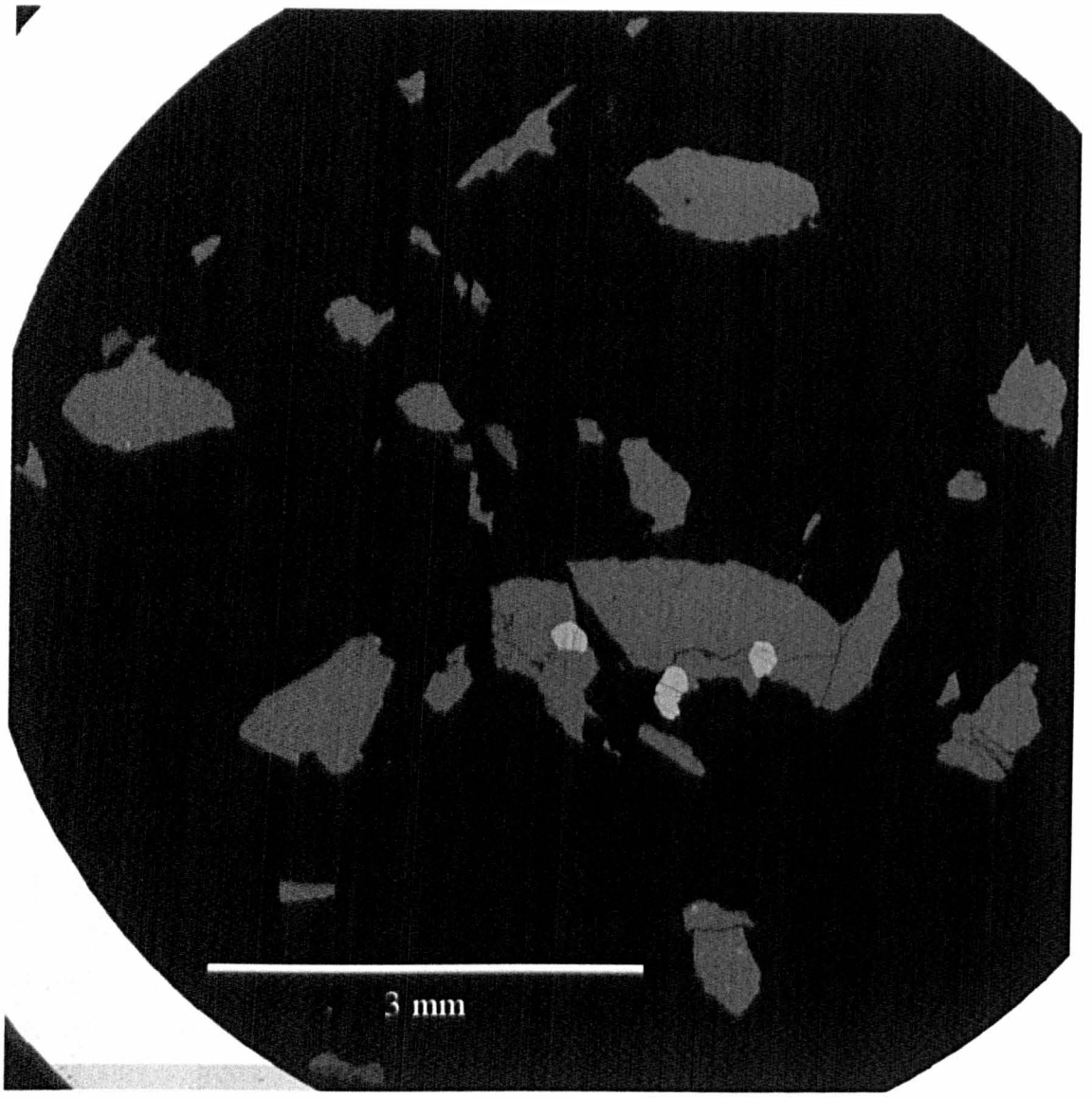

Figure 2-5. SEM BSE image of sample *ALH-section-C*.

2.1.2 NWA 6234

A description of the sample is found in Section 1.5.1. The sample was polished and coated with carbon for use in an EPMA (see Section 2.3 for a details on EPMA).

2.1.3 Terrestrial orthopyroxenite analogues for ALH 84001

Unaltered terrestrial orthopyroxenite rock samples resembling the bulk composition of ALH 84001 were sought in in order to experimentally produce in them (under controlled conditions) carbonate minerals compositionally similar to the ones in ALH 84001 (see Chapter 5). Five thin sections from four orthopyroxenite hand specimens were supplied by the Natural History Museum in London, but as further material for use in the alteration experiments could not be sourced, their analyses are not relevant to this work.

Following consultation of Dr. John Faithfull (curator at the Hunterian Museum and Art Gallery, University of Glasgow), a fieldwork was conducted in the North-West Scottish Highlands and the South-East of the Isle of Harris (Outer Hebrides) in August of 2013 to collect a sufficient amount of orthopyroxenite for the experiments. Of the sites visited and samples collected, the metaperidotite orthopyroxenite rocks outcropping at Loch an Daimh Mòr (Upper Badcall, Sutherland; see Chapter 5 for loacation details and maps) were considered the least altered and most suitable for the experimental setup, on the basis of mass collected (~ 1 kg) and composition (see Chapter 5). The Loch an Daimh Mòr (LADM) orthopyroxenite has been described as belonging to a metamorphosed layered ultramafic complex, bound by masses of serpentinite and calc-chlorite (Bowes et al., 1964). A standard (30 μm thick) thin section of the LADM sample was prepared using Struers EpoFix resin on a glass slide and carbon-coated for EPMA work.

Further sample preparation, detailed descriptions and analytical work was carried out to support the alteration experiments and is described in Chapter 5.

2.2 Energy Dispersive X-ray Spectroscopy/Scanning Electron Microscopy

Energy Dispersive Spectroscopy (EDS) is used as a means to analyse the composition of the samples. EDS analysers are typically composed of an X-ray detector, which detects and converts X-rays to voltage signals (via an ionising semiconductor crystal and then a preamplifier), and pulse processors, which measure these signals and quantify the energy of the X-rays. In scanning electron microscopes (SEM), an electron beam is focused on the sample, which reflects a portion of the electrons from the beam back as backscattered electrons (BSE) as a result of interaction between the negatively charged beam and the positively charged nuclei in the sample. Secondary electrons (SE) are also emitted from the sample due to the interaction of the beam with the electrons enveloping the nuclei of the sample. As electrons ejected from the sample's atoms' inner shells are replaced by electrons from higher shells, X-ray photons are emitted (Figure 2-6). The energies of the X-ray photons emitted are characteristic of the binding energies of the ejected and replacing orbital electrons, and therefore, of specific elements.

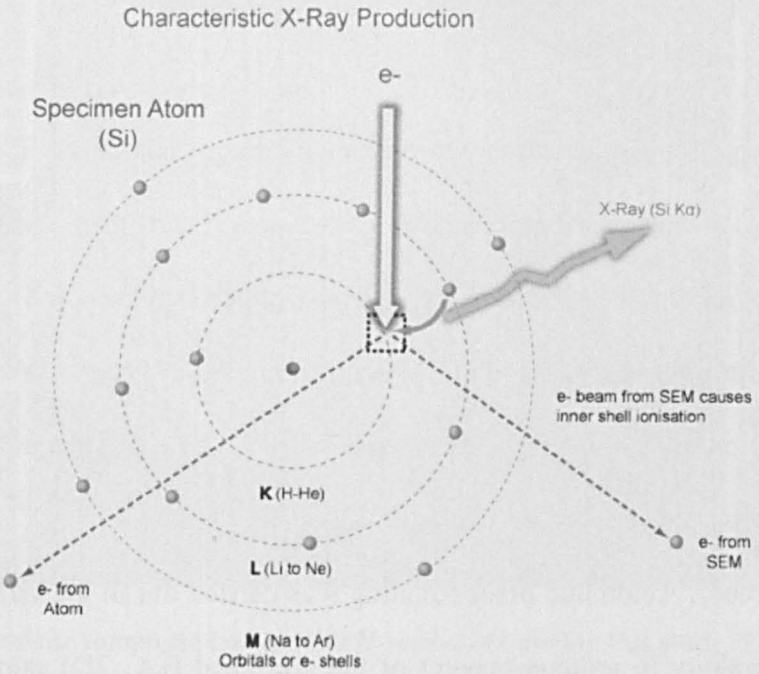

Figure 2-6. Diagram showing the interaction of the focused electron beam with the orbital electrons surrounding a nucleus in a Si atom. As an electron is ejected from the K shell (secondary electron), it is substituted by one in a higher shell (in this case, from the L shell). The excess energy from this transition to a lower energy state is released as a characteristic X-ray photon (Kα, in this case). Image from the Australian Microscopy and Microanalysis Research Facility.

2.2.1 Instrument and mapping

The SEM used in this study was a FEI Quanta 200 3D at the Department of Physical Sciences at the Open University. The EDS was an Oxford Instruments X-Max^N 80 mm^2, and the software designed to interface with it and perform analyses was Oxford Instruments' INCA.

Standard operating parameters were: 20 kV accelerating voltage, typically a 0.6 nA beam current and a 4.5 – 5 μm spot size. Magnification varied for each sample, but was typically × 200 or greater. Similarly, map image resolution, beam dwell time, processing time and

number of frames acquired were different between samples and are reported for each image.

The INCA software allows for the automated acquisition of combined BSE and elemental concentration images across a large sample, known as a 'smart map', which may be tiled and montaged. For the identification of separate mineral phases and joining different elemental concentration maps, the GNU Image Manipulation Program (GIMP) was used. Single element concentration greyscale images were given a colour and combined with other element concentration images to create false colour composites (FCC, typically using red, green and blue). Automatic pixel counting was carried out in the GIMP to determine the modal mineralogy in volume percent of the sectioned (i.e., 2D) samples. For this, a variety of thresholds were used in GIMP when selecting phases according to pixel colour (not brightness) in order to adequately separate phases of similar colour values in FCCs, and still overlook small compositional variations within. The advantage of using FCCs and pixel colour to determine modal mineralogy over simple BSE images and pixel brightness is that different mineral phases are more easily distinguishable using FCCs, where at least three element concentration maps (parameters) are used. In contrast, BSE image pixel brightness may not distinguish between minerals with low pixel brightness contrast (similar compositions, e.g., orthopyroxene and augite). Figure 2-7 illustrates the process used to calculate the modal mineralogy.

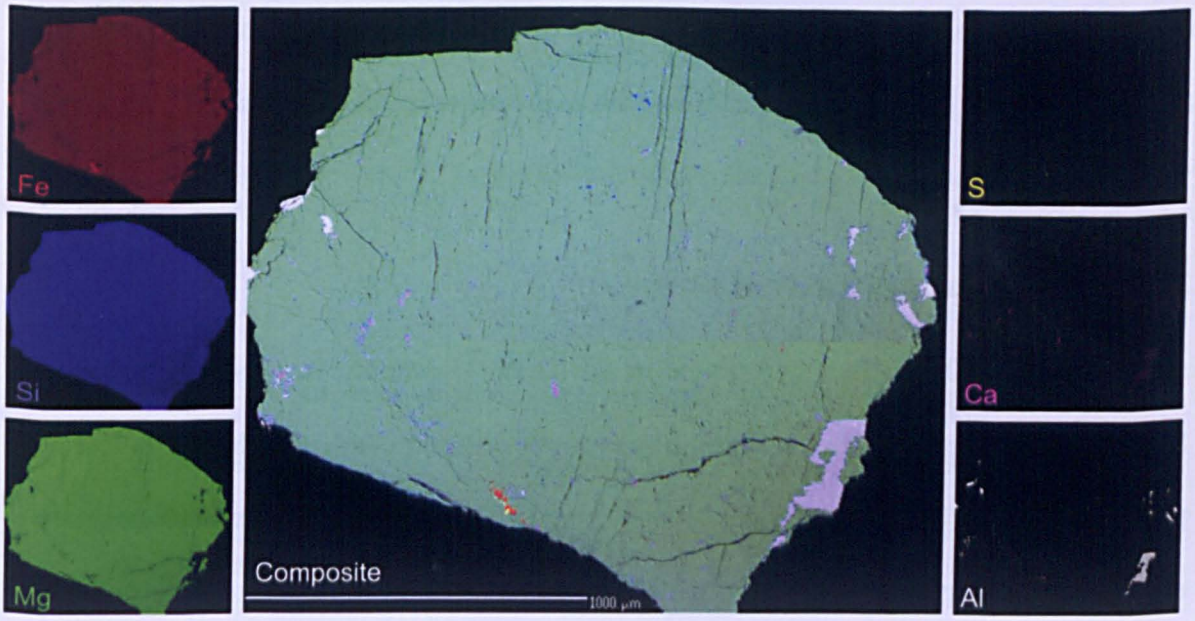

Figure 2-7. False colour composite image of *ALH-section-A1* used in this study. This FCC image is constructed by adding the element concentration maps of Fe (red), Si (blue), Mg (green), S (yellow), Ca (magenta) and Al (white). Separate phases are easily distinguished in the FCC image (centre) and pixel counts for the phases provide a modal mineralogy (in volume %) for this particular sample (~ 97.2 % orthopyroxene, ~ 1.9 % maskelynite, ~ 0.8 % carbonate, ~ 0.07 % chromite, ~ 0.07 % sulfide and 0.02 % silica). Spot analyses on the phases were required to obtain precise compositions.

2.3 Wave Dispersive Spectroscopy/Electron Microprobe

Wave dispersive spectroscopy (WDS) improves detection limits in samples for all elements with respect to EDS, as elemental peaks (characteristic X-rays) are identified and isolated from background X-rays at higher resolution. Element concentrations in a sample are determined by comparison to well characterised standards when using WDS. Standards are regularly used to calibrate the WDS detectors, and the detectors are each tuned to the peak positions of the characteristic X-rays of elements. As such, each spectrometer on a WDS microprobe can only analyse one element at a time. X-rays emitted by the sample as

a result of interaction with the electron beam are dispersed by a diffractor crystal in each of the spectrometers, and detected by the detector at the specified characteristic wavelength.

2.3.1 Instrument and analyses setups

A Cameca SX100 electron microprobe at the Open University was used in this study. Standards consisted of natural minerals and synthetic compounds (Table 2-1). Operating parameters were, unless otherwise stated (e.g., for phosphates, see below), 20 kV accelerating voltage, 20 nA current, a 10 μm spot size for spot analyses, and a 1 μm spot size for element maps. Fe was corrected for the interference with Mn. For elemental maps, the GIMP was used to create false colour composite images combining individual element concentration map, as with the EDS images (see Section 2.2.1).

The Cameca SX100 has five separate spectrometers which can measure the elemental abundance of five elements simultaneously. The diffracting crystals used consist of 1) thallium acid phthalate and large thallium acid phthalate (TAP and LTAP), 2) pentaerythritol and large pentaerythritol (PET and LPET), and 3) large lithium fluoride (LLiF).

A different procedure was used to analyse phosphate minerals in order to prevent the potential loss or mobility of volatiles (F, Cl and OH) in their structure as a result of interaction with the electron beam. A study by Barnes et al. (2013) suggested that electron microprobe beam currents of up to 20 nA did not significantly affect the OH content of an apatite standard. Small-scale variation of the OH concentration within the apatite standard was considered a larger contributor to the variation of OH concentration measured, compared to the effect of exposure to the electron beam. However, as a precaution against the possible mobility of volatiles, the beam parameters for analysing phosphates here were as follows: 20 kV voltage, 4 nA current, and a 10 μm (defocused) spot size. F and Cl

detection was validated with the *Ap005* Atlas Mountain apatite standard reported by (McCubbin et al., 2012). OH was calculated by difference (OH = 1 – Cl – F). Mineral calibration standards for volatiles in *Ap005* were SrF_2 for F, tugtupite for Cl and barite for S.

Table 2-1. Calibration standards used in regular WDS microprobe analyses.

Element	Standard	Crystal and spectrometer number	3 σ Detection limit (ppm)
F	LiF-4	LTAP 2	502
Na	jadeite-bm4	TAP 1	257
Mg	forsterite-bm4	LTAP 2	169
Al	fspr-In5	LTAP 2	103
Si	fspr-In5	TAP 1	138
P	apatite-BM4	PET 5	261
	YPO_4-Sm4	PET 5	293
S	barite-ast3	LPET 4	181
	pyrite-PP5	LPET 4	217
Cl	sylvite-BM4	LPET 4	159
K	fspr-In5	LPET 4	121
Ca	bustamite-ast3	LPET 4	113
Ti	rutile-BM4	PET 5	317
Cr	crocoite-ast3	PET 5	584
	Cr_2O_3-JB4	PET 5	753
Mn	bustamite-ast3	LLiF 3	258
Fe	hematite-ast3	LLiF 3	296
	pyrite-PP5	LLiF 3	295
Co	cobaltite-ast3	LLiF 3	416
Ni	Ni metal-JB4	LLiF 3	377
Cu	Cu metal-2	LLiF 3	316
Zn	willemite-ast3	LLiF 3	437
Rb	RbBr separate	LTAP 2	676
Sr	SrTi ox separate	LPET 4	771
Ba	barite-ast3	PET 5	1095

2.3.1.1 Post-analyses stoichiometric corrections

All EPMA spot analyses were checked for stoichiometry. Stoichiometric corrections allow assigning cations to their corresponding crystallographic sites according to their valence and size. Furthermore, Fe^{3+}, which is not directly measured by EPMA can be calculated

from stoichiometric corrections. The exact corrections applied were different for each mineral.

2.3.1.1.1 Pyroxene corrections

Pyroxene EPMA analyses were corrected using a modified version of the Brady and Perkins (2012) recalculation spreadsheet. Table 2-2 contains an example of raw oxide weight % data output by the EPMA for a spot analysis. The correction steps taken are shown in the rows beside it, ending in the site assignations for each cation and the compositional classification as a function of the wollastonite, enstatite and ferrosilite endmembers. Figure 2-8 illustrates the structure of orthopyroxene, highlighting the positions of the cation sites, while Figure 2-9 shows the preferential order of cation placement within the sites.

Table 2-2. Example of the corrections made from the raw EPMA spot analysis of a pyroxene in ALH 84001. From the oxide weight %, the number of cations and oxygen atoms are derived (columns 3 – 6). The lower than ideal charge calculated from the cations (+11.992, rather than 12; row 14) is corrected by adding Fe_2O_3 from available FeO.

Oxides	Analysis wt %	Mole cations	Mole oxygen	Norm. cations	Norm. oxygen	Atom units	Norm. Oxygen	Norm. Wt %	M2 (VI)	M1 (VI)	T (IV)	Wo (%)	En (%)	Fs (%)
SiO_2	54.19	0.902	1.804	1.977	3.954	1.977	3.954	54.19	-	-	1.977			
TiO_2	0.20	0.002	0.005	0.005	0.011	0.005	0.011	0.20	-	0.005	-			
Al_2O_3	0.49	0.010	0.015	0.022	0.032	0.022	0.032	0.50	-	-	0.022			
Cr_2O_3	0.34	0.004	0.007	0.010	0.015	0.010	0.015	0.34	-	0.010	-			
Fe_2O_3	-	-	-	-	-	0.008	0.013	0.30	-	0.008	-			
FeO	18.04	0.251	0.251	0.550	0.550	0.542	0.542	17.77	0.263	0.279	-			
MnO	0.48	0.007	0.007	0.015	0.015	0.015	0.015	0.48	0.015	-	-			
MgO	24.93	0.619	0.619	1.356	1.356	1.356	1.356	24.93	0.657	0.699	-			
CaO	1.56	0.028	0.028	0.061	0.061	0.061	0.061	1.56	0.061	-	-			
Na_2O	0.06	0.002	0.001	0.004	0.002	0.004	0.002	0.06	0.004	-	-			
Total	100.30	1.825	2.736	4.000	5.996	4.000	6.000	100.33	1.000	1.002	1.998	3.10	68.92	27.98
Ideal	-	-	-	-	-	4.000	6.000		1.000	1.000	2.000			
Calc. charge	-	5.741	-5.741	11.992	-11.992	12.000	-12.000							

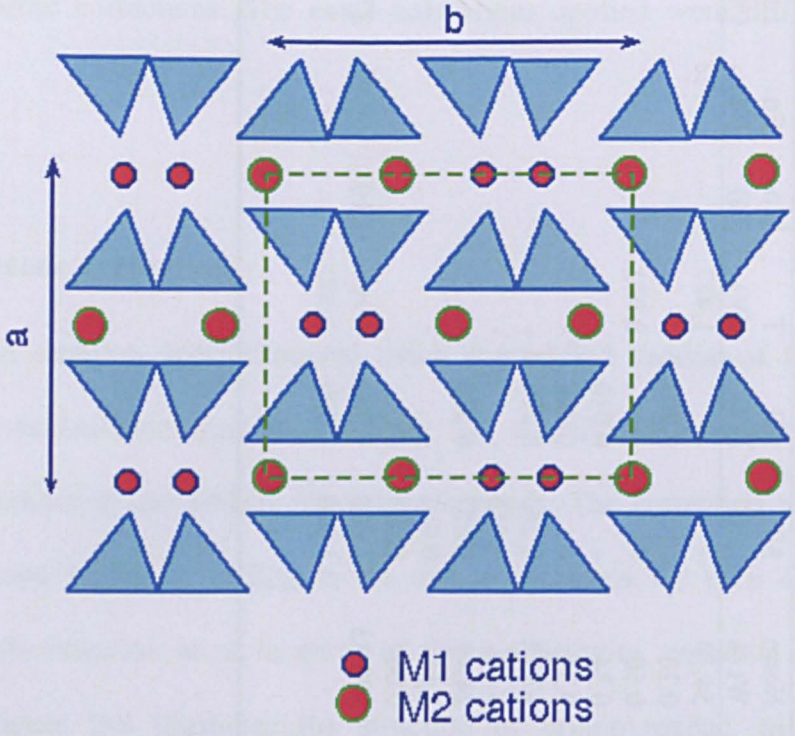

Figure 2-8. Generic cell structure of orthopyroxene, after Sandiford (n.d.) viewed parallel to the c-axis (perpendicular to the plane of the page). Blue triangles represent the silicate tetrahedra, which form chains along the c-axis. The dashed green line represents the unit cell. Si in the silicate tetrahedral may be substituted by Al^{3+} and Fe^{3+} (Morimoto, 1988).

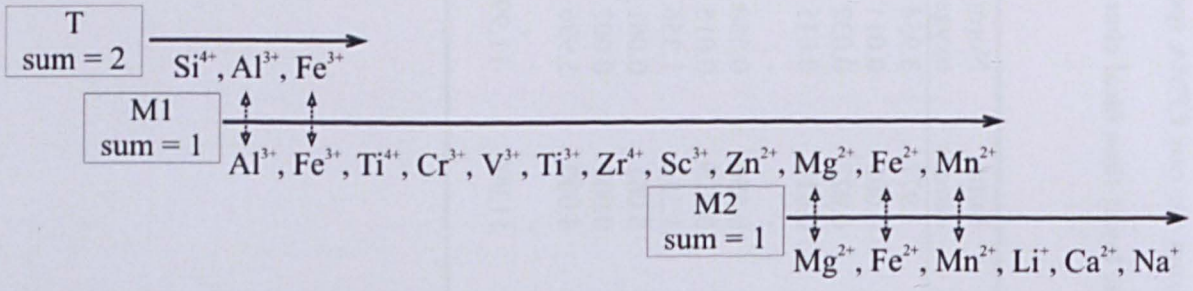

Figure 2-9. Order of cation substitution and their assigned sites in pyroxenes, after Morimoto (1988). Two tetrahedral (T) cations are needed per unit cell, while one cation is needed for each of the octahedral sites (M1 and M2).

2.3.1.1.2 Feldspar corrections

Feldspar phases in ALH 84001 consist solely of maskelynite, so assigning elements to cation sites on the basis of EPMA data may be prone to error given the intense deformation that the pre-existing plagioclase experienced and the possible modification of the main element chemistry by aqueous alteration. Nevertheless, assuming the analysed composition represents the original composition of the plagioclase, theoretical (if not necessarily actual) cation sites may be calculated and the proportion of anorthosite, albite and orthoclase endmembers can be reported.

As with the pyroxene analyses, Fe^{3+} content was not analysed by EPMA and is derived from cation charge corrections. Table 2-3 contains an example of a point analysis on maskelynite (in weight % oxides), the corrections made and cation site occupancies.

2.3.1.1.3 Chromite corrections

The energy peaks of the fluorine Kα emission line and the chromium, manganese, and iron Lα emission lines overlap at similar wavelengths and so quantifying them is not possible when they are analysed at the same time using the Cameca SX100 EPMA at the Open University. As such, when analysing F, Cr, Mn, and Fe simultaneously on chromite, the F content is assumed to not be present.

Fe_2O_3 content was calculated assuming full cation site occupancy and 24 cations for every 32 oxygen anions in the chromite formula.

Table 2-3. Example of an EPMA point analysis of maskelynite in ALH 84001 (column 2). Cations and oxygen atoms are calculated from the oxide weight %, and Fe_2O_3 is calculated from the charge. In this case, the cation charge (+5) is ideal so no Fe^{3+} is necessary. Site occupancies and endmember proportions follow from the atoms per formula unit.

48/1	Analysis wt %	Mole cations	Mole oxygen	Norm. cations	Norm. oxygen	Atom units	Norm. Wt %	Site 1	Site 2	An (%)	Ab (%)	Or (%)
SiO_2	61.03	1.025	2.050	2.726	5.452	2.726	61.60	2.726				
TiO_2	bdl*	0.000	0.000	0.000	0.000	0.000	0.00	0.000				
Al_2O_3	24.42	0.479	0.718	0.718	1.910	1.274	24.42	1.274				
Cr_2O_3	0.14	0.002	0.003	0.003	0.007	1.274	0.14	0.005				
Fe_2O_3	-	-	-	0.000	0.000	0.000	0.00	0.000				
FeO	0.79	0.011	0.011	0.029	0.029	0.029	0.79		0.029			
MnO	0.03	0.000	0.000	0.001	0.001	0.001	0.03		0.001			
MgO	0.66	0.016	0.016	0.044	0.044	0.044	0.66		0.044			
CaO	6.32	0.113	0.113	0.300	0.300	0.300	6.32		0.300			
BaO	0.03	0.000	0.000	0.001	0.001	0.001	0.03		0.001			
Na_2O	6.67	0.215	0.108	0.573	0.286	0.573	6.67		0.573			
K_2O	0.72	0.015	0.008	0.041	0.020	0.041	0.72		0.041			
SrO	0.02	0.000	0.000	0.001	0.001	0.001	0.02		0.001			
Rb_2O	0.24	0.003	0.001	0.007	0.003	0.007	0.24		0.007			
Total	101.67	1.880	3.029	5.000	8.055	5.000	101.40	4.004	0.996	38.37	57.52	4.11
Ideal						5.000		4.000	1.000			
Calc. charge		6.059	-6.059	16.110	-16.110	16.110						

*Below detection limit

2.3.1.2 Post-analyses mixed-phase unmixing

On occasion, mineral phases are too small to be analysed by the EPMA electron beam with certainty, and results represent mixed analyses of different mineral phases. These problematic EPMA spot analyses are easily distinguished by the resulting imperfect sums of oxides (far from the ideal 100 ± 2 wt. %) or sums of cations (when not analysing anhydrous silicates or oxides) and are typically discarded. However, in some cases it may be useful to determine the exact proportions of mineral phases forming the analysed mixed phase, such as when phases of interest are melts composed of mixed fractions of other known components in a sample. Mixed phase analyses, in which the individual components forming the mixed phases are known but have an associated error value, could be solved with a simple linear regression, but if so, the multiple errors associated to compositions of the individual components would be neglected. For example, a mixed phase may be composed of olivine, plagioclase and pyroxene, the compositions of these minerals would be determined by analyses (e.g., on EPMA) and given as oxides (SiO_2, TiO_2, Al_2O_3, MgO, ...) which would be associated to statistical error because of compositional variation within the mineral phases, and the error inherent to the analytical technique. Using mean values for the composition of the components (olivine, pyroxene, plagioclase) to perform a linear regression on the mean values of the analytically obtained mixed phase analysis would be imprecise and would neglect the compositional variation existing in natural geological systems.

The harmonic mixing (HMX) calculation FORTRAN program developed by Stöckleman and Reimold (1989) is a good solution for these mixed phase analyses, which allows specifying multiple analytical errors for individual components and the mixed phase. It provides a harmonic least-squares regression and non-linear optimisation analysis, and has been successfully applied to study the compositions of diverse impact rocks on Earth (e.g.,

Koeberl et al., 1998; Reimold et al., 1990a, 1990b). Mixed phase analyses of importance gathered in this study were deconvolved with the HMX program, using endmember components and compositions gathered in the same samples the mixed phase analyses were obtained from, and reported where relevant. Details on the algorithms used in HMX and implementation can be found in Stöckleman and Reimold (1989).

2.4 Raman spectroscopy

2.4.1 Background

Raman spectroscopic investigations of ALH 84001 by (Steele et al., 2012a, 2007) uncovered the presence of macromolecular carbon (MMC), most likely graphitic in nature. The presence of graphite places fO_2, P and T restrictions on the conditions that ALH 84001 must have been subjected to (see Section 1.4 in Chapter 1) before, during or after the deposition of the carbonates.

To confirm whether graphite is indeed present and to understand its temporal and spatial relationship (and its possible genetic relationship) with the carbonates, Raman spectroscopy was carried out in similar analytical conditions to the investigations by (Steele et al., 2012a) using a green 514 nm laser and a ~ 0.6 mW power output.

Raman spectroscopy is a technique of vibrational spectroscopy able to resolve molecular structures. Essentially, Raman spectroscopy involves the interaction of electromagnetic radiation (an incident beam of photons in the form of a monochromatic laser) with molecular vibrations from molecular structures in the sample. Photons are backscattered inelastically, with a different frequency (i.e., different energy, e.g., Larkin, 2011) to the incident beam's. For the Raman effect to be observed, the molecular vibration must change

the polarisability of the molecule, i.e., the vibration must cause a deformation in the electron cloud surrounding the molecule (e.g., Larkin, 2011b). This change in the distribution of charge induces a dipole:

$$\mu = \sigma E \qquad (1)$$

where μ is the induced dipole moment, σ is the polarisability, and E is the electric field that produces the dipole moment.

Figure 2-10 depicts the types of photon scattering that occur when an incident photon beam ($\tilde{\upsilon}_L$) interacts with the molecule. Rayleigh (elastic) scattering is the most common and occurs when a photon raises the molecule to a virtual excited state (i.e., not an excited electronic state, as would occur in fluorescence) from a ground state, to which it returns, not gaining or losing any net energy. The photon is scattered in the same frequency it had when it interacted with the molecular vibration. Stokes Raman scattering occurs less frequently (~ 1 in 10^7 photons; "DoITPoMS - TLP Library Raman Spectroscopy - Raman scattering," 2007), and occurs when the molecule returns to a higher energy (vibrational) state than the ground state after being excited by the photon. The photon scattered has a lower energy (longer wavelength). Anti-Stokes Raman scattering occurs when a molecule in an already higher vibrational state interacts with a photon and emits one with higher energy (shorter wavelength) after the molecule is raised to an excited state and returns to the ground state,

It is the Stokes Raman scattering which is measured by a Raman spectrometer. For crystalline materials, molecular vibrations are quantised as phonons. Only those phonons whose interaction with the laser beam results in a change in polarisability induce Raman scattering, and so only certain minerals and crystal structures are Raman active and have characteristic shifts.

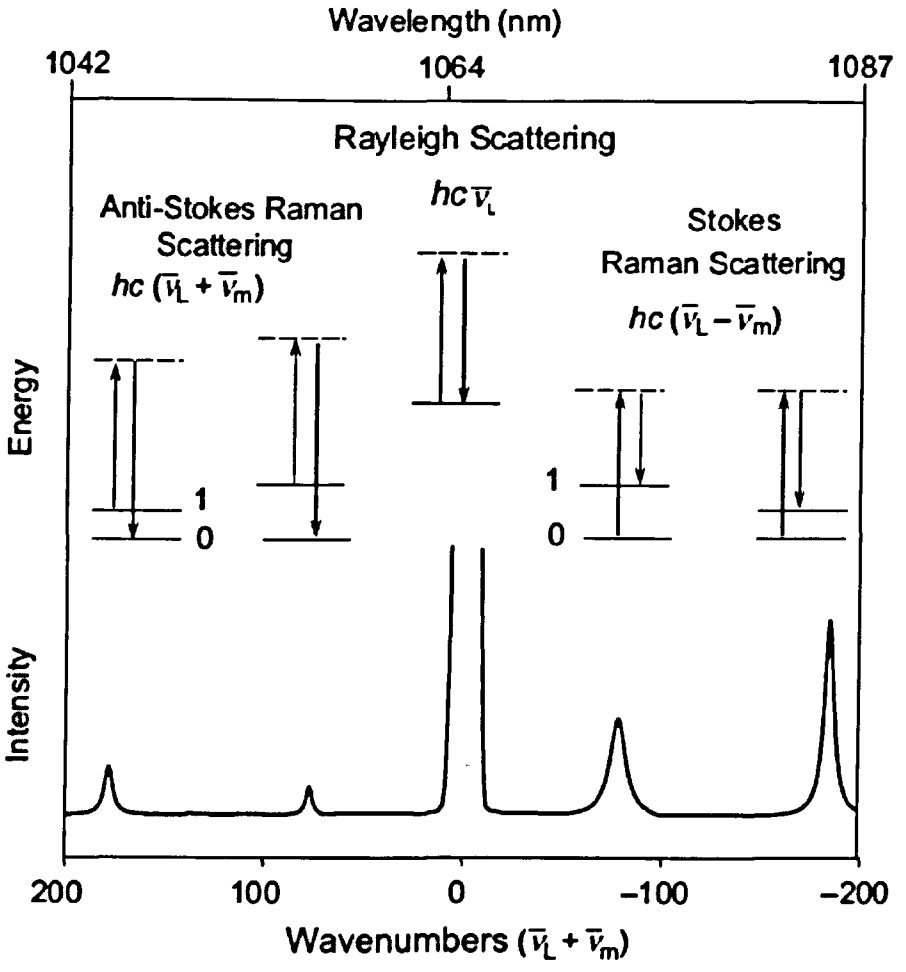

Figure 2-10. Schematic illustration of types of photon scattering, adapted from (Larkin, 2011b). Rayleigh scattering is the most common form, with the highest intensity. Photons are scattered elastically with no gain or loss of energy. Stokes and anti-Stokes Raman scattering scatter photons inelastically, lowering and raising the frequency of the scattered photon respectively after reaching a virtualexcited state (dashed line). The vibrational state of the molecule returns to a higher energy state (1) in Stokes scattering and the ground state (0) in anti-Stokes scattering.

2.4.2 Analytical method and instrumentation

Analyses with Raman spectroscopy were carried out at the Open University's Jobin Yvon Labram HR laser Raman, for which only the Stokes Raman scattering effect on photons is measured and presented here. Figure 2-11 is a schematic representation of the instrument's workings.

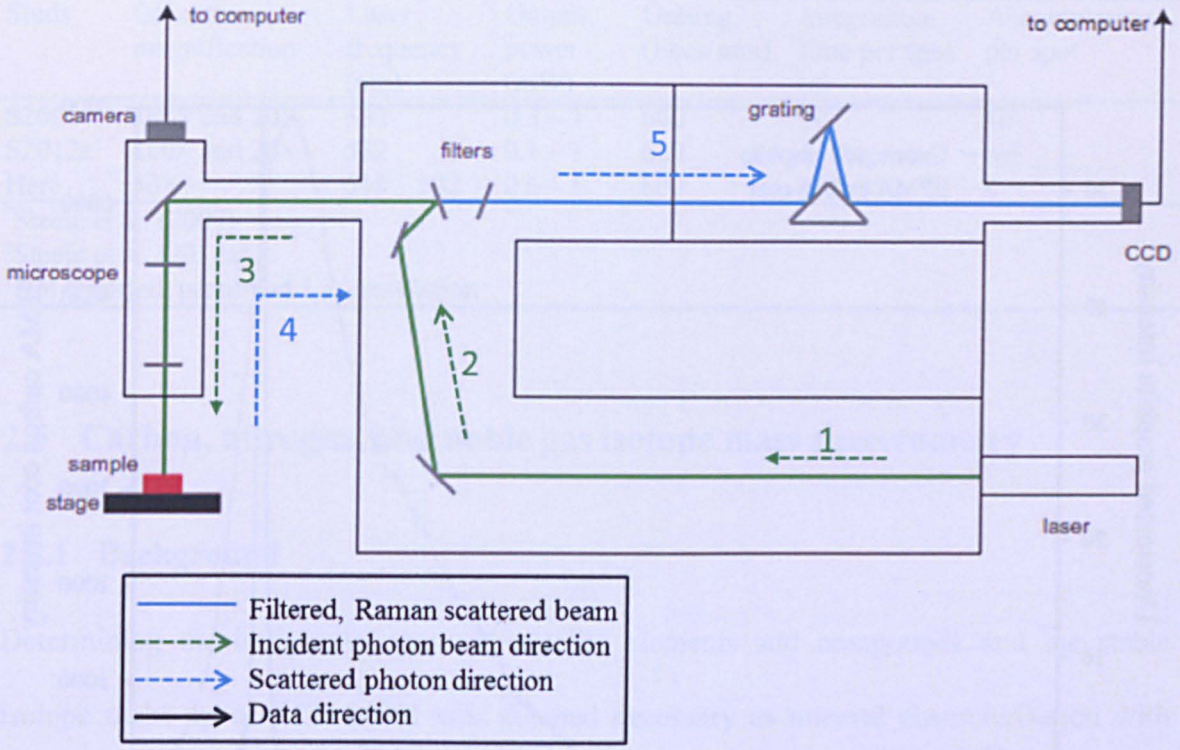

Figure 2-11. Schematic diagram of the Raman instrument, adapted from "DoITPoMS - TLP Library Raman Spectroscopy - Raman scattering," (2007). Charged-coupled devices (CCDs) in the microscope's camera and the detector transform optical signals to electronic ones, which are interpreted by a computer.

Appropriate areas for analyses were identified with the SEM and EPMA work described in this chapter. Areas with a high proportion of carbonate material were sought, as that is where the MMC was described in the work by Steele et al. (2012a, 2007). The thick section samples (*ALH-section-A*, *ALH-section-B*, and *ALH-section-C*) were previously imaged and analysed with EPMA and were therefore carbon-coated. The carbon coat has a distinctive broad peak in its Raman spectrum, which interferes with part of the graphite Raman spectrum (Figure 2-12). However, only part of the graphite spectrum is obscured. The main narrow graphite peak centred at ~ 1580 cm^{-1} is distinguished over the broad carbon coat peak (centred at ~ 1530 cm^{-1}) where graphite is present (Figure 2-12).

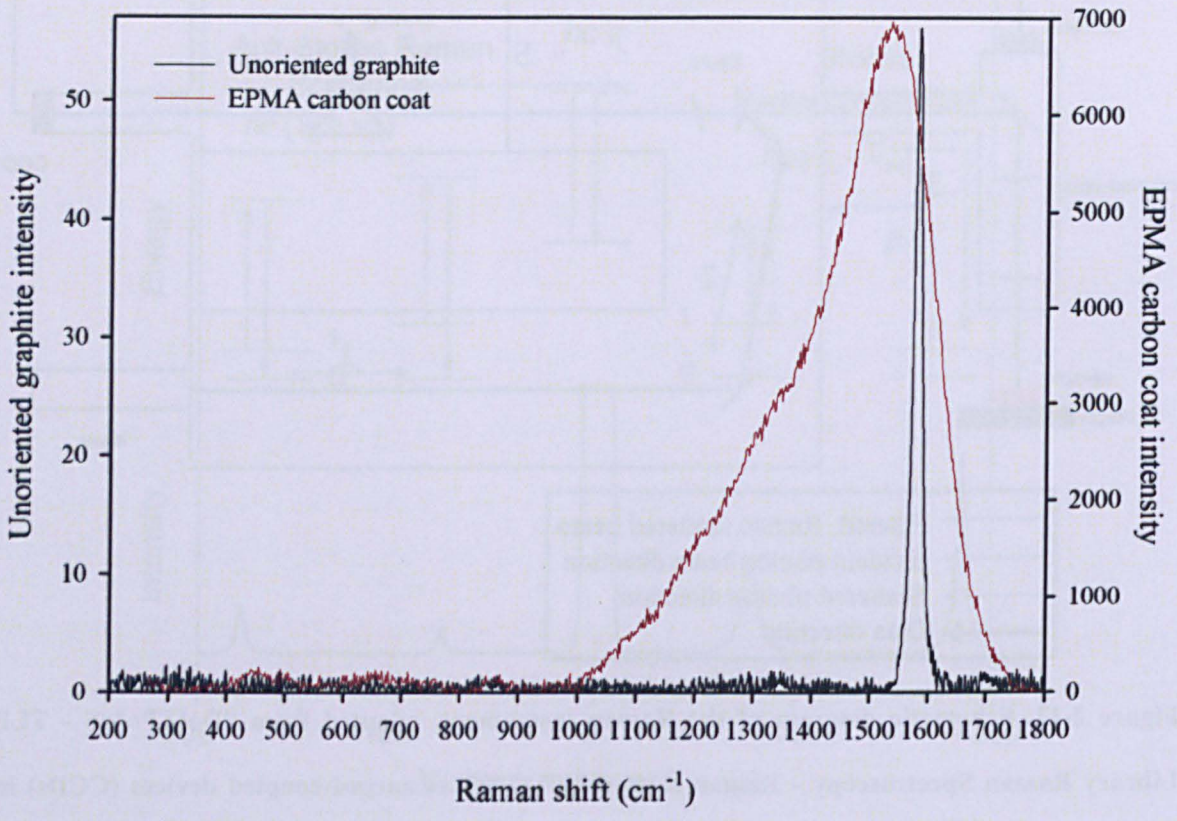

Figure 2-12. Comparison of a typical Raman spectrum of unoriented graphite (from the RRUFF™ database, acquired at a laser frequency of 532 nm), showing a narrow peak at ~ 1580 cm^{-1}, with a spectrum of an EPMA carbon coated thin section (from a measurement with the Jobin Yvon Labram HR laser Raman at the Open University with a frequency of 514 nm), showing a broad peak at ~ 1530 cm^{-1}.

As the ALH 84001 samples analysed by Steele et al. (2007) were uncoated thin sections and the samples analysed here were carbon coated thick sections, slight changes in the experimental setup had to be made in order to obtain comparable results. The exact settings are summarised in Table 2-4, and are given in detail for the results (Section 3.1.2).

Table 2-4. General Raman spectrometer laser and analytical settings.

Study	Objective magnification	Laser frequency (nm)	Output power (mW)	Grating (lines/mm)	Integration time per spot (s)	Accumulations per spot
S2007*	100× and 20×	532	0.3 – 1	600	30	10
S2012a†	100× and 20×	532	0.1 – 1	600	1 – 6	na‡
Here	50×	514 – 532	0.6 – 1	600	15 – 30	2

*Steele et al. (2007)
†Steele et al. (2012a)
‡Not reported, presumed 1 accumulation

2.5 Carbon, nitrogen, and noble gas isotope mass spectrometry

2.5.1 Background

Determining the indigenous mass of volatile elements and compounds and the stable isotope make-up of ALH 84001 was deemed necessary as mineral characterisation with EDS and WDS techniques, and geochemical modelling work progressed. It was essential to understand the amount and composition of a possible gas phase (e.g., the early martian atmosphere) coeval with the carbonate formation, and to reconcile the composition with possible formation environments.

2.5.2 Techniques and instrumentation: Finesse

Several analytical techniques are able to discern the isotopic abundances of carbon, nitrogen, and noble gases, but given how unique ALH 84001 is, it was important to use a technique that could attain high analytical precision and accuracy with a small amount of sample. The custom-built Finesse machine at the Open University was developed from its origins as a stepped combustion and pyrolysis system, and mass spectrometer to determine nitrogen stable isotopes (Boyd et al., 1988; Wright et al., 1988) to a machine capable of

analysing minute stable isotope variations for multiple elements in small masses of geological samples (Abernethy, 2014; Mikhail, 2011; Shelkov, 1997).

A description of the components of Finesse, and their workings and automation were given in detail most recently by Mikhail (2011), and information pertaining to analytical precision and blank corrections was most recently reported by Abernethy (2014). What follows here is a brief overview of Finesse, and information relevant to understanding sample preparation, its operation, and the interpretation of results.

Finesse operates under a static mode (as opposed to a continuous flow) high vacuum ($\sim 10^{-8}$ mbar), whereby the analysed sample is combusted in discreet steps and the gas released from it is separated and analysed by a series of mass spectrometers (exact species analysed in this thesis are outlined in Table 2-5). Figure 2-13 (modified from Mikhail, 2011) shows a simple schematic of the instrument and its different components.

A sample need not be powdered but must be contained within a small (< 5 mm diameter) Pt foil envelope. The foil allows the sample to be placed in a loading chamber without disaggregating, and facilitates dropping the full sample into the furnace from the loading chamber. Furthermore, the Pt acts as catalyser in the reaction of nitrous oxides to N_2 (Boyd et al., 1988), thus avoiding a possible low temperature path to mass dependant fractionation of ^{15}N between nitrous oxides and N_2, and aiding the combustion of CH_4 and CO to CO_2 (thus avoiding the interference in the analyses between molecules with the same mass, e.g., CO and N_2; Mikhail, 2011). Prior to wrapping the sample in the Pt foil, the foil is decontaminated while placed in a vacuum sealed glass-blown SiO_2 tube with a CuO pellet and heated to ~ 900 °C for 24 hours. This allows organic contaminants to oxidise to CO_2 (g), which is released when the tube is opened. Sample preparation takes place in a class 1000 cleanroom (ISO 6; $\leq 10^6$ particles/m^3 of air).

Table 2-5. Species and isotopes analysed by Finesse

Element	Specific mass spectrometer	Species	Mass	Isotopologues
C	TCMS*	CO_2	44	$^{12}C^{16}O_2$,
			45	$^{13}C^{16}O_2$, $^{12}C^{16}O^{17}O$
			46	$^{12}C^{16}O^{18}O$
			47	$^{12}C^{18}O^{17}O$
N	NMS†	N‡	14	^{14}N
		N_2	28	$^{14}N^{14}N$
			29	$^{14}N^{15}N$
			30	$^{15}N^{15}N$
Ar	NMS	Ar	36	^{36}Ar
			37	^{37}Ar
			38	^{38}Ar
			40	^{40}Ar
He	QMS§	He	4	^{4}He
Ne	QMS	Ne	20	^{20}Ne
			21	^{21}Ne
			22	^{22}Ne

*Triple collector mass spectrometer
†Nitrogen mass spectrometer.
‡Used for a rough measurement of N abundance in the released gas.
§Quadrupole mass spectrometer.

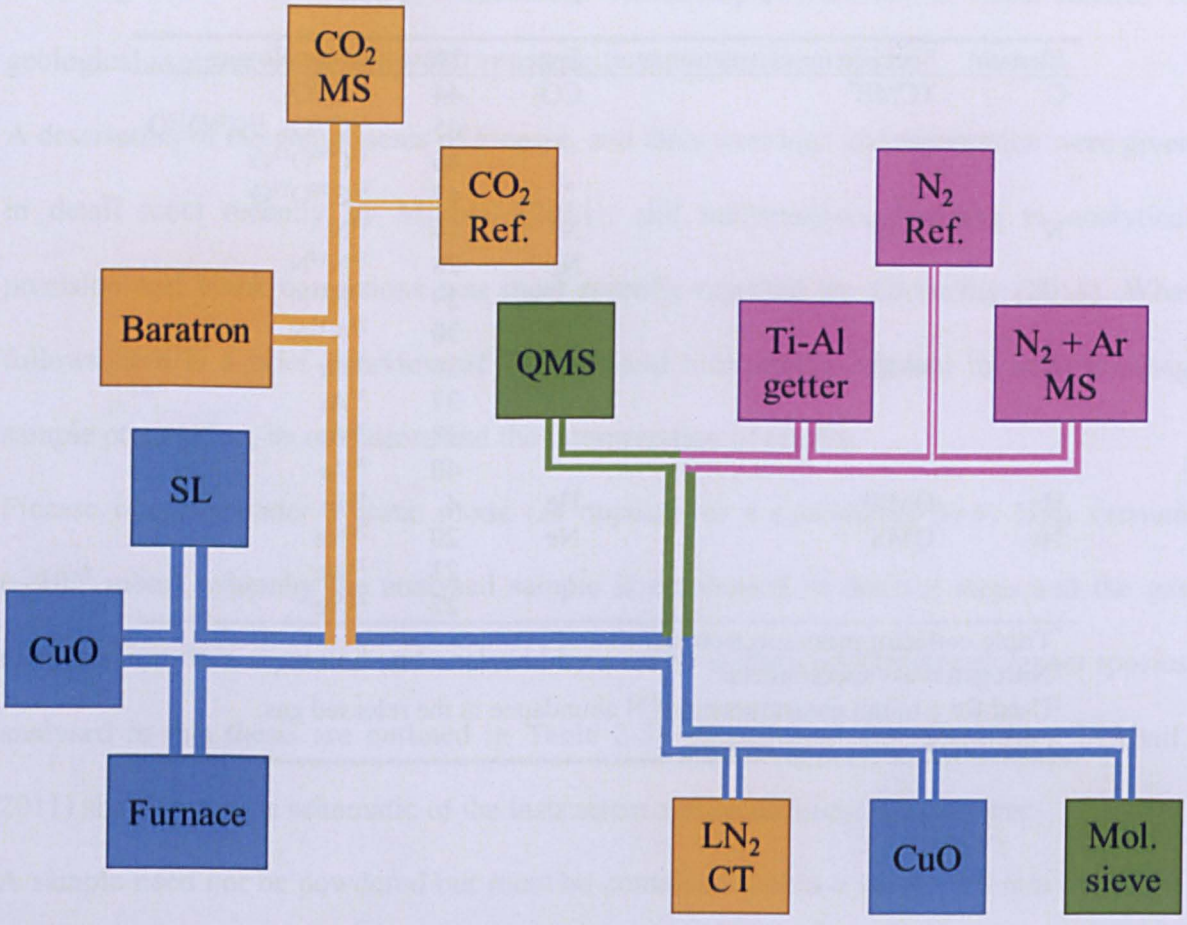

Figure 2-13. Simple schematic diagram of Finesse, based on Mikhail (2011). Blue elements are pipes and mechanisms used by all gases, yellow objects are part of the carbon line, green ones are used by noble gases and nitrogen, and pink objects are used for sampling nitrogen and argon. Acronyms are: SL (sample loader), CuO (copper oxide oxidiser/reducer), Ref. (reference gases), LN_2 CT (liquid nitrogen cold trap), Mol. sieve (molecular sieve), and MS (mass spectrometer). Pneumatic valves, ion and rotary pumps, cold fingers and gas expansion chambers are not pictured for simplicity.

After the system has been pumped down, the prepared sample is dropped into the furnace (capable of up to 1400 °C) and is subsequently combusted in a pure O_2 environment (produced by heating powdered CuO). The time of combustion (typically 30 minutes for each step), and the number and temperature of the steps are determined by the user through a computer, using a customised interface built with the LabVIEW programming software.

Gas released from the sample as it is combusted at each temperature step is carried along (expanded into the vacuum) with the aid of rotary pumps through steel pipes to be separated by a liquid nitrogen (LN_2) cryotrap at approximately −160 °C, which traps (freezes) the CO_2 and H_2O in it. A molecular sieve kept below −190 °C traps the N_2 and Ar portion of the gas. The now separated 'pure' gas portions are ready for analysis, which begins with the He and Ne aliquout, which is not trapped by the cryotrap or molecular sieve. He and Ne gas is sent to the quadrupole mass spectrometer (QMS) for isotopic analyses.

Next, the cryotrap holding the CO_2 and H_2O is heated to ~ −75 °C, allowing the CO_2 to sublimate while keeping the H_2O frozen. A calibrated capacitance manometer, the MKS Baratron, measures the abundance of released CO_2 in the gas aliquot (in ng of C), with an accuracy of ± 1 % (Mikhail, 2011). A portion of this CO_2 gas (~ 1 ng) is sent to a dedicated mass spectrometer for isotopic analysis, while the H_2O is pumped after heating the cryotrap to 60 °C.

Subsequently, the molecular sieve is heated up to 250 °C to sublimate the N_2 and Ar gas fraction. Any CO that may have been trapped in the molecular sieve is oxidised to CO_2 by O_2 released by heated CuO powder. This avoids the mass 28 interference that may occur in the static mass spectrometer if N_2 and CO are analysed in the same aliquot. The cryotrap is cooled down to −140 °C to trap any remaining or newly formed CO_2. An aliquot of the N_2 and Ar-rich gas is then sent to a Ti-Al getter which adsorbs the N_2. The purified Ar gas is then sent to the N mass spectrometer, where an average of 50 repeat measurements of the ion peak intensities of masses 36, 37, 38 and 40 are taken (Mikhail, 2011; Mortimer et al., 2014).

N_2 is measured separately, first in the QMS from mass 14 for a rough calculation of the N abundance of the released gas, as it is unaffected by any possible remaining CO (mass 28)

in the aliquot. Finally, the total N_2 abundance is measured in the dedicated N mass spectrometer and isotopic analyses are made for masses 28, 29, and 30 (Abernethy, 2014; Mikhail, 2011; Mortimer et al., 2014).

Throughout the operation of Finesse, reference gases (air for N; and an empty, 'zero' measurement as well as a CO_2 reference for C) are analysed by the mass spectrometers between combustion steps to allow standardisation between measurements and to identify possible analytical, computational and mechanical errors and background values (Mikhail, 2011; Mortimer et al., 2014). The $^{13}C/^{12}C$ ratio is reported relative to the VPDB standard (see Chapter 1) and $^{15}N/^{14}N$ is reported in ‰ deviation from the terrestrial air standard in $\delta^{15}N$.

Prior to introducing samples into Finesse, a 'blank' is prepared and analysed in the same way as the sample will be, following the same combustion steps. A 'blank' consists of a Pt foil envelope from the same Pt sheet the sample's Pt envelope is made from, and of similar mass and size to the sample, prepared in the same clean conditions as the sample is. The purpose of 'running a blank' is to allow correcting for background values of the analysed elements, which can be subtracted from the measured sample values. An average of blank values from 01/04/2010 to 26/03/2013, for each temperature step was compiled by Abernethy (2014) and is given in Table 2-6 for C and N, and in Table 2-7 for Ar. These values were used in lieu of the blank carried out before the experiment, as it was found that above average blank levels of C and N were measured in the blank, probably because of contaminants in the blank or the vacuum line.

Sulfur cannot be measured accurately by Finesse due to mass interferences between sulfur compounds and carbon compounds. Additionally, sulfur compounds resulting from combustion tend to be trapped in the dedicated carbon mass spectrometer. As such, it is

important to select samples bearing lower amounts of sulfur than carbon. ALH 84001 generally fulfils this requirement, but due to the heterogeneous distribution of the carbonates, selecting an aliquot with more sulfides than carbonates was a possibility.

Table 2-6. Blank values for C and N isotopes from Finesse analyses.

Temperature step (°C)	C		$\delta^{13}C$		No. of analyses	N		$\delta^{15}N$		No. of analyses
	Abundance (ng)	1σ SD	$\delta^{13}C$	1σ SD		Abundance (ng)	1σ SD	$\delta^{15}N$	1σ SD	
200	19.98	19.49	-27.17	6.55	28	0.95	0.72	+0.77	19.27	18
300	68.95	62.77	-26.61	2.16	20	2.13	2.52	-4.61	10.89	14
400	84.23	79.97	-24.81	5.51	29	2.52	3.09	+1.24	9.46	18
500	29.10	55.73	-21.75	7.41	40	1.24	1.05	+1.98	8.50	18
550	26.31	36.00	-24.16	5.35	20	0.51	0.36	-0.29	13.09	14
600	19.60	22.23	-24.10	6.11	29	0.96	1.12	+1.36	13.23	18
650	11.64	17.04	-25.13	8.09	20	0.46	0.38	+1.42	12.39	14
700	10.14	11.67	-25.42	7.91	22	0.54	0.56	+5.19	13.04	16
750	4.65	2.82	-27.89	6.25	19	0.59	0.66	+4.29	15.02	14
800	6.34	4.83	-24.88	7.77	35	0.54	0.51	-4.18	9.73	28
850	3.60	1.43	-27.44	6.56	20	0.62	0.68	+5.58	13.80	15
900	5.01	5.71	-27.42	6.82	24	1.05	1.43	+9.80	18.71	18
950	3.49	1.23	-28.12	6.95	20	0.91	1.43	+10.80	15.30	15
1000	4.36	1.85	-23.27	11.91	39	0.72	0.77	+0.37	23.35	28
1100	5.07	2.41	-25.15	8.71	30	0.64	0.60	-0.75	11.74	23
1200	6.43	4.28	-24.02	8.09	43	0.64	0.51	+1.57	17.32	32
1300	8.10	4.63	-25.61	8.72	29	0.41	0.21	+0.32	18.50	22
1400	9.35	7.61	-22.54	14.87	39	0.63	0.48	-4.88	15.08	29

Table 2-7. Blank values for Ar isotopes from Finesse analyses.

Temperature step (°C)	Num. of analyses	^{40}Ar		^{36}Ar		$^{38}Ar/^{36}Ar$		$^{37}Ar/^{36}Ar$		$^{40}Ar/^{36}Ar$	
		Abundance ($10^{-8}cm^3$)	1σ SD	Abundance ($10^{-8}cm^3$)	1σ SD	Ratio	1σ SD	Ratio	1σ SD	Ratio	1σ SD
200	11	0.173814	0.135633	0.004515	0.001049	0.440518	0.432201	0.537066	0.33244	267.7074	264.7792
300	5	0.333926	0.333191	0.001314	0.001423	0.462155	0.4422115	0.111037	0.099614	269.2822	278.3941
400	11	0.319158	0.264043	0.001225	0.001038	0.319780	0.286825	0.232193	0.116469	266.7832	250.9423
500	5	0.287167	0.238341	0.001335	0.001045	0.249928	0.201684	0.224908	0.17448	214.481	206.8532
550	5	0.290507	0.28266	0.001161	0.001194	0.382458	0.226872	0.143727	0.148952	277.6585	236.7917
600	11	0.296738	0.257713	0.001053	0.001105	0.410098	0.430834	0.147744	0.097541	303.5203	269.3903
650	5	0.278719	0.30818	0.001038	0.0009	0.307383	0.344977	0.340683	0.303099	286.3621	298.3462
700	5	0.254082	0.204931	0.00102	0.001008	0.392187	0.407048	0.132815	0.104455	262.4225	265.8792
750	5	0.266848	0.241555	0.001042	0.000909	0.400419	0.288749	0.223935	0.168687	267.5711	251.9453
800	11	0.283652	0.23981	0.001172	0.001061	0.373877	0.426689	0.167239	0.138887	293.2878	279.9682
850	6	0.292241	0.299447	0.00127	0.001216	0.347178	0.221137	0.107312	0.104405	244.2838	259.9156
900	6	0.3314	0.327152	0.001271	0.001321	0.330565	0.332206	0.112626	0.113762	260.4446	274.6195
950	6	0.327866	0.285603	0.00099	0.001003	0.284828	0.310278	0.20814	0.118234	347.0032	345.5963
1000	11	0.364075	0.326233	0.001334	0.001339	0.379454	0.362008	0.166204	0.118234	289.2627	274.5151
1100	5	0.384675	0.383413	0.00152	0.001461	0.451721	0.442208	0.153514	0.119234	259.1435	262.5045
1200	11	0.473534	0.452166	0.004344	0.002468	0.238582	0.237039	0.122583	0.142882	257.0694	245.9662
1300	5	0.670762	0.663463	0.003805	0.002888	0.276118	0.281631	0.1023	0.1023	259.359	270.7666
1400	11	0.661867	0.61125	0.003227	0.003028	0.256292	0.250378	0.058929	0.047123	267.1144	267.5497

2.5.3 Sample description

The sample consisted of a number of fragmented (but not powdered) chips of ALH 84001 inside a Pt foil envelope. After correcting for the mass of the Pt envelope, the total mass of ALH 84001 inside the envelope was 14.823 mg ± 0.003 (n = 5). This mass was considered an adequate mass to counteract any effect on the carbon isotope and mass measurements due to any present sulfur-bearing phases (e.g., pyrite, Greenwood et al., 2000) in the sample, as the heterogeneous distribution of the carbonates in the sample could have possibly allowed sulfur-bearing phases to predominate over carbon bearing phases.

One empty Pt foil envelope was prepared in order to perform the blank correction.

3 Analytical results and discussion

In this chapter, results from the analytical procedures described in Chapter 2 are presented.

3.1 Characterisation of ALH 84001

3.1.1 Petrography and mineralogy

Table 3-1 summarises the modal mineralogy of the three samples obtained from SEM imaging. It was not possible to resolve different minerals of similar composition (e.g., augite and pigeonite) in SEM images of the whole samples due to the low resolution of whole-sample imaging. Differentiating minerals of similar composition was accomplished with the EPMA work described below. Figure 3-1 and Figure 3-3 show general EPMA element map composites of the samples.

EPMA work on individual phases revealed their detailed composition, reported here in weight % of oxides (Table 3-2) and as mineral endmember compositions (Table 3-3).

Table 3-1. Approximate modal mineralogy of the ALH 84001 samples, estimated from SEM images.

Sample	Sample area (mm^2)	Modal mineralogy (% area) Pyroxene	Maskelynite	Chromite and sulfide	Carbonate	Phosphate
A	2.72	97.6	1.6	0.1	0.7	bdl*
B	3.51	94.8	3.8	1.1	bdl	0.3
C	2.26	96.4	1.4	2.2	bdl	bdl
Avg.	-	96.3	2.3	1.1	0.2	0.1
Wtd. Avg.	-	96.1	2.4	1.1	0.2	0.1

*Below detection limit.

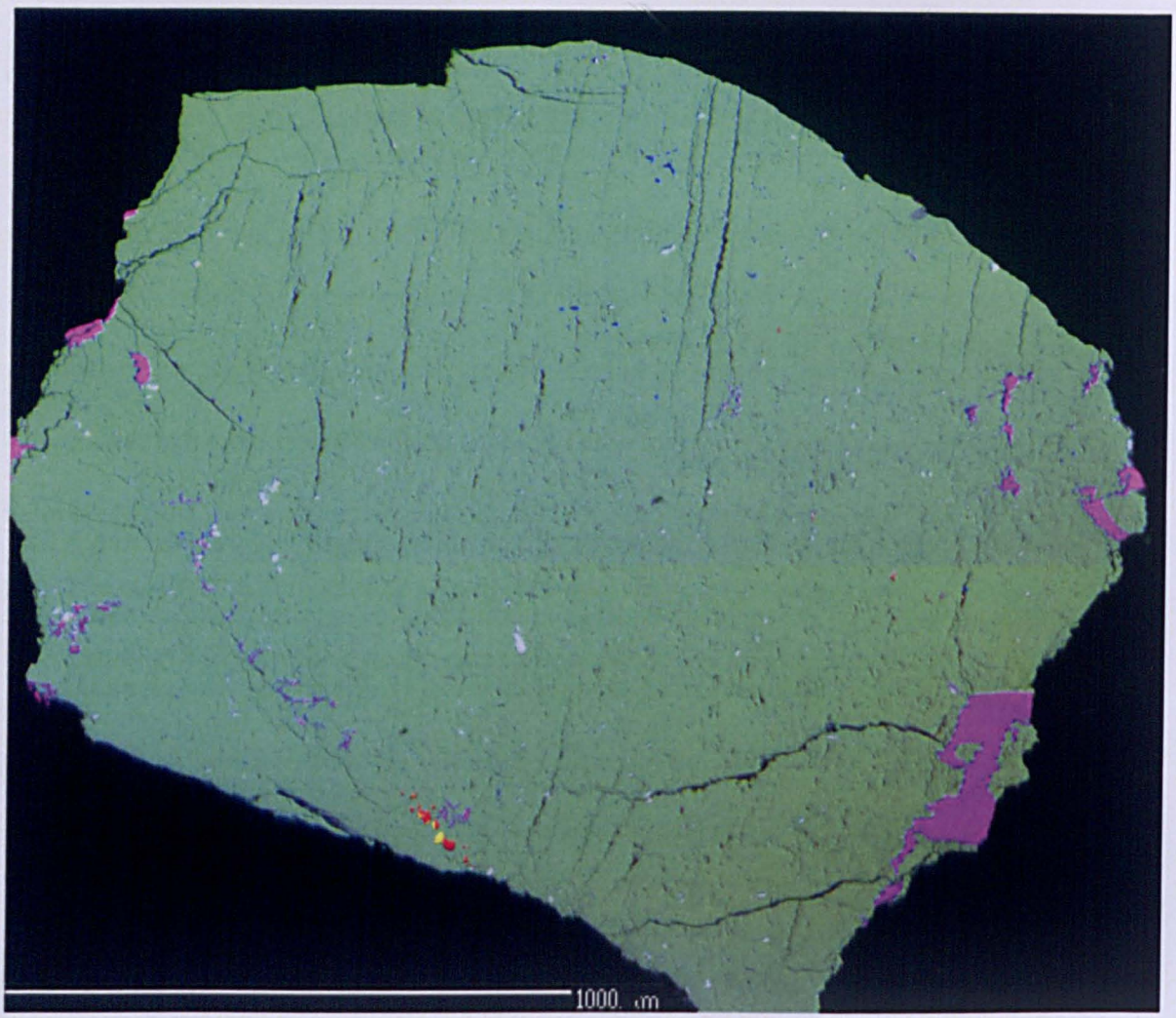

Figure 3-1. EPMA element map composite of sample *ALH-section-A*, grain 1. Red = Fe, green = Mg, blue = Si, yellow = S, white = Ca, and magenta = Al. The visible split along the middle of the image is an artefact from joining element maps taken separately, and the effect of the electron beam interacting with a surface that is not perfectly flat.

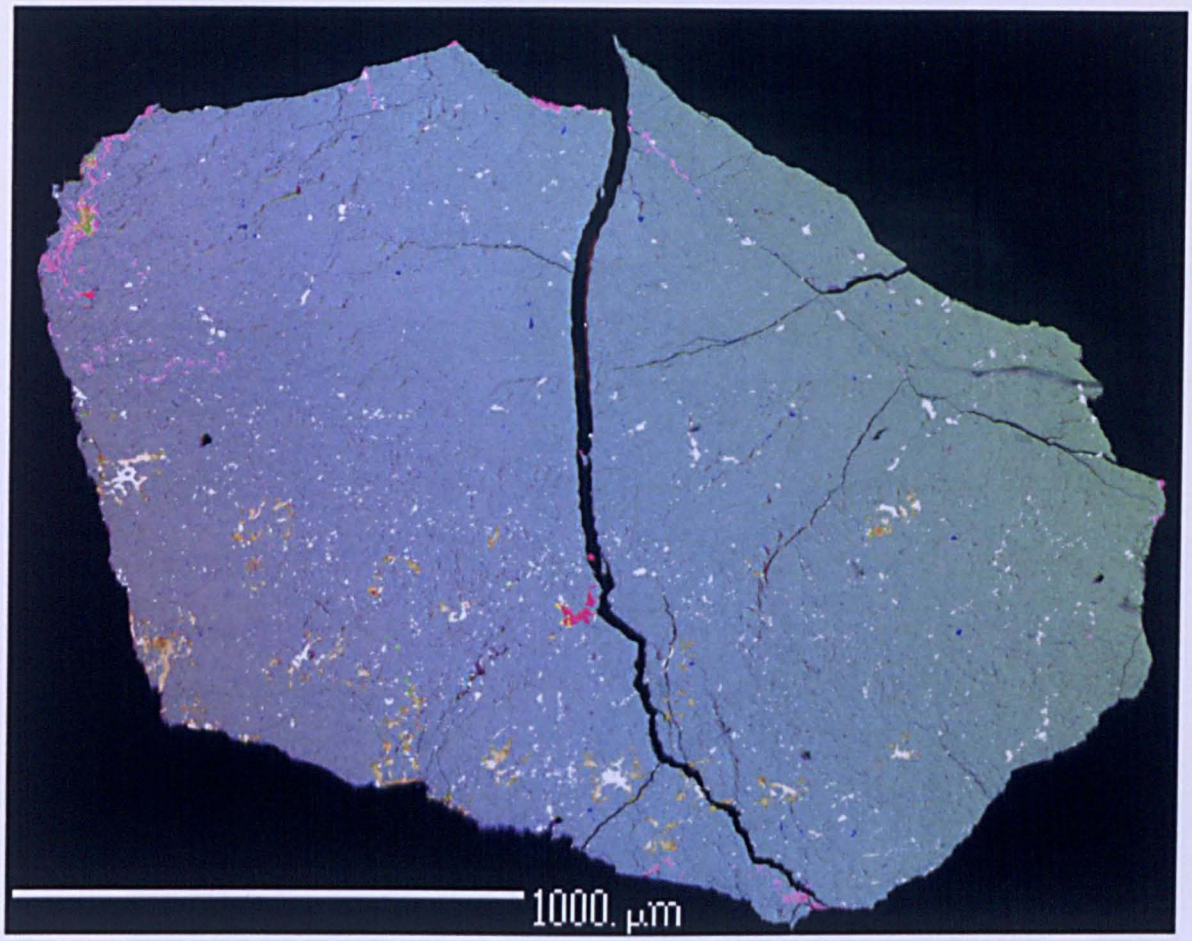

Figure 3-2. EPMA element map composite of sample *ALH-section-A*, grain 2. Red = Fe, green = Mg, blue = Si, yellow = S, white = Ca, and magenta = Al. While the orthopyroxene (most abundant, blueish, phase) is of identical composition as in Figure 3-1 and Figure 3-3, the difference in colour is a result of artefacts from the electron beam on a surface that is not perfectly flat.

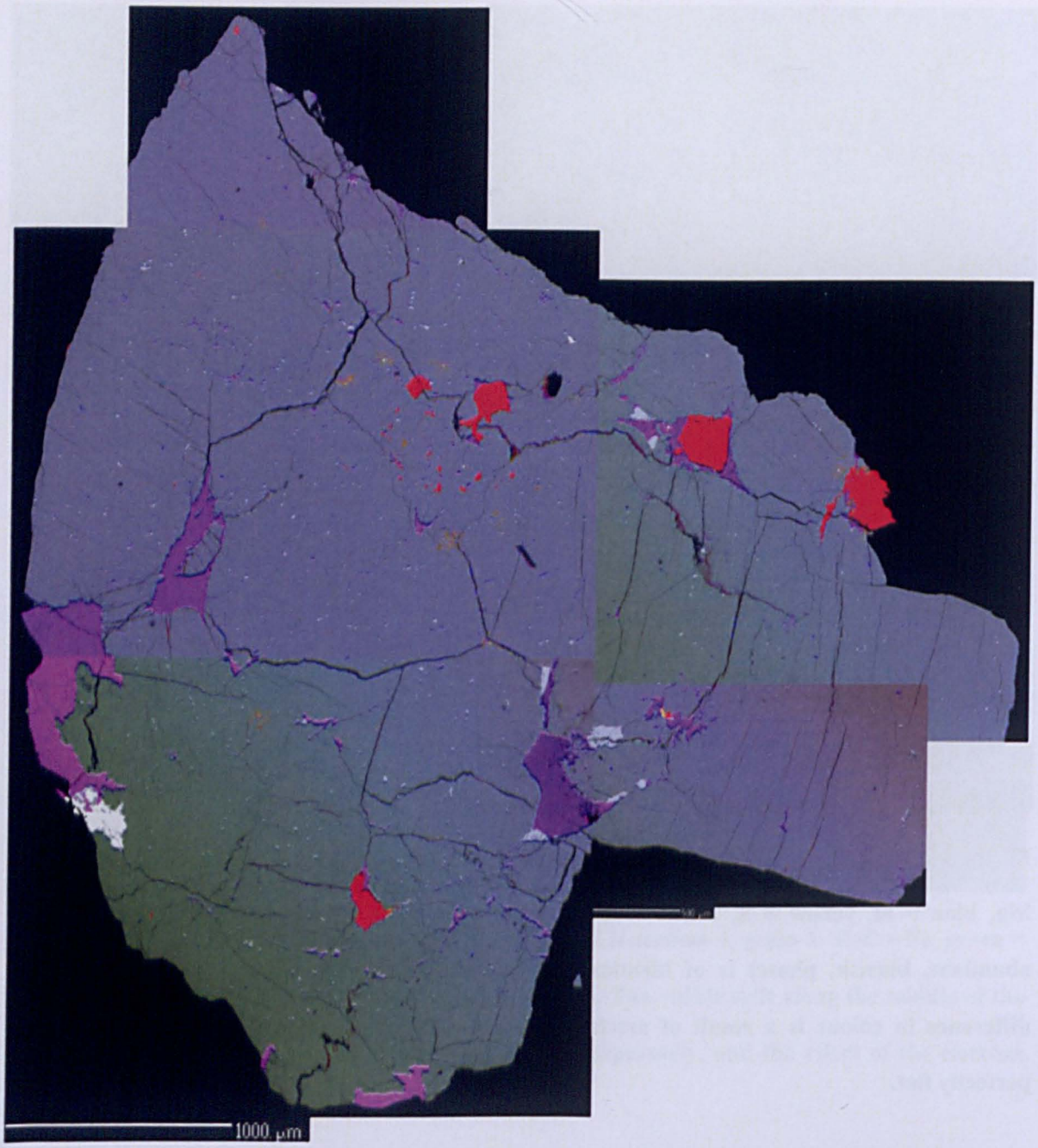

Figure 3-3. EPMA element map composite of sample *ALH-section-B*. Red = Fe, green = Mg, blue = Si, yellow = S, white = Ca, and magenta = Al. The slight gradation from blue to green in the orthopyroxene is not a result of compositional gradation, but an effect of the electron beam interacting with surfaces which are not perfectly flat. Obvious straight-line splits are a result of joining separate composition maps to produce the mosaic.

Table 3-2. EPMA analyses of ALH 84001. For phosphates, Setup A is the same setup used for silicates and oxides, Setup B is the analytical setup used by Barnes et al. (2013), specific for phosphate analyses (see Section 2.3.1). Fe_2O_3 was calculated from FeO (see Section 2.3 in the Methods).

	Opx			Opx (excess Si, n = 8)		Aug			Pgt (n = 1)	Msk (n= 14)		Chr (n = 10)		Phs (setup A**)			Phs (setup B**, n = 4)	
	Avg. (wt. %)	1 σ SD	n	Avg. (wt. %)	1 σ SD	Avg. (wt. %)	1 σ SD	n	Avg. (wt. %)	Avg. (wt. %)	1 σ SD	Avg. (wt. %)	1 σ SD	Avg. (wt. %)	1 σ SD	n	Avg. (wt. %)	1 σ SD
SiO_2	53.60	0.76	94	54.47	0.42	53.32	0.61	5	52.65	60.84	1.02	0.08	0.01	0.16	0.07	3	0.15	0.14
TiO_2	0.17	0.04	94	0.16	0.04	0.23	0.04	5	0.22	0.03	0.02	2.42	0.33	0.02	0.00	1	-	-
Al_2O_3	0.61	0.46	94	0.51	0.06	0.86	0.17	5	0.53	24.51	0.48	7.40	0.86	0.02	0.00	1	-	-
Cr_2O_3	0.40	0.20	94	0.36	0.13	0.62	0.02	5	0.38	0.02	0.04	49.39	2.30	bdl	0.00	1	-	-
Fe_2O_3*	0.64	1.14	94	0.00	0.00	0.54	1.20	5	1.24	0.00	0.00	5.77	0.64	-	-	-	-	-
FeO	17.16	1.08	94	17.66	0.37	7.47	1.26	5	15.79	0.31	0.23	30.28	0.41	0.78	0.00	1	0.72	0.03
NiO	0.01	0.01	74	bdl	bdl	-	-	-	-	bdl	bdl	0.01	0.01	bdl	0.00	1	-	-
MnO	0.38	0.20	74	0.46	0.03	0.22	0.13	5	0.00	0.01	0.01	0.30	0.03	0.03	0.00	1	0.02	0.00
MgO	24.53	0.74	94	23.81	0.41	15.27	0.56	5	24.23	0.10	0.18	3.18	0.16	3.36	0.10	8	3.49	0.10
CaO	1.62	0.16	94	1.53	0.16	20.84	0.10	5	2.97	6.78	0.45	0.01	0.01	47.37	0.57	8	46.35	0.12
BaO	bdl	0.01	94	0.01	0.01	bdl	bdl	5	0.03	0.02	0.02	0.02	0.01	bdl	0.00	1	-	-
Na_2O	0.05	0.08	94	0.03	0.02	0.36	0.04	5	0.08	6.65	0.14	0.03	0.02	2.26	0.00	1	2.49	0.03
K_2O	bdl	0.02	94	bdl	bdl	0.01	0.01	5	bdl	0.77	0.29	bdl	-	0.09	0.00	1	-	-
SrO	0.03	0.02	94	0.03	0.03	bdl	bdl	5	bdl	0.05	0.01	0.60	0.04	bdl	0.00	1	-	-
Rb_2O	0.34	0.02	94	0.33	0.02	0.32	0.03	5	0.37	0.26	0.03	bdl	-	0.01	0.00	1	-	-
P_2O_5	0.01	0.01	94	0.01	0.01	0.28	0.24	5	bdl	0.04	0.02	0.01	0.01	45.42	0.75	8	46.02	0.35
Ce_2O_3	bdl	bdl	20	-	-	bdl	-	1	0.38	-	-	na	na	-	-	-	0.03	0.01
ZrO_2	0.01	0.02	20	-	-	0.02	-	1	bdl	-	-	na	na	-	-	-	-	-
SO_2	0.01	0.01	94	0.01	0.01	0.01	0.01	5	bdl	0.01	0.01	0.02	0.03	0.01	0.00	1	0.01	0.01
Y_2O_3	-	-	-	-	-	-	-	-	-	-	-	na	na	-	-	-	0.02	0.02
F	bdl	0.01	94	bdl	bdl	0.03	0.03	5	bdl	0.02	0.02	na	na	2.53	0.17	8	0.01	0.02
Cl	0.01	bdl	94	0.01	0.00	0.01	0.01	5	bdl	0.00	0.00	na	na	0.01	0.01	8	0.01	0.02
Total	99.51	0.82	94	99.37	0.40	100.30	0.65	5	98.38	100.42	1.17	99.51	0.43	99.22	0.69	8	99.32	0.31

Table 3-3. Composition of the major minerals, as endmembers.

	Opx (n = 94)		Opx (excess Si, n = 8)		Aug (n = 5)		Pgt (n = 1)	Msk (n= 14)	
	Avg. (wt. %)	1 σ SD	Avg. (wt. %)	1 σ SD	Avg. (wt. %)	1 σ SD	Avg. (wt. %)	Avg. (wt. %)	1 σ SD
Wo	3.28	0.36	3.16	0.33	43.15	0.61	5.95		
En	68.80	0.80	68.39	0.74	43.99	1.06	67.59		
Fs	27.92	0.65	28.45	0.46	12.85	0.45	26.46		
Si excess*			0.02	0.02					
An								34.37	2.22
Ab								60.98	0.99
Or								4.65	1.76

*Si excess in atoms per formula unit

3.1.1.1 Pyroxene

As the samples were not a thin section but mounted chips, petrographic textures and features were not easy to discern. Nevertheless, observations fit the description in previous literature (e.g., Mittlefehldt, 1994; Treiman, 1998a, 1995). On the whole, the orthopyroxene crystals are very fractured, sub-euhedral, and show no clear signs of weathering. Crystal size was difficult to distinguish in mounts, but appeared to be in the range of 0.5 – 1.5 mm. Pyroxene analyses were checked for stoichiometry and charge balanced as described in Chapter 2 (Section 2.3.1.1.1). Stoichiometric orthopyroxene had an average composition of $Wo_{3.3}En_{68.8}Fs_{27.9}$ (n = 94), which agrees well with the measurements by Mittlefehldt (1994): $Wo_{3.3}En_{69.4}Fs_{27.3}$ (n = 204). An observation from the measurements presented here is that not all orthopyroxene in ALH 84001 is stoichiometrically accurate. Eight spot analyses show a slight Si excess which, in ideal pyroxene crystals, cannot occupy sites other than the tetrahedral ones. The possible significance of the excess Si is discussed in Section 3.1.4.

Trace amounts of other pyroxenes exist in ALH 84001. Also obtained were one analysis of pigeonite ($Wo_{6.0}En_{67.6}Fs_{26.5}$) and five analyses of augite ($Wo_{43.2}En_{44.0}Fs_{12.9}$; which compare well with the two augite analyses by Mittlefehldt (1994), $Wo_{42.2}En_{45.1}Fs_{12.7}$).

3.1.1.2 Maskelynite

Maskelynite fills spaces between orthopyroxene crystals (Figure 3-4) and very often occurs between chromite grains and orthopyroxene (Figure 3-5). It also appears to be injected into cracks or to have grown filling in cracks (Figure 3-6). Carbonates are also found in maskelynite, where they appear to replace the maskelynite but not the orthopyroxene (Figure 3-7). However, carbonates are found enclosed by orthopyroxene as well, replacing it in other areas; see Section 3.1.1.5.

The irregular distribution of Si, Al, K and Na in the maskelynite, leads to the appearance of thin 'veinlets' in the maskelynite which may be related to flow textures (Figure 3-4). These textures do not appear to have been described in literature of ALH 84001 (e.g., Gleason et al., 1997; Kring et al., 1998; Mittlefehldt, 1994; Treiman, 1998a, 1995), and in fact, the solid transformation from plagioclase to maskelynite as a consequence of high pressure (> 31 Gpa; Kring et al., 1998) shock metamorphism is usually invoked to explain the formation of the maskelynite in ALH 84001. Very likely, the effects of shock were heterogeneous among the minerals of ALH 84001, and may have lead to local melting and textures known as "schlieren" in the maskelynite (e.g., Chen and El Goresy, 2000).

Maskelynite compositions ($An_{34.4}Ab_{61.0}Or_{4.7}$) measured in this study differ slightly from those measured by Mittlefehldt (1994; $An_{31.1}Ab_{63.2}Or_{5.7}$) and are more similar to the representative composition reported by Gleason et al. (1997; $An_{35.6}Ab_{60.1}Or_{4.3}$).

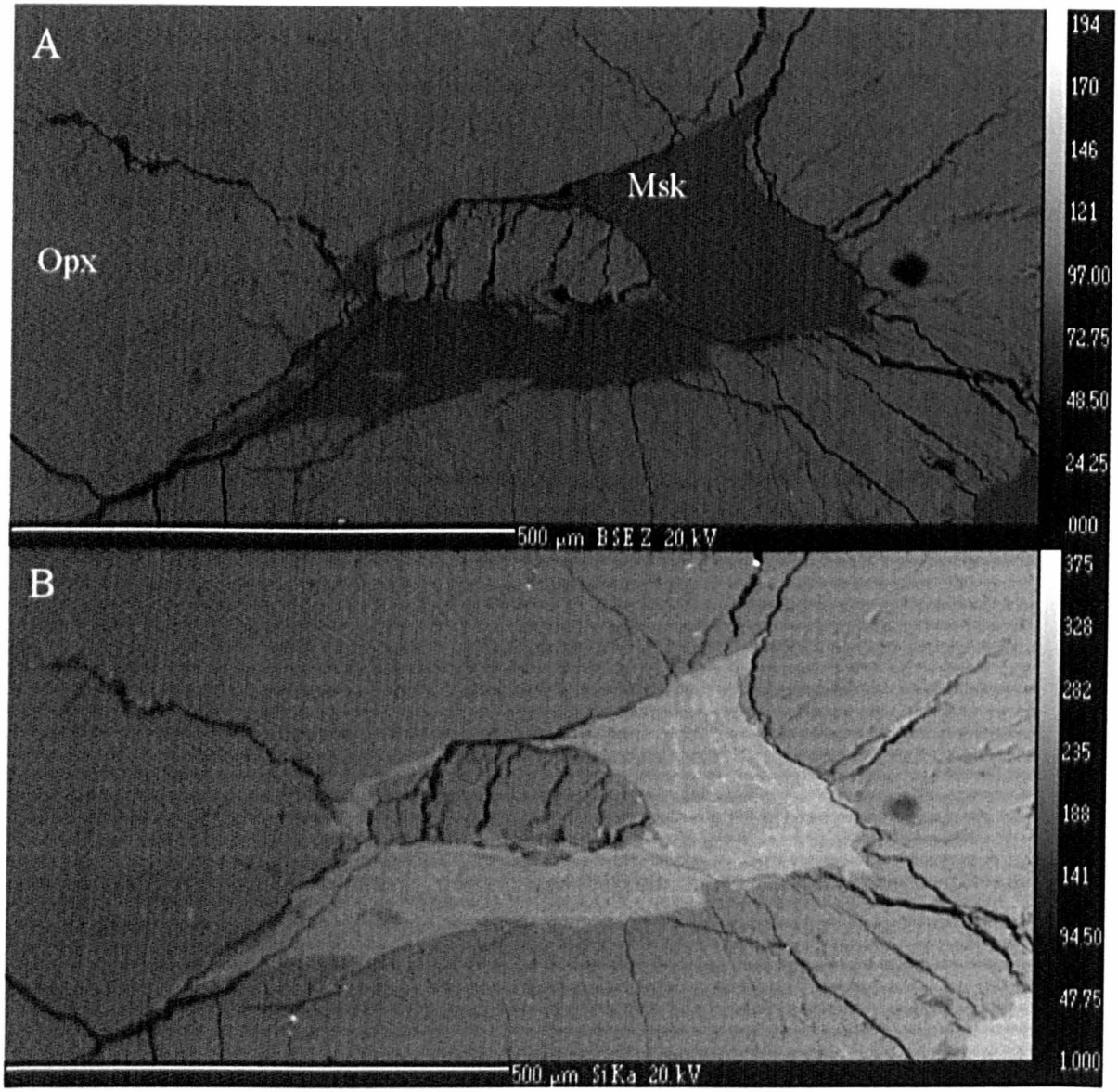

Figure 3-4. EPMA images of maskelynite occurring between orthopyroxene grains in ALH 84001 (*ALH-section-B*). Operating conditions: 20 kV. Numbers on the right are intensity values related to concentration and pixel brightness. Msk = maskelynite, Opx = orthopyroxene. A) BSE image. B) Si map, showing 'veinlets' in the maskelynite, possibly related to flow textures, see Section 3.1.1.2.

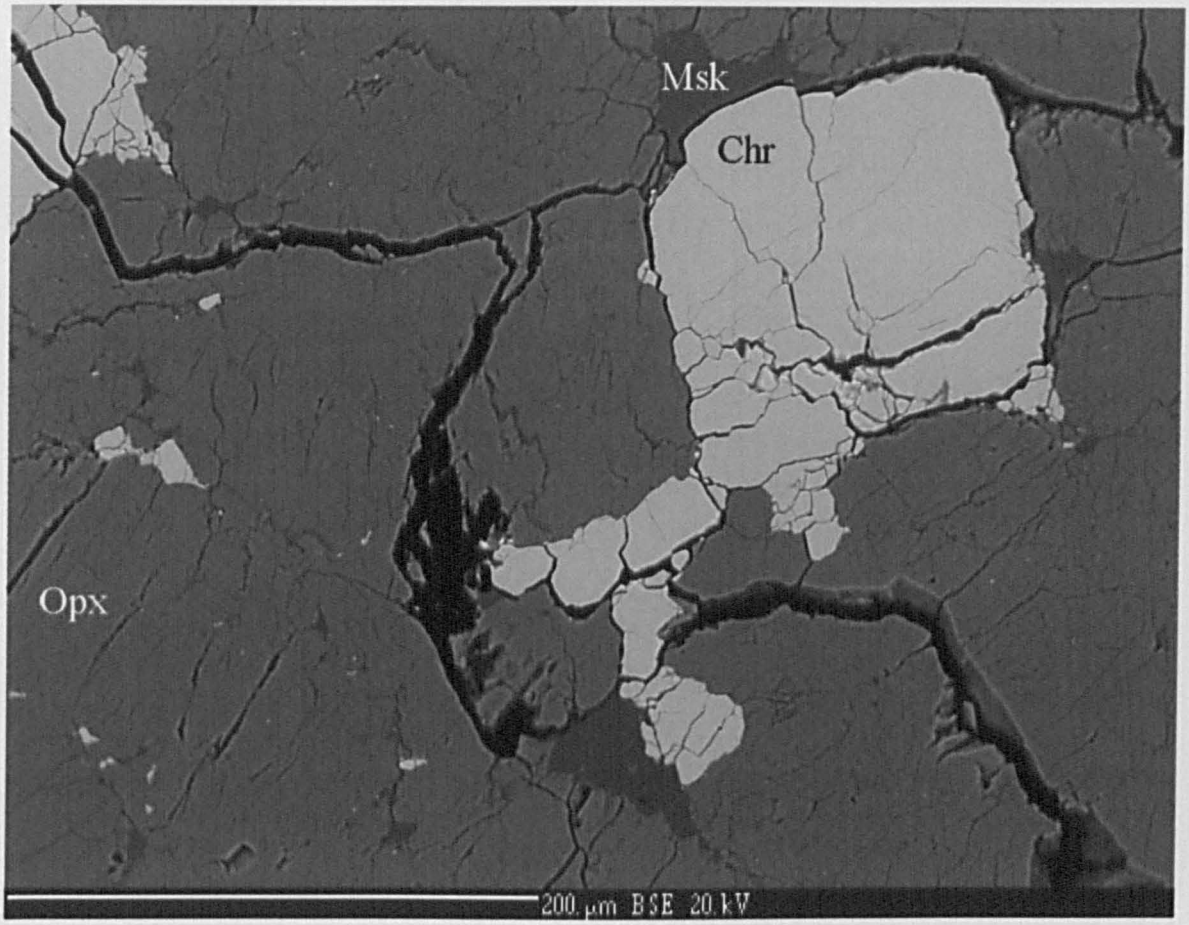

Figure 3-5. EPMA BSE image of textural relationships between maskelynite (Msk), orthopyroxene (Opx) and chromite (Chr) in ALH 84001 (*ALH-section-B*). Maskelynite often occurs between chromite grains and orthopyroxene.

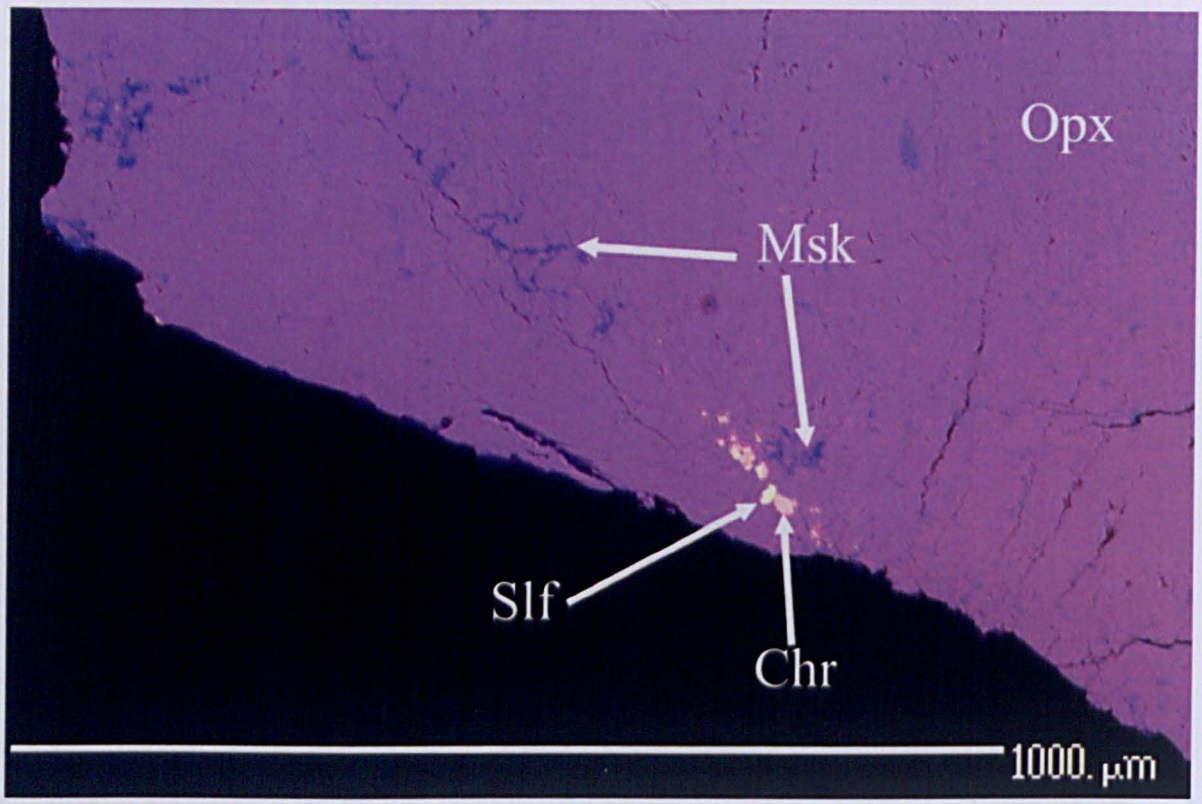

Figure 3-6. EPMA colour composite (red = Fe, green = S, blue = Si) overlapped over a BSE image showing maskelynite inside cracks in *ALH-section-A* and intergrown sulfide and chromite grains. Msk = maskelynite, Opx = orthopyroxene, Chr = chromite, Slf = sulfide.

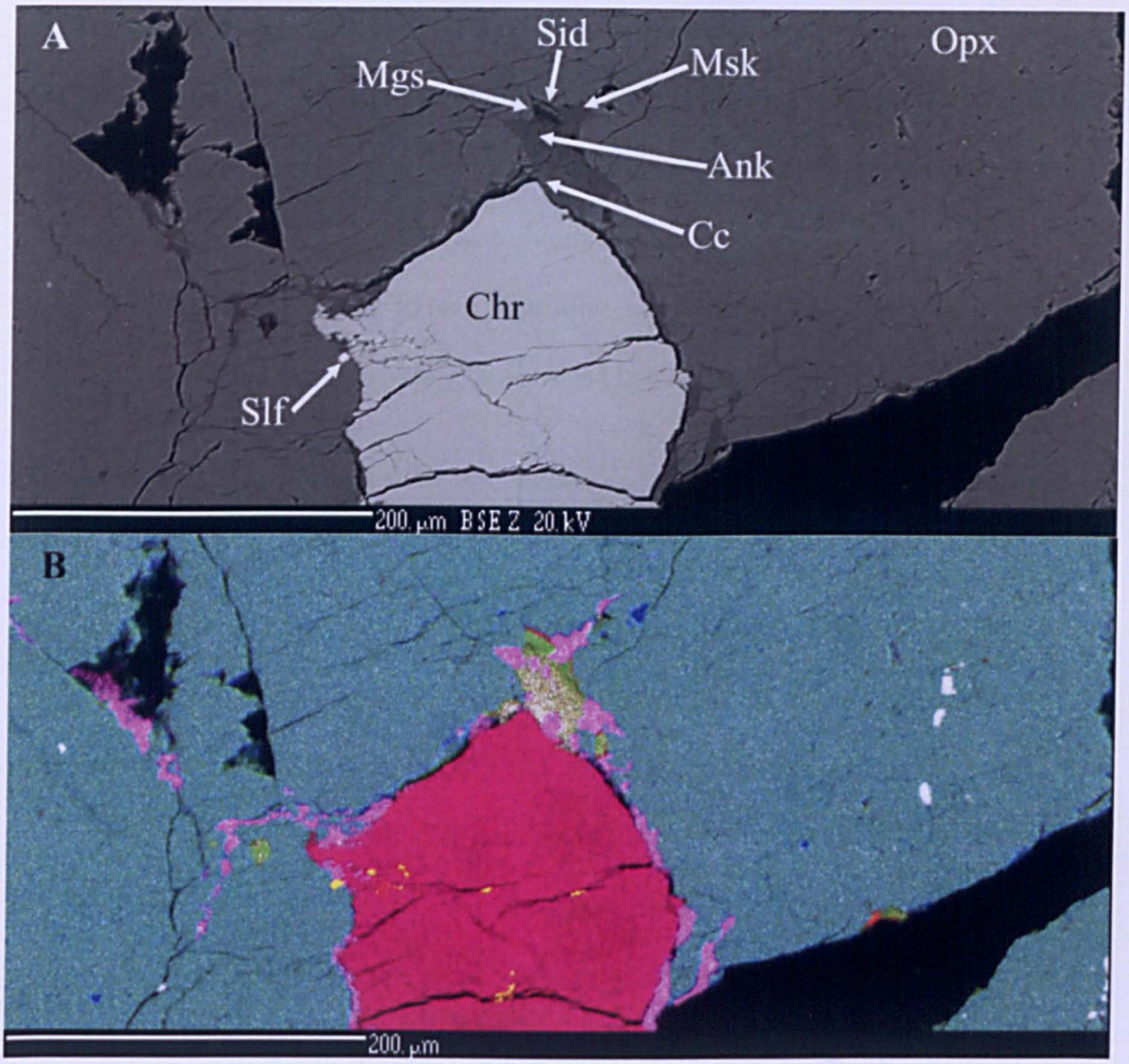

Figure 3-7. EPMA images of a typical carbonate rosette (zoned calcium carbonate (Cc) to ankerite (Ank), surrounded by a magnesite rim (Mgs) and a siderite rim (Sid)) replacing maskelynite (Msk) between orthopyroxene (Opx) and chromite (Chr) grains in sample *ALH-section-C*. Sulfides (Slf) occur intergrown within chromite and in chromite cracks. A) BSE image. B) Colour composite image. Red = Fe, green = Mg, blue = Si, yellow = S, white = Ca, and magenta = Al.

3.1.1.3 Chromite

Chromite grains are sub-euhedral, severely fragmented and are associated with intergrown sulfides, which also occur within the chromites' cracks (Figure 3-5 – Figure 3-7).

Chromite analyses are in agreement with the average of 103 analyses reported by Mittlefehldt (1994) and the representative compositions reported by Gleason et al. (1997). The Al_2O_3 content (~ 7.4 wt. %) and the calculated amount of Fe_2O_3 (~ 5.8 wt. %) are slightly lower (~ 1.5 wt. % lower) in the samples analysed here compared to the analyses by Mittlefehldt (1994), and are in line with analyses by Berkley and Boynton (1992; 5.3 wt. %), which suggests compositional heterogeneity among the chromite phases.

3.1.1.4 Phosphate

Merrilite and apatite were both described in ALH 84001 by Greenwood et al. (2003), but only anhydrous merrilite (Figure 3-8) was observed in the samples allotted for this study, as shown by EPMA analytical totals close to 100 (phosphates containing OH show lower oxide totals, and the OH content would be calculated from the difference).

The different analytical conditions used (see Section 2.3.1 in Chapter 2) resulted in similar compositions (within analytical uncertainty) of the same phosphate phase with the notable exception of the F content (Table 3-2 and Figure 3-9). While the regular setup (used for silicates and oxides) systematically resulted in the detection of ~ 2.5 % F in the phosphate phase, the analyses setup proposed by Barnes et al. (2013) did not detect much F (typically ~ 0.01 %), and EPMA analysis totals were close to 100 % for both procedures. The results prompted the question as to which analytical procedure was most adequate for mapping and spot analyses of phosphates. EPMA mapping with both analytical procedures (as opposed to spot analyses) of the F abundance in the sample shows that the phosphate indeed contains a small amount of F according to the regular analytical setup (~ 6 counts per second over the background value; Figure 3-10), and so the wider beam used in the analytical procedure by Barnes et al. (2013) was not suitable for point analyses of this sample, as it underestimates the F content, despite the relatively large size of the phosphate

in the sample (> 100 μm crystal, Figure 3-9). X-ray peak interferences exist between F, Cr, Fe and Mn, as seen in the F map in Figure 3-10A where both chromite and the phosphate phase appear to contain F. A phosphorus element map reveals that P is only found in the phosphate (Figure 3-10B).

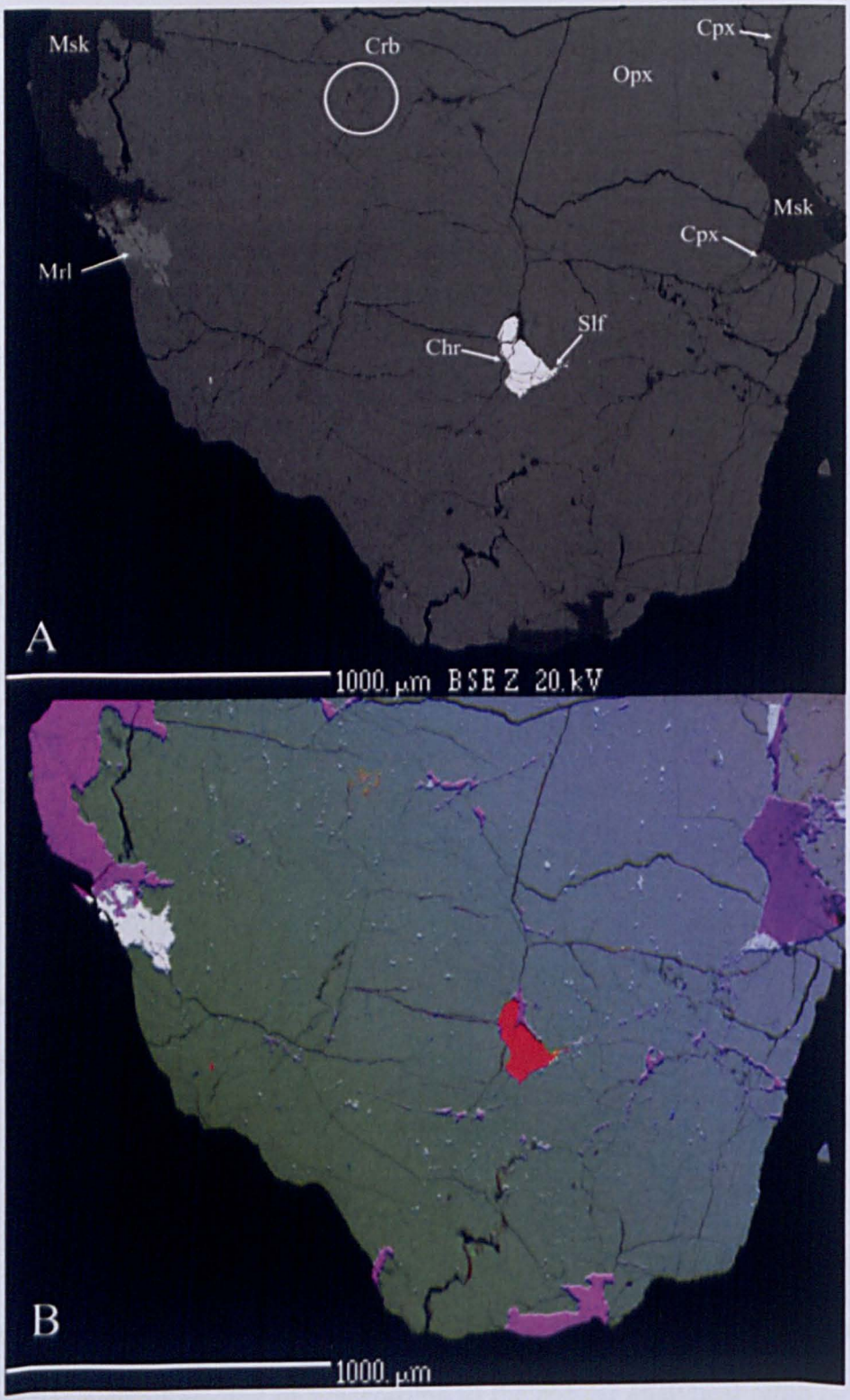

Figure 3-8. EPMA images of a phosphate grain (merrilite) in the context of *ALH-section-B*. A) BSE image. Chr = chromite, Cpx = clinopyroxene, Crb = carbonate, Mrl = merrilite, Msk = maskelynite, Opx = orthopyroxene, Slf = sulphide. B) Colour composite image of EPMA element maps. Red = Fe, green = Mg, blue = Si, yellow = S, magenta = Al, white = Ca.

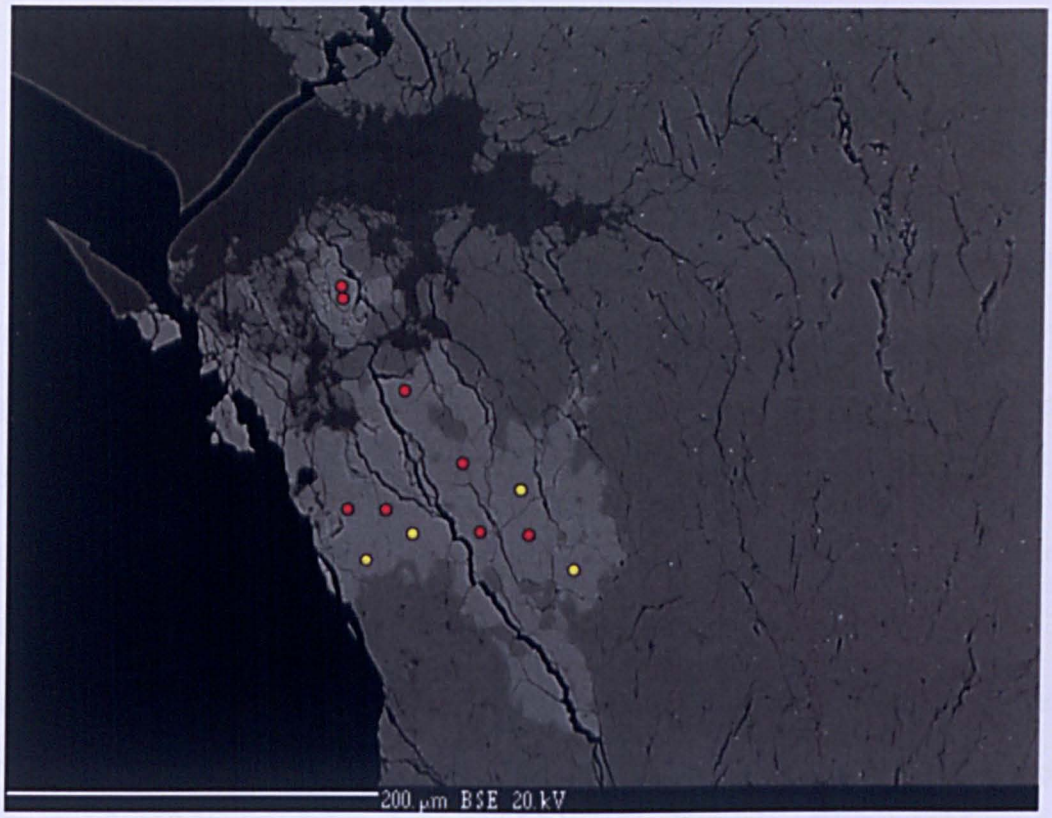

Figure 3-9. EPMA BSE map of the phosphate (merrilite, light grey) analysed with both analytical procedures. Red spots are analysed points with the regular setup (for silicates and oxides), while the yellow spots are analysed points with the procedure used by Barnes et al. (2013).

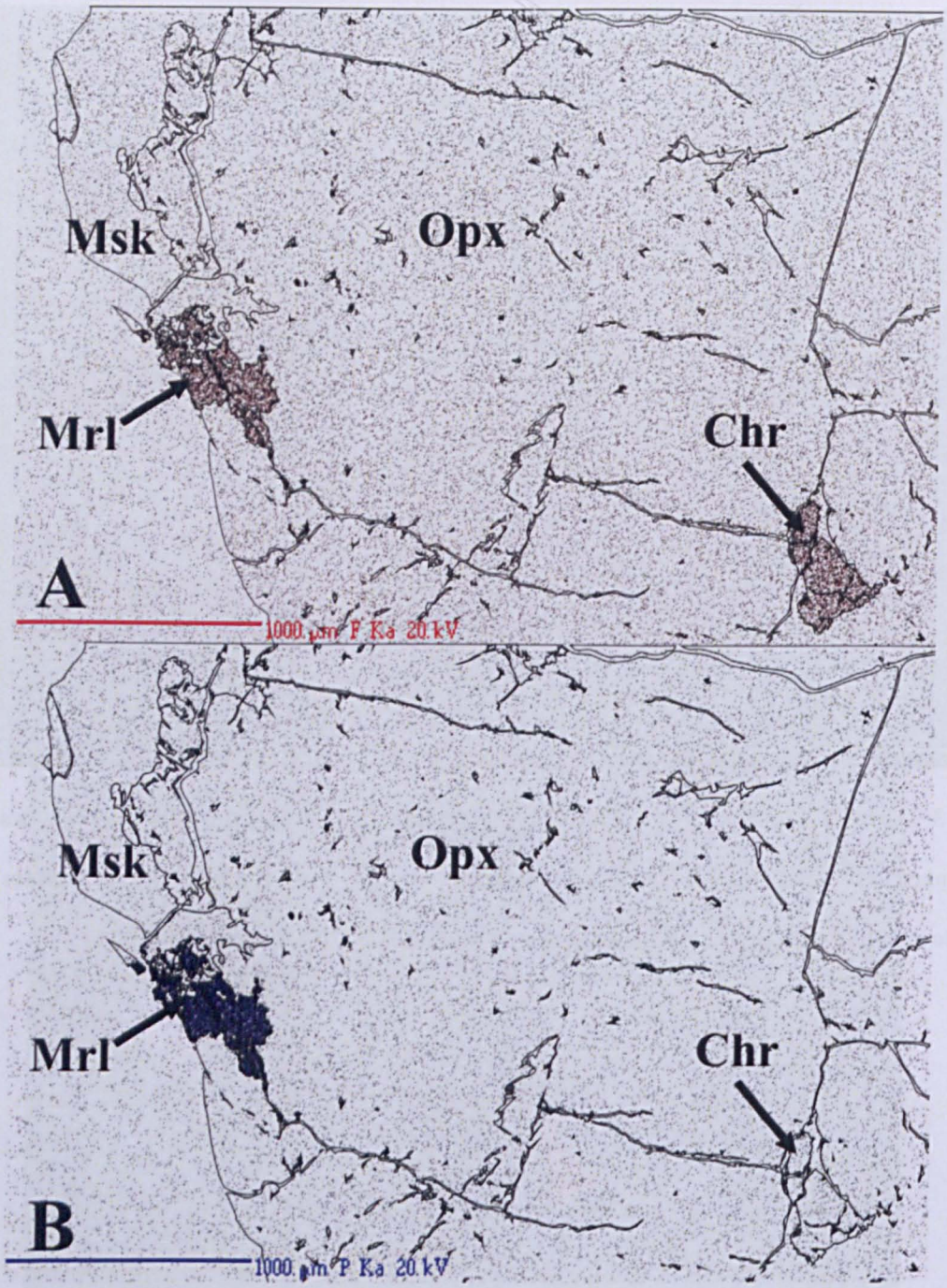

Figure 3-10. EPMA element abundance maps draped over the outline of ALH-sample-B (cf. Figure 3-8 and Figure 3-9). Draping element maps over sample outlines (drawn from BSE images) allows for visualising element abundances which show little contrast between phases due to their low abundance and low detection limit. Chr = chromite, Mrl = merrilite, Msk = maskelynite, Opx = orthopyroxene. A) Fluorine map, B) phosphorus map. Note that F appears to be in both merrilite and chromite, but P only appears to be in merrilite. This effect is caused by the X-ray peak energy interference between P, and Fe, Mn and Cr (see text).

3.1.1.5 Carbonates

Only one EPMA analysis of carbonate could be carried out (Table 3-4), but the composition is representative of the carbonate phases in ALH 84001 when compared to the more numerous and in-depth analyses of the carbonates by EPMA (e.g., Corrigan and Harvey, 2004; Eiler et al., 2002b). The carbonate analysed here is zoned (as appears typical for "rosette-type" ALH 84001 carbonate concretions throughout the sample) from high Ca carbonate in the centre to increasing Fe (ankeritic) content towards the exterior. There is an abrupt change in composition with an Mg-carbonate rim enveloping the ankeritic concretion, and finally a Fe-carbonate rim enveloping the Mg-carbonate rim (Figure 3-7). No "slab-type" carbonates (Eiler et al., 2002b) are apparent in the samples here, although the fragmented nature of some carbonates meant that some carbonates could not be definitively identified as either "rosette-type" or "slab-type".

Carbonate minerals are typically found in the maskelynite, where they appear to replace it, and end where they are in contact with the orthopyroxene (Figure 3-7). However, carbonate minerals appear hosted in the orthopyroxene too (Figure 3-11), where they seem to replace it. While the possibility of pre-existing maskelynite in these latter carbonate locations cannot be ruled out, the absence of relict maskelynite associated to these areas, and the occurrence of unreplaced maskelynite nearby indicates that the carbonate replaced orthopyroxene exclusively here.

Table 3-4. Carbonate EPMA spot analysis of the phase in Figure 3-11. Carbonate composition was calculated using linear least-square deconvolution with HMX (see Section 2.3.1.2 in Chapter 2 for details on the method). HMX deconvolution revealed the analysis was 11.69 ± 1.09 % orthopyroxene, 43.02 ± 1.20 % magnesite, 39.44 ± 1.13 % siderite and 5.85 ± 1.19 % calcite.

	Weight %	Calculated carbonate composition (wt. %)
SiO_2	3.82	-
TiO_2	bdl	-
Al_2O_3	0.04	-
Cr_2O_3	0.08	-
FeO	23.35	44.66
MnO	0.25	0.00
MgO	26.02	48.71
CaO	4.68	6.62
BaO	0.01	-
Na_2O	0.20	-
K_2O	bdl	-
SrO	0.02	-
Rb_2O	0.04	-
P_2O_5	0.10	-
SO_2	0.17	-
F	bdl	-
Cl	0.02	-
Total	58.80	50.00

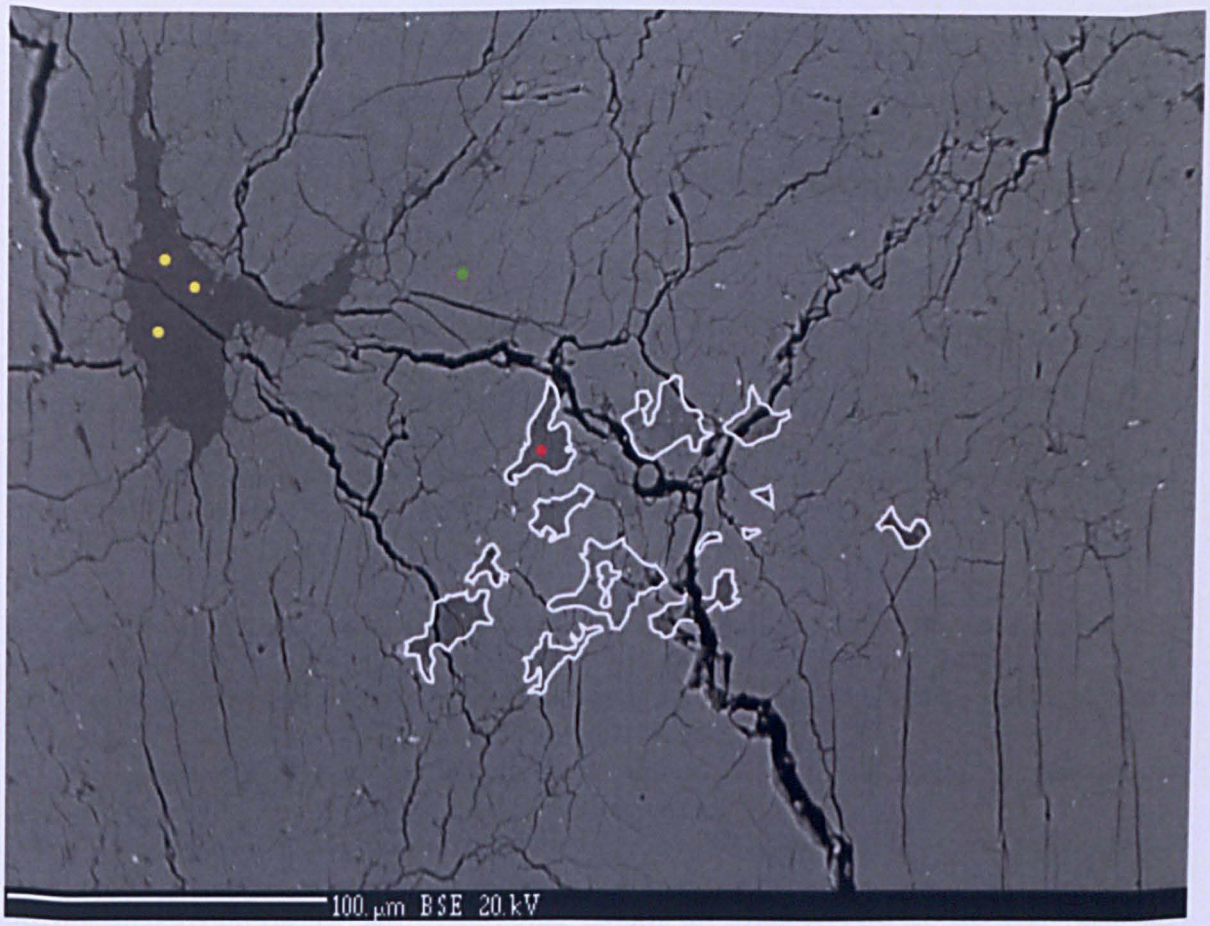

Figure 3-11. EPMA BSE map of carbonate (outlined in white) in orthopyroxene. Dots indicate EPMA spot analyses sites. Red = carbonate, green = orthopyroxene, yellow= maskelynite. Note that large cracks in the orthopyroxene host also cut across some carbonates, signifying that an event of brittle deformation occurred after the deposition of the carbonates.

3.1.1.6 Other minerals.

Minerals which have been identified in previous studies include trace amounts of olivine (Shearer et al., 1999) and phyllosilicates (Brearley, 2000; Shearer et al., 1999), but despite careful analyses, none of these were observed in the ALH 84001 samples studied here. Magnetite, which appears to be found admixed within the carbonates (e.g., McKay et al., 1996) was not directly observed with the SEM and EPMA, probably because the crystals are reported to be very small (10 – 150 nm; e.g., Thomas-Keprta et al., 2009). Iron-rich

zones in the carbonates, as in Figure 3-7 could host the magnetite nanocrystals and/or may be siderite. Further analyses of those areas to determine the presence of magnetite are beyond the scope of this study. Magnetite has been painstakingly studied in depth by other workers (e.g., Barber and Scott, 2002; Bradley et al., 1996; Thomas-Keprta et al., 2009, 2000; Treiman and Essene, 2011), so the focus was on identifying other phases. Field emission gun secondary electron microscopy (FEG-SEM) or transmission electron microscopy (TEM) would have been more apt to study the nanocrystalline magnetite.

Silica typically appears in the samples imaged as small (up to ~ 10 μm) amorphous phases in orthopyroxene. Element maps confirm that no other analysed elements are found in these phases (e.g., Figure 3-7). EPMA spot analyses of the silica grains were not successful (oxide totals far from 100 ± 2 %) due to their small grain size (typically < 5 μm).

Sulfides were observed directly in EPMA element maps (e.g., Figure 3-6 – Figure 3-7), but analyses with the EPMA resulted in mixed chromite/sulfide or orthopyroxene/sulfide compositions (Table 3-5), as the sulfides are typically on the order of 5 – 30 μm and are hosted in the chromite and orthopyroxene.

Table 3-5. Representative mixed analysis of sulfide hosted in orthopyroxene. Deconvolving the contributions of the different endmembers with HMX was not attempted as the exact composition of the sulfide is unknown from this study.

	Weight %
SiO_2	26.89
TiO_2	0.09
Al_2O_3	0.20
Cr_2O_3	0.52
FeO*	48.75
NiO	0.01
MnO	0.13
MgO	5.52
CaO	0.59
BaO	0.02
Na_2O	0.06
K_2O	bdl†
SrO	0.02
Rb_2O	0.22
P_2O_5	0.01
SO_2	25.37
F	bdl
Cl	0.01
Total	108.43

*Includes Fe_2O_3.
†Below detection limit.

3.1.2 Raman spectroscopy

Carbonate-rich areas mapped with Raman spectrometry are shown in Figure 3-12, and the exact points analysed are shown in Figure 3-13.

The Raman spectra, in most cases, were affected by the carbon coat on the sample (see Section 2.4.2), but most minerals were clearly identified by spectral features at Raman shifts unaffected by the coat. Minerals clearly identified in the mapped regions by comparison with the Raman spectra in the RRUFF database include orthopyroxene (Figure 3-14), carbonates (Fe and Ca-Mg carbonates; Figure 3-14 and Figure 3-16), and graphite (Figure 3-15).

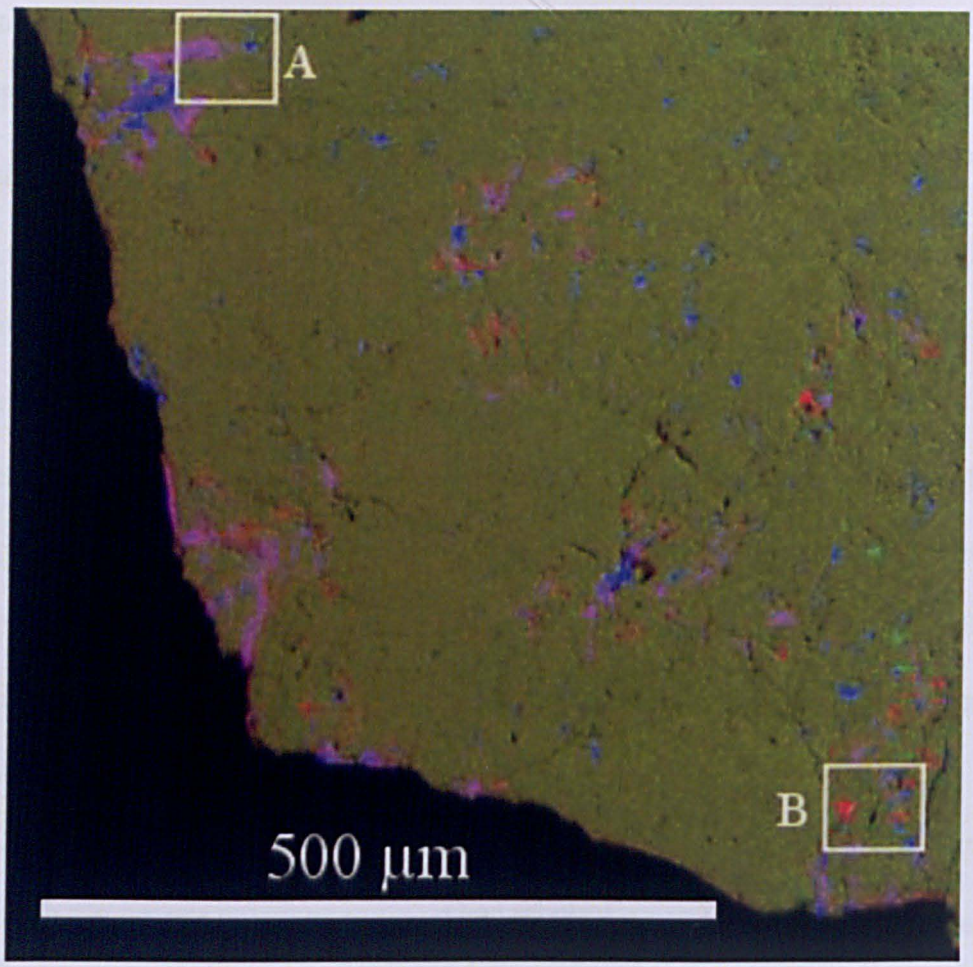

Figure 3-12. RGB FCC EPMA image of carbonate-rich areas in ALH 84001 (*ALH-sample-A*) analysed with the Raman spectrometer. Red = Fe, green = Mg, blue = Ca.

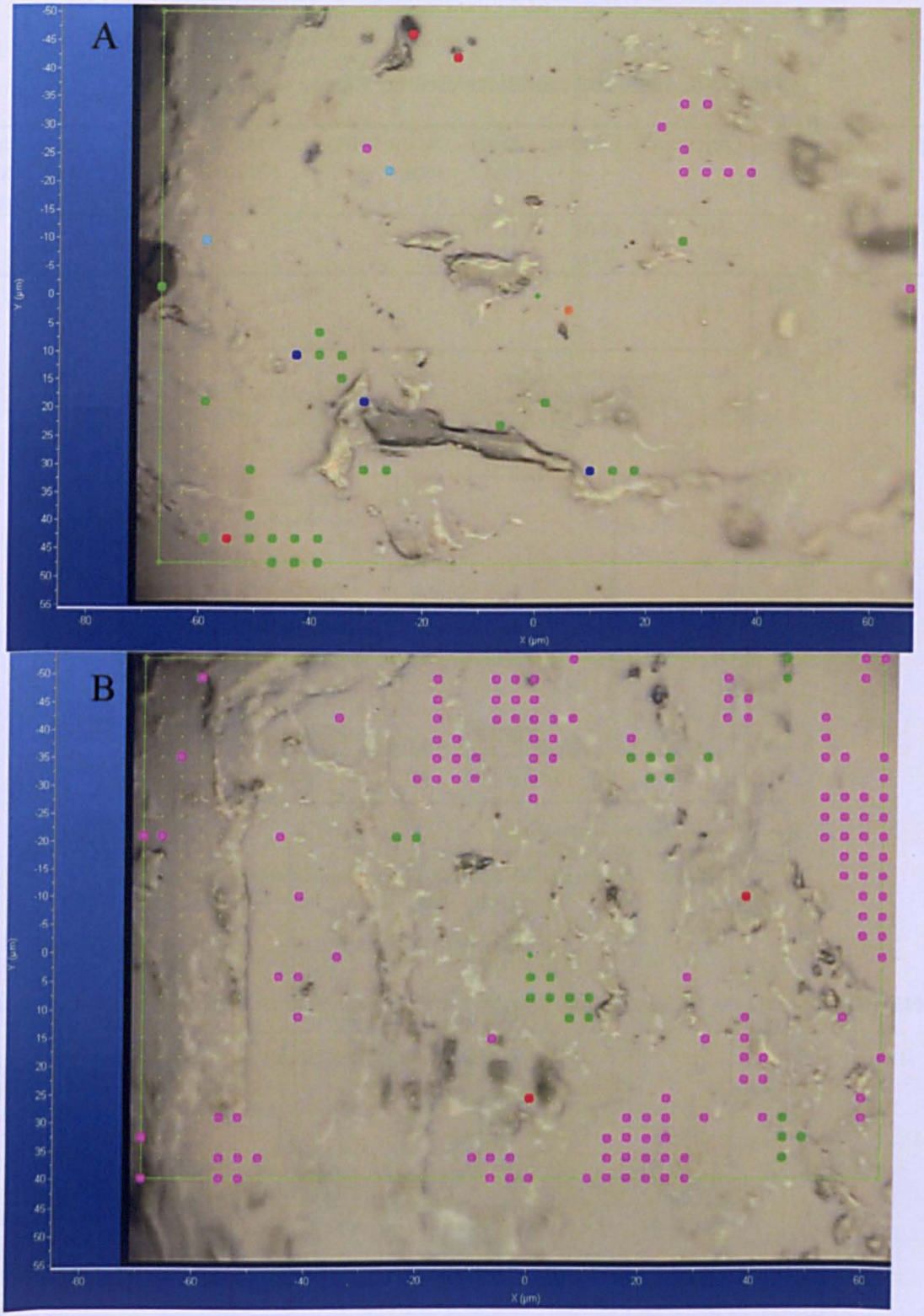

Figure 3-13. Points analysed with Raman spectroscopy in maps A and B. Analytical settings are detailed in Table 3-6. Possible minerals identified from Raman spectra are as follows: red = graphite, green = carbonates, blue = hematite, cyan = silica, magenta = orthopyroxene, orange = possible garnet.

Table 3-6. Analytical conditions used for Raman maps A and B.

Map	Laser frequency (nm)	Objective	Grating	Filter (%)	Acquisition time (s)	Number of accumulations per spot	Step size (μm)
A	514.53	×50	600	10	15	2	4
B	514.53	×50	600	10	30	2	3.5

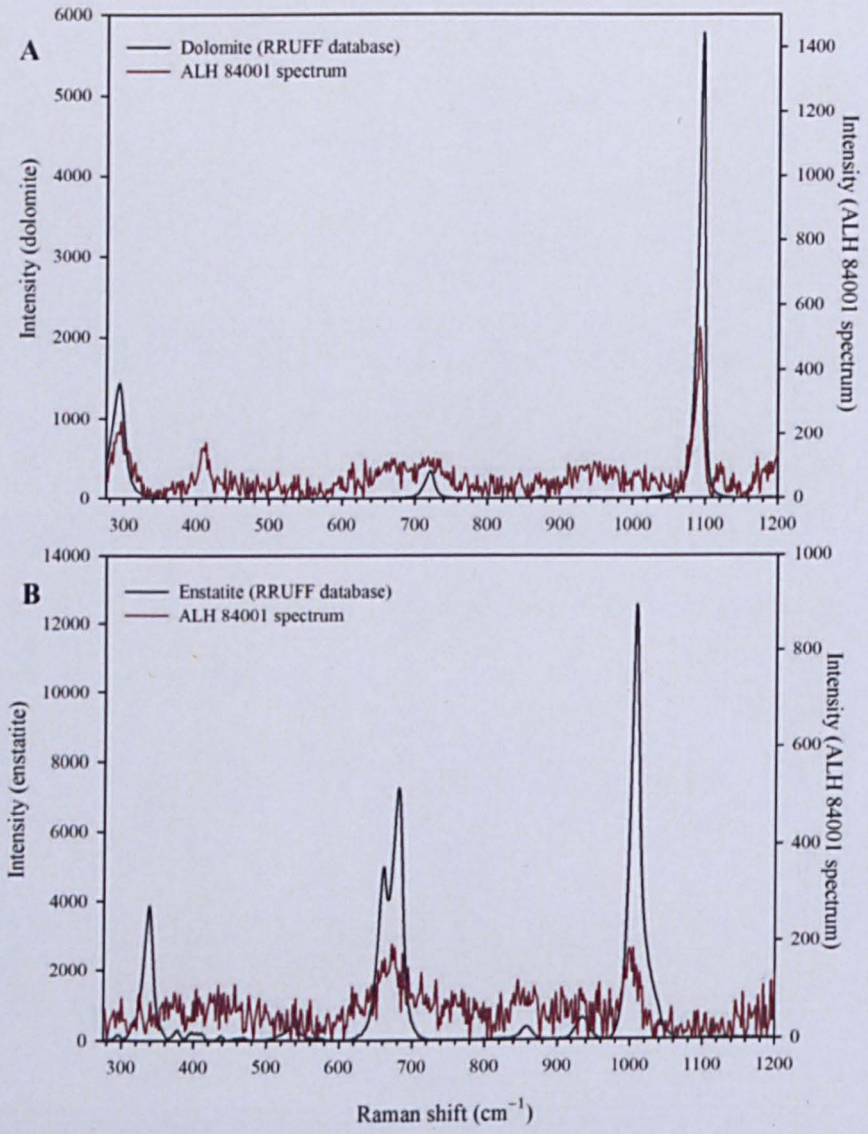

Figure 3-14. Representative Raman spectra of A) carbonate, and B) orthopyroxene in ALH84001, and possible mineral candidates from the RRUFF database.

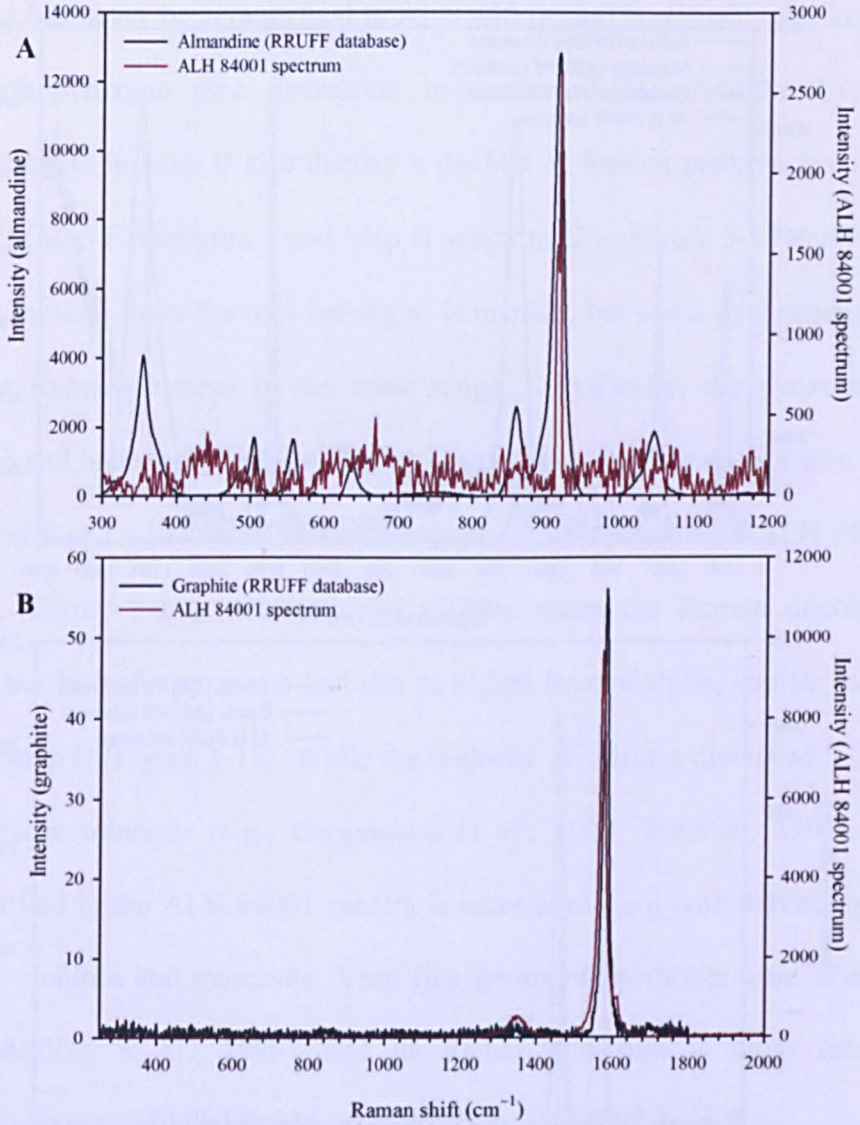

Figure 3-15. Representative Raman spectra of A) possible garnet and B) graphite in ALH 84001, and mineral candidates from the RRUFF database.

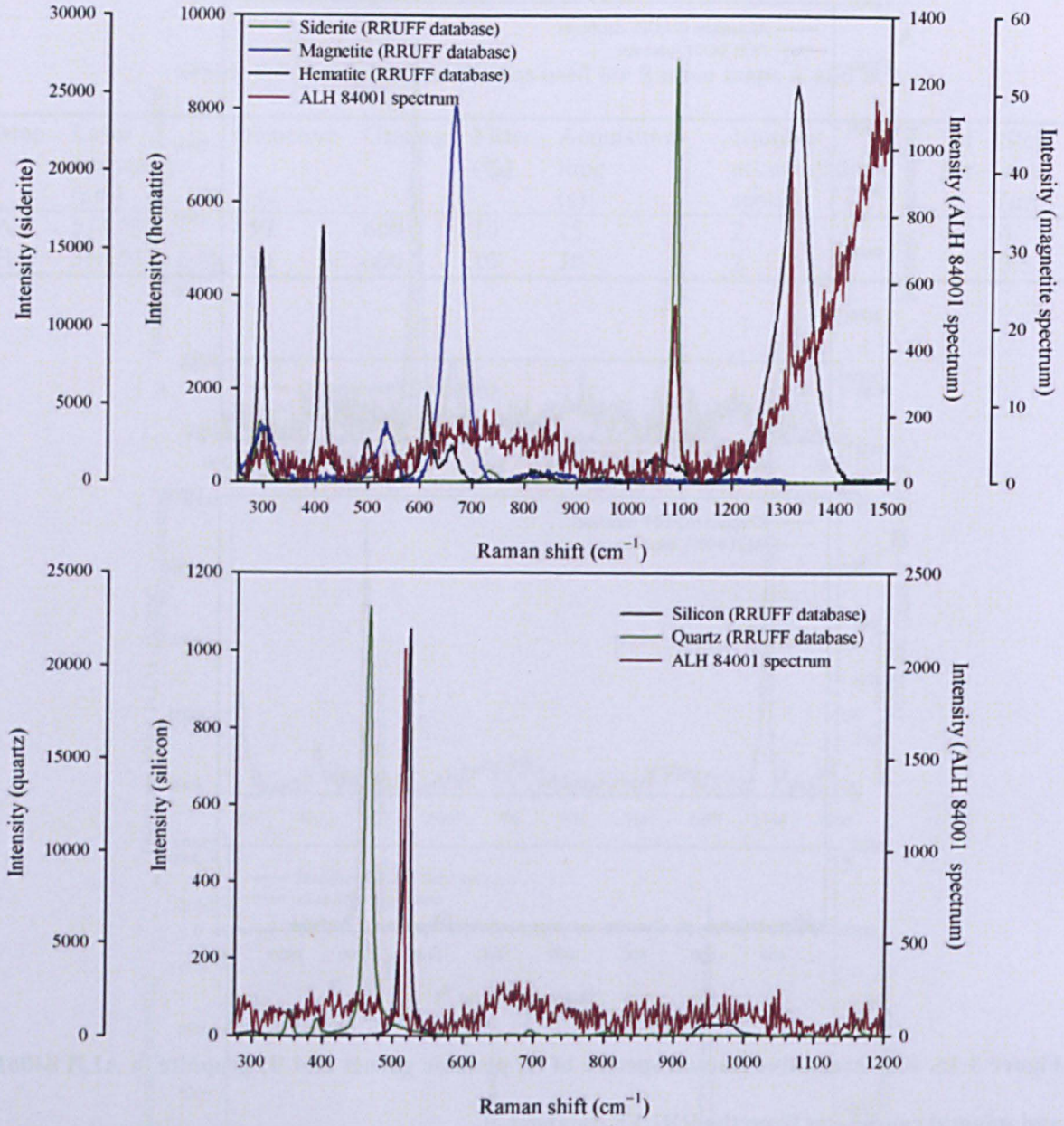

Figure 3-16. Representative Raman spectra of A) carbonate (possibly siderite) in ALH 84001 with possible hematite, and B) possible silica in ALH 84001 (the RRUFF database does not contain amorphous silica, so quartz and Si are depicted instead). Magnetite is shown for comparison in map A, but although it contains a feature at ~300 cm^{-1}, it lacks the feature at ~1300 cm^{-1} that the hematite and analysed ALH 84001 spectra have.

Other minerals were less obvious, and include garnet (possibly almandine; Figure 3-15), hematite (occurring together with Fe-carbonate; Figure 3-16) and amorphous silica (Figure

3-16). Garnet has never been described in ALH 84001, and is probably unlikely to coexist with the orthopyroxene (see discussion in section 3.1.4). Additionally, two spots containing graphite in Map B also display a doublet of Raman positive features at ~ 315 and 370 cm^{-1} (Map B spectrum 1 and Map B spectrum 2 in Figure 3-17 and Figure 3-18). The specific mineral these features belong to is unclear, but some pyroxenes and sulfides share similar Raman features in the same range. Specifically, the pyroxenes diopside ($CaMgSi_2O_6$) and hedenbergite ($CaFeSi_2O_6$) share the same features, but also have strong features at ~665 and ~1015 cm^{-1}, similar to enstatite, but which the ALH 84001 Map B spectra lack (Figure 3-17). Alternatively, sulfides share the Raman doublet at lower frequencies, but lack the pyroxene features at higher Raman shifts, similar to the spectra measured in Map B (Figure 3-18). While the majority of sulfides identified in ALH 84001 have been pyrite minerals (e.g., Greenwood et al., 2000; Treiman, 1995) the Raman doublet identified in the ALH 84001 spectra is more consistent with argentopyrite, and to some extent, violarite and marcasite. Very fine grains of pyrrhotite have been identified previously (McKay et al., 1996), and its Raman spectrum is more similar to the ALH 84001 spectra than the pyrite spectra is (Figure 3-18).

Table 3-7 contains the details of minerals from the RRUFF database used for comparison with the ALH 84001 Raman spectra.

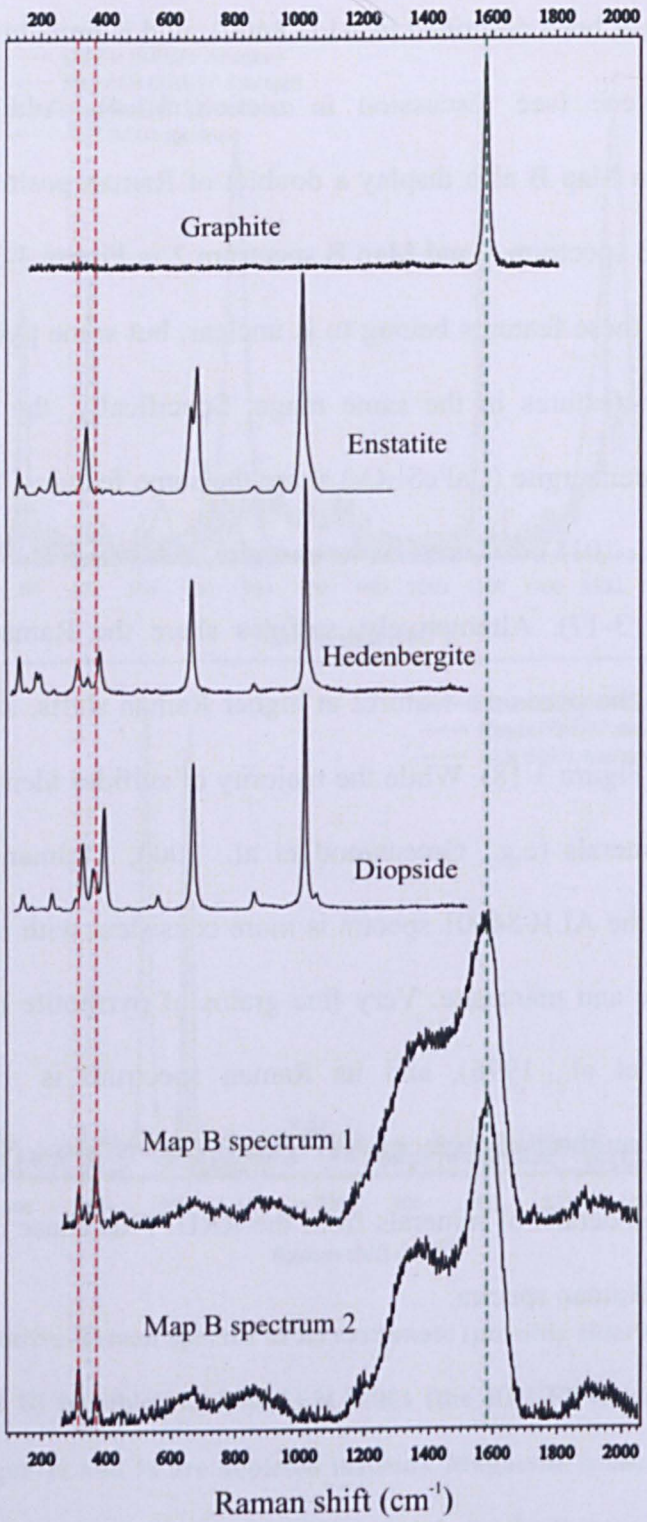

Figure 3-17. Candidate pyroxenes and graphite (from the RRUFF database) for the ALH 84001 Raman spectra in Map B. Analytical conditions and chemical formulae for the pyroxenes are detailed in Table 3-7. Red dashed lines show the common Raman features between the ALH 84001 Map B spectra and some pyroxenes (hedenbergite and diopside). The green dashed line shows the location of the graphite feature.

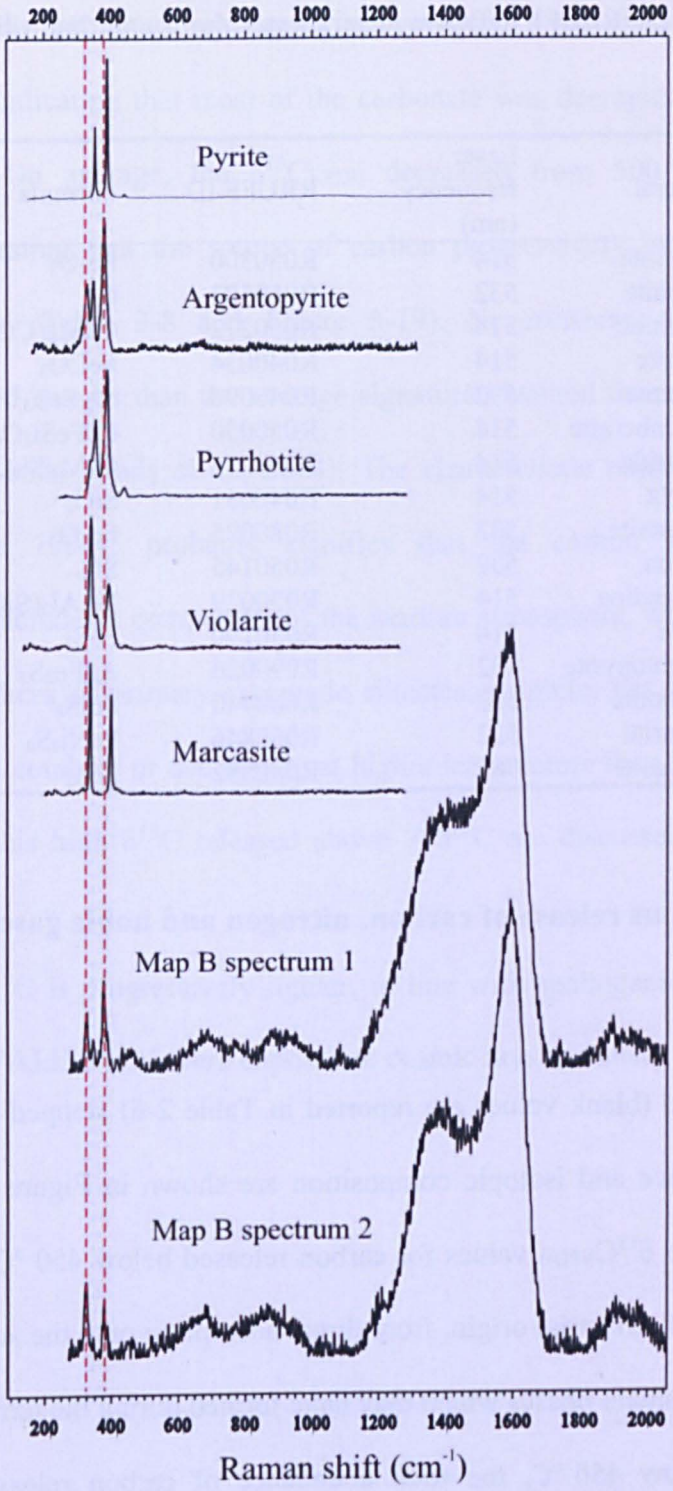

Figure 3-18. Sulfide candidates for the ALH 84001 Raman spectra in Map B. Raman spectra for the sulfides were obtained from the RRUFF database. Analytical conditions and chemical formulae for the sulfides are detailed in Table 3-7. Red dashed lines show the common Raman features between the ALH 84001 Map B spectra and some sulfides.

Table 3-7. Details of the RRUFF database minerals used for comparing with the Raman spectra of ALH 84001 above.

Mineral	Laser frequency (nm)	RRUFF ID	Formula
Hematite	514	R050300	Fe_2O_3
Graphite	532	R050503	C
Dolomite	514	R050272	$CaMg(CO_3)_2$
Siderite	514	R040034	$FeCO_3$
Enstatite	532	R040093	$MgSiO_3$
Hedenbergite	514	R050030	$CaFeSi_2O_6$
Diopside	514	R060276	$CaMgSi_2O_6$
Quartz	514	R040031	SiO_2
Magnetite	532	R080025	Fe_3O_4
Silicon	532	R050145	Si
Almandine	514	R050029	$Fe_3Al_2(SiO_4)_3$
Pyrite	514	R050190	FeS_2
Argentopyrite	532	R090026	$AgFe_2S_3$
Pyrrhotite	532	R060440	Fe_7S_8
Violarite	532	R060846	$FeNi_2S_4$
Marcasite	785	R060882	FeS_2

3.1.3 Simultaneous release of carbon, nitrogen and noble gases

3.1.3.1 Carbon

The blank corrected (blank values are reported in Table 2-6) stepped combustion results for carbon abundance and isotopic composition are shown in Figure 3-19 and listed in Table 3-8. Negative $\delta^{13}C_{VPDB}$ values for carbon released below 450 °C probably indicate that the carbon is of terrestrial origin, from direct adsorption onto the surfaces of the chips and possible contaminant phases which may have formed during the terrestrial residence of the meteorite. Below 450 °C, the total abundance of carbon released in combustion amounted to 28.6 % of the total release. From 400 to 450 °C, the large increase in $\delta^{13}C_{VPDB}$ (−20.69 to +6.66 ‰) indicates that the source of carbon may be a mixture of indigenous martian components and terrestrial contaminants. It was at the 450 – 500 °C step where most of the carbonates decomposed and the release of carbon was largest (53.4 % of the total abundance), and the $\delta^{13}C_{VPDB}$ (+39.91 ± 0.36 ‰) is consistent with measurements by

other authors (Table 3-9). At temperatures above 500 °C, the yield and abundance of carbon tailed off, indicating that most of the carbonate was decrepitated in the previous temperature step. On average, the $\delta^{13}C_{VPDB}$ decreased from 500 °C towards higher temperatures suggesting that the source of carbon progressively included the primary magmatic minerals (Table 3-8 and Figure 3-19). Nevertheless, the magmatic $\delta^{13}C$ (+3.90 ‰) remained heavier than the average signature obtained from 11 shergottites and Chassigny (−20 ± 4 ‰; Grady et al., 2004). The characteristic relatively heavy $\delta^{13}C$ in ALH 84001 above 700 °C probably signifies that the carbon sampled at higher temperatures also includes a component of the martian atmosphere, which may be lodged as: coating on surfaces of primary magmatic silicates, graphite, gas trapped in glass, or other phases which combust or decrepitate at higher temperature than the carbonates. The possible hosts of this high $\delta^{13}C$ released above 700 °C are discussed in more detail in Section 3.1.4.

Above 1100 °C, $\delta^{13}C$ is progressively lighter, in line with spallogenic production as the primary silicates of ALH 84001 were exposed to cosmic rays in transit.

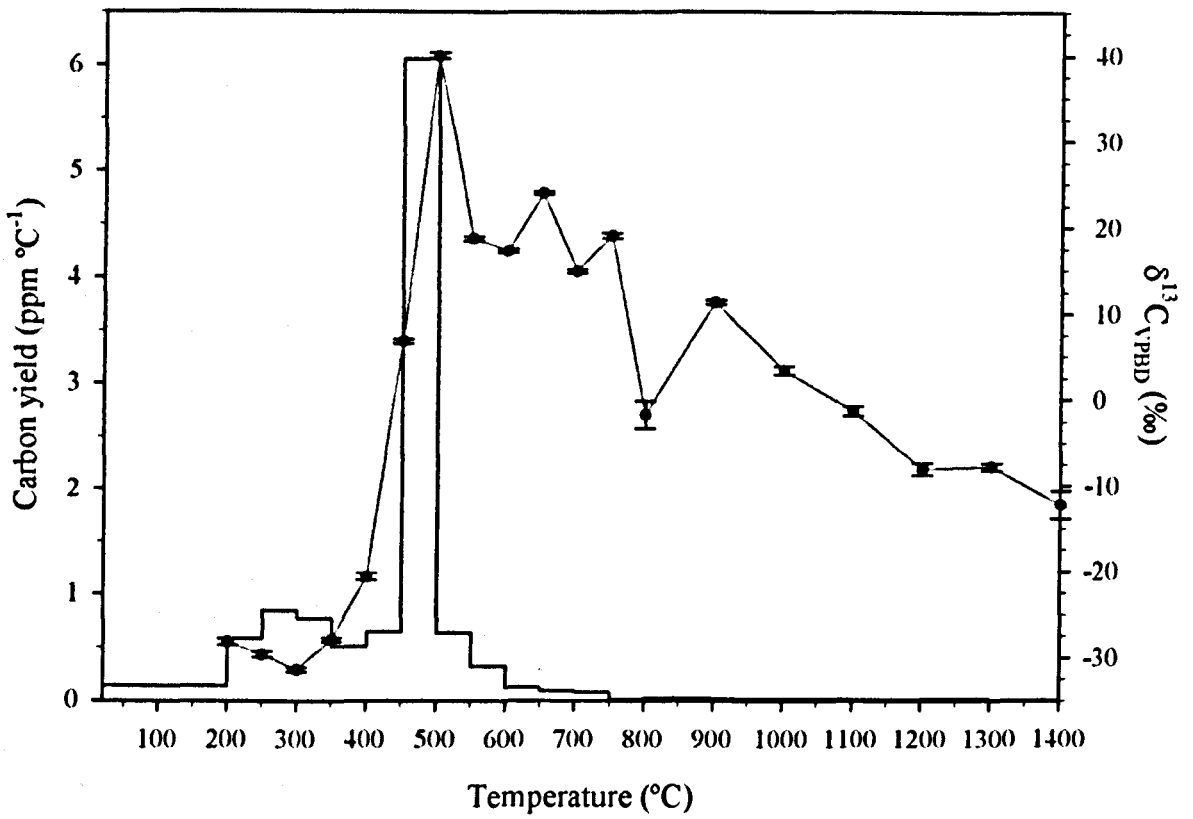

Figure 3-19. Stepped combustion profile for carbon in ALH 84001. Carbon yield is represented as a histogram and isotopic composition is shown as black dots at each of the temperature steps joined by a grey line. Error bars in the $\delta^{13}C$ are 1σ. The start of the combustion experiment was from room temperature.

Table 3-8. Stepped combustion results for carbon in ALH 84001.

Temp. step (°C)	C abundance (ppm)	C yield (ppm °C^{-1})	$\delta^{13}C_{VPDB}$		Possible hosts
			‰	1σ	
200	26.864	0.134	-28.20	0.38	TC*, organics
250	29.302	0.586	-29.66	0.33	TC, organics
300	42.228	0.845	-31.40	0.25	TC, organics
350	38.428	0.769	-27.94	0.22	TC, organics
400	25.446	0.509	-20.69	0.40	TC, organics, Fe carbonates
450	32.203	0.644	+6.66	0.26	TC , organics, Fe carbonates, AC†
500	302.870	6.057	+39.91	0.36	Fe-Mg carbonates, AC
550	31.651	0.633	+18.60	0.28	Fe-Mg-Ca carbonates
600	16.219	0.324	+17.13	0.17	Mg-Ca carbonates
650	6.058	0.121	+23.93	0.17	Mg-Ca carbonates
700	4.572	0.091	+14.81	0.22	Mg carbonates, graphite
750	3.725	0.074	+19.01	0.31	Graphite
800	0.354	0.007	-1.78	1.59	Graphite, maskelynite, SiO_2
900	1.890	0.019	+11.33	0.24	Graphite, maskelynite, SiO_2
1000	1.532	0.015	+3.40	0.46	Magmatic silicates (Opx)
1100	1.149	0.011	-1.23	0.55	Magmatic silicates (Opx)
1200	0.952	0.010	-8.05	0.69	Spallogenic (Opx)
1300	1.116	0.011	-7.77	0.43	Spallogenic (Opx)
1400	0.936	0.005	-12.21	1.63	Spallogenic (Opx)

*Terrestrial contaminants, including adsorbed carbon and secondary phases formed during the meteorite's terrestrial residence.
†Amorphous carbon.

Table 3-9. Comparison of carbon yield and isotopic signature of ALH 84001 between the stepped combustion analyses by Grady et al. (1994), Jull et al. (1998) and this study. The sample masses were 5.099, 268 and 14.823 mg respectively. 'Carbon-bearing components' as defined by Grady et al. (1994), where 'organics' are defined by the temperature range room temperature – 450 °C, 'carbonate' at 450 – 525 °C, and 'magmatic carbon' 700 – 1200 °C. As temperature steps differed between the studies, the "components" are identified in this study by the ranges room temperature – 450 °C for 'organics', 450 – 500 °C for 'carbonate' and 700 – 1200 °C for 'magmatic carbon'. In the study by Jull et al. (1998), 'organics' release carbon at 300 – 430 °C, and 'carbonate' at 500 – 600 °C. See text for discussion.

Carbon-bearing components	This study		Grady et al. (1994)		Jull et al. (1998)	
	Yield (ppm)	$\delta^{13}C^{*}$ (‰)	Yield (ppm)	$\delta^{13}C$ (‰)	Yield (ppm)	$\delta^{13}C$ (‰)
Organics	194.47	−23.98	257.1	−21.5	112	−23.43
Carbonate	302.87	+39.91	284.1	+40.1	254	+39.96
Magmatic carbon	9.60	+3.90	12.8	+0.8	nd	nd
Total	565.44	-3.53	600.6	+10.6	nd	nd

* Weighted average

3.1.3.2 Nitrogen

Blank corrected nitrogen stepped combustion results are shown in Figure 3-20 and Table 3-10. Combustion began from room temperature to 1400 °C, but the nitrogen yield and abundance in the 1300 – 1400 °C step was below the detection limit, so the $\delta^{15}N$ in the final step was not calculated. Moreover, the nitrogen abundance at the 1100 – 1200 °C was very low (0.003 ppm), so the standard error calculated for the ^{15}N is high.

A first order comparison of the yields and abundances of nitrogen here and other studies shows that there is a significant difference among studies. Whereas the 600 – 1000 °C range released 0.264 ppm N_2 in this study and was comparable to a previous value (0.222 ppm; Grady et al., 1998), a stepped pyrolysis experiment released 22.9 ppm in the same temperature range (Marti and Mathew, 2000).

The negative $\delta^{15}N_{AIR}$ measured here up to 250 °C is most likely indicative of terrestrial nitrogen, organics, and possible martian and terrestrial nitrates which may also have been present (Grady et al., 1998, 1995), but have never been observed as distinct phases. Over 50 % of all measured nitrogen in the sample was released up to the 350 °C step.

A local maximum of released nitrogen (0.431 ppm, ~ 12.07 % of the total nitrogen released in the experiment) was observed at the 450 – 500 °C step, which coincided with the largest carbon release from decrepitation of the carbonates (see Section 3.1.3.1). The $\delta^{15}N$ isotopic signature of the nitrogen in this step (+9.61 ± 0.39 ‰) is, however, fairly indistinct from the previous steps (+5.60 ± 2.08 ‰ from 300 to 450 °C). While compositional analyses of the carbonates in ALH 84001 do not note them to be nitrogen enriched, the local maximum and the tailing off of the nitrogen abundance in subsequent temperature steps is suggestive of simultaneous release with the carbon from the carbonates (Figure 3-19 and Figure 3-20). However, in comparison to $\delta^{15}N$ estimates for the martian atmosphere from stepped combustion of ALH 84001 by other authors (e.g., ≥ +46 ‰, Murty and Mohapatra, 1997; ≤ +200 ‰, Grady et al., 1998; +351 – 462 ‰, Miura and Sugiura, 2000), the $\delta^{15}N$ measured at this step was light, as the other authors contend that the atmospheric nitrogen component is hosted in shocked silicates (mainly maskelynite) and is released at higher temperature steps. On the other hand, it is similar to the heaviest $\delta^{15}N$ measured by pyrolysis (+4 ± 2 ‰; Marti and Mathew, 2000). More importantly, any early martian atmospheric nitrogen incorporated into the carbonate structures would have been subject to the effects of fractionation by the process of carbonate formation (e.g., transported and deposited by fluids), and the composition of the martian atmosphere when the carbonate was formed may have been different to when nitrogen was implanted by shock.

The $\delta^{15}N$ signature reached a maximum (ignoring steps above 1000 °C, where cosmogenic nitrogen is released from silicates) at 700 °C. At this temperature step, all the carbonates

have probably decrepitated (see Section 3.1.3.1), and graphite begins to combust. Graphite in meteorites can host nitrogen (e.g., Grady et al., 2002; Grady and Wright, 2003; Hoppe et al., 1995), and theoretical studies show that increased nitrogen substitution in graphite changes its crystal structure (dos Santos and Alvarez, 1998).

From 700 to 1000 °C, the nitrogen isotopic signature becomes progressively lighter, but is still heavier than the signature in previous steps. Maskelynite appears to soften between 700 and 800 °C, probably releasing shock-implanted atmospheric gas (Grady et al., 1998). Above 1000 °C, nitrogen yields are the lowest measured in the sample and $\delta^{15}N$ are the highest, owing to the release from either shock implanted gas components, trapped nitrogen in magmatic minerals (namely orthopyroxene), or spallogenically produced nitrogen (principally from oxygen).

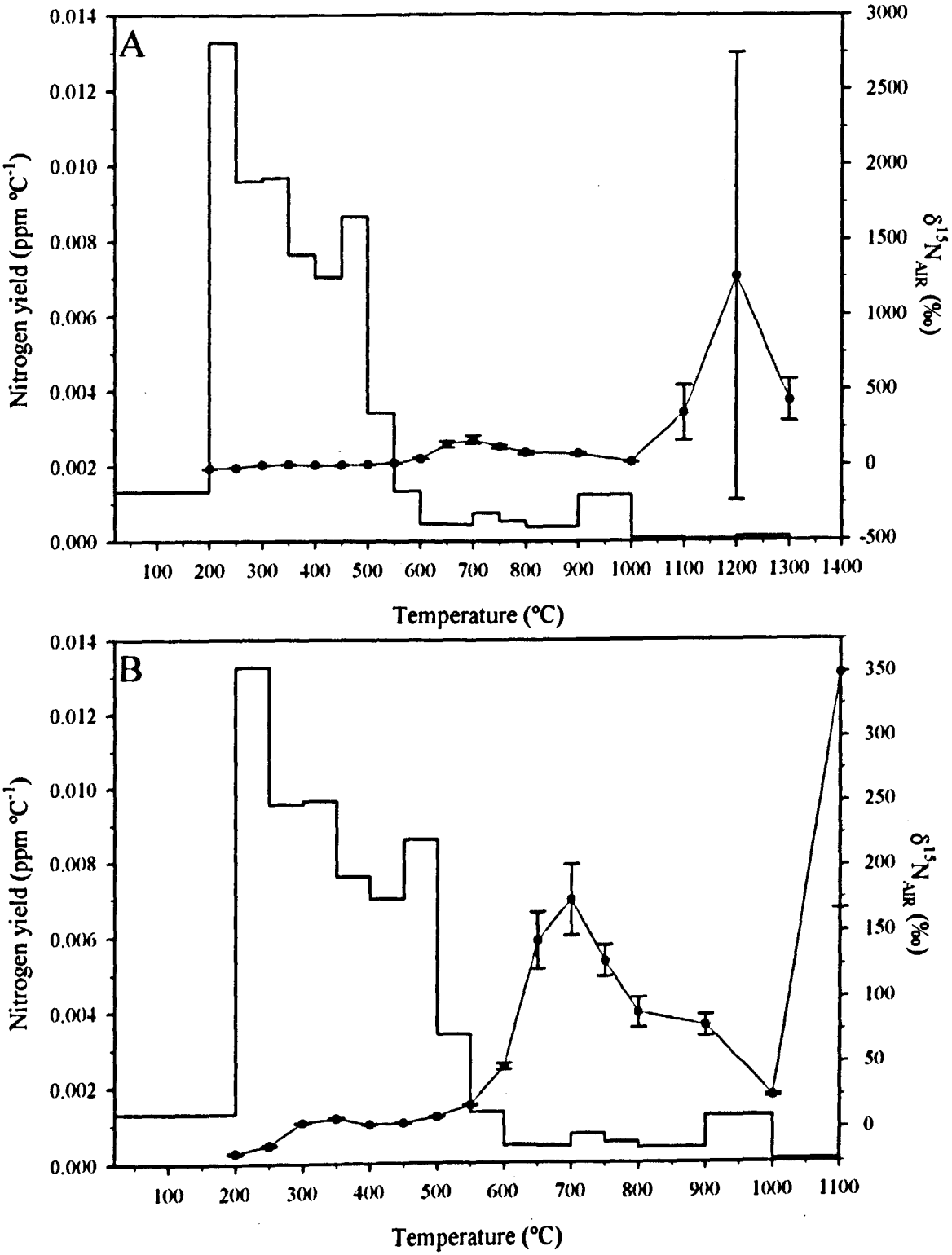

Figure 3-20. Nitrogen release profile from the stepped combustion experiment. Yield of N is given as a histogram and isotopic composition is shown as dots connected by a grey line. Error bars for isotopic compositions are 1σ. The combustion experiment started from room temperature. A) Total range. B) Close-up up to 1100 °C.

Table 3-10. Stepped combustion results for nitrogen. See text for a discussion on the possible hosts of nitrogen.

Temp. step °C	N abundance (ppm)	N yield (ppm °C^{-1})	^{15}N ‰	^{15}N 1σ	Possible hosts
200	0.262	0.0013	−16.75	0.46	TC*, organics, nitrate
250	0.664	0.0133	−11.41	0.34	TC, organics, nitrate
300	0.478	0.0096	+5.35	0.47	TC, organics, nitrate
350	0.483	0.0097	+8.55	0.39	TC, organics, nitrate
400	0.380	0.0076	+3.75	0.34	TC, organics, nitrate, carbonate
450	0.350	0.0070	+4.74	0.35	TC, organics, nitrate, carbonate, AC†
500	0.431	0.0086	+9.61	0.39	Carbonate, AC
550	0.171	0.0034	+17.98	0.59	Carbonate
600	0.066	0.0013	+46.98	2.53	Carbonate
650	0.022	0.0004	+143.26	21.43	Carbonate
700	0.022	0.0004	+174.21	27.20	Graphite
750	0.037	0.0007	+127.78	11.82	Graphite, maskelynite
800	0.026	0.0005	+88.07	11.54	Graphite, maskelynite
900	0.037	0.0004	+78.24	7.85	Graphite, maskelynite
1000	0.121	0.0012	+24.47	0.93	Magmatic silicates (Opx)
1100	0.007	0.0001	+348.90	182.32	Spallogenic (Opx)
1200	0.003	2.56×10^{-5}	+1256.57	1492.38	Spallogenic (Opx)
1300	0.010	0.0001	+430.57	138.53	Spallogenic (Opx)
1400	0	0	-	-	bdl‡

*Terrestrial contamination
†Amorphous carbon
‡Below detection limit

3.1.3.3 Argon

Argon analyses were affected by the low amounts of (blank corrected) ^{36}Ar released between temperature steps, leading to isotopic ratios with large errors, in steps where the ratios could be calculated. Total abundances of each isotope of ^{36}Ar, ^{38}Ar and ^{40}Ar released along the stepped combustion run of the sample are shown in Figure 3-21, and a three-isotope plot, comparing ^{38}Ar/^{36}Ar and ^{40}Ar/^{36}Ar ratios to values obtained in other studies is shown in Figure 3-22.

In general, the amount of Ar released is low until ~ 400 °C, where it rises sharply, peaking at 550 – 750 °C (Figure 3-21). This temperature range coincides with the highest release of C from ALH 84001 (see Section 3.1.3.1). Ratios in this range could only be calculated for 600 and 700 °C steps, with large errors (Figure 3-22). Nevertheless, the blank corrected,

instrumental mass fractionation corrected, and terrestrial ratio corrected value at 600 °C is a plausible one, within the range of analyses by previous workers. Specifically, the ratios at 600 °C ($^{40}Ar/^{36}Ar \approx 7526$, $^{38}Ar/^{36}Ar \approx 0.61$) are not dissimilar to those at 700 °C ($^{40}Ar/^{36}Ar \approx 8848$, $^{38}Ar/^{36}Ar \approx 0.57$) from Mathew and Marti (2001), 800 °C ($^{40}Ar/^{36}Ar \approx 8801$, $^{38}Ar/^{36}Ar \approx 0.48$) from Swindle (1995), and at 1000 °C ($^{40}Ar/^{36}Ar \approx 6330$, $^{38}Ar/^{36}Ar \approx 0.58$) from Murty and Mohapatra (1997). The isotopic ratios at 700 and 800 °C are unusual, in that both $^{38}Ar/^{36}Ar$ and $^{40}Ar/^{36}Ar$ ratios are fairly high, and in a range where no other values for ALH 84001 have been reported (Figure 3-22).

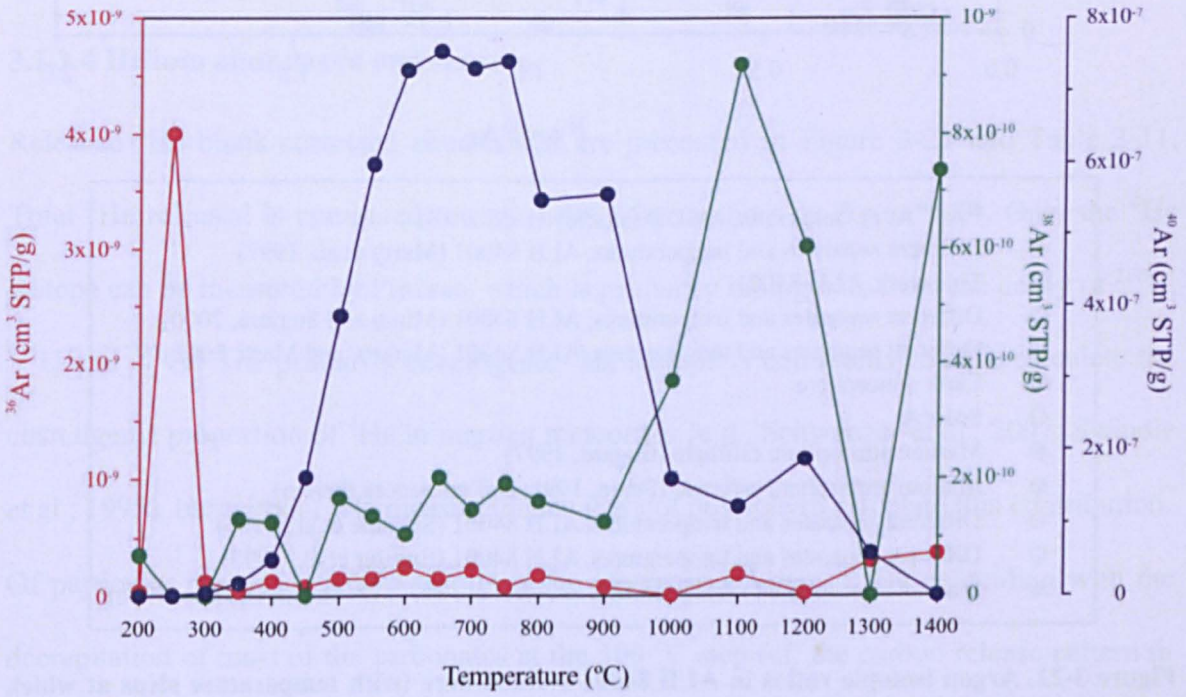

Figure 3-21. Argon released in the stepped combustion experiment of ALH 84001. Points at 0 cm³/g in the graph are simply below the detection limit of the argon (and nitrogen) mass spectrometer of Finesse.

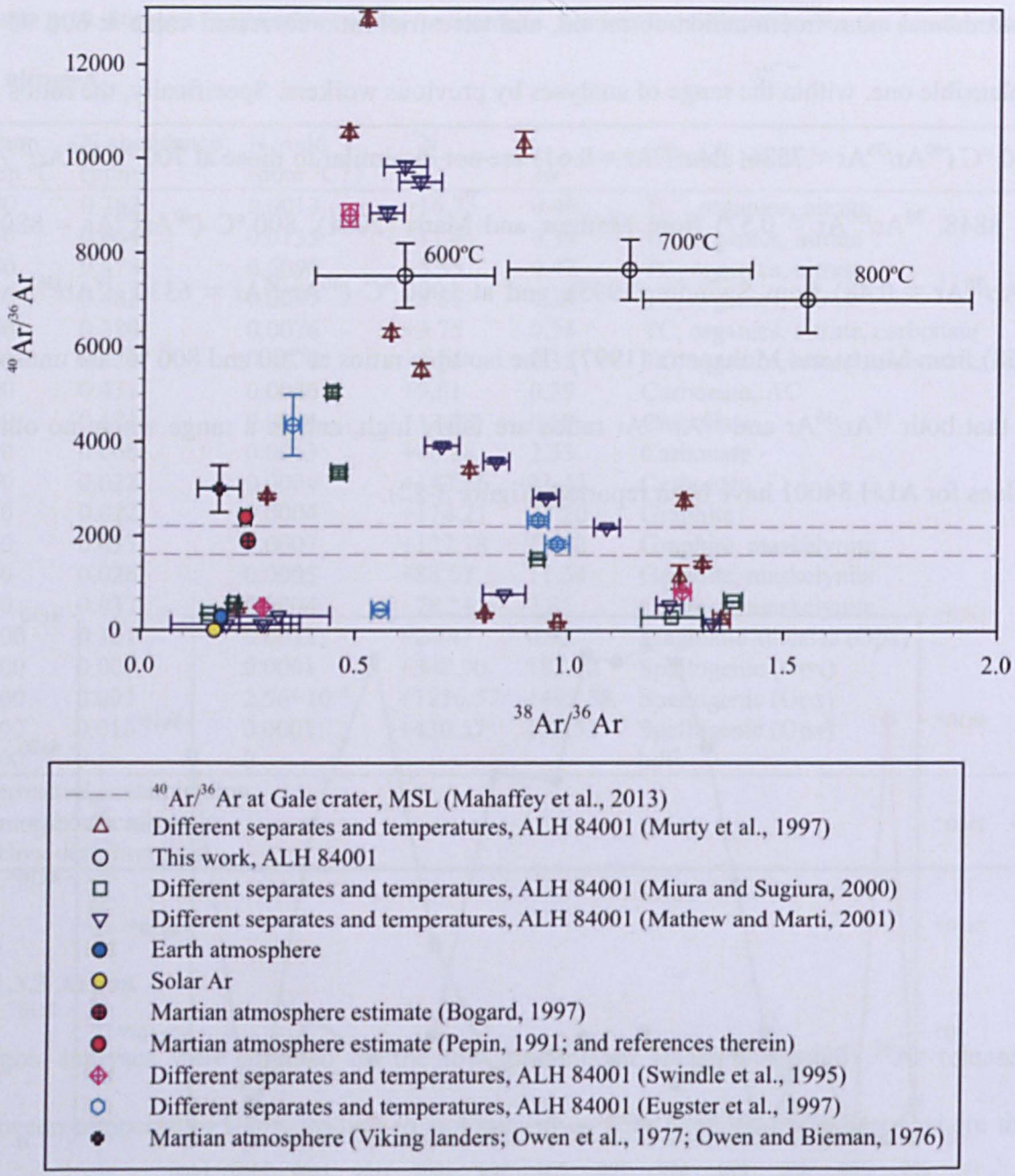

Figure 3-22. Argon isotopic ratios in ALH 84001 studied here (with temperature steps at which they were sampled), and studies of ALH 84001 by other workers (Eugster et al., 1997; Mathew and Marti, 2001; Miura and Sugiura, 2000; Murty and Mohapatra, 1997; Swindle et al., 1995). For comparison, solar, terrestrial, and the modern martian atmospheric ratios are plotted, using data from MSL (Mahaffy et al., 2013), the Viking landers (Owen et al., 1977; Owen and Biemann, 1976), and estimates from meteorites (Bogard, 1997; Pepin, 1991). Error bars in the data points obtained as part of this study are relatively large because of low Ar yields, among other reasons (see text for details).

With the Ar data collected from the sample, it is difficult to argue that a trapped early martian atmospheric component is present, since the isotopic signatures vary greatly from the present martian atmospheric value, and from the early atmospheric values sampled by other authors in ALH 84001 (Figure 3-22). Other authors have sampled this early martian atmospheric component in the maskelynite, where it is thought to have been shock-implanted (e.g., Swindle, 2002; Turner et al., 1997). Here instead, the Ar systematics argue for a source from a different reservoir, most likely magmatic, with a cosmogenic contribution.

3.1.3.4 Helium abundance and sources

Released ^{4}He blank-corrected abundances are presented in Figure 3-23 and Table 3-11. Total ^{4}He released is compared to data from other authors in Figure 3-24. Only the ^{4}He isotope can be measured by Finesse, which is primarily radiogenic, from the decay of ^{238}U, ^{235}U and ^{232}Th. The primarily cosmogenic ^{3}He isotope is commonly used to calculate the cosmogenic proportion of ^{4}He in martian meteorites (e.g., Schwenzer et al., 2007; Swindle et al., 1995), but without ^{3}He measurements, it is not possible to calculate this contribution. Of particular interest from the results is the increased release of ^{4}He coinciding with the decrepitation of most of the carbonates at the 500 °C step (cf. the carbon release pattern in Figure 3-19). Possible sources and sinks for the He in ALH 84001 are discussed in further detail in Section 3.1.4.

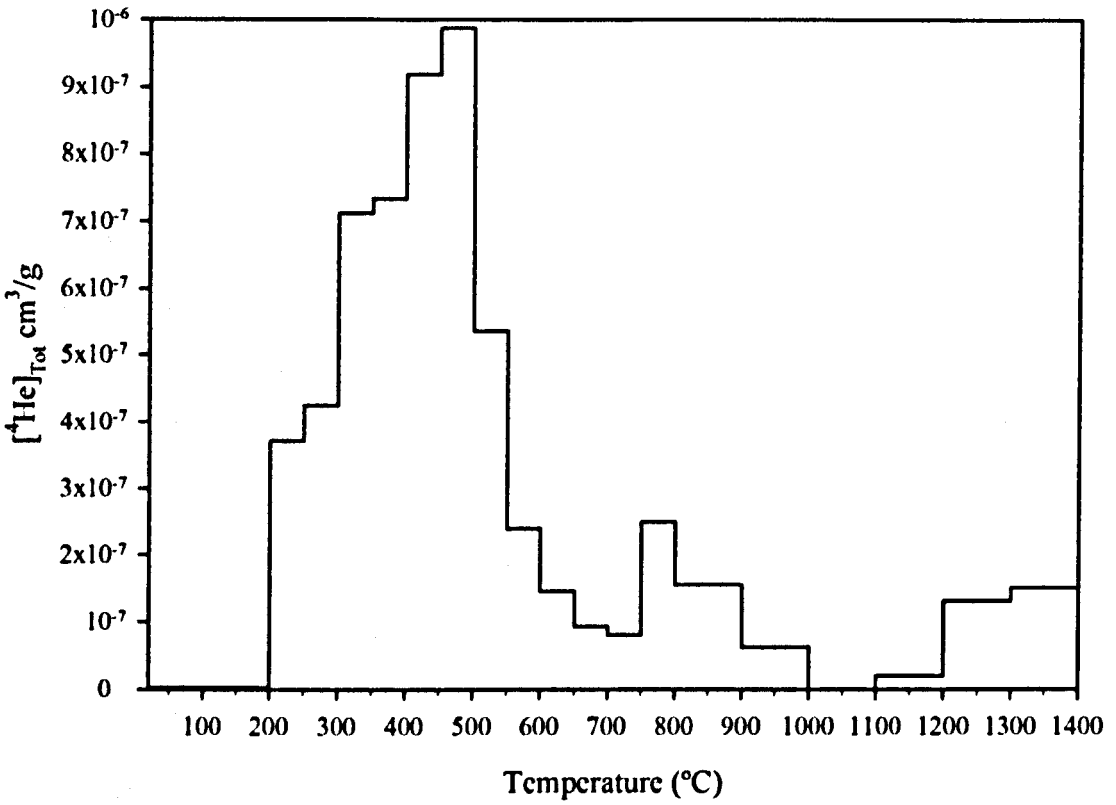

Figure 3-23. Total ^{4}He release pattern from the sample in the stepped combustion experiment.

Table 3-11. Total ^{4}He abundance released from the ALH 84001 sample step combusted in this study.

Step (°C)	$[^4He]_{Tot}$ (cm^3/g)
200	2.18×10^{-9}
250	3.72×10^{-7}
300	4.25×10^{-7}
350	7.13×10^{-7}
400	7.34×10^{-7}
450	9.19×10^{-7}
500	9.88×10^{-7}
550	5.36×10^{-7}
600	2.39×10^{-7}
650	600×10^{-7}
700	9.34×10^{-8}
750	8.02×10^{-8}
800	2.51×10^{-7}
900	1.56×10^{-7}
1000	6.27×10^{-8}
1100	bbl*
1200	1.96×10^{-8}
1300	1.32×10^{-7}
1400	1.51×10^{-7}
Total	6.02×10^{-6}

*Below blank level

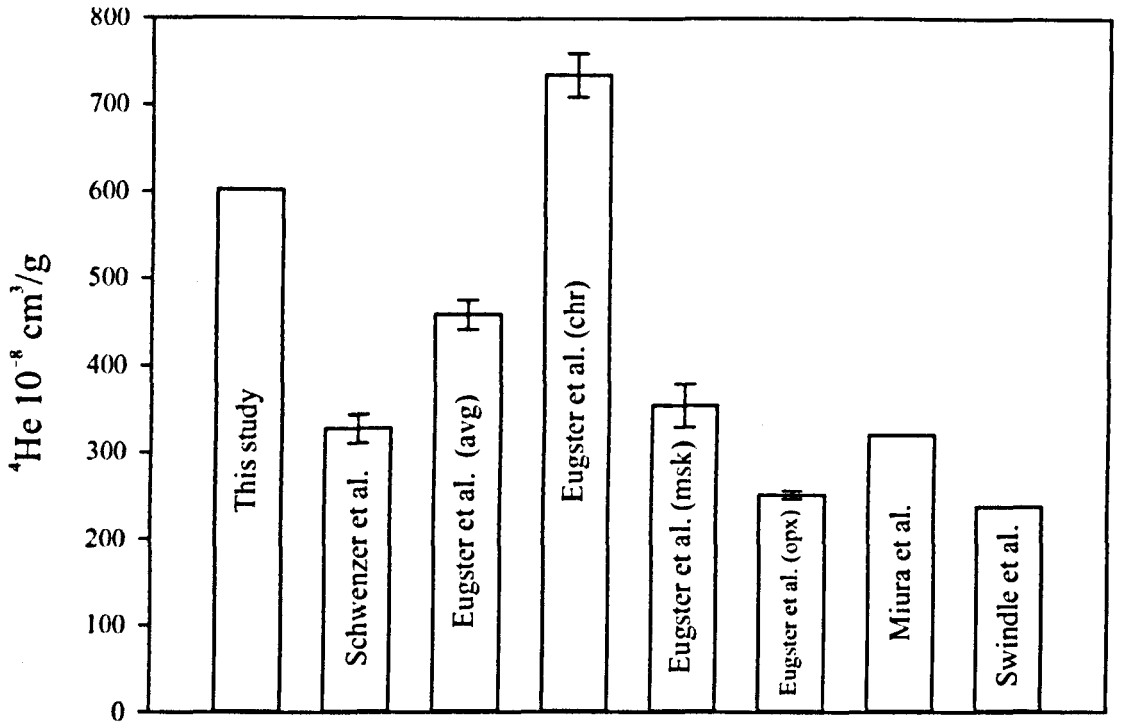

Figure 3-24. Comparison of total ^{4}He released from ALH 84001 from several studies. References are as follows: Eugster et al. (1997), Miura et al. (1995), Schwenzer et al. (2008), and Swindle et al. (1995). Eugster et al. (1997) report values for a weighted average of two samples(avg), and values for separated chromite (chr), maskelynite (msk) and orthopyroxene (opx).

3.1.3.5 Neon abundances, isotopic ratios and sources

Blank and background corrected neon isotope abundances are presented in Table 3-12, together with the isotope ratios corrected for the blank, atmospheric reference, background and instrumental mass fractionation. Assuming a cosmogenic ^{21}Ne/^{22}Ne ratio of 0.9 and a trapped (terrestrial atmospheric) ratio of 0.03 (see Chapter 2 for Ne isotope corrections), 99.3 % of total the ^{21}Ne measured was found to be cosmogenic (cf. > 99.9 % from Eugster et al., 1997).

The neon isotope measurements made in this experiment revealed ratios that have not been reported in ALH 84001 previously. Figure 3-25 depicts the relationship between ^{21}Ne/^{22}Ne and ^{20}Ne/^{22}Ne isotope ratios in the sample in context with results from other authors.

Cosmogenic Ne isotope ratios fall near or within the solid grey field in the figure, but at least two non-cosmogenic values are clearly observed. The extractions at 1300 °C and 1400 °C, particularly, are far removed from cosmogenic values. The 1400 °C extraction is above the highest $^{20}Ne/^{22}Ne$ ratio (~ 11; see Swindle (2002) and references therein) typically reported for martian atmospheric values and appears to approach solar Ne values. The 1300 °C extraction is below the lowest martian atmospheric $^{20}Ne/^{22}Ne$ ratio (~7; Swindle (2002) and references therein) but tends to both terrestrial and martian atmospheric values, and could represent a mixture of cosmogenic and atmospheric components. If a trend line is calculated for the six valid Ne isotope data points of this study, solar, terrestrial atmospheric and martian atmospheric values all fall within the 95 % confidence interval of the line (Figure 3-25).

Assessing whether the cosmogenic $^{21}Ne/^{22}Ne$ values are affected by a contribution of solar cosmic-ray Ne as opposed to solely galactic cosmic-ray Ne is possible because cosmogenic $^{21}Ne/^{22}Ne$ values are sensitive to elemental abundances in the meteorite, especially Mg, Si and Al (Eugster et al., 1997; Garrison et al., 1995). Figure 3-26 shows the relationship between Mg, Si and Al abundance, and cosmogenically produced $^{21}Ne/^{22}Ne$ in a number of martian meteorites, compared to the data from this study. Apparently, there is a non-galactic cosmic-ray Ne component in the ALH 84001 sample analysed here. This could either be a) Solar cosmic-ray Ne, especially if the sample is from near the exterior of the meteorite, or b) a non-cosmogenic component, with a near-solar Ne isotopic signature, such as can be found in mantle plume minerals on Earth, which presumably originates from the dissolution of solar nebula Ne into the magmas of the growing proto-Earth (Marty, 2012). Given the ancient age of ALH 84001, a solar Ne signature is not out of the question.

Table 3-12. Step combustion results of neon in ALH 84001 from this study.

Step	Abundances (cm^3/g)				$^{21}Ne/^{22}Ne$		$^{20}Ne/^{22}Ne$	
	$[^{20}Ne]_{Tot}$*	$[^{21}Ne]_{Tot}$	$[^{21}Ne]_{Cosm}$†	$[^{22}Ne]_{Tot}$	Ratio	1σ	Ratio	1 σ
200	bbl‡	1.06×10^{-14}	4.48×10^{-11}	bbl	–§		–	
250	3.81×10^{-10}	1.66×10^{-14}	bbl	3.89×10^{-10}	–		–	
300	6.68×10^{-9}	1.65×10^{-10}	1.48×10^{-10}	2.01×10^{-10}	–		–	
350	8.73×10^{-9}	1.53×10^{-10}	9.77×10^{-11}	5.92×10^{-10}	–		–	
400	3.93×10^{-9}	2.34×10^{-10}	1.79×10^{-10}	bbl	–		–	
450	bbl	4.61×10^{-10}	3.66×10^{-10}	9.42×10^{-10}	–		–	
500	4.86×10^{-9}	9.47×10^{-10}	8.64×10^{-10}	6.25×10^{-10}	–		–	
550	4.57×10^{-9}	1.10×10^{-9}	1.01×10^{-9}	8.48×10^{-10}	–		–	
600	5.83×10^{-9}	2.03×10^{-9}	1.91×10^{-9}	2.43×10^{-9}	–		–	
650	5.72×10^{-9}	4.40×10^{-9}	4.28×10^{-9}	4.86×10^{-9}	–		–	
700	8.30×10^{-9}	5.61×10^{-9}	5.50×10^{-9}	6.24×10^{-9}	–		–	
750	2.65×10^{-10}	3.97×10^{-9}	3.89×10^{-9}	3.62×10^{-9}	–		–	
800	1.01×10^{-8}	5.41×10^{-9}	5.32×10^{-9}	5.67×10^{-9}	0.71	0.04	0.72	0.13
900	1.85×10^{-8}	1.46×10^{-8}	1.44×10^{-8}	1.72×10^{-8}	0.77	0.03	0.88	0.05
1000	1.20×10^{-8}	1.08×10^{-8}	1.08×10^{-8}	1.18×10^{-8}	0.79	0.03	0.94	0.08
1100	2.61×10^{-9}	4.74×10^{-9}	4.77×10^{-9}	4.98×10^{-9}	0.67	0.04	1.01	0.13
1200	bbl	2.92×10^{-9}	3.04×10^{-9}	2.77×10^{-9}	0.60	0.04	1.74	0.20
1300	3.18×10^{-10}	1.26×10^{-9}	1.46×10^{-9}	1.29×10^{-9}	0.42	0.04	4.74	0.37
1400	bbl	5.19×10^{-13}	2.90×10^{-10}	bbl	0.16	0.03	11.39	0.76
Total	9.27×10^{-8}	5.87×10^{-8}	5.84×10^{-8}	6.45×10^{-8}				

*Blank-corrected total value, including cosmogenic
†Cosmogenic only
‡Below blank level
§Not determined

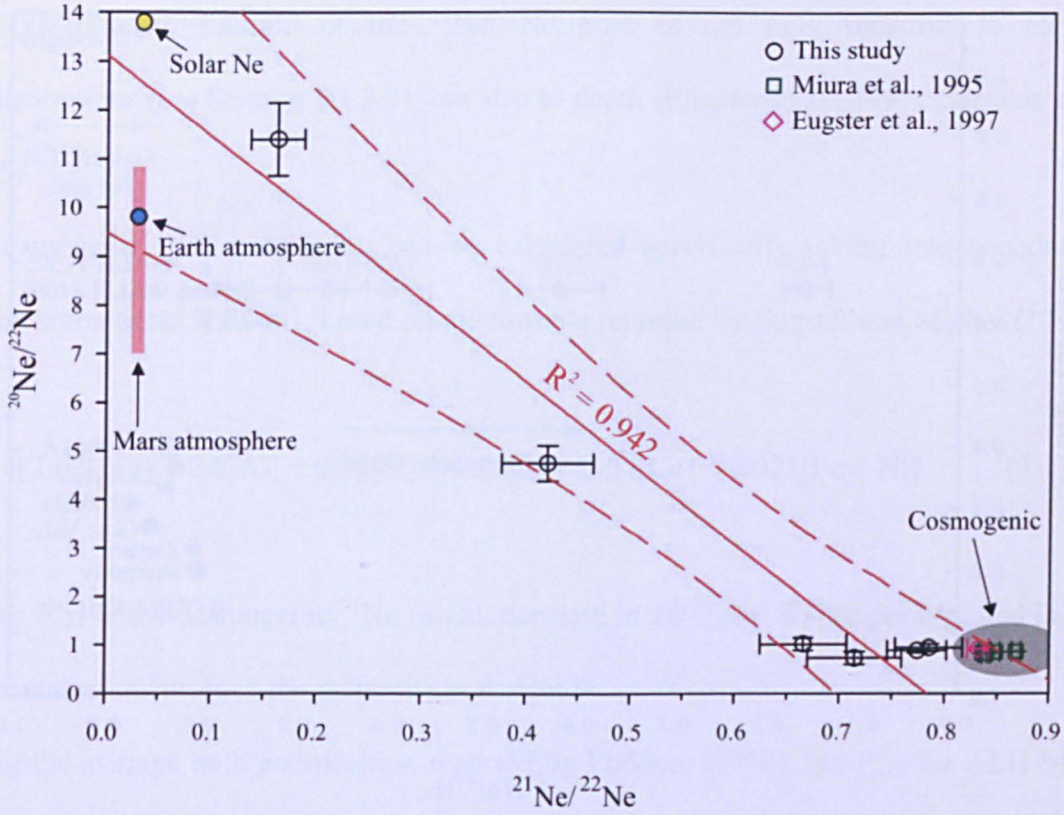

Figure 3-25. Neon isotope ratio results from this study, compared to step combustion results from Miura et al. (1995) and a weighted average result for bulk samples of ALH 84001 from Eugster et al. (1997). The Ne isotope values by these authors are representative of all other work on the Ne in ALH 84001 (e.g., see data compiled by Schultz and Franke, 2004). Bi-directional error bars are 1σ for this work and Miura et al. (1995), and 2σ for Eugster et al. (1997). A red trend line is plotted using all data points in this study. A goodness of fit value is given as a R^2 value calculated from the regression line, and a 95 % confidence interval is represented as dashed line curves surrounding the trend line. The pink field indicates the estimated $^{20}Ne/^{22}Ne$ ratio of the martian atmosphere, from Swindle et al. (2002), Pepin (1991) and references therein. Martian atmospheric $^{21}Ne/^{22}Ne$ is not well constrained, but is typically reported as 0.03 from trapped Ne in shergottites (e.g., Mohapatra et al., 2003; Ott and Lohr, 1992). The Solar and terrestrial atmosphere Ne isotope values are as reported by Lupton et al. (2012).

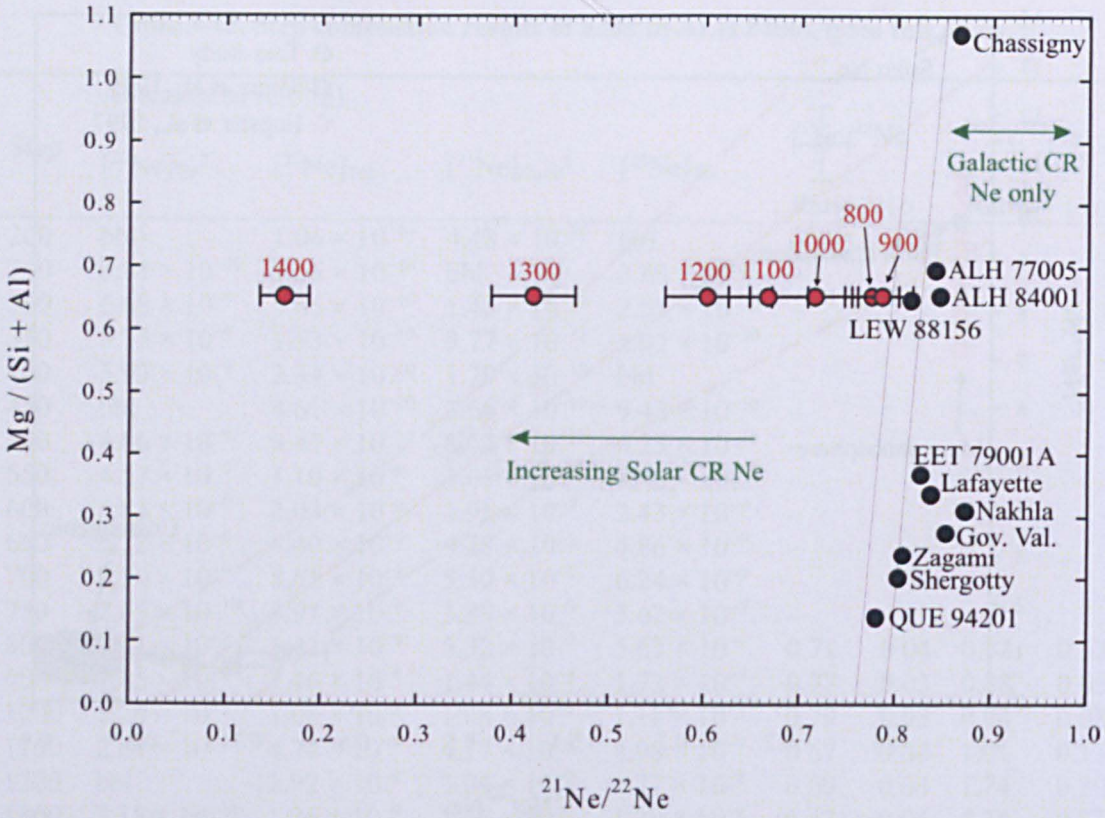

Figure 3-26. Cosmogenic $^{21}Ne/^{22}Ne$ ratios versus bulk Mg/(Si + Al) elemental concentration ratios in several martian meteorites, after Eugster et al. (1997) and Garrison et al. (1995). Red dots are from the stepped combustion results presented in this study, and red numbers above them are temperature steps where they were sampled. Black dots are martian meteorite values from literature. The cosmogenic $^{21}Ne/^{22}Ne$ data for the meteorites are as reported by Eugster et al. (1997). The bulk compositional data are as reported by Eugster et al. (1997), and by Lodders (1998), where unreported by Eugster et al. (1997). The grey lines represent the boundary between pure galactic cosmic-ray Ne (right) and increased solar cosmic-ray Ne abundance towards the left. Invariably, different mineral components combust at different temperatures, but even if all Ne released at 800 and 900 °C is from the maskelynite (bringing their (Mg/Si+Al) values lower, and closer to galactic $^{21}Ne/^{22}Ne$ values), higher temperatures are still in the Solar CR range.

3.1.3.5.1 Ne cosmic-ray exposure age

A cosmic-ray exposure age can be calculated using the Ne isotope results, which probably coincides with the ejection age of the rock off the surface of Mars (Eugster et al., 1997).

The cosmogenic fraction of the $^{22}Ne/^{21}Ne$ ratio is not only sensitive to element concentrations (see Section 3.1.3.5), but also to depth (Eugster et al., 1997; Garrison et al., 1995).

A cosmogenic ^{21}Ne production can be calculated specifically taking into account the composition of ALH 84001, based on the formula reported by Eugster and Michel (1995):

$$P'_{21} = 1.63[Mg] + 0.6[Al] + 0.32[Si] + 0.22[S] + 0.07[Ca] + 0.021[Fe + Ni] \qquad (3\text{-}1)$$

where P'_{21} is the cosmogenic ^{21}Ne production rate in 10^{-10} cm^3 STP/g per Ma, and [x] are elemental abundances in the meteorite in weight %.

Using the average bulk composition reported by Lodders (1998), the P'_{21} for ALH 84001 calculated here is 3.33×10^{-7} cm^3 STP/g per Ma, and the cosmic ray exposure age is calculated to be 17.52 Ma for the sample studied here, using the data in Table 3-12.

Without considering the effects of shielding from cosmic rays as a function of depth, and a possible interference on the ^{21}Ne abundances from solar cosmic rays, primordial solar ^{21}Ne, and/or martian atmospheric ^{21}Ne, the calculated age is similar to ^{21}Ne cosmic ray exposure ages calculated by other authors (Table 3-13).

Table 3-13. Comparison of cosmogenic ^{21}Ne exposure ages in literature.

Reference	Exposure age (Ma)
This work	17.52
Eugster (1994)	17.0
Miura et al. (1995)	15.4
Swindle et al. (1995)	17.7
Eugster et al. (1997), bulk	13.3
Eugster et al. (1997), opx	15.4
Garrison and Bogard (1998)	14.1

3.1.4 Alteration in ALH 84001: Discussion based on analytical results

Aside from the obvious carbonates, mineralogical evidence of alteration in ALH 84001 appears scarce, and certainly, identifying whether the alteration process was of a high or low temperature is not possible. There was no evidence for phyllosilicates in the sample studied. However, less obvious compositional and mineralogical evidence points to aqueous alteration having taken place:

- Electon microprobe analyses showed that some orthopyroxene contains excess silica (about 0.02 atoms per formula unit in Si excess; Section 3.1.1.1.). Two reasons related to alteration could explain this. Possibly, SiO_2 was precipitated along surfaces of the orthopyroxene from a fluid. However, no excess is seen in the maskelynite analyses. More likely, the Si excess is not, in fact, an excess of silica, but a depletion of Mg, Fe and Ca from the orthopyroxene, leaving a relative excess of Si in the orthopyroxene. This would plausibly occur if fluids leached Mg, Fe, and Ca from the orthopyroxenes.
- Raman analyses showed possible detections of hematite (Section 3.1.2), which could hint at precipitation from a fluid, or from the alteration of other phases, possibly magnetite. (An in depth discussion on the possible origin of hematite and magnetite is found in Chapter 4, taking into account geochemical considerations.)

- Raman analyses also showed a possible sulfide mineral, which did not coincide so much with the pyrite spectrum as with other sulfide spectra (Section 3.1.2). A diverse sulfide assemblage may be the result of different origins, as some could be magmatic and other of subsequent hydrothermal or low temperature aqueous alteration.

The gases released from the ALH 84001 aliquot studied aided greatly in verifying and interpreting the nature of the alteration. Principally, the C released when the carbonates decrepitated is almost certainly from the martian atmosphere (see Section 3.1.3.1) However, carbon released above 700 °C also provides some insight into alteration and magmatic sources, in light of the mineralogical studies carried out here. The possible hosts of this high $\delta^{13}C$ released above 700 °C are:

a) Coating on the surfaces, cracks and pores of primary magmatic silicates (mainly orthpyroxene). However, weakly bonded carbon on the surfaces of primary minerals would have been sampled at lower temperature steps, and the unaltered aspect of the primary minerals precludes carbon being released from the surfaces of primary magmatic minerals.

b) Graphite. Graphite tends to combust at 700 – 800 °C (Grady et al., 2002), so any carbon from graphite would have been sampled between these steps. With evidence for graphite in ALH 84001 (Steele et al., 2012a), secondary graphite, formed by high P-T conditions upon impact events and ejection could be a likely candidate for an atmospheric carbon host. The 750 – 800 °C step is, however, intriguing because it sampled the lowest abundance and yield of carbon in the whole experiment (0.1 % of the whole abundance), and the negative $\delta^{13}C$ (−1.78 ± 1.59 ‰) is unlike the positive isotopic signature sampled in the temperature steps immediately prior

to and after it (Table 3-8 and Figure 3-19). The main source of the carbon in this step is unlikely to be the martian atmosphere (as a positive $\delta^{13}C$ would be expected, as in the carbonates) and could be primary magmatic minerals which "soften" (begin to melt) in this step (e.g., SiO_2 and orthopyroxene), or trace amounts of primary magmatic graphite. Since identified with Raman spectroscopy (Section 3.1.2), a contribution from graphite appears likely.

c) Gas trapped in glass. Possible martian atmospheric carbon shock-implanted into glass (mainly the maskelynite and SiO_2) was further expanded on taking account the nitrogen release, in Section 3.1.3.2.

d) Phases that combust at higher temperatures than carbonates. Apatite ($Ca_{10}(PO_4)_6(OH, F, Cl)_2$ is known to incorporate CO_3^{2-} into its structure in exchange for the OH^-, F^- and Cl^- anions (e.g., Elliott, 1994; Haas and Banewiez, 1980; Yi et al., 2013), and releases the majority of its volatiles in stepped combustion at 800 – 900 °C (Nadeau et al., 1999; Peck and Tumpane, 2007). The phosphates in ALH 84001 are texturally magmatic, however, post-crystallisation aqueous alteration may have permitted the ionic exchange with dissolved atmospheric bicarbonate. The heavy $\delta^{13}C$ (+11.33 ± 0.24 ‰) at the 800 – 900 °C step strongly suggests that a component not indigenous to the martian mantle is present.

Helium is generally incompatible with alteration phases: atmospheric He does not adsorb in any meaningful quantity into alteration minerals. Helium is lost with relative ease from the martian atmosphere to ionisation and solar wind (e.g., Krasnopolsky and Gladstone, 1996), and current He in the lower atmosphere of Mars amounts to only 10 ± 6 ppm, with virtually no recharge mechanism other than solar wind α particles (Krasnopolsky and

Gladstone, 1996, 2005). However, atmospheric He would have probably been more abundant when the carbonates formed, ~ 3.9 Ga ago, and He released from the martian interior by the higher impact and volcanic rates may have contributed to atmospheric recharge, and possible incorporation into the secondary phases. On the other hand, the numerous impacts ALH 84001 experienced, coupled with the fact that He is 'leaky' (i.e., it diffuses readily, although diffusion rates are very dependent on P–T and mineral species; Baxter, 2010), would have significantly depleted the original ^{4}He (Nyquist et al., 2001; Schwenzer et al., 2008). It is unlikely the ^{4}He measured here in the sample is atmospheric, and yet, the highest ^{4}He release occurred at the height of carbonate decreptitation. Spatially resolved analyses of the He in the carbonates would be greatly beneficial.

Neon behaves in a similar way to He, in that not much is adsorbed into secondary minerals from the atmosphere. Over 99 % of the ^{21}Ne sampled from ALH 84001 was cosmogenic, further expounding the fact that the ^{4}He is unlikely to be atmospheric.

To summarise, the best evidence found here for aqueous alteration near the surface of early Mars in ALH 84001 is (apart from the conspicuous carbonates) the carbon and nitrogen abundances and isotopic signatures, which are almost certainly of the ancient martian atmosphere. The other findings of the analytical studies in this chapter (e.g., graphite, possible hematite, noble gas observations...) help to contextualise the source of the meteorite, the alteration process on Mars, and the transit of the meteorite. These data are used in the rest of this thesis to address the context of the alteration in ALH 84001.

3.2 Shergottite NWA 6234

3.2.1 Petrography, major and minor phases

The petrography and petrology of the ~1.5 mm^2 NWA 6234 sample studied here for the consortium (Figure 1-4) were in agreement with the previous consortium studies, reported in Filiberto et al. (2012) and Gross et al. (2013). Here, I re-examined the compositions of all major phases (olivine, clinopyroxene and maskelynite), which were all within range of representative compositions reported in the aforementioned studies (Table 3-14).

Table 3-14. Composition of the major phases in NWA 6234 analysed here and comparison with representative analyses reported in our previous work (Gross et al., 2013). FeO analyses from Gross et al. (2013) include Fe_2O_3.

	Olivine				Pyroxene				Maskelynite	
	Average (n = 20)	1σ SD	Large Ol core (Gross et al., 2013)	Matrix Ol (Gross et al., 2013)	Average (n = 22)	1σ SD	Pyx core (Gross et al., 2013)	High Ca Pyx (Gross et al., 2013)	Average (n = 25)	1 σ SD
SiO_2	34.92	0.79	39.17	34.10	50.54	1.45	53.16	49.95	54.11	1.12
TiO_2	0.02	0.02	bdl*	0.04	0.34	0.15	0.25	1.09	0.08	0.03
Al_2O_3	0.09	0.11	0.12	bdl	2.96	2.83	1.95	1.81	27.66	0.96
Cr_2O_3	0.13	0.30	0.03	0.01	0.32	0.14	0.27	0.13	0.01	0.02
Fe_2O_3	0.41	0.36	nd†	nd	0.64	0.63	nd	nd	1.33	1.03
FeO	36.60	4.88	20.36	45.53	18.56	2.45	18.39	15.79	0.26	1.58
MnO	0.66	0.11	0.43	0.88	0.59	0.09	0.54	0.58	0.03	0.04
MgO	25.87	3.74	40.06	20.02	16.09	3.05	24.75	12.67	0.32	0.37
CaO	0.21	0.17	0.15	0.13	8.60	3.17	1.20	17.73	10.51	0.52
NiO	na‡	-	0.08	0.04	na	-	0.02	na	na	-
CoO	na	-	bdl	na	na	-	na	na	na	-
ZnO	na	-	0.03	na	na	-	na	na	na	-
P_2O_5	na	-	0.05	0.05	na	-	0.03	0.51	na	-
BaO	0.01	0.01	na	na	0.01	0.01	nd	nd	0.01	0.02
Na_2O	0.01	0.01	na	bdl	0.26	0.28	0.11	0.25	4.76	1.10
K_2O	bdl	nd	na	bdl	0.01	0.02	bdl	0.01	0.34	0.05
F	bdl	nd	na	nd	bdl	0.01	nd	nd	0.03	0.04
Cl	0.01	0.01	na	nd	0.01	0.01	nd	nd	0.01	0.01
Total	98.93	0.70	100.49	100.79	98.92	0.65	100.40	100.52	99.45	0.87
Endmembers§										
Olivine										
Te	0.80	0.15								
Fo	54.75	6.78	77.81	43.94						
Fa	44.12	6.73								
Ca-Ol	0.33	0.25								
Pyroxene										
Wo					18.89		2.40	37.19		
En					47.85		68.89	36.96		
Fs					33.26		28.71	25.85		
Feldspar										
An									55.45	9.82
Ab									42.51	9.62
Or									2.03	0.31

*Below detection limit

†Not determined

‡Not analysed or reported

§Endmember composition abbreviations: tephroite (Te, Mn_2SiO_4), forsterite (Fo, Mg_2SiO_4), fayalite (Fa, Fe_2SiO_4), Ca-olivine (Ca-Ol, Ca_2SiO_4), wollastonite (Wo, $CaSiO_3$), enstatite (En, $MgSiO_3$), ferrosilite (Fs, $FeSiO_3$), anorthite (An, $CaAl_2Si_2O_8$), albite (Ab, $NaAlSi_3O_8$), orthoclase (Or, $KAlSi_3O_8$).

3.2.2 The shock melt vein and the unknown phases within

The melt vein in NWA 6234 was probably generated by the impact that launched the meteorite from Mars, shocking the rock and most likely preferentially melting it along the boundaries of mineral phases (Filiberto et al., 2012; Gross et al., 2013). A typical melt vein composition was reported by Gross et al. (2013), and is shown in Table 3-15, compared to the composition of the bulk rock as reported by Filiberto et al. (2012). The vein itself cuts across the meteorite in a relatively straight line, and is about 10 – 100 μm thick. Textural and compositional analyses of the melt vein yielded striking results in this work, of what appear to be distinct minor phases previously unidentified in the meteorite. These melt vein unknown phases (hereafter MVUP) are amorphous, occur always in contact with olivine, appear to be growing from it, and are always inside the melt vein. Figure 3-27 shows one example of such a phase, and element distribution maps of the same area are shown in Figure 3-28. An EPMA line analysis across the melt vein and a MVUP is shown in Figure 3-29.

A CIPW norm (standard normative mineralogy after Cross, Iddings, Pirsson and Washington) calculation carried out here using the general melt vein composition reported in Gross et al. (2013) and Table 3-15 reveals that the melt vein is composed of approximately 36 % olivine, 29 % enstatite-ferrosilite solid solution ($(Fe,Mg)SiO_3$), ~ 17 % plagioclase, 13 % diopside and smaller amounts of oxides and apatite (see Table 3-16 for precise details).

Table 3-15. Comparison of the bulk rock and melt vein composition in NWA 6234, and composition of the unknown phase in the melt vein.

	Bulk rock composition (Filiberto et al., 2012)		Melt vein composition (Gross et al., 2013)	Melt vein unknown phases (this work)		
	wt. %	± 1 σ		wt. %	± 1 σ	Num. analyses
SiO_2	44.6	0.52	44.54	29.94	4.99	27
TiO_2	0.82	0.04	1.13	0.91	0.49	27
Al_2O_3	5.17	0.13	4.86	4.61	1.66	27
Cr_2O_3	0.64	0.03	1.04	0.65	0.39	27
FeO_T	21.3	0.35	23.77	38.68	4.79	27
MnO	0.56	0.03	0.58	0.50	0.23	27
MgO	17.1	0.38	17.01	7.00	4.08	27
CaO	6.77	0.19	6.15	4.51	1.14	27
Na_2O	1.04	0.04	0.90	0.27	0.08	27
K_2O	0.08	0.01	0.07	0.72	0.08	27
P_2O_5	0.81	0.04	0.82	0.52	0.12	17
F	nd	-	nd	bdl	-	27
Cl	nd	-	nd	0.18	0.20	27
SO_2	nd	-	nd	0.22	0.07	17
Ba (ppm)	184	5	nd	2327	363	27
Ni (ppm)	17.4	2.2	nd	492	164	17
Sr (ppm)	77.2	8.5	nd	2669	368	17
Total	99.0		100.87	88.71		

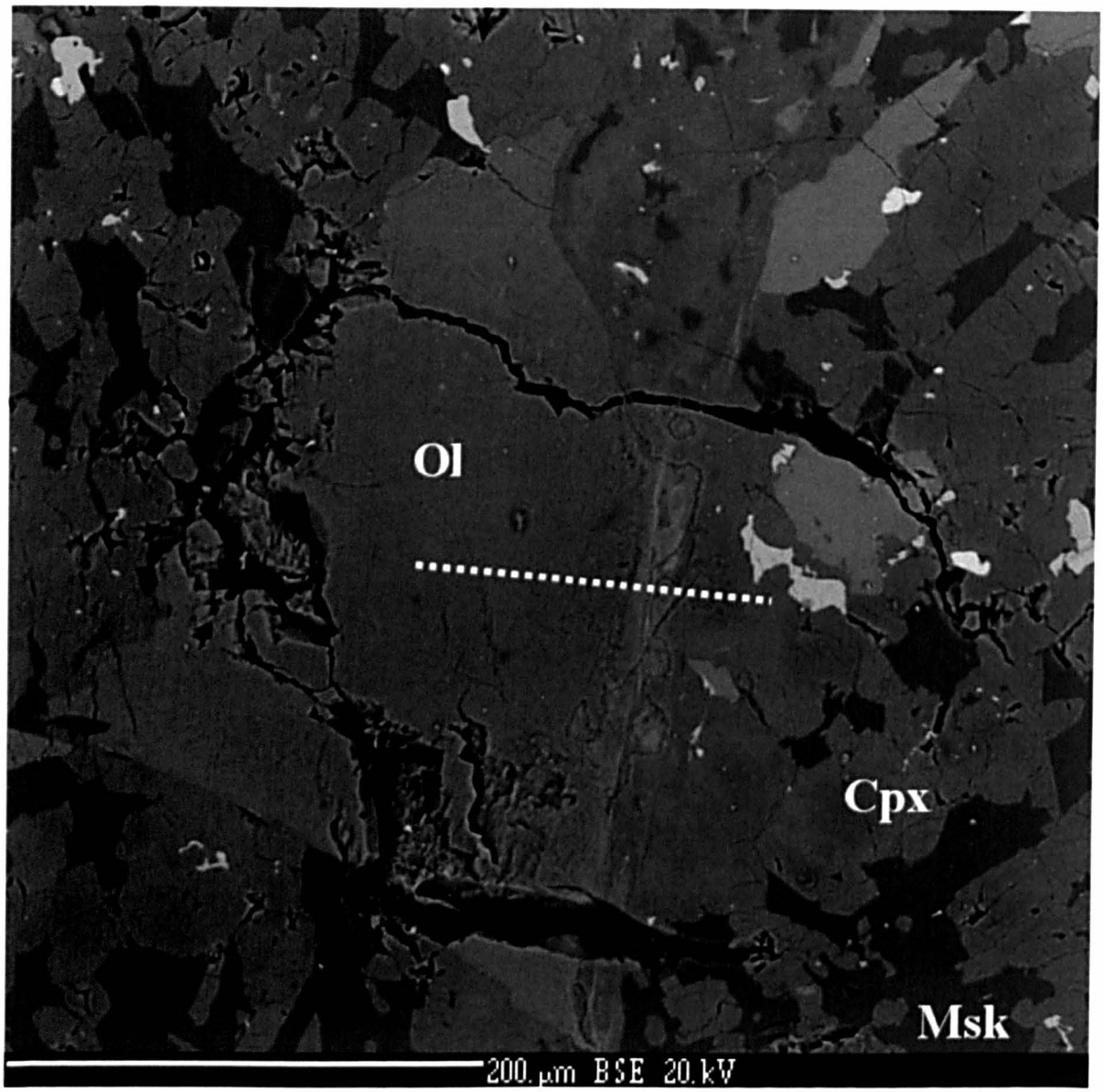

Figure 3-27. BSE image of the newly identified phase in the melt vein of NWA 6234. The dotted line indicates the location of an EPMA compositional analysis across the unknown phase (result in Figure 3-29). The dashed line crosses the melt vein (N-S orientation in the image) between an olivine phenocryst (left of the vein) and a clinopyroxene crystal from the matrix (right of the vein). Ol = olivine, Cpx = clinopyroxene, and Msk = maskelynite. Element maps which include the same area are shown in Figure 3-28.

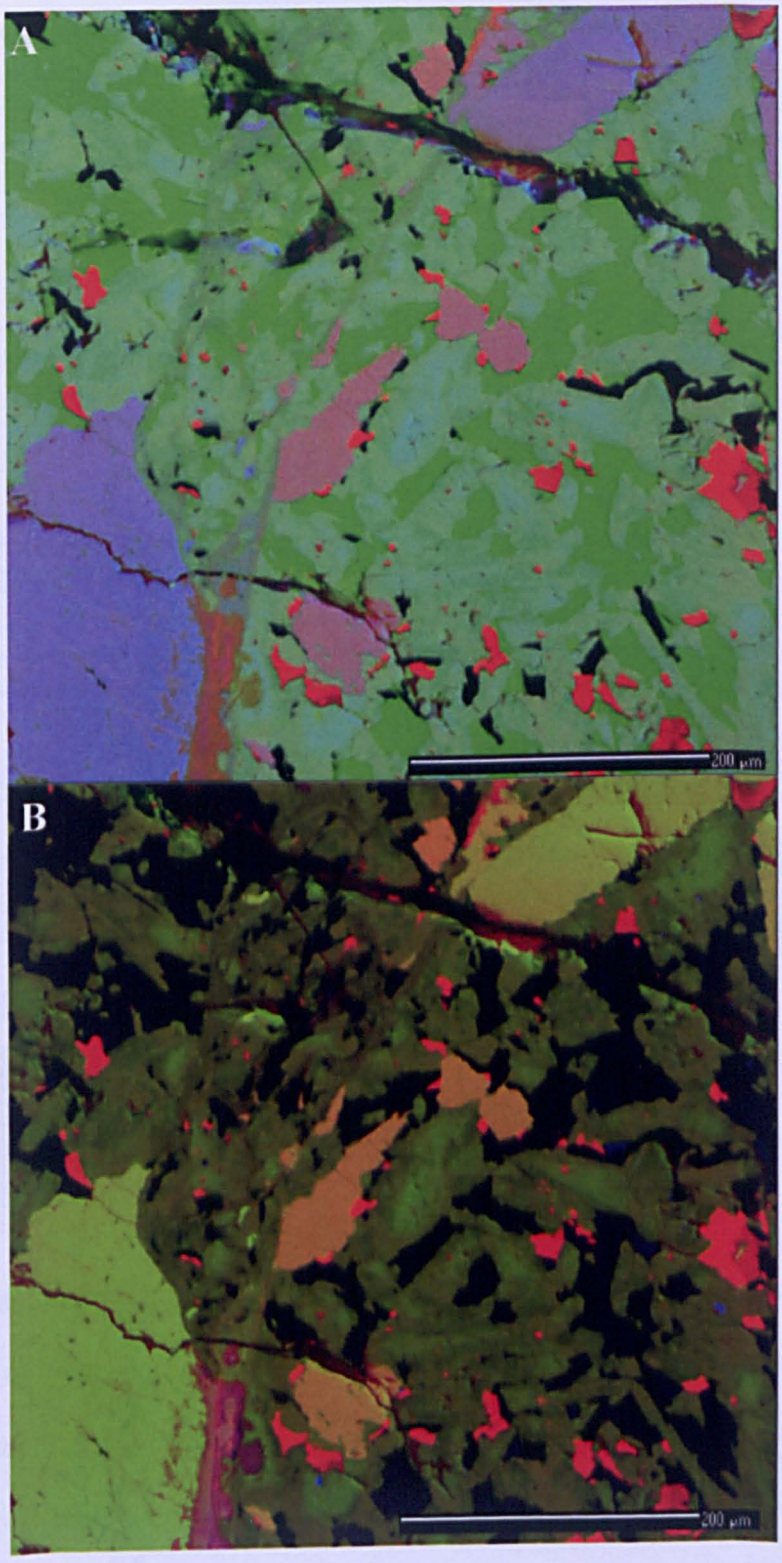

Figure 3-28. False colour composite images of element distribution maps in the melt vein (cf. BSE SEM image in Figure 3-27) of NWA 6234, from EPMA analyses. A) Red = Fe, green =Mg, blue = Si. B) Red = Fe, green = Mg, blue = K. The unknown phases are observable in the melt vein, on the edge of an olivine crystal.

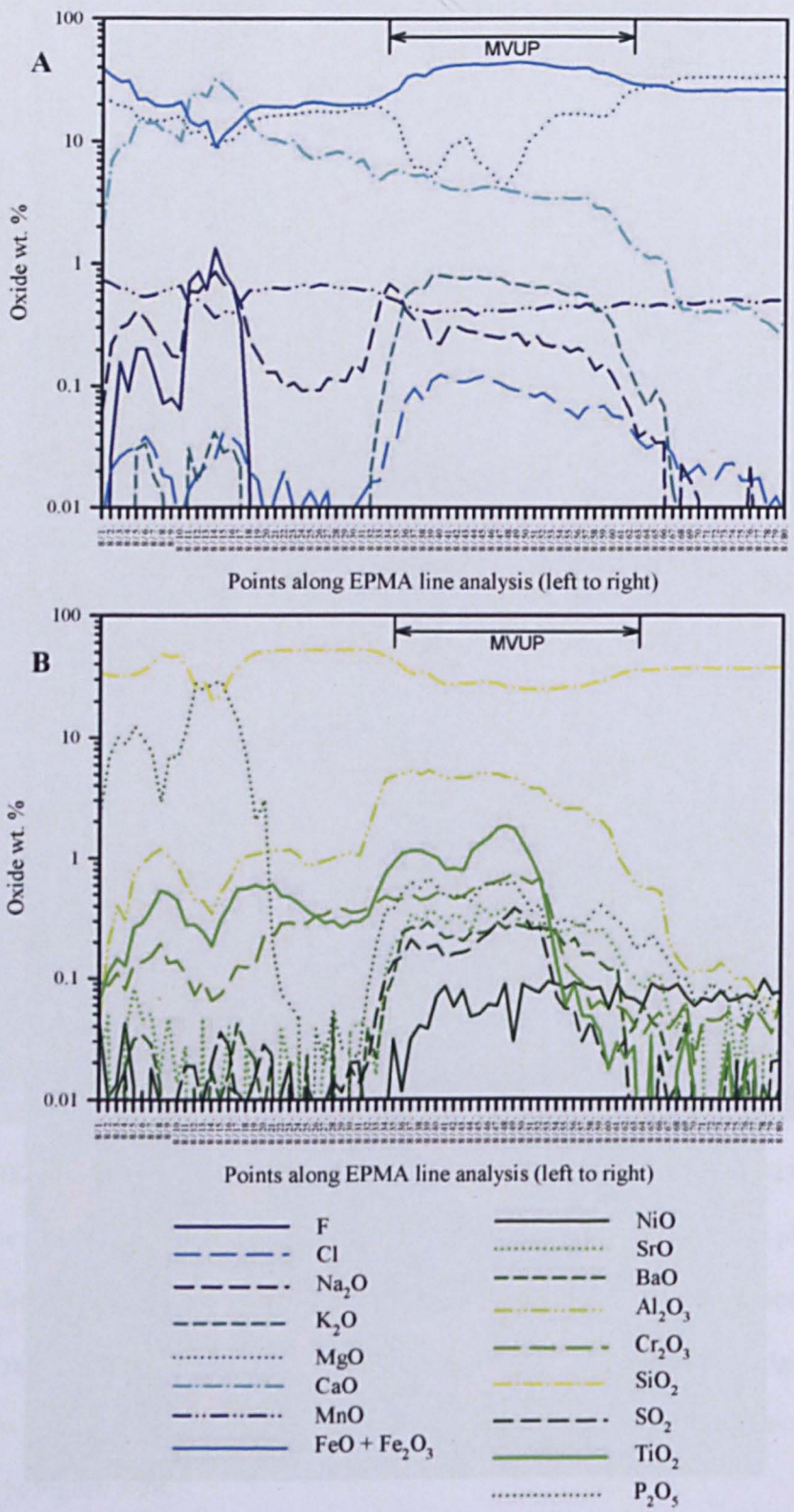

Figure 3-29. EPMA line analysis across the melt vein shown in Figure 3-27 and Figure 3-28. Analyses over the unknown phase in the melt vein (MVUP) are shown under the double-ended arrow. Note the line begins over olivine (left) and ends over clinopyroxene (right). A) and B) show the different elements analysed over the same line.

Table 3-16. Results of the CIPW normative mineralogy calculation, in weight %.

Minerals	Melt vein composition (Gross et al., 2013)	Melt vein unknown phase (not normalised to 100%)	Melt vein unknown phase (normalised)
Plagioclase	16.63	9.98	11.14
Orthoclase	0.41	0	0
Leucite	0	4.08	4.53
Diopside	13.35	5.17	5.78
Enstatite-Ferrosilite	29.14	0	0
Olivine	35.77	63.82	71.21
Lernite	0	1.20	1.32
Ilmenite	2.15	1.73	1.94
Apatite	1.90	1.20	1.34
Chromite	1.53	1.53	1.71
Pyrite	0	0.23	0.25
Halite	0	0.34	0.37
Total	100.88	89.26	99.59

The CIPW calculation, although useful for approximating compositions to ideal minerals, does not take into account the actual mineral variability of the meteorite and compositional variation within minerals. For instance, neither pure diopside nor pure enstatite-ferrosilite are found in the meteorite, but instead, clinopyroxene of compositions intermediate to these endmembers is present. For this reason, linear deconvolution using the mineral compositions in the meteorite as endmembers instead of ideal mineral compositions can help discern the exact proportions of the minerals contributing to the composition of the melt vein, assuming that the composition of all minerals in the meteorite are known. Linear deconvolution of the melt vein composition was carried out with HMX (see section 2.3.1.2 in Chapter 2 for method details), using as endmembers the average NWA 6234 mineral compositions previously reported (olivine, pyroxene, chromite and merrilite; Gross et al. 2013), including associated errors, and the maskelynite composition analysed here (Table 3-14). None of the mineral endmembers were forced to be in the mix, and their total contribution to the mix was not bound to 100 %. The results are summarised in Figure 3-31, and show that, contrary to the results of the CIPW norm, the melt phase composition could

be formed by ~88 wt. % pyroxene and ~10 wt. % maskelynite (as defined by their composition in NWA 6234), and minor amounts of chromite and merrilite.

Table 3-17. HMX deconvolution results for the melt vein composition, and the unknown phases in the melt vein.

NWA 6234 minerals	Melt composition		Melt vein unknown phases (MVUP)					
			Condition A		Condition B		Condition C	
	wt. %	1σ	wt. %	1σ	wt. %	1σ	wt. %	1σ
Olivine	0	0.55	46.44	10.32	70.31	8.54	553.54	89.05
Pyroxene	87.54	4.83	30.37	10.14	0	0.85	−673.4	110.15
Maskelynite	9.63	2.55	9.34	3.15	27.5	4.5	216.48	24.41
Chromite	1.11	0.69	0.89	0.63	1.08	0.66	2.31	0.75
Merrilite	1.72	0.15	-	-	-	-	-	-
Sulfide	-	-	1.11	0.38	1.11	0.38	1.06	0.19
Total	100		88.15		100		99.99	
$(\sum R)^2$ (no unit)	0		73.82		58.63		0.45	

EPMA analyses of the MVUPs did not yield oxide weight percentages close to 100 (Table 3-15), most likely due to the undersampling of one or more elements. The composition of the MVUPs is distinct from other known phases in the meteorite. This is most easily observed when comparing element abundance plots between the different phases of NWA 6234 and the MVUPs. Comparison between major element chemistry in the MVUPs, and that of other mineral phases of NWA 6234 shows that the MVUPs appear to be compositionally intermediate to the major minerals (Figure 3-30). The MVUPs are lower in Mg than the olivines of NWA 6234, and somewhat lower than the pyroxenes (Figure 3-30A), indicating that aside from olivine and pyroxene, lower Mg phases such as the plagioclase or the spinels may contribute to the composition of the MVUPs. The relatively low sum of SiO_2 and Al_2O_3, and high total FeO (Figure 3-30B) suggests that the component is principally spinel rather than plagioclase (or maskelynite).

Minor element chemistry of the MVUPs shows however, a composition unrepresented in the other phases of NWA 6234. Compared to the other mineral phases, the K_2O content of

the MVUPs (~ 0.7 wt. %) is especially high, as well as the SO_2 (~ 0.22 wt. %), Sr (~ 2669 ppm) and Ba content (~ 2327 ppm) to some extent (Figure 3-31A, Figure 3-31B, and Table 3-15). Chlorine (Cl) is also relatively high in MVUPs, and may have been contributed by the phosphates of NWA 6234, except that the elevated Cl content in MVUPs does not correlate with elevated P_2O_5 content, as would be expected from a phosphate contribution (Figure 3-31C).

In order to understand the origin of the MVUPs, a CIPW norm was carried out (Table 3-16), both with a non-normalised and a normalised (to ~ 100 total oxide wt. %) average MVUP composition. The CIPW analysis revealed that the average MVUP composition is largely composed of olivine, plagioclase, and diopside, but no enstatite-ferrosilite pyroxenes.

HMX unmixing analyses were ideal for the MVUP compositions, since the error (spread) in the data of the MVUP compositions could be accounted for, and the primary mineralogy of NWA 6234 reported here and in Gross et al. (2013) could be used as endmembers, instead of the idealised minerals used in CIPW standardisation. HMX unmixing was carried out under three conditions: Condition A was carried out without the requirement for any of the endmember minerals to be present in the mix and without normalisation to 100 %. Condition B required the total contribution from the endmember minerals to the MVUP compositions to equal 100 %. Finally, Condition C also required the total contribution of the endmembers to equal 100 %, but the contribution of the individual endmembers could be negative, i.e., they could be extracted from the mix. The results of the HMX unmixing analyses are shown in Table 3-17. Under all conditions, olivine is the main contributor to the composition of the MVUPs and there is a constant ~ 1 % contribution from NWA 6234 sulfides, but the very high residual sum of squares from the results of Conditions A and B, and the extreme fractionation of pyroxene from the

composition of the MVUPs under Condition C (Table 3-17), strongly suggests that an as yet undetected mineral phase in NWA 6234 contributed to the composition of the MVUPs.

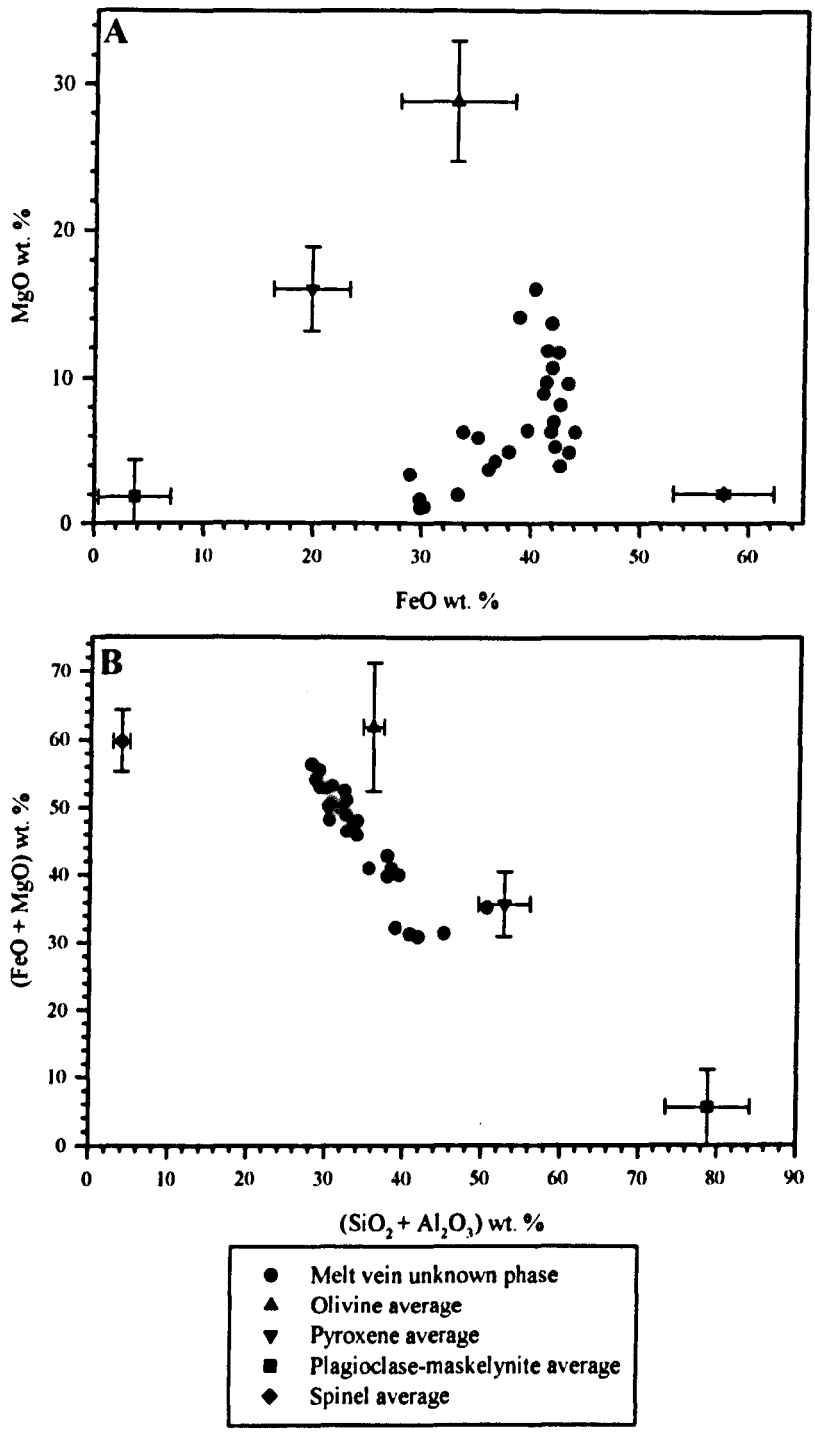

Figure 3-30. Oxide composition comparisons between the unknown phase in the melt vein and all major phases in the sample of NWA 6234 studied here. A) FeO wt. % versus MgO wt. %. B) Sum of SiO_2 and Al_2O_3 content versus the sum of FeO (including Fe_2O_3) and MgO content, in wt. %. Representative EPMA spot analyses of the unknown phase lie between the compositions of the major phases, according to major element chemistry.

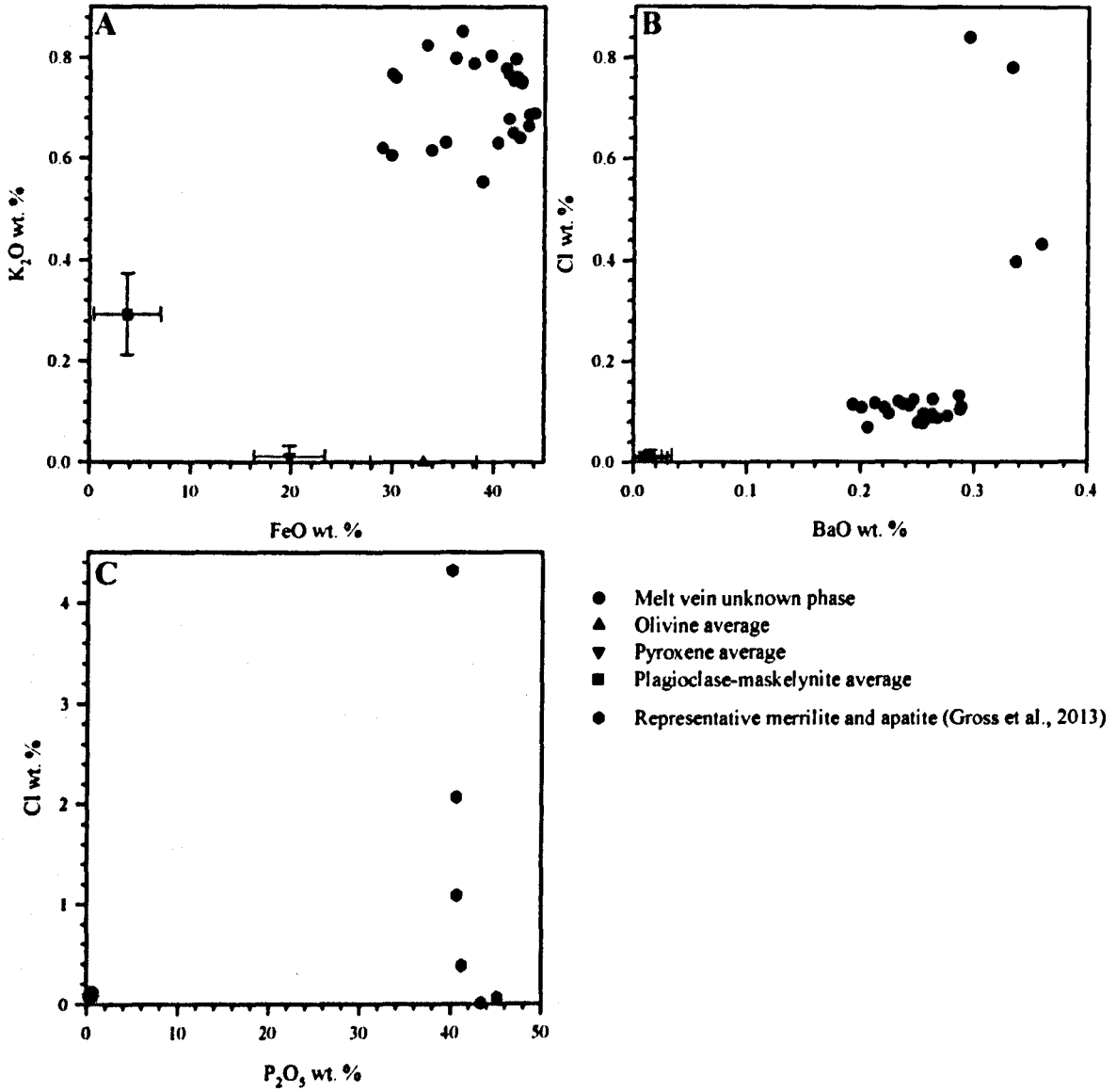

Figure 3-31. Comparison of compositions (in wt. %) between the unknown phase in the melt vein and major and minor minerals in NWA 6234. A) FeO (including Fe_2O_3) versus K_2O. B) BaO versus chlorine (Cl). C) P_2O_5 versus Cl in the unknown phase and phosphate data reported by Gross et al. (2013). Minor element chemistry of the unknown phase in the melt vein appears distinct from that in the other mineral phases of NWA 6234.

3.2.3 Possible aqueous alteration in NWA 6234: Discusssion

The discovery of the unknown phases in the melt vein of NWA 6234 and their unique minor chemistry compared to the rest of the meteorite prompts the question as to whether

they may be alteration minerals. Texturally, they appear to grow from olivine, and only within the melt vein. It is therefore unlikely that they were there before the impact that formed the shock melt vein occurred, unless the melt vein formed only where the MVUPs were, which would have been possible since the contrasting densities between the primary mineralogy and the MVUP precursor minerals may have caused the melt vein to preferentially form at the grain boundaries of these minerals (e.g., Ozawa et al., 2009). It is also unknown whether the MVUPs formed on Mars or during the terrestrial residence of the meteorite; in order to ascertain their origin, isotopic analyses (particularly oxygen isotope systematics) of the MVUPs would need to be carried out. Nevertheless, the non-crystalline, amorphous aspect of the MVUPs (Figure 3-27) may relate to the effects of shock and melting, and if so, were formed prior to ejection from Mars, between two impact-related deformation events which could be named D_1 and D_2. Hypothetically, after crystallisation of the mantle melt from which NWA 6234 formed (Filiberto et al., 2012; Gross et al., 2013), D1 occurred, leading to the formation of the shock melt vein. Subsequently, the precursor minerals to the currently observed MVUPs formed along the vein, in contact with olivine. Finally, D_2 caused the launch and ejection of NWA 6234 from Mars. The relatively high K, Ba, Sr, S and Cl content, and the low analytical totals of the MVUPs (Table 3-15) is an argument for a phase rich in volatile elements, formed from the alteration of olivine at the melt vein. Presumably, the melt vein created a pathway for (perhaps hydrothermal) aqueous alteration in which the precursor minerals to the currently observed MVUPs precipitated. The interface between the melt vein and the host rock could have acted as the pathway for fluids. The composition of the precursor minerals is unknown, but, based on the minor chemistry of the MVUPs (Table 3-15), possible candidates could be made for the sulfates jarosite ($KFe_3(SO_4)_2(OH)_6$) and/or alunite ($KAl_3(SO_4)_2(OH)_6$).

A parallel could be drawn between the MVUPs and the alteration minerals in the nakhlite group of martian meteorites. The crystallisation of the nakhlites predates that of the shergottites (~ 1.3 Ga and 165 – 475 Ma, respectively; Nyquist et al., 2001), but they are well known to contain minerals (mainly carbonates, Fe-oxyhydroxides and smectites) in veins, produced from the hydrothermal alteration of olivine (e.g., Bridges et al., 2001; Bridges and Grady, 2000, 1999; Changela and Bridges, 2010; Hicks et al., 2014; Treiman, 2005; Treiman et al., 1993). Other shergottites are contended to contain alteration minerals (mainly sulfates), although their formation is attributed to evaporative processes (Bridges et al., 2001; Gooding et al., 1988; Wentworth et al., 2000)

Further work must be carried out to confirm whether the MVUPs are indeed martian alteration minerals, modified by a shock event. X-ray diffraction may provide better compositional and crystallinity data, along with field emission gun (FEG) SEM and transmission electron microscopy (TEM) analyses. Spatially resolved isotope analyses of oxygen isotopes may discern whether the MVUPs are martian or terrestrial, although even simple thin section petrography can aid petrographical interpretation greatly beyond studying mounted chips. Further, hydrogen isotope systematics of the MVUPs and the bulk sample can aid interpretation of the source of the water that formed the MVUP mineral precursors, if any.

As the NWA 6234 sample studied is part of a consortium study (Filiberto et al., 2011) and is not an early martian meteorite, further work was not considered directly relevant to this thesis, and not carried out as part of this work. Nevertheless, the use of techniques (mainly EPMA and statistical analyses) and the discovery of the possible alteration phases were important outcomes of the project. If the discovered phases are indeed martian alteration phases, the important implication is that aqueous alteration continued well into the Amazonian period, but minerals produced (possibly sulfates) were compositionally

different to those formed in earlier periods (e.g., carbonates in ALH 84001, and carbonates, smectites and evaporites in the nakhlites), probably because of different alteration fluids and mechanisms.

4 Geochemical models of the aqueous alteration in ALH 84001

A large part of this chapter is eing prepared for peer review in the publication by Melwani Daswani et al. (in prep.). Work leading to the content in this chapter was reported in conference abstracts by Melwani Daswani et al. (2014, 2013).

4.1 Introduction

Geochemical (software) models applied to understand the formation of the alteration in ALH 84001 have been discussed briefly in the Introduction, Section 1.4.2.5. Geochemical models offer several advantages over laboratory experiments attempting to reproduce the P-T-X conditions that the rock was subjected to in order to recreate the alteration phases, including:

a. The ready ability to experiment with, iterate and change P-T-X conditions quickly, often even within a single experimental run.
b. The fact that a laboratory, samples, and specialist equipment such as batch/chemical reactors and analytical facilities are not needed to carry out experiments.
c. The existence of a database of compiled published data on minerals, aqueous species and gases under wide experimental conditions contributed by many authors, ensuring that results are based on a large range of independently verified constants and reaction pathways.
d. The fact that many of the reactions, especially at low temperatures, take too long to complete in experimental settings or be observed in nature.

e. The ease of sharing data and results that are output from models, which may be reviewed and scrutinised by third parties.

Despite these advantages, geochemical modelling does not produce tangible products that can be analysed. Therefore, in order to complement the results of this chapter, experimental models were carried out and are reported in Chapter 5.

4.1.1 Choice of geochemical modelling software

Many geochemical modelling programs are available to compute and simulate a variety of chemical reactions and geological environments. All models have limitations depending on the sets of equations they use to determine thermodynamic properties in the system that is being simulated, and the available thermodynamic and chemical data for aqueous and/or melt species, minerals and gases. As such, no single software package is apt for all imaginable P-T-X conditions, and programs tend to be specialised for solving particular geological thermodynamic problems. As discussed in Section 1.4.2, the P-T-X conditions purported to have altered ALH 84001 on Mars are incredibly varied (e.g., see Figure 1-3), but certain constraints can be described from previous studies (see Section 1.4.2 for further details): there is overwhelming consensus that the carbonates were formed by the involvement of a relatively low temperature (< 100 °C) aqueous or carbonic fluid and not by an anhydrous melt (see, however, the contrasting view by Harvey and McSwen, 1996; and Scott et al., 1997). Furthermore, the general consensus also concludes that biological activity did not play a role in the alteration of the meteorite (but see the contrasting view by e.g., McKay et al., 1996; and Thomas-Keprta et al., 2002, 2000).

With the mentioned constraints in mind, high P-T condition simulators like MELTS and pMELTS (Asimow and Ghiorso, 1998; Ghiorso et al., 2002; Ghiorso and Sack, 1995) are not adequate for describing and solving this problem. FrezChem (Marion et al., 2010)

allows for simulations only under 25 °C, and cannot compute reactions for silicate systems. CHIM-XPT (Reed et al., 2012; Reed, 1998, 1982; Spycher and Reed, 1988), PHREEQC (Parkhurst and Appelo, 2013) and The Geochemist's Workbench® (GWB, Bethke and Yeakel, 2014; *The Geochemist's Workbench*, 2014) are all similarly adequate for the purported alteration conditions of ALH 84001, but GWB is commercial closed source software. PHREEQC has previously been used to model the carbonate formation in ALH 84001 (van Berk et al., 2011), but control over PT conditions in PHREEQC is mostly limited to H_2O liquid vapour saturation conditions, and control over non-gas related pressure (e.g., lithostatic pressure) is limited. If the carbonates in ALH 84001 were formed at or near to the martian subsurface, as many studies have suggested (see Chapter 1), then being able to test different possible total pressures would be necessary. CHIM-XPT was chosen as it allows for this form of control. CHIM-XPT and (its predecessor, CHILLER) is most often used to model terrestrial basaltic hydrothermal environments (e.g., Palandri and Reed, 2004; Reed, 1998, 1983) and terrestrial sedimentary waters (e.g., Palandri and Reed, 2001), but has also been used for hydrothermal reaction modelling of the alteration phases in the nakhlites (Bridges and Schwenzer, 2012) as well as hydrothermal and fluvial systems associated with impacts on Mars (Filiberto and Schwenzer, 2013; Schwenzer and Kring, 2013, 2009) and low temperature (13 °C) aqueous alteration conditions postdating hydrothermal activity at a Noachian-aged impact site (Filiberto and Schwenzer, 2013). A comparison of P-T conditions for the geochemical modelling software discussed is depicted in Figure 4-1.

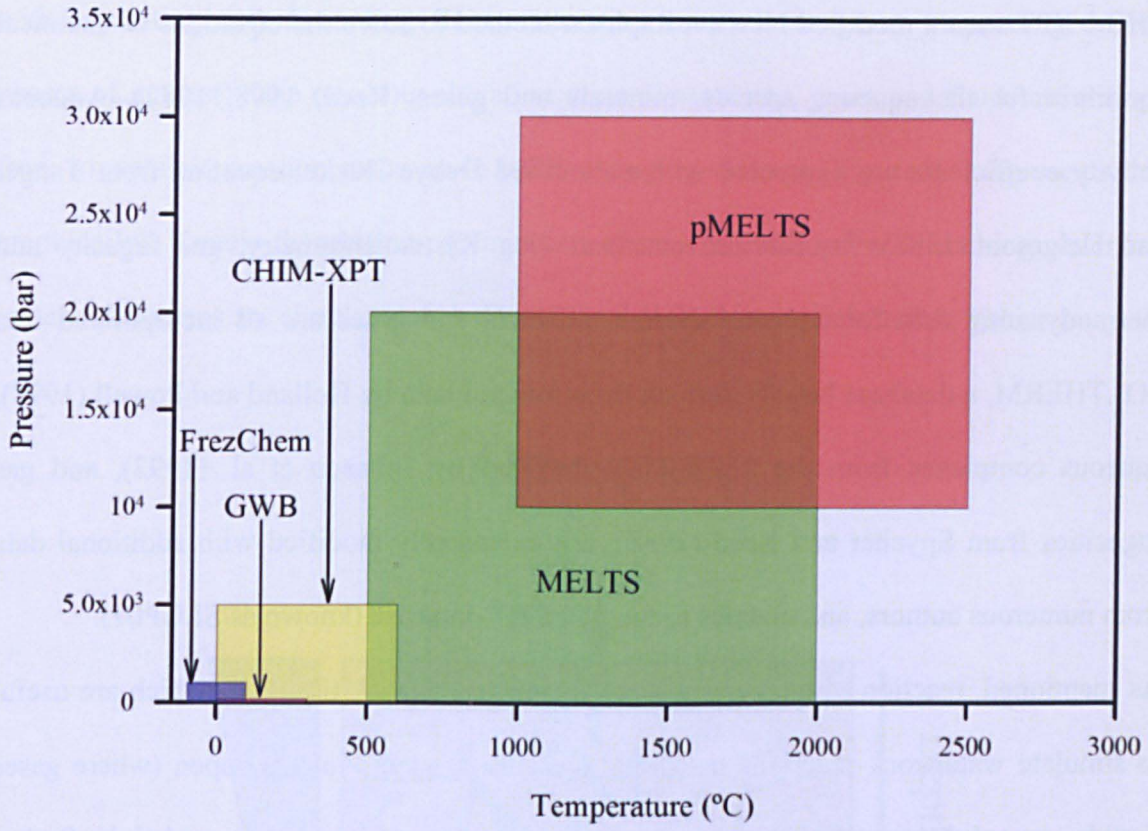

Figure 4-1. P-T space comparison of the different geochemistry software discussed.

4.1.2 Description and capabilities of CHIM-XPT

In essence, CHIM-XPT is a FORTRAN computer program that can be used to solve multicomponent and multiphase gas, liquid and aqueous equilibria for a wide variety of (changing) total pressures (1 – 5000 bar), temperatures (0.01 – 600 °C), and chemical compositions. The gas-liquid-aqueous equilibrium distributions are calculated along the geological reaction path simulated, the reaction path being controlled by changing one (or more) of the variable parameters (P, T, X, and enthalpy) in incremental steps. Often, the reaction paths are represented as rock titrations into a fluid, wherein a rock (of a specified composition) is added in increments to a fluid, so a range of W/R can be tested to solve equilibrium distributions.

CHIM-XPT uses a modified Newton-Raphson method to solve the equations of chemical equilibria for the aqueous species, minerals and gases (Reed, 1998, 1982). Aqueous activity coefficients are computed with a modified Debye-Hückel equation from Tanger and Helgeson (1988). Equilibrium constants (log K), stoichiometry, gas fugacity and thermodynamic data for aqueous species, minerals and gases are all incorporated into SOLTHERM, a database largely derived from mineral data by Holland and Powell (1998), aqueous complexes from the SUPCRT92 database by Johnson et al. (1992), and gas fugacities from Spycher and Reed (1988), but extensively modified with additional data from numerous authors, and updates to the SUPCRT database (known as SLOP07).

As mentioned, reaction paths are frequently computed as rock titrations, which are useful to simulate water-rock reactions in natural systems. Systems may be open (where gases liquids, or solids, specified by the user, may be separated and disregarded in further computations) or closed (where gases, liquids and solids are kept in the system and are only affected by their equilibrium states). Natural systems most resemble the modelled open systems, which is where a fluid evaporates and precipitates minerals (e.g., sabkha evaporites), or where fast flowing fluvial or groundwater fluids are involved. However, in cases where fluid transport is slow, temperature is high (> 75 °C), fluid-rock interaction takes place over a long time (e.g., oceanic crust), or fluid is continuously replenished (e.g., hydrothermal vents), closed system equilibrium between fluids and minerals is a valid assumption, and mimics natural systems (e.g., Palandri and Reed, 2004, 2001).

Non-equilibrium thermodynamics, as in the case of an open system rock-flowing fluid reaction, can be modelled in CHIM-XPT assuming local equilibrium, i.e., equilibrium occurs between the reacting rock and the fluid at an extremely small scale. To simulate this, mineral-liquid-gas equilibria are specified to be calculated at minute increments (usually, 10^{-6} g of fresh unaltered rock sequentially added at every step, per 1 litre of H_2O), coupled

with separating and discarding fluids, alteration minerals or gases (depending on the phases of interest). The resulting alteration mineral sequence, gases and fluids are formed from irreversible reaction paths, as in open, changing systems (Figure 4-2 represents this graphically). Kinetic dissolution-precipitation of minerals and mineral leaching occurring in natural systems are simulated as 1-dimensional (1D) flow models in this fashion.

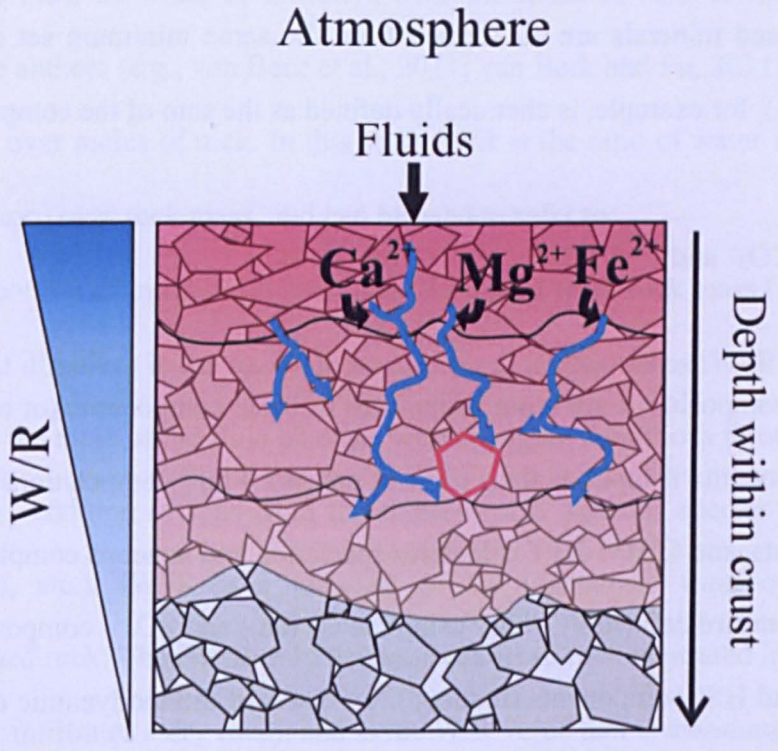

Figure 4-2. A schematic of an open system with an infiltrating fluid in contact with the atmosphere. The region of interest (red outline) may be studied out of its original context in a non-equilibrium 1D flow model. As the fluid infiltrates the subsurface, chemical alteration of the host rock occurs, and secondary minerals form. Components (e.g., divalent cations) from the host rock are leached and incorporated into the fluid, altering its composition and affecting the composition of minerals precipitated. Simplistically, the weathering grade is related to the water to rock content, and decreases with depth, as illustrated with the graded colours.

4.1.2.1 Inputs

Input parameters and variables for CHIM-XPT are covered in detail by Reed et al. (2012) and Reed (1998, 1982). Only the basics to understand the modelling process are described here.

Inputs are constrained by the phase rule. The fluids, gases and minerals in CHIM-XPT are defined chemically as sets of components in order to simplify calculations. Aqueous species, gases and minerals are all formed from the same minimum set of components. Calcite ($CaCO_3$), for example, is chemically defined as the sum of the components:

$$+1\ Ca^{2+},\ +1\ HCO_3^-\ \text{and}\ \ -1\ H^+ \qquad (4\text{-}1)$$

Rock and gas compositions are input as the sum of basic components (or are converted to the basic components if input as their mineral names). Fluid compositions are defined by their components, and CHIM-XPT calculates speciation and aqueous complexes formed. Redox conditions are defined by either using the O_2 (aq.) and SO_4^{2-} components (oxidised), or the SO_4^{2-} and HS^- components (reduced). Two sets of thermodynamic data exist in the CHIM-XPT data base for all minerals and gases depending on which redox-indicating components are used.

Initial temperature, initial total pressure and step increments (whether they are increased titrations, temperature changes or fluid mixing) are necessarily defined by the user. Density of the initial fluid (if not calculated by its composition) enthalpy, temperature of a mixing solution, density of the rock, porosity of the rock (if not calculated with the rock density), and other parameters are optionally assigned by the user.

The pH may be defined by the user as well if it is not calculated from the activity of the hydrogen ion ($pH = -\log[aH^+]$) in the solution, which is particularly sensitive to the

composition of the fluid and its temperature. Defining the pH of the alteration fluid is covered in more detail in Section 4.2.2.1.

4.1.2.2 Defining the water to rock ratio (W/R)

The water to rock ratio (W/R) is defined differently by different authors. Typically, it is a measure of the mass of water in a system over the mass of rock in the same system. However, some authors (e.g., van Berk et al., 2011; van Berk and Fu, 2011) define W/R as moles of water over moles of rock. In this study W/R is the ratio of water mass (including species in solution) over rock mass, and can be used to refer to:

a. the proportion of initial fluid mass over the added fresh rock mass (*total* amount of rock that dissolves in the fluid), in which case it is denoted as iW/iR ('i' for initial). Though the mass of the fluid changes with changing conditions throughout a model run (e.g., addition of ions from the titrated rock, aqueous species precipitated as minerals, etc.), iW/iR is a measure of the unchanged fluid over the added unchanged rock. The iW/iR only decreases as fresh rock is titrated into the fluid (or as water infiltrates a dry rock), and is the W/R value that is automatically output by CHIM-XPT. This is useful for 1D flow models, to describe the fluid infiltration process, as iW/iR reflects the relative penetration depth at which the computed alteration products are produced, if an estimate of the density, porosity and permeability of the unreacted host rock can be given.
b. The proportion of the resulting fluid mass over the resulting alteration mineral mass, in which case it is denoted as rW/rR ('r' for resulting). This measurement is useful for describing the mineral, gas and fluid assemblage at a certain stage (a 'window'), separate from the rest of the experiment, or to describe the final assemblage after all reactions have taken place. The rW/rR typically decreases with increased rock

titration, but as a result of water-rock reaction, may also increase with more titrated rock (e.g., as phyllosilicates are dissolved releasing water, and anhydrous minerals are preferentially precipitated). In this work, equilibrium reactions are best described with rW/rR.

Alteration assemblages occurring at high W/R are those occurring close to pores or fractures (and where fluid flow may be high), whereas low W/R alteration assemblages are those that form far from factures and where unaltered fresh rock may still be present (Palandri and Reed, 2004). In the context of infiltration and 1D fluid flow models, high W/R represents where a fluid has not penetrated deeply, and has not come into contact with a large volume of rock. Conversely low W/R tends to mean that the initial fluid has infiltrated a large total mass of rock, and the fluid mass has probably decreased as a result of fluid-rock reaction (e.g., forming phyllosilicates).

Evaporation can be quantified in terms of W/R (i.e., mass of water remaining over mass of rock and alteration minerals in the system), but to avoid confusion, evaporation will be quantified as % of water evaporated, from a specified rW/rR.

4.1.2.3 Limitations of CHIM-XPT

CHIM-XPT is a powerful program for the computation of mineral-liquid-gas equilibria, accounting for aqueous complexation, mineral dissolution and precipitation, redox reactions and changes, gas dissolution and exsolution, and ion exchange. However, it is not strictly speaking a 'transport model', i.e., although reasonable estimates for the depths of fluid infiltration can be calculated from iW/rR, the geometrical distribution of alteration products cannot be simulated along the reaction path. Reflecting on this, mineral crystallinity, sizes of crystals (or lack, thereof), isotope fractionation and chemical reaction times are not model outputs, and cannot be directly specified in the model.

Chemical kinetic effects are not accounted for by CHIM-XPT. For instance, metastable minerals that form in natural alteration systems (e.g., metastable kaolinite and illite in favour of muscovite at moderately low temperature, see Aja et al., 1991; Vidal and Dubacq, 2009) can be omitted by the program in favour of more stable minerals (Palandri and Reed, 2004). As such, it is important to have an understanding of the occurrence of alteration minerals in natural systems, and manually, to select and disallow minerals that may be kinetically retarded. Minerals considered to be kinetically retarded (and therefore disallowed in the model) are reported for all specified modelled conditions below.

Thermodynamic data for a number of solid solutions (e.g., the pyroxenes diopside and hedenbergite) exist in CHIM-XPT, but often, the user must identify which minerals form solid solutions in the calculated mineral assemblage (e.g., some carbonates).

Finally, Ti-bearing minerals are missing from the SOLTHERM database (as of version 47), so if Ti is titrated into a fluid, it remains in solution throughout the experiment. Ti must therefore be omitted from calculations, or exist in such a small concentration that it can justifiably stay in solution throughout the run. (Cr minerals are also similarly not included in the thermodynamic database, but aqueous Cr species are also absent, and so will not be included in the models.)

4.2 Modelled scenarios

4.2.1 Kinetically allowed and disallowed minerals

At the low temperatures studied, kinetic effects suppress the nucleation and precipitation of many minerals which would otherwise be stable. CHIM-XPT does not automatically take into account kinetic effects that affect the solubility and precipitation of minerals, but minerals can be disallowed from forming by the user. All minerals that were disallowed

are listed in Table 4-1, along with the lowest T-P conditions in which they are thought to form from a variety of observational, synthesis and thermodynamic studies.

Magnesite and dolomite, for example, were actively suppressed in the low temperature models carried out here because they are kinetically retarded under low temperature conditions (e.g., Arvidson and Mackenzie, 1999; Hänchen et al., 2008), though the Mg-bearing carbonates huntite ($Mg_3Ca(CO_3)_4$) and hydromagnesite ($Mg_5(CO_3)_4(OH)_2 \cdot 4H_2O$) were allowed. Both huntite and hydromagnesite can serve as precursors to magnesite, the latter by the loss of crystalline water and dehydroxylation with a brief temperature increase (> 220 °C, Hollingbery and Hull, 2010) consistent with the observation of high T and high P magnetite and graphite in the meteorite (Steele et al., 2012b; Treiman and Essene, 2011). Minerals that form solid solutions in nature and that precipitated in the models are grouped in endmembers for simplicity, e.g., 'chlorite' includes the solid solution series clinochlore ($Mg_5Al_2Si_3O_{10}(OH)_8$), chamosite ($Fe_5Al_2Si_3O_{10}(OH)_8$), penantite ($Mn_5Al_2Si_3O_{10}(OH)_8$) and "Al-free chlorite" ($Mg_6Si_4O_{10}(OH)_8$). An assumption made when reporting carbonate compositions formed in the models is that they form solid solutions, so ternary diagrams are used graphically to represent carbonate compositions. Further solid solutions and minerals grouped are detailed in Table 4-2.

Table 4-1. Kinetically disallowed minerals at 15 – 25 °C and total pressure of 1 – 2 bar

Mineral	Low T-P aqueous occurrences	References
Aegirine	Na clinopyroxene. May be authigenic and synthesised, but at ≥ 200 °C	Decarreau et al. (2004), Laverne (1987), Redhammer et al. (2000)
Amesite	Serpentine group, low T metamorphism.	Deer et al. (2013)
Andradite	Garnet group, can be metasomatic in Ca-silicate systems at > 200 °C, but typically ≥ 300 °C and at depth	Bird et al. (1984), Easton et al. (1977)
Antigorite	Serpentine group, hydrothermally produced at ≥ 250 °C at low P	Evans (2004), Hemley et al. (1977)
Anthopyllite	Typically metamorphic amphibole, metasomatic at > 500 °C	Hemley et al. (1977), Kanaris-Sotiriou and Angus (1979)
Biotite	Mica, metasomatic in Ca-silicates at ≥ 325 °C	Bird et al. (1984), Wones and Eugster (1965)
Carpholite	Metamorphic, > 300 °C, > 8 kbar	Theye et al. (1997)
Diaspore	Metastable phases (gibbsite) more likely at < 100 °C	Perkins et al. (1979), Theye et al. (1997)
Dolomite	At ambient T in sulfate reducing conditions, but typically at higher T	Arvidson and Mackenzie (1999), Shatkay and Margaritz (1987)
Ferro-actinolite	Typically metamorphic amphibole. Metasomatised at > 200 °C, typically > 300 °C	Bird et al. (1984), Jenkins and Bozhilov (2003)
Glaucophane	Amphibole hydrothermally produced at ≥ 150 °C	Maruyama and Liou (1988)
Grossular	Garnet group, can be metasomatic in Ca-silicate systems at > 200 °C, typically ≥ 300 °C and at depth	Bird et al. (1984)
Grunerite	Low metamorphic grade (> 325 °C) amphibole	Forbes (1977), French(1973)
Magnesite	Metastable hydrous phases (see text) form quicker at 20 °C. Magnesite easily precipitated at higher T	Hänchen et al. (2008), Hollingbery and Hull (2010), Saldi et al. (2009)
Manganosite	Other Mn oxides precipitate more easily (e.g., pyrolusite). Low grade metamorphic and hydrothermal systems > 300 °C, low fO_2	Klingsberg and Roy (1959), Miyano and Beukes (1987), Ostwald (1992)
Magnesiocarpholite	Carpholite group, HPLT metamorphic, > 230 °C, 7 kbar	Theye et al. (1997), Vidal et al. (1992) and references therein
Muscovite	Mica, can be authigenic at > 175°C (?). Kaolinite, illite and smectite favoured instead at low T	Aja et al. (1991), Vidal and Dubacq (2009)
Paragonite	Low grade metamorphic, > 350 °C mica	Vidal (1997)
Pyrophyllite	Low grade metamorphism and hydrothermal alteration, ≥ 230 °C	Haas and Holdaway (1973), Marumo ,(1989) Vidal (1997)
Pyroxmangite	Metamorphic and metasomatic, ≥ 400 °C	Deer et al. (1992), Peters et al. (1978)
Riebeckite	Typically metamorphic amphibole (≈ 400 °C), but similar magnesio-arfvedsonite can be authigenic sedimentary (< 100 °C)	De Ros et al. (1994), Ernst (1962)
Tremolite	Like actinolite, metasomatic at >200 °C, more commonly at >300 °C	Bird et al. (1984), Huang and Rubenbach (1995)
Wollastonite	In geothermal systems at > 200 °C, more typically at > 300 °C	Bird et al. (1984)

Table 4-2. Grouped minerals formed at 15 – 25 °C and total pressure of 1 – 2 bar.

Group	Minerals	Formula used in models
Apatite	Hydroxylapatite	$Ca_5(PO_4)_3(OH)$
Carbonates	Ankerite	$CaFe(CO_3)_2$
	Artinite	$Mg_2(OH)_2(CO_3)\cdot 3H_2O$
	Calcite	$CaCO_3$
	Dawsonite	$NaAlCO_3(OH)_2$
	Huntite	$CaMg_3(CO_3)_4$
	Hydromagnesite	$Mg_5(OH)_2(CO_3)_4\cdot 4H_2O$
	Rhodochrosite	$MnCO_3$
	Siderite	$FeCO_3$
Celadonite	"Fe-celadonite"	$KFeAlSi_4O_{10}(OH)_2$
Chlorite	"Al-free chlorite"	$Mg_6Si_4O_{10}(OH)_8$
	Chamosite	$Fe_5Al_2Si_3O_{10}(OH)_8$
	Clinochlore	$Mg_5Al_2Si_3O_{10}(OH)_8$
	Penantite ("Mn-chlorite")	$Mn_5Al_2Si_3O_{10}(OH)_8$
Feldspar	Albite	$NaAlSi_3O_8$
	Microcline	$KAlSi_3O_8$
Gibbsite	Gibbsite	$Al(OH)_3$
Hematite	Hematite	Fe_2O_3
Kaolinite	Kaolinite	$Al_2Si_2O_5(OH)_4$
Magnetite	Magnetite	Fe_3O_4
Nontronite	"Ca-nontronite"	$Ca_{0.165}Fe_2Al_{0.33}Si_{3.67}O_{12}H_2$
	"H-nontronite"	$H_{0.33}Fe_2Al_{0.33}Si_{3.67}O_{12}H_2$
	"K-nontronite"	$K_{0.33}Fe_2Al_{0.33}Si_{3.67}O_{12}H_2$
	"Mg-nontronite"	$Mg_{0.165}Fe_2Al_{0.33}Si_{3.67}O_{12}H_2$
	"Na-nontronite"	$Na_{0.33}Fe_2Al_{0.33}Si_{3.67}O_{12}H_2$
Serpentine	Chrysotile	$Mg_3Si_2O_5(OH)_4$
SiO_2	Quartz	SiO_2
Stilbite	Stilbite	$CaAl_2Si_7O_{11}(OH)_{14}$
Sulfides	Alabandite	MnS
	Pyrite	FeS_2
Talc	Fe-Talc	$Fe_3Si_4O_{10}(OH)_2$
	Talc	$Mg_3Si_4O_{10}(OH)_2$
Tobermorite	Tobermorite	$Ca_{0.833}SiO_2(OH)_{1.667}(H2O)_{0.5}$

4.2.2 Pre-alteration compositions

4.2.2.1 Composition of the initial alteration fluid

The simplest fluid composition compatible with the aqueous alteration scenario of ALH 84001 is a H_2O + CO_2 fluid. While ALH 84001 is very likely to have primary, magmatic carbon (see Sections 3.1.3.1 and 3.1.4, and Grady et al., 2004, 1994), the source of the carbon in the secondary carbonates is widely attributed to the early martian atmosphere (see Sections 3.1.3.1 and 3.1.4, where a $\delta^{13}C \approx +40$ was measured in

ALH 84001 as part of this work, and e.g., Halevy et al., 2011; Jull et al., 1997; Romanek et al., 1994; Valley et al., 1997). The carbon in the fluids modelled is therefore assumed to be atmospheric and to be *initially* in chemical equilibrium with the partial pressure of atmospheric CO_2 (pCO_2). Specifically, the models were treated as closed systems to CO_2, where CO_2 was a limiting factor: CO_2 used in carbonate formation and other reactions was not replenished, so it is treated as a higher end value. Assuming the plausible scenario of 1 and 2 bar CO_2 fugacity (fCO_2) for early Mars calculated by climate models (Forget et al., 2013; Wordsworth et al., 2013), and temperatures (15, 20 and 25 °C) consistent with the "clumped" isotope estimate of the temperature of the carbonate formation in ALH 84001 (18 ± 4 °C; Halevy et al., 2011), the aqueous CO_2 (i.e., in solution) activity in the fluid may be calculated using Henry's law. A pCO_2 of 1 bar appears to be consistent with the early martian atmospheric pressure estimated by global circulation models which allow for transient liquid water on the surface (Wordsworth et al., 2013), and near the upper limit to account for ancient crater sizes (Kite et al., 2014), although lower atmospheric pressures (<400 mbar; Cassata et al., 2012) have been proposed for the surface of the early martian atmosphere. Other atmospheric species (such as O_2, N_2 and SO_2) were not introduced into the initial composition of the reactant fluid in the models, as the early martian atmosphere was probably principally composed of CO_2 (Forget et al., 2013; Jakosky and Phillips, 2001; Pollack et al., 1987; Wordsworth et al., 2013), although relatively large partial pressures of other constituents (e.g., SO_2; Halevy et al., 2007) have been proposed to have coexisted with CO_2. CO_2 is also the most abundant gas in the martian atmosphere at present (Mahaffy et al., 2013; Owen et al., 1977).

The following established (simplified) reactions (Stumm, 1996, pp. 94, 152) detail the equilibria between pure water and atmospheric CO_2:

$$CO_2\,(g) + H_2O\,(l) \rightleftharpoons CO_2\,(aq) + H_2O\,(l) \rightleftharpoons H_2CO_3\,(aq) \qquad (4\text{-}2)$$

Carbonic acid, H_2CO_3 (formed from atmospheric CO_2 as a function of the Henry's constant (K_H) for CO_2 in Equation 4-2) is a weak diprotic acid (it dissociates twice). Only a small amount of H_2CO_3(aq) remains dissolved as such (but it is convenient to express all dissolved inorganic carbon species with this notation, or DIC to avoid confusion), most reacts in the following way:

$$H_2CO_3\,(aq) \rightleftharpoons HCO_3^-\,(aq) + H^+\,(aq) \qquad (4\text{-}3)$$

$$HCO_3^-\,(aq) \rightleftharpoons CO_3^{2-}\,(aq) + H^+\,(aq) \qquad (4\text{-}4)$$

Reaction 4-3 is the first dissociation of carbonic acid, where the log dissociation constants of H_2CO_3 ($\log K(H_2CO_3)$) at 1 bar total pressure are −6.42, −6.38 and −6.35 for 15, 20 and 25 °C respectively. Reaction 4-4 is the second dissociation, where the dissociation constants ($\log K(HCO_3^-)$) used were −10.43, −10.38 and −10.33 for 15, 20 and 25 °C respectively.

The equations above may be multiplied by $[H^+]^2$ and combined with the self-ionisation constant of water (Kw) into the following polynomial (Equation 4-4) to solve the pH of the fluid (Sparks, 2003):

$$[H^+]^3 - [H^+] \cdot (K\text{w} + K(H_2CO_3) \cdot K_H \cdot pCO_2) - 2K(HCO_3^-) \cdot K_H \cdot pCO_2 = 0 \qquad (4\text{-}5)$$

where $[H^+]$ is the concentration of hydrogen in moles/kg H_2O (assumed to be equal to the H^+ activity in pure water here ≤ 25 °C). *K*w is the self-ionisation constant of water (log*K*w = −14.34, −14.16 and −14 at 15, 20 and 25 °C respectively). Other variables as described above and in equations 4-2 to 4-4.

The pH and compositions were calculated with the above formulae for the initial alteration fluids in all P-T conditions modelled, and are detailed in Table 4-3.

Table 4-3. Dissolved inorganic carbon and pH of the initial fluids used in the alteration models.

T (°C)	fCO_2 (bar)	pH	DIC (mol/kg H_2O)
15	1	3.89	0.0445
15	2	3.74	0.0891
20	1	3.90	0.0374
20	2	3.75	0.0752
25	1	3.92	0.0326
25	2	3.77	0.0659

The theoretical calculations above are useful approximations to the actual chemical composition of the fluids modelled. While $pCO_2 \approx fCO_2 \approx P$ at the low P-T conditions considered here, CHIM-XPT automatically calculates DIC, pH and the precise speciation of carbon compounds in a fluid, given a specific T and P. CHIM-XPT also accounts for the non-ideal behaviour of real gases, which results in a calculation for fH_2O and a difference in the fourth decimal place of the DIC values with respect to the theoretically calculated values in Table 4-3.

4.2.2.2 Composition of the unaltered host rock

The presumed prealtered chemical composition of ALH 84001 was used, i.e., ALH 84001 without the carbonates. Given that the mineralogical characterisation carried out in this

work (see Section 3.1) did not vary significantly from previously published work, the published mineral proportions and compositions by Mittlefehldt (1994) were used for the geochemical aqueous alteration models below for ease of comparison to work by other authors. The composition of the unaltered ALH 84001 host used is given in Table 4-4.

All rocks and minerals are specified in the SOLTHERM thermodynamic database as sums of elemental molar abundances. Ti and Cr compounds were not included as reactants in the models because the database does not include Ti and Cr species and minerals. Given the relative insolubility of Ti(IV) and Cr(III) oxides in natural waters under ambient conditions (e.g., Imahashi and Takamatsu, 1976; Richard and Bourg, 1991), and their low abundance in ALH 84001 (principally in accessory chromite), their addition to the model and their possible influence on secondary mineral composition and chemical speciation of solutes is considered negligible.

Table 4-4. Composition (in wt. %) of the pre-altered ALH 84001 rock used as the reactant in the models The composition of the ALH 84001 unaltered host was modified from Mittlefehldt (1994), using 98.9 vol. % orthopyroxene, 1 vol. % maskelynite and 0.1 vol. % apatite. Sulfur for ALH 84001 was added from Lodders (1998). Secondary phases (carbonates and magnetite) were not included, whereas chromites and Ti in the analyses from literature were not included due to insufficient data for Cr- and Ti-bearing minerals available in the thermodynamic database (see text).

Oxide (wt. %)	ALH 84001 host*
SiO_2	54.00
Al_2O_3	0.88
Fe_2O_3	0.74
FeO	16.83
MnO	0.48
MgO	24.91
CaO	1.78
Na_2O	0.11
K_2O	0.01
P_2O_5	0.07
S (ppm)	110

*Does not include the carbonate or chromite

4.2.3 Batch equilibrium formation of the ALH 84001 carbonates

In the simplest case, a near-surface geological setting where pooled water was present and in contact with the host orthopyroxenite (such as a lacustrine environment) would have been conducive to forming the carbonates in ALH 84001. The initial fCO_2 is assumed in this model to be governed by the atmospheric CO_2 (see Section 4.2.2.1), and the system remains in poor contact with the atmosphere thereafter as the reaction progresses (Halevy et al., 2011), signifying that the CO_2 in the system is limited. This scenario is, in essence, a batch equilibrium, closed system reaction between the orthopyroxenite host and a low-temperature fluid, in line with results from Niles et al. (2009) and van Berk et al. (2011). The models tested here were at 15, 20 and 25 °C, and 1 and 2 bar fCO_2 (= total pressure) for each of the temperatures, for a total of six models.

4.2.3.1 Batch equilibrium model results and discussion

For simplicity and clarity, graphs of chemical composition are plotted from a minimum of 10^{-12} moles/kg H_2O. Note that the reaction progress in the graphs is read from high W/R to low W/R (right to left). A summary of the carbonates produced for all batch equilibrium models (15 – 20 °C and 1 and 2 bar fCO_2) are detailed in Table 4-5 and a comparison of the total amount of carbonate formed in the batch equilibrium models is shown in Figure 4-3. As the aqueous species for the fluids in all the tested conditions showed similar concentrations, only the dissolved species plots for the 20 °C equilibrium alteration model at 1 bar fCO_2 are shown here (Figure 4-4 to Figure 4-6). Minerals formed in all models were also present in similar proportions and concentrations, so only those formed at 20 °C and 1 bar fCO_2 are shown here (Figure 4-6B). The carbonate compositions at different rW/rR, however, varied significantly between the models tested (Figure 4-7) and are discussed in detail below.

Table 4-5. Main results for the carbonates formed in the equilibrium alteration models. All values reported at maximum carbonate replacement (MCR) for each of the models, i.e., when carbonates formed the largest mass % of the alteration assemblage produced. Model names are shortened to the format "XXCYb", where "XXC" is the temperature in degrees Celsius and "Yb" is the initial fCO_2 in bar.

Equilibrium model	MCR* (wt. %)	rW/rR	fCO_2 (bar)	pH	Carbonate composition (mol %)			
					$FeCO_3$	$MgCO_3$	$CaCO_3$	MnCO3
15C1b	40.33	319.81	0.03	7.55	63.68	25.86	8.62	1.83
15C2b	40.94	195.36	0.26	6.85	64.31	25.40	8.47	1.83
20C1b	40.36	370.65	0.28	7.57	63.67	25.87	8.62	1.83
20C2b	40.33	194.62	0.11	7.21	63.65	25.89	8.63	1.84
25C1b	40.36	438.02	0.03	7.45	63.73	25.84	8.62	1.82
25C2b	40.35	217.18	0.08	7.35	63.65	25.88	8.66	1.84
Mean	40.45	289.30	0.13	7.33	63.78	25.79	8.60	1.83

*Maximum carbonate replacement.

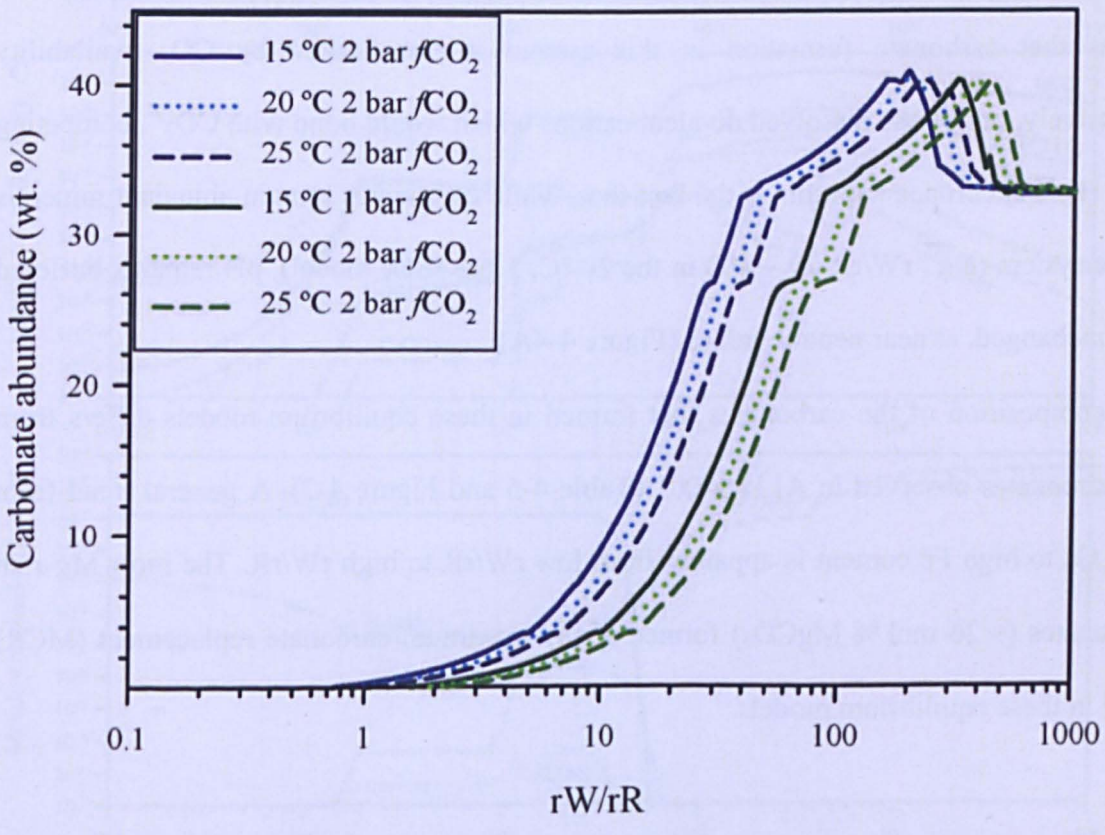

Figure 4-3. Proportion of carbonate in the precipitated secondary mineral assemblages, computed in the closed, no-flow, batch equilibrium alteration models, as a function of water to rock ratio (W/R). CO_2 fugacities are initial fCO_2 pressures.

Despite different temperature and initial fCO_2 conditions, the equilibrium models all resulted in the production of very similar amounts of carbonate produced (on average 40.45 % of all mineral mass produced at specific rW/rR). As carbonate precipitation is an exothermic reaction, higher amounts of carbonate replacement of the original (mostly) orthopyroxene mineralogy would be expected at higher temperature, but the results do not show this (Table 4-5). Similarly, the only source of CO_3^{2-} in the model is the atmospheric CO_2 initially allowed into the system, so increased carbonate replacement would be expected at higher fCO_2, but no appreciable increase is observed in the results. Instead, Le Chatelier's principle is conserved, in that an increase in CO_2 (aq) also leads to an increase in H_2CO_3, which in turn dissociates and produces H^+ (Equations 4-2 to 4-4), resulting in the capture of CO_3^{2-} to form bicarbonate again. This is a significant observation since it means that carbonate formation in this system is not limited by CO_2 availability exclusively, but by the dissolved divalent cations which would bond with CO_3^{2-}, competing with H^+. Concordant with this is the fact that, while carbonates remain abundant minerals in the system (e.g., rW/rR 70 – 400 in the 20 °C, 1 bar fCO_2 model), pH remains buffered and unchanged, at near neutral values (Figure 4-4A).

The composition of the carbonates that formed in these equilibrium models differs from the carbonates observed in ALH 84001 (Table 4-5 and Figure 4-7). A general trend from high Ca to high Fe content is apparent from low rW/rR to high rW/rR. The most Mg-rich carbonates (~ 26 mol % $MgCO_3$) formed at the maximum carbonate replacement (MCR) level in these equilibrium models.

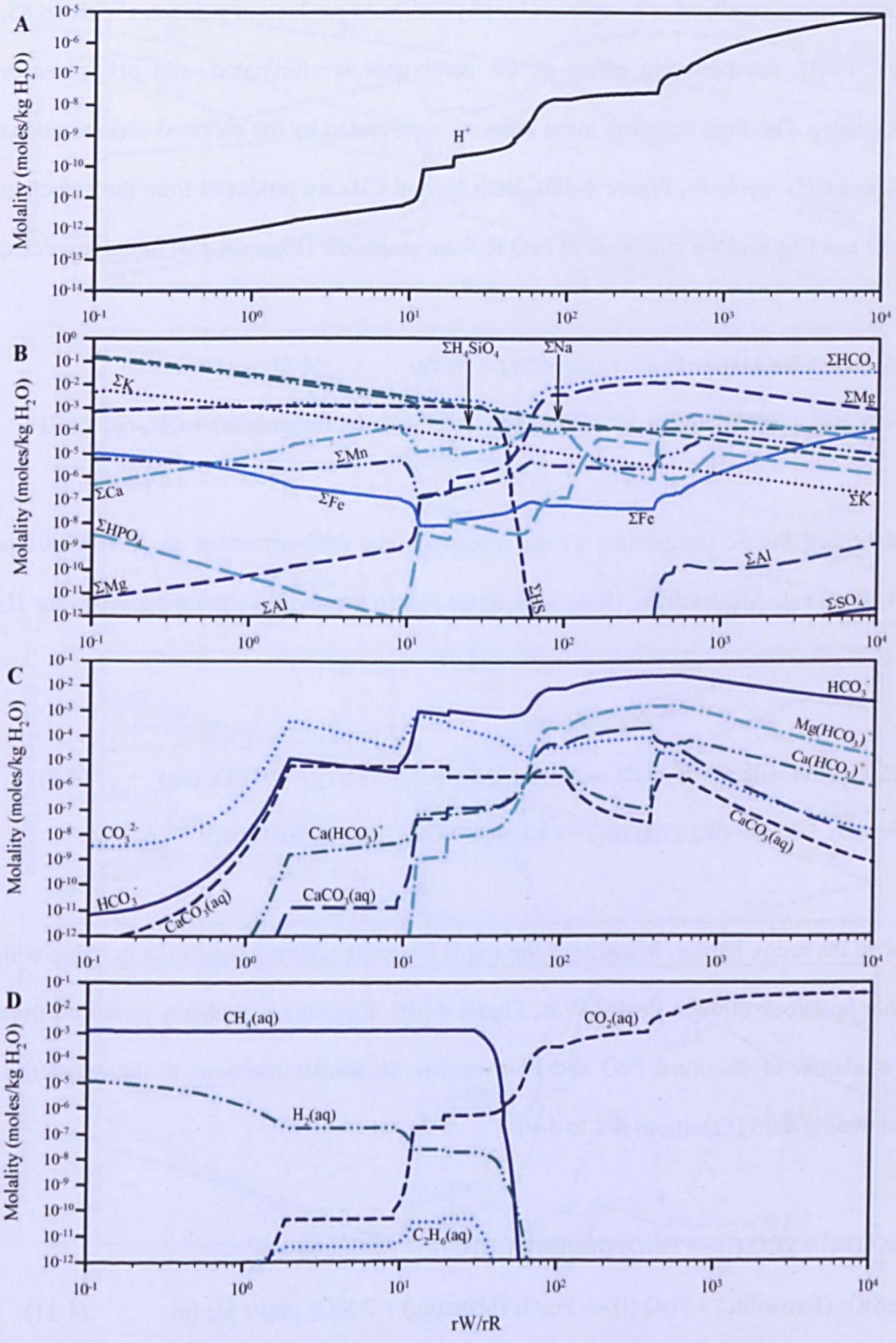

Figure 4-4. Aqueous species in the 20 °C, 1 bar fCO_2 equilibrium alteration model. A) Aqueous H concentration, B) total aqueous components, C) aqueous bearing components, D) dissolved gases.

As carbonate mineralisation is replaced by phyllosilicate production at lower rW/rR (< 85, Figure 4-6B), the buffering effect of the carbonates is eliminated, and pH increases significantly. The fluid becomes more reduced, as revealed by the elevated concentrations of H_2 and CH_4 (methane, Figure 4-4D). Both H_2 and CH_4 are produced from the reduction of H_2O and CO_2 and the oxidation of FeO to form magnetite (Figure 4-6B) in the reactions:

$$3\ FeO\ (aq) + H_2O\ (l) \rightarrow Fe_3O_4\ (magnetite) + H_2\ (g) \qquad (4\text{-}6)$$

$$12\ FeO\ (aq) + HCO_3^-\ (aq) + H^+\ (aq) + H_2O\ (l) \rightarrow 4\ Fe_3O_4\ (magnetite) + CH_4\ (g) \quad (4\text{-}7)$$

Oxidation of the Fe endmember of the orthopyroxene (orthopyroxene in ALH 84001 is ~ $En_{70}Fe_{27}$, e.g., Mittlefehldt, 1994) with water and CO_2 provides similar pathways for H_2 and CH_4 generation while precipitating magnetite:

$$3\ FeSiO_3\ (ferrosilite) + H_2O\ (l) \rightarrow Fe_3O_4\ (magnetite) + H_2\ (g) + 3\ SiO_2\ (aq) \qquad (4\text{-}8)$$

$$12\ FeSiO_3 + 2\ H_2O\ (l) + CO_2\ (aq) \rightarrow 4\ Fe_3O_4 + CH_4\ (g) + 12\ SiO_2\ (aq) \qquad (4\text{-}9)$$

Prior to the redox barrier, hematite is the stable Fe-oxide whereas magnetite is stable with further host rock titration (lower W/R, Figure 4-6B). Hematite is probably produced from the oxidation of dissolved FeO and Fe-pyroxene, in similar reactions to the magnetite-precipitating ones (Equations 4-6 to 4-9):

$$2\ FeO\ (aq) + H_2O\ (l) \rightarrow Fe_2O_3\ (hematite) + H_2\ (g) \qquad (4\text{-}10)$$

$$2\ FeSiO_3\ (ferrosilite) + H_2O\ (l) \rightarrow Fe_2O_3\ (hematite) + 2\ SiO_2\ (aq) + H_2\ (g) \qquad (4\text{-}11)$$

$$4\ FeSiO_3 + 8\ H_2O\ (l) + CO_2\ (aq) + 4\ H^+\ (aq) \rightarrow 2\ Fe_2O_3 + 4\ H_4SiO_4\ (aq) + CH_4\ (g) \qquad (4\text{-}12)$$

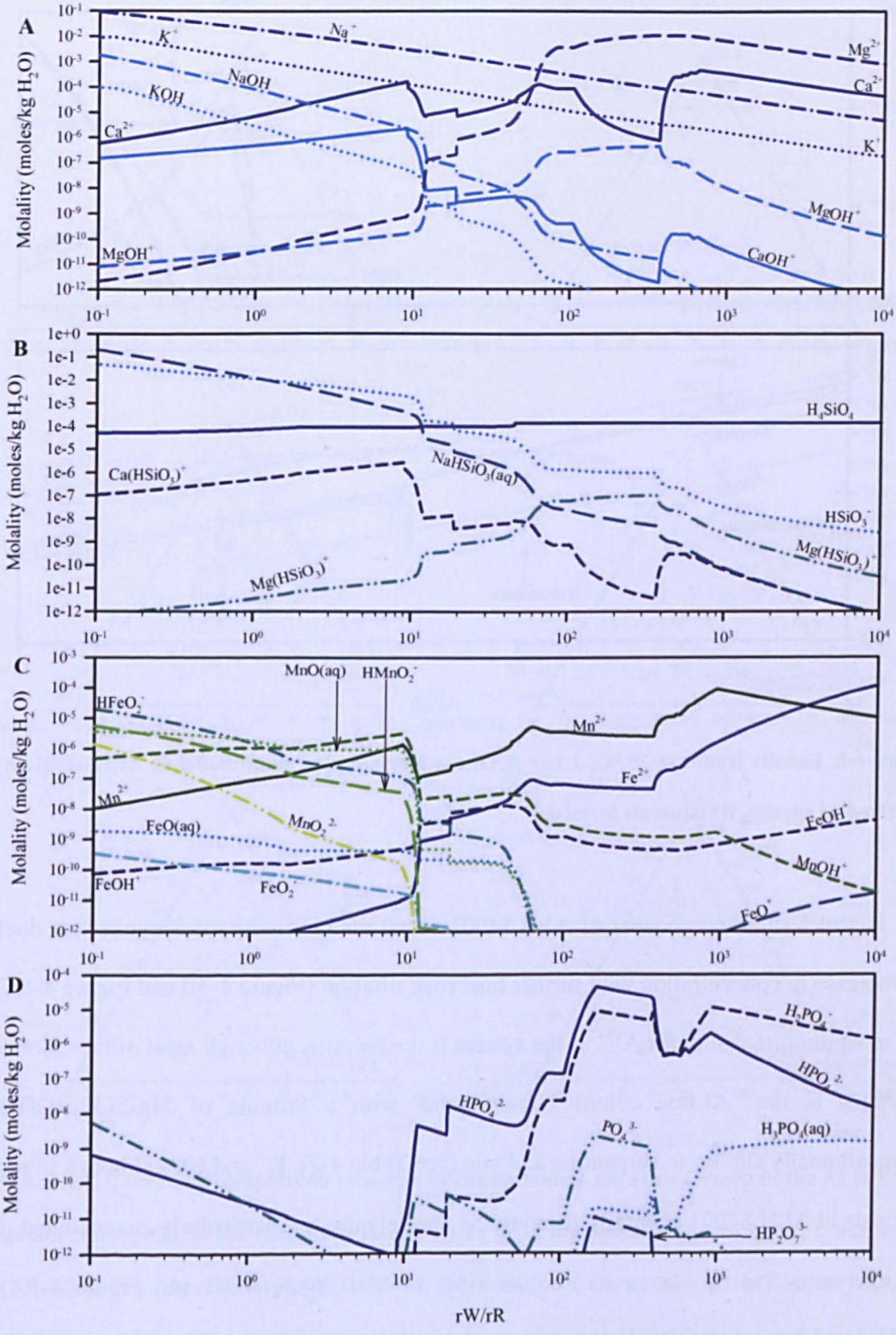

Figure 4-5. Dissolved species in the 20 °C, 1 bar fCO_2 batch alteration model. A) Alkaline and alkaline earth species, B) Si-bearing species, C) Fe and Mn species, D) dissolved phosphate species.

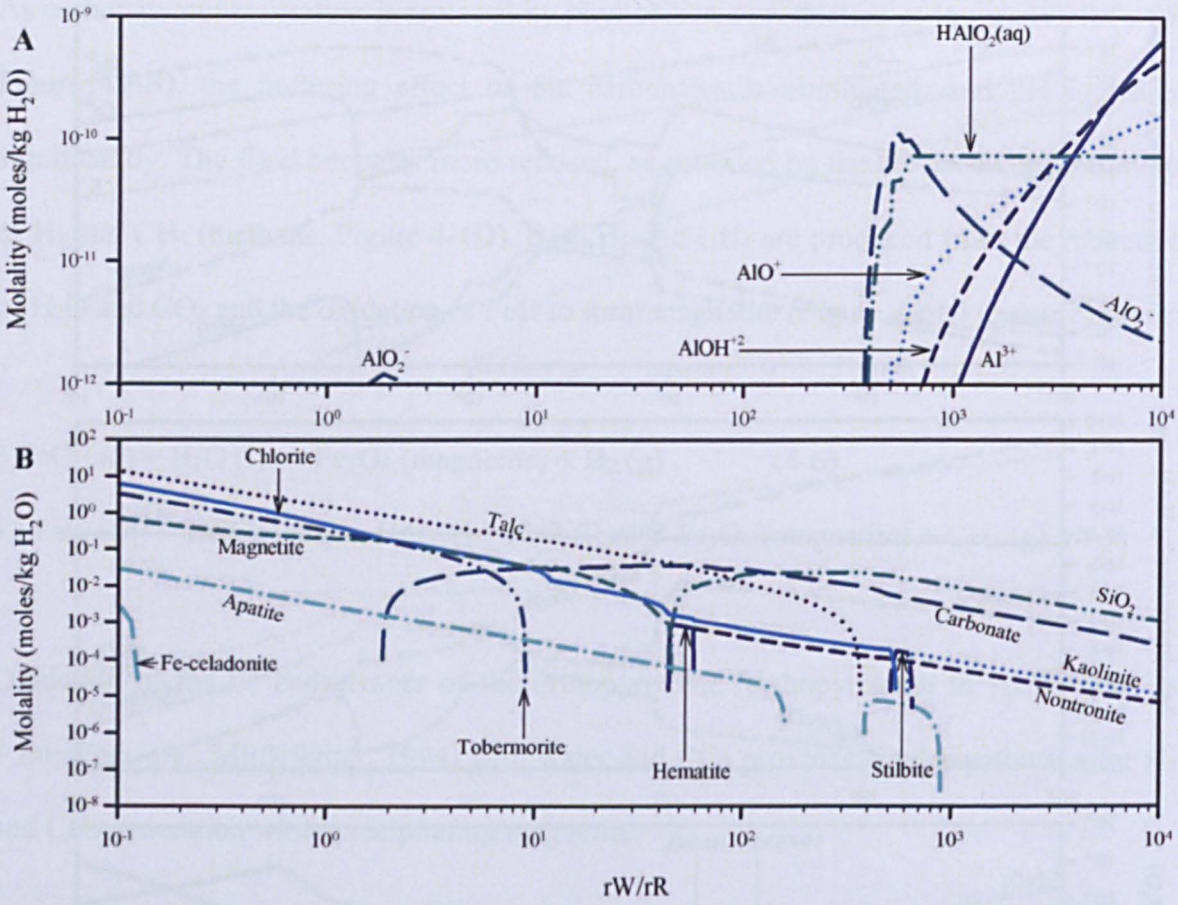

Figure 4-6. Results from the 20 °C, 1 bar fCO_2 equilibrium alteration model of ALH 84001. A) Dissolved Al species, B) minerals formed.

Al^{3+} is also a small component of ALH 84001 found mainly in the maskelynite, but does not increase in concentration with further host rock titration (Figure 4-4B and Figure 4-6A). The most important sink for Al^{3+} in the system is the chlorite, although most of the chlorite deposited is the "Al-free chlorite" endmember with a formula of $Mg_6Si_4O_{10}(OH)_8$, compositionally similar to serpentine and talc (see Table 4-2). K^+ and Na^+, although minor elements in ALH 84001 primarily forming the maskelynite, are particularly concentrated in the alteration fluid at increased titration (low rW/rR, Figure 4-4B and Figure 4-5A). Chloride salts, which would be major sinks for K^+ and Na^+, do not form due to the reactant water not containing Cl, although celadonite sequesters K^+ at very low W/R.

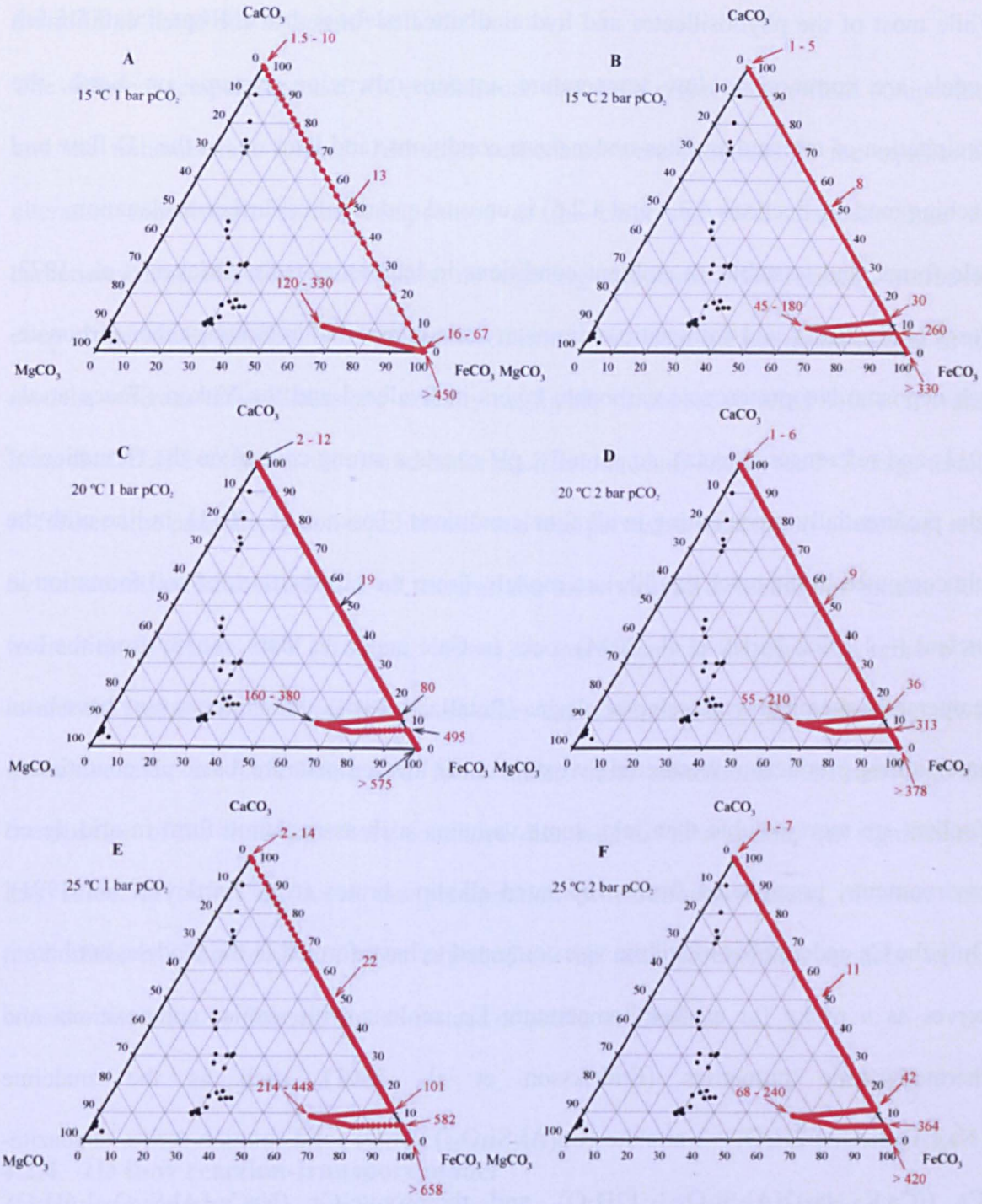

Figure 4-7. Carbonate composition ternaries of the carbonate minerals formed in the ALH 84001 equilibrium models at the conditions tested: A) 15 °C, 1 bar initial fCO_2, B) 15 °C, 2 bar initial fCO_2, C) 20 °C, 1 bar initial fCO_2, D) 20 °C, 2 bar initial fCO_2, E) 25 °C, 1 bar initial fCO_2, F) 25 °C, 2 bar initial fCO_2. Carbonate endmembers are in mol % ($MnCO_3$ is ignored here). Black dots are carbonate compositions measured by Corrigan and Harvey (2004). Red numbers are rW/rR.

While most of the phyllosilicates and hydrated silicates formed in the batch equilibrium models are common in low temperature aqueous alteration systems on Earth, the precipitation of talc and zeolites under these conditions (and later on, in the 1D flow and leaching models, Sections 4.2.4 and 4.2.5) is unusual and requires further explanation.

Talc forms, and is stable, at ambient conditions in laboratory tests (Bricker et al., 1973; Tosca et al., 2011), and authigenic sedimentary talc is reported in (among other carbonate-rich deposits) Neoproterozoic carbonate layers in Svalbard and the Yukon (Tosca et al., 2011; and references therein). Apparently, pH exerts a strong control on the formation of talc, preferentially precipitating in alkaline conditions (Tosca et al., 2011), in line with the talc computed in the batch equilibrium models. From the observations of soil formation in ancient (~ 4.2 Ga; Farley et al., 2014) rocks in Gale crater on Mars, mostly from the low temperature chemical weathering of olivine (Retallack, 2014), talc minerals may have been precipitating products of weathered pyroxene under low temperature, basic pH conditions.

Zeolites are more soluble than talc, some varieties such as analcime form in arid desert environments, precipitated from evaporated alkaline brines (e.g., Hartley et al., 1991). Only the Ca endmember of stilbite was computed to have formed in the models, but here it serves as a proxy for all low temperature Ca zeolites with similar compositions and thermodynamic properties (Fridriksson et al., 2001), such as the analcime ($Na_2(Al_2Si_4O_{12})\cdot 2H_2O$) – wairakite ($Ca(Al_2Si_4O_{12})\cdot 2H_2O$) solid solution series, chabazite-Ca ($(Ca,K_2,Na_2)2[Al_2Si_4O_{12}]_2\cdot 12H_2O$), and thomsonite-Ca ($NaCa_2[Al_5Si_5O_{20}]\cdot 6H_2O$). Furthermore, the thermodynamic database of CHIM-XPT does not contain data for chabazite and thomsonite, so precipitated 'stilbite' may replace them in the models as a general, low temperature, Ca zeolite.

4.2.3.2 Batch equilibrium models: Conclusion

The different temperature and fCO_2 conditions had little effect on the fluid composition and the minerals that formed. Although carbonates were produced in the equilibrium alteration models above, the composition of the carbonates was different from the carbonates in ALH 84001 (particularly, no high Mg-carbonates were formed). Moreover, even at the MCR, phyllosilicates and silica formed ~ 60 % of the alteration phases in the models, whereas these phases are actually negligible or absent in ALH 84001. It would seem that ALH 84001 was not altered under equilibrium conditions in the P-T range tested. A further clue pointing to non-equilibrium, and less pervasive dissolution of the host rock by an alteration fluid is the lack of textural and mineralogical evidence for intense fluid interaction in ALH 84001 (Treiman, 1998a). A mechanism to dissolve and remove (or inhibit the formation of) secondary phases other than carbonate must have been in place if the carbonates in ALH 84001 did form under these conditions. Alternatively, the composition of the fluid must have contained dissolved divalent cations but significantly less silica, in order to favour the precipitation of carbonates instead of silica and phyllosilicates. This idea is further explored in the next geochemical models, which consider alteration by flowing liquids instead of batch equilibrium.

4.2.4 1D flow reaction-transport model

As seen from the equilibrium models in the previous section, a possible medium to produce carbonates in ALH 84001 in favour of phyllosilicates at low temperature could be by increasing the divalent cation content of the alteration fluid while avoiding incorporating silica in the fluid. Non-equilibrium models may be used to simulate reaction-flow paths and open systems more resembling natural systems (see Section 4.1.2). As the alteration fluid percolates through the rock, components are leached from the host rock,

and alteration minerals that formed remain in the host and no longer react with the infiltrating fluid. Given that silica forms largely in the equilibrium models at high rWrR (Figure 4-6B), a simple mechanism to discard silica from further reaction is the continued infiltration of the fluid, leaving behind precipitated silica while the alteration front progresses.

The inputs for this model are the same as for the equilibrium models (Section 4.2.2), with the exception that the amount of rock titrated at each step is small throughout the run (~ 10^{-6} g/kg H_2O) and all solids formed are discarded and not allowed to interact with the fluid further. Temperatures and fCO_2 conditions tested in the equilibrium models did not change results significantly (particularly the composition and total amount of carbonates formed, see Section 4.2.3.1), so only a 20 °C 1 bar fCO_2 system is shown here. An added benefit of 1D flow models is that $fCO_2 < 1$ bar is also tested for their potential to precipitate phases of interest in the system, since all mineral precipitates (including CO_2-produced carbonates) are removed from the system as the fluid percolates unaltered host rock, thereby automatically reducing the fCO_2 of the fluid.

Finally, H_2O is allowed to evaporate isothermally from the system (removed in steps) at the MCR point as a hypothetical process that could eliminate the water in the system. This is in line with the purported evaporation processes that led to the formation of the carbonates according to e.g., Warren (1998) and McSween and Harvey (1998).

4.2.4.1 1D flow model results and discussion

The progressive alteration of the host rocks with continued infiltration of the reactant fluid (read from high to low iW/iR in Figure 4-8 to Figure 4-10, i.e., right to left) shows that carbonate production occurs from the onset, but prior to the maximum carbonate replacement (MCR) point, SiO_2 is the alteration mineral preferentially precipitated (at least

at iW/iR of 500 – 10000); after the stage of carbonate production, phyllosilicates (especially talc and chlorite) are produced (Figure 4-10). Interestingly, the reaction progress from higher iW/iR to lower iW/iR (i.e., increased infiltration or transport) near the MCR point shows an oscillation from Fe-rich to Mg-rich and back to Fe-rich carbonate, and finally Ca-rich carbonate at low iW/iR (Figure 4-11). Evaporation of almost all the H_2O at the MCR leads to the formation of high-Mg carbonate (Figure 4-11). A summary of the carbonate compositions at MCR is detailed in Table 4-6, and the compositional changes with progressing infiltration and evaporation are represented in a carbonate ternary (Figure 4-11).

Table 4-6. Main carbonate composition results for the 1D flow alteration model. All values given at maximum carbonate replacement (MCR) of the alteration phases formed.

1D reaction flow model	MCR* (% mass)	Water fraction	pH	Carbonate composition (mole %)			
				$FeCO_3$	MgCO3	CaCO3	MnCO3
Leaching	62.00	iW/iR 455.7 rW/rR 631.7	6.95	23.44	56.80	18.93	0.83
Evaporation, post-leaching	98.92	99.92 % H_2O evaporated	7.02	0.22	96.80	2.83	0.12

*Maximum carbonate replacement

The general secondary mineralogy formed in the 1D flow model resembles the equilibrium model both in composition and proportion, but the carbonation reaction appears to be more effective because silica exits the system and competes less for divalent cations. While CO_2, carbonate and bicarbonate ions are in solution (Figure 4-8), the carbonation reaction takes place. The limiting factor to the carbonation in this 1D flow system is the availability of dissolved CO_2 (more than $\sim 2\ 10^{-4}$ mol/kg H_2O of total dissolved inorganic carbonate (DIC), i.e., $\sum HCO_3$ in Figure 4-8B, is needed to maintain the reaction). The end of carbonate mineralisation at approximately iW/iR ~ 85 also marks a change in redox and pH conditions as the initially relatively reduced reactant fluid becomes strongly basic – the

same process that occurs in the equilibrium models (see Section 4.2.3.1). CH_4 and H_2 are also produced together with magnetite at the expense of FeO and DIC, as in the batch equilibrium models (Section 4.2.3.1)

Aqueous silica (H_4SiO_4) remains relatively constant throughout the reaction (Figure 4-9B) signifying that any SiO_2 from the fluid deposited as phyllosilicates and removed from the system is replenished by SiO_2 leached from the host rock (of ALH 84001 composition). Mg^{2+}, Ca^{2+}, Fe^{2+} and Mn^{2+} are effectively removed from the system in phyllosilicates after carbonation has stopped (Figure 4-8B, Figure 4-9A and Figure 4-10B).

Other dissolved species follow similar patterns and concentrations to the equilibrium models, including the increased K^+ and Na^+ at low iW/iR (increased infiltration).

4.2.4.2 Conclusion of the 1D flow leaching-evaporating model

It appears that the formation of carbonate minerals with the composition observed in ALH 84001 is possible via this 1D flow reaction pathway, plus an isothermal removal of liquid H_2O. Moreover, the formation of alteration minerals other than carbonate are minimised greatly (> 33 % decrease) relative to the equilibrium models at selected water to rock ratios. Of particular importance is the oscillatory carbonate composition produced with changing iW/iR (Figure 4-11).

This result can validate geological settings where these physical processes occur (low temperature fluid infiltration and evaporation) as possible sources of the ALH 84001 meteorite on Mars. Geological settings where impact debris (such as ALH 84001) was subject to seepage and evaporation of surface water on Mars have been proposed (Baker, 2001; Baker et al., 1991). Two such settings were expanded on by Warren (1998), specifically attempting to explain the carbonate formations in ALH 84001: playa lakes or

sabkhas, and the related dolocrete depositional settings. Possible settings are discussed with further evidence in Section 4.3 of this chapter.

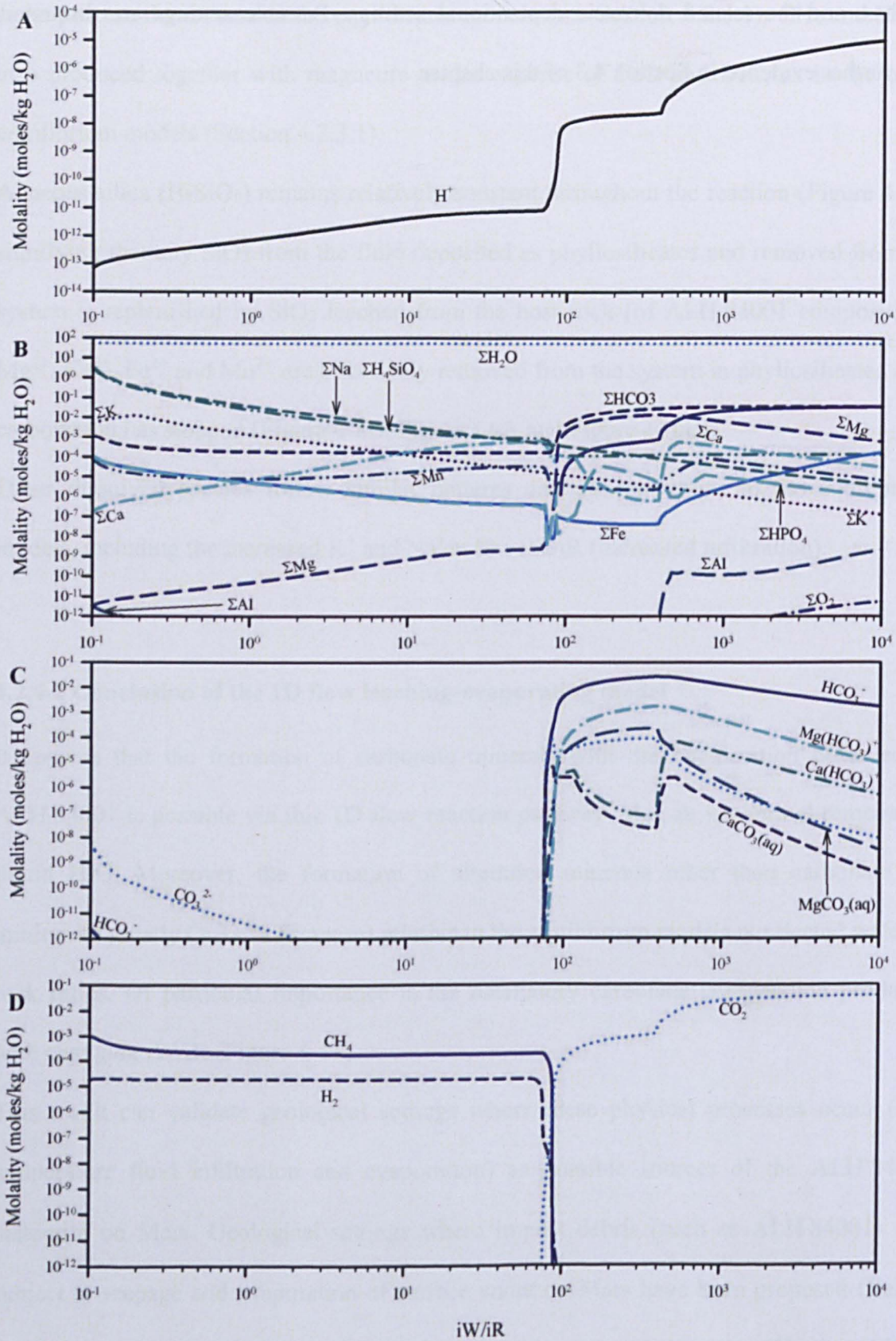

Figure 4-8. Aqueous species in the 20 °C, 1 bar fCO_2 leaching alteration model. A) Aqueous H concentration, B) total aqueous components, C) aqueous bearing components, D) dissolved gases.

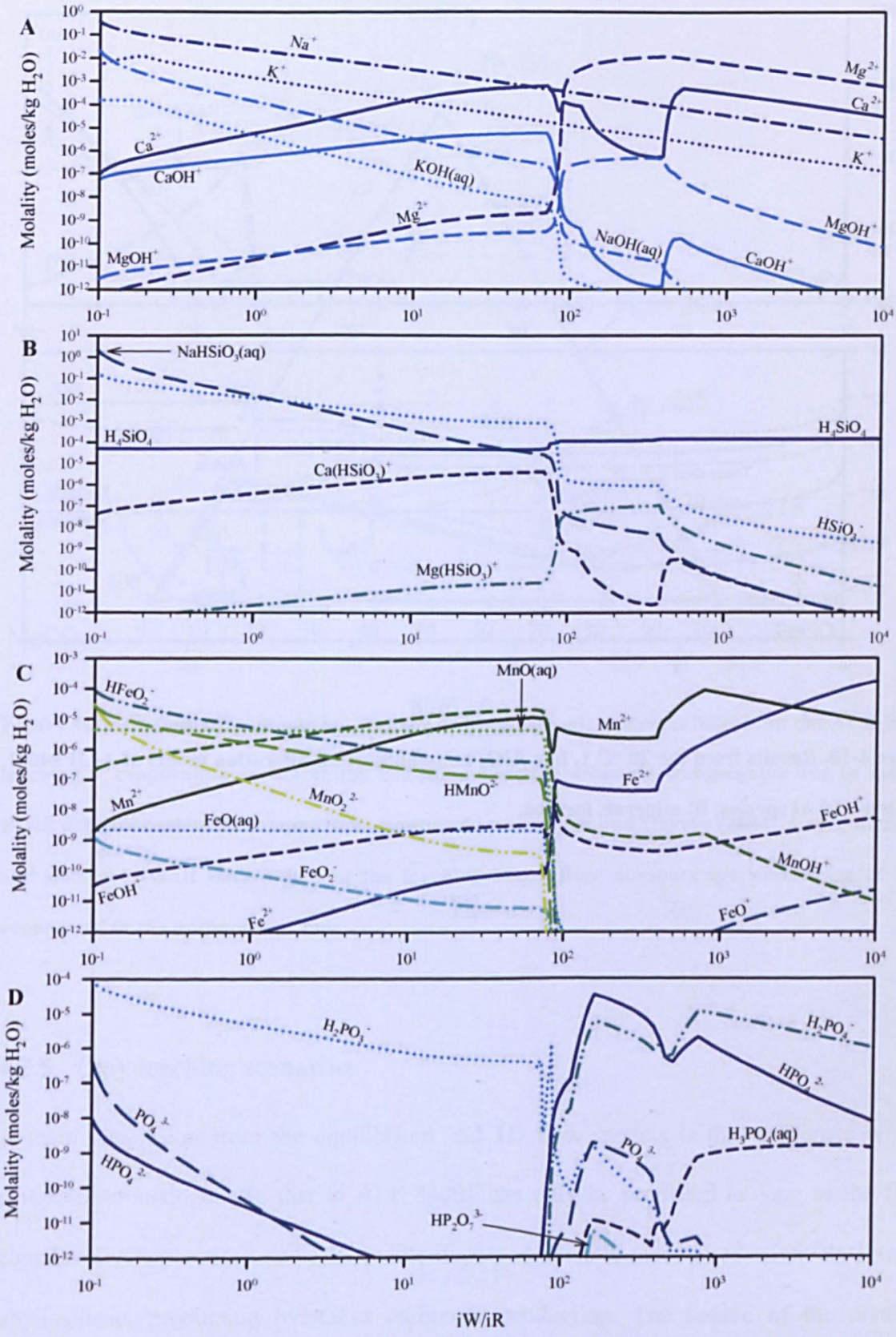

Figure 4-9. Dissolved species in the 20 °C, 1 bar fCO_2 leaching alteration model. A) Alkaline and alkaline earth species, B) Si-bearing species, C) Fe and Mn species, D) dissolved phosphate species.

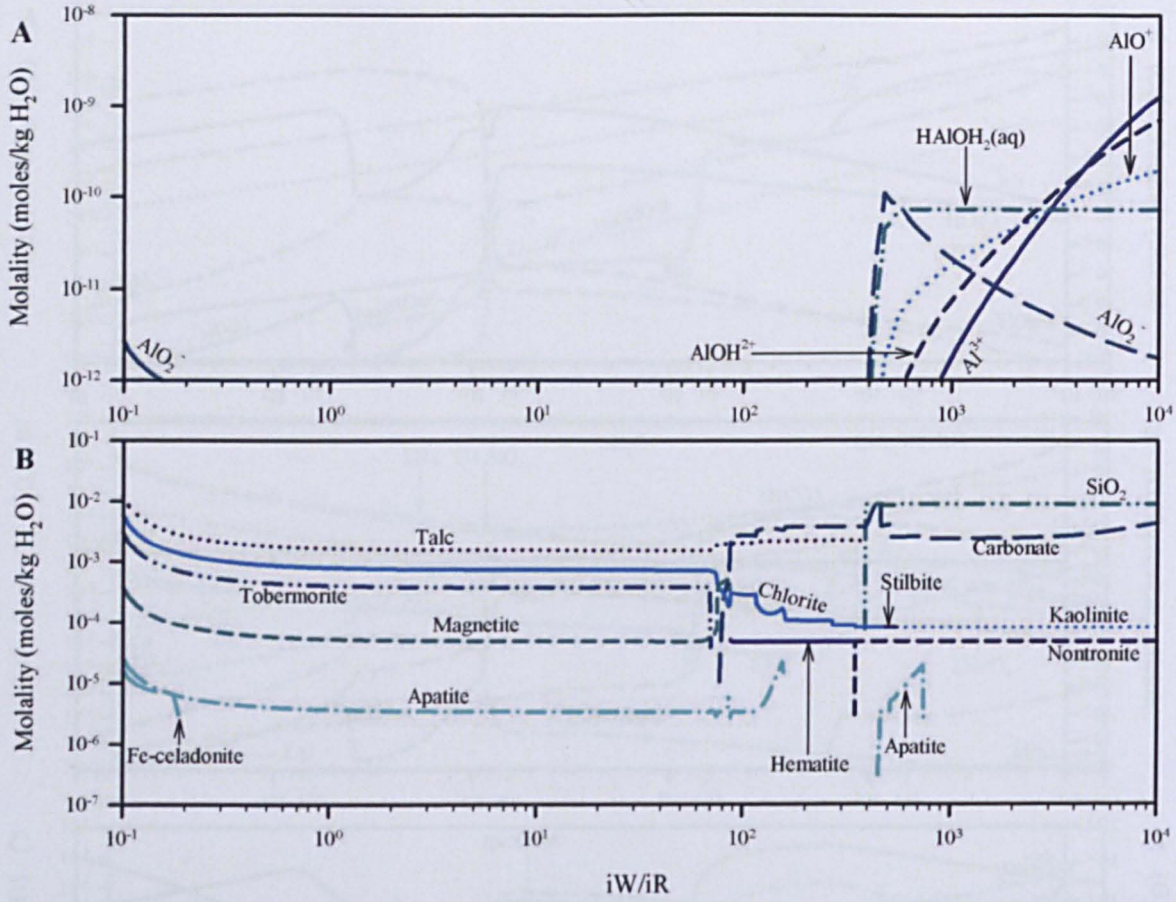

Figure 4-10. Results from the 20 °C 1, bar fCO_2 non-equilibrium alteration model of ALH 84001.

A) Dissolved Al species, B) minerals formed.

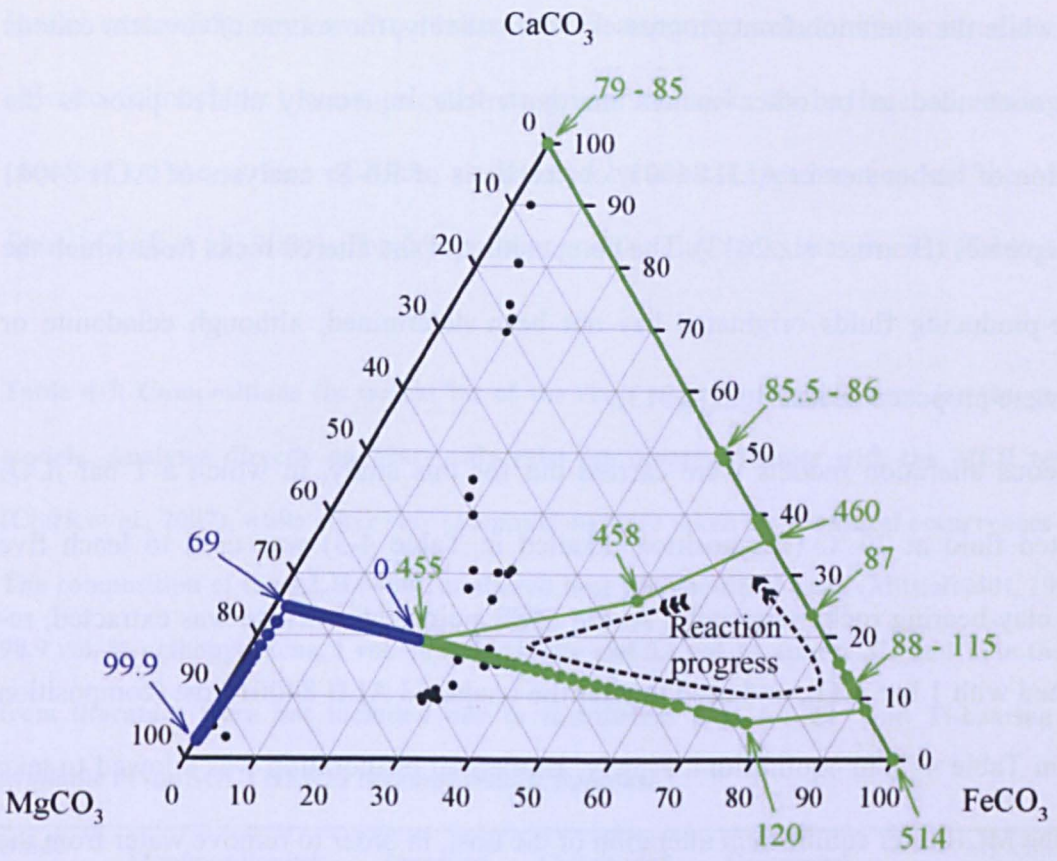

Figure 4-11. Carbonate composition ternary of the carbonate minerals formed in the ALH 84001 leaching + evaporation model at the condition tested. Carbonate endmembers are in mol %. Black dots are carbonate compositions measured by Corrigan and Harvey (2004). Green numbers and dots are iW/iR data points in the leaching stage. Blue numbers are percentage of H_2O evaporated in the evaporation stage.

4.2.5 Clay leaching scenarios

A main conclusion from the equilibrium and 1D flow models is that carbonate with a composition analogous to that in ALH 84001 can only be produced as long as the fluid contains divalent cations and DIC, while dissolved silica is maintained relatively low, or phyllosilicate production overtakes carbonate production. The source of the divalent cations in the aforementioned models was the ALH 84001 host rock itself, and the SiO_2 leached from the orthopyroxene can be extracted from the system if it precipitates (mainly

as silica) while the alteration front progresses. Alternatively, the source of divalent cations has been contended to be other ancient martian rocks, aqueously altered prior to the precipitation of carbonates in ALH 84001, on the basis of Rb-Sr analyses of ALH 84001 mineral separates (Beard et al., 2013). The composition of the altered rocks from which the carbonate-producing fluids originated has not been determined, although celadonite or smectite were proposed (Beard et al., 2013).

Five aqueous alteration models were carried out for this study, in which a 1 bar fCO_2 equilibrated fluid at 20 °C (composition detailed in Table 4-3) was used to leach five different clay-bearing rocks separately. At the MCR point, the leachate was extracted, re-equilibrated with 1 bar fCO_2, and used to alter the unaltered ALH 84001 host (composition detailed in Table 4-7) in equilibrium. Finally, isothermal evaporation was allowed to take place at the MCR after equilibrium alteration of the host, in order to remove water from the system. A schematic example of the physical setting is shown in Figure 4-12.

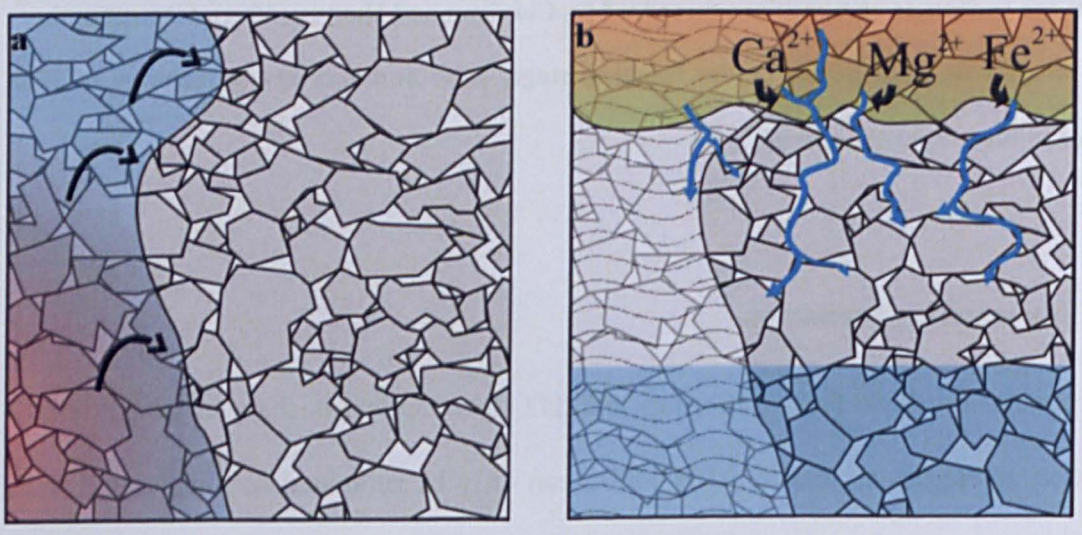

Figure 4-12. Schematic of the physical setting for the clay leaching alteration scenario. A) An event produces clays in the vicinity of the host rock of ALH 84001 (e.g., upwelling hydrothermal waters in impact breccia). B) Subsequent atmospherically equilibrated fluids leach the clays and transport cations to form carbonates at depth.

Rocks containing martian "montmorillonite", saponite, celadonite, nontronite, and Mg-chlorite (clinochlore) were selected as precursor rocks to be leached, owing to their presence on the surface of Mars, as detected by orbital spetrometers and the MER rover *Spirit* (Clark et al., 2007). The compositions of the clay rocks are given in Table 4-7.

Table 4-7. Compositions (in weight %) of the clays prior to leaching used for the geochemical models. Analyses directly on Mars only exist for montmorillonite with the MER rover Spirit (Clark et al., 2007), while other clay compositions were taken from natural occurrences on Earth. The composition of the ALH 84001 unaltered host was modified from (Mittlefehldt, 1994), using 98.9 vol. % orthopyroxene, 1 vol. % maskelynite and 0.1 vol. % apatite. Cr and Ti in the analyses from literature were not included due to insufficient data for Cr- and Ti-bearing minerals available in the SOLTHERM thermodynamic database.

Oxide	Montmorillonite[b]	Saponite[c]	Celadonite[d]	Nontronite[c]	Mg-chlorite (clinochlore)[c]
SiO_2	61.9	50.25	55.61	51.46	27.12
Al_2O_3	23.2	4.44	0.79	2.2	27.68
Fe_2O_3	2.4	0.50	17.19	24.7	0.20
FeO	N.D.[e]	N.D.	4.02	N.D.	1.24
MnO	0.2	0.02	0.09	0.03	0.54
MgO	7.0	23.81	7.26	3.27	30.96
CaO	1.7	1.7	0.21	1.45	N.D.
Na_2O	0.9	0.76	0.19	1.06	N.D.
K_2O	1.3	0.1	10.03	0.24	N.D.
P_2O_5	N.D.	N.D.	N.D.	N.D.	N.D.
H_2O[f]	N.D.	18.01	4.88	15.34	12.83

[a]Does not include the carbonate and chromite.
[b]Corrected MC-Assemblee analysis by *Spirit*'s alpha particle x-ray spectrometer at Columbia Hills, Mars (Clark et al., 2007).
[c] From Deer et al. (1992).
[d] From Foster and Washing (1967).
[e]ND = no data/not reported, or below detection limit
[f]Includes both adsorbed and crystalline water.

4.2.5.1 Results and discussion of the clay leachate scenarios

As a general result observed in all modelled scenarios, W/R has an impact on both the amount and the type of carbonates formed. Carbonate composition evolved from $FeCO_3$ at

high W/R to $CaCO_3$ at low W/R. The carbonate compositions formed under these leaching scenarios are summarised in Table 4-8.

Table 4-8. Compositions of the carbonates and carbonate weight % of secondary minerals produced in the alteration models. All values reported at maximum carbonate replacement (MCR) for each of the models.

Model code	MCR (wt. %)	W/R (mass)	H_2O evap. (wt. % H_2O)	fCO_2 (bar)	pH	Carbonate composition (mol %)			
						$FeCO_3$	$CaCO_3$	$MgCO_3$	$MnCO_3$
Leachate production with 20 °C 1 bar initial pCO_2 carbonic acid fluid									
Reactant rock									
Celadonite	28.1	182.2	N.A.	0.09	7.21	17.8	20.4	61.2	0.6
Clinochlore	6.6	16.7	N.A.	$2 \cdot 10^{-3}$	9.19	25.1	0	62.7	12.2
Montmorillonite	1.1	276.4	N.A.	0.54	6.19	0	0	0	100
Nontronite	14.1	46.2	N.A.	0.07	7.21	0	24.9	74.7	0.4
Saponite	47.5	405.7	N.A.	0.18	6.90	0	25.0	75.0	0
Alteration of ALH 84001 host with leachate									
Leachate used									
Celadonite	41.5	431.7	N.A.	0.18	7.14	59.9	9.6	28.8	1.8
Clinochlore	27.0	207.9	N.A.	$7 \cdot 10^{-3}$	7.85	65.4	8.1	24.2	2.4
Nontronite	42.9	390.7	N.A.	0.14	7.19	58.3	10.0	30.1	1.7
Saponite	46.2	505.3	N.A.	0.31	6.84	49.8	12.2	36.6	1.4
Evaporation of fluids after alteration of ALH 84001 host									
Leachate used									
Celadonite	67.3	N.A.	98.6	0.98	7.60	22.0	3.6	73.8	0.7
Clinochlore	38.4	N.A.	99.9	0.22	7.55	43.6	5.8	49.1	1.6
Nontronite	66.3	N.A.	99.6	0.99	7.93	23.0	4.3	72.0	0.7
Saponite	72.9	N.A.	99.9	0.99	7.26	16.7	4.4	78.4	0.5

*Not applicable.

The leachate compositions varied widely between the different clays, as did the carbonate compositions at MCR. Dissolved components in the leachates are shown in Figure 4-13 and Figure 4-14. As the martian "montmorillonite" leaching experiment produced a maximum of ~ 1 % carbonate mass, all of which was rhodochrosite, further experiments to alter ALH 84001 with the "montmorillonite" leachate were discontinued. Moreover,

uncertainty exists over the Mn composition of the clay minerals detected by *Spirit*'s APXS (Clark et al., 2007).

Equilibrium alteration of the ALH 84001 unaltered host, with the leachates, produced similar mineralogy throughout the reaction at different rW/rR, but slight differences are observable in the proportions of minerals (Figure 4-15 and Figure 4-16) and the carbonate compositions produced at MCR (Figure 4-17). Particularly, the celadonite leachate was the only fluid to produce microcline feldspar in the host rock in lieu of stilbite (Figure 4-15A), the clinochlore leachate was the only fluid to produce gibbsite (Figure 4-15B), and the saponite leachate was the only one not to produce nontronite in the host rock at all (Figure 4-16B).

With the celadonite, nontronite and saponite leachates altering the ALH 84001 host, carbonate replacement peaked at slightly higher values (~ 41.5 – 46.2 % mass of all secondary phases, as opposed to ~ 40 %) than in the simple batch equilibrium alteration models. The proportion of Mg-bearing carbonate was also higher (up to ~ 36.6 mol %, as opposed to 25.6 mol %, Figure 4-17). The resulting carbonate compositions in the alteration by clay leachates scenarios did not precisely match the carbonate compositions in ALH 84001, however, isothermal evaporation of the water, after alteration of the host rock by the clay leachates, produces a significant increase (> 25 %) in the relative mass of carbonates and Mg-carbonate (~ 73.8 mol % for nontronite leachates, but up to ~ 78.4 mol % for saponite, Figure 4-17 and Table 4-8), falling close to the range of carbonate compositions in ALH 84001.

The amount of Al in the fluids derived from leaching the phyllosilicates appears to affect the carbonation process. Specifically, the high Al leached from the martian Mg-chlorite prevents large amounts of carbonate from forming in ALH 84001 and favours the precipitation of phyllosilicates instead. Saponite, celadonite and nontronite all contain

lower amounts of Al, and mainly differ from each other by their Fe, Mg, K and H_2O content (Table 4-7). Fluids derived from leaching these phyllosilicates reflect the compositions of their source rocks. The fluids, in turn, determine the compositions of the carbonates formed in ALH 84001, e.g., Mg-rich saponite leachates form the most magnesian carbonates in ALH 84001, whereas more Fe-rich fluids derived from celadonite produce Fe-rich carbonates (Table 4-8).

4.2.5.2 Conclusions of the clay leaching models

While carbonate produced in the host rock by alteration with celadonite, nontronite and saponite leachates produced considerable amounts of secondary carbonate, the composition of this carbonate resembled the composition obtained from equilibrium reaction of the host rock. It was the evaporation that drove the carbonate composition to significant Mg-enrichment and higher proportions of carbonate relative to other secondary phases, although pure Mg-carbonate compositions are not attained. Further conclusions taking into account of the results of the previous models, may be found in Section 4.3 of this chapter.

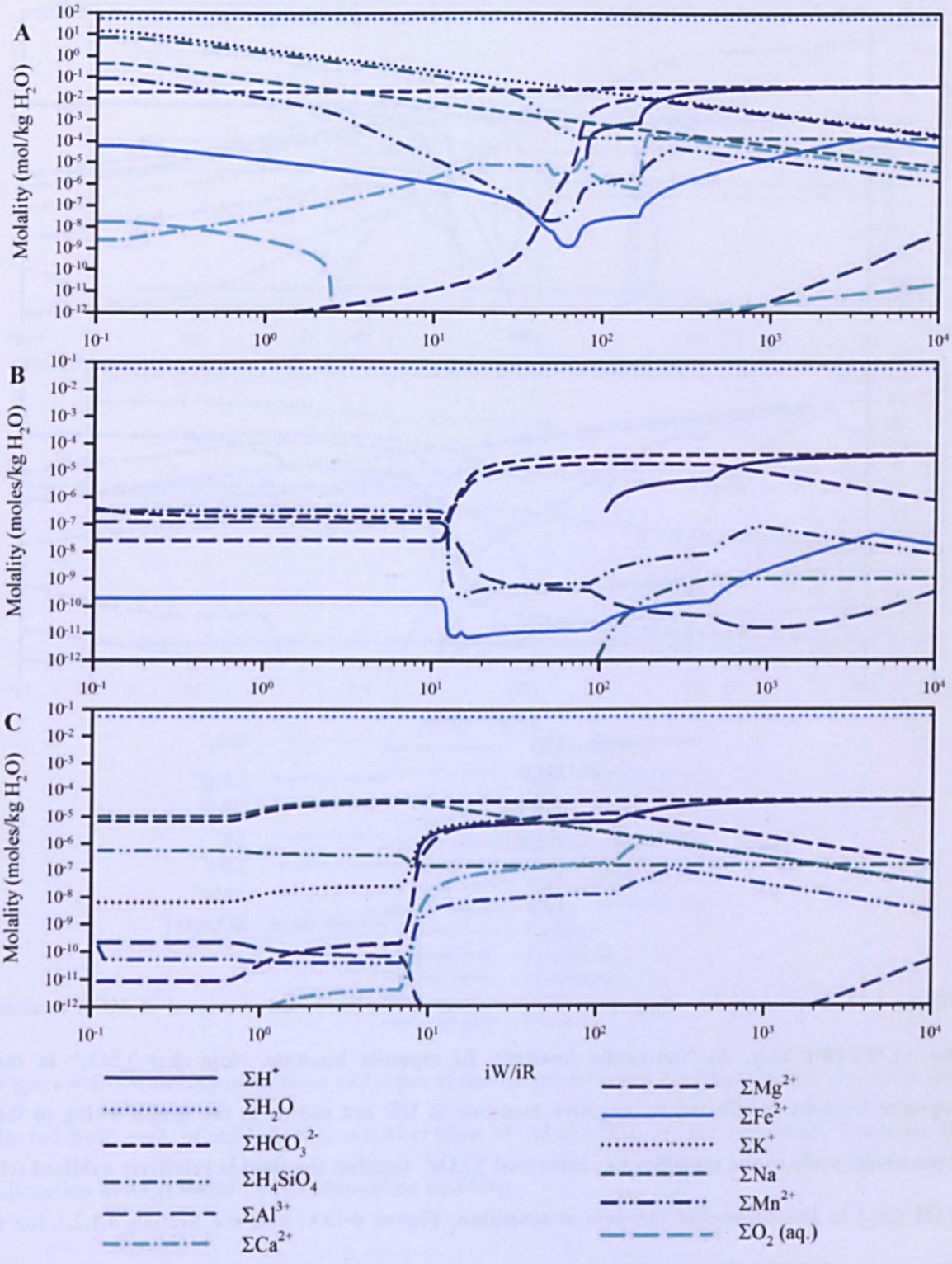

Figure 4-13. Total aqueous component compositions of the leachates, extracted at MCR to alter the ALH 84001 host. A) Celadonite leachate, B) clinochlore leachate, C) martian "montmorillonite" leachate.

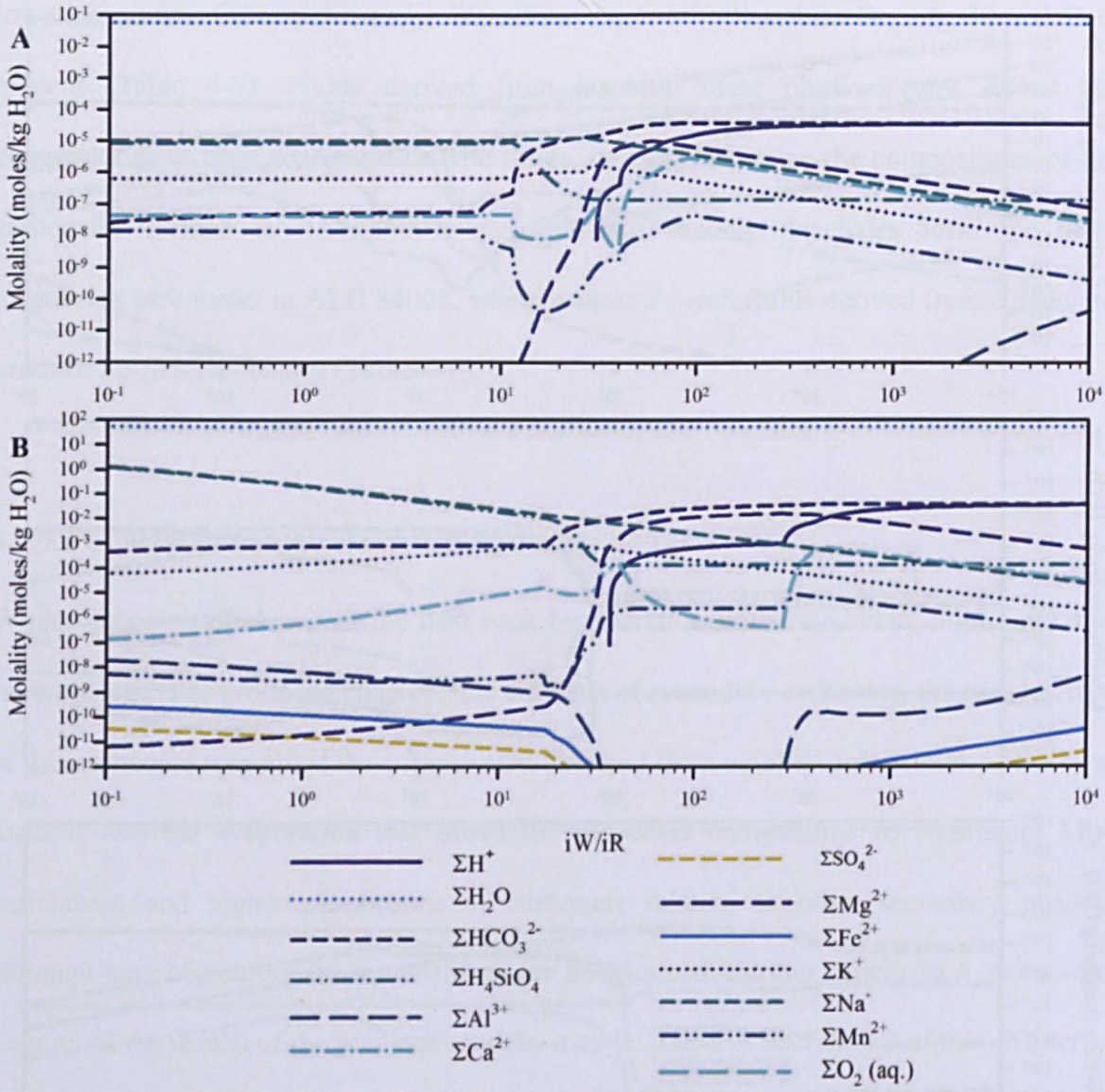

Figure 4-14. Total aqueous component compositions of the leachates, extracted at MCR to alter the ALH 84001 host. A) Nontronite leachate, B) saponite leachate. Note that $\sum SO_4^{2-}$ in the saponite leachate is affected by negative amounts of HS^- not shown in the graph owing to the logarithmic scale of the molality, i.e., increased $\sum SO_4^{2-}$ signifies the fluid is relatively oxidised (cf. $\sum O2$ (aq.) in the celadonite leachate composition, Figure 4-13A, and see Section 4.1.2.1 for a description of CHIM-XPT inputs.)

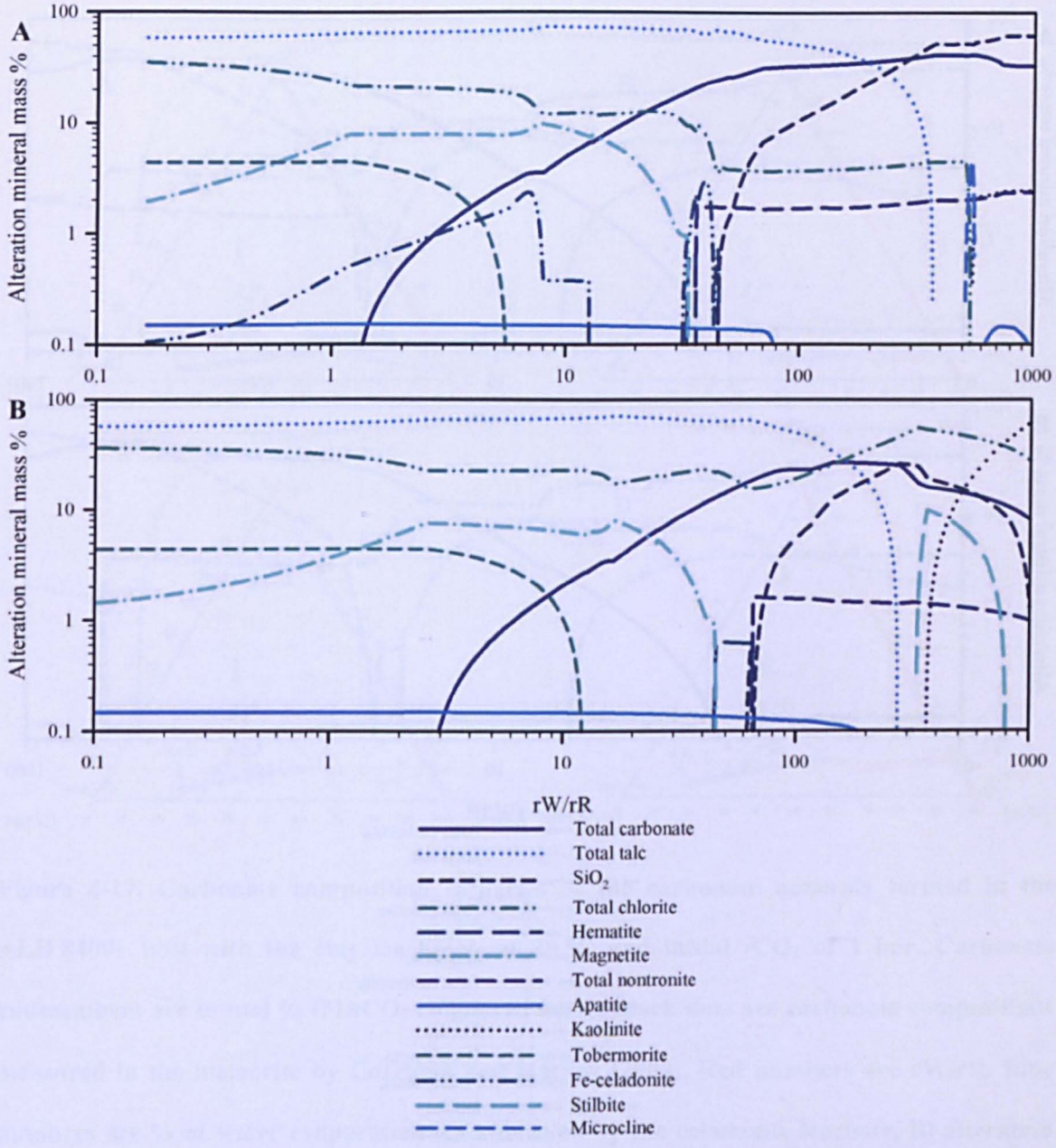

Figure 4-15. Mineral proportions and types of secondary minerals produced by the clay leachates in the host rock of ALH 84001. A) Alteration of ALH 84001 by the celadonite leachate, B) alteration of ALH 84001 by the clinochlore leachate.

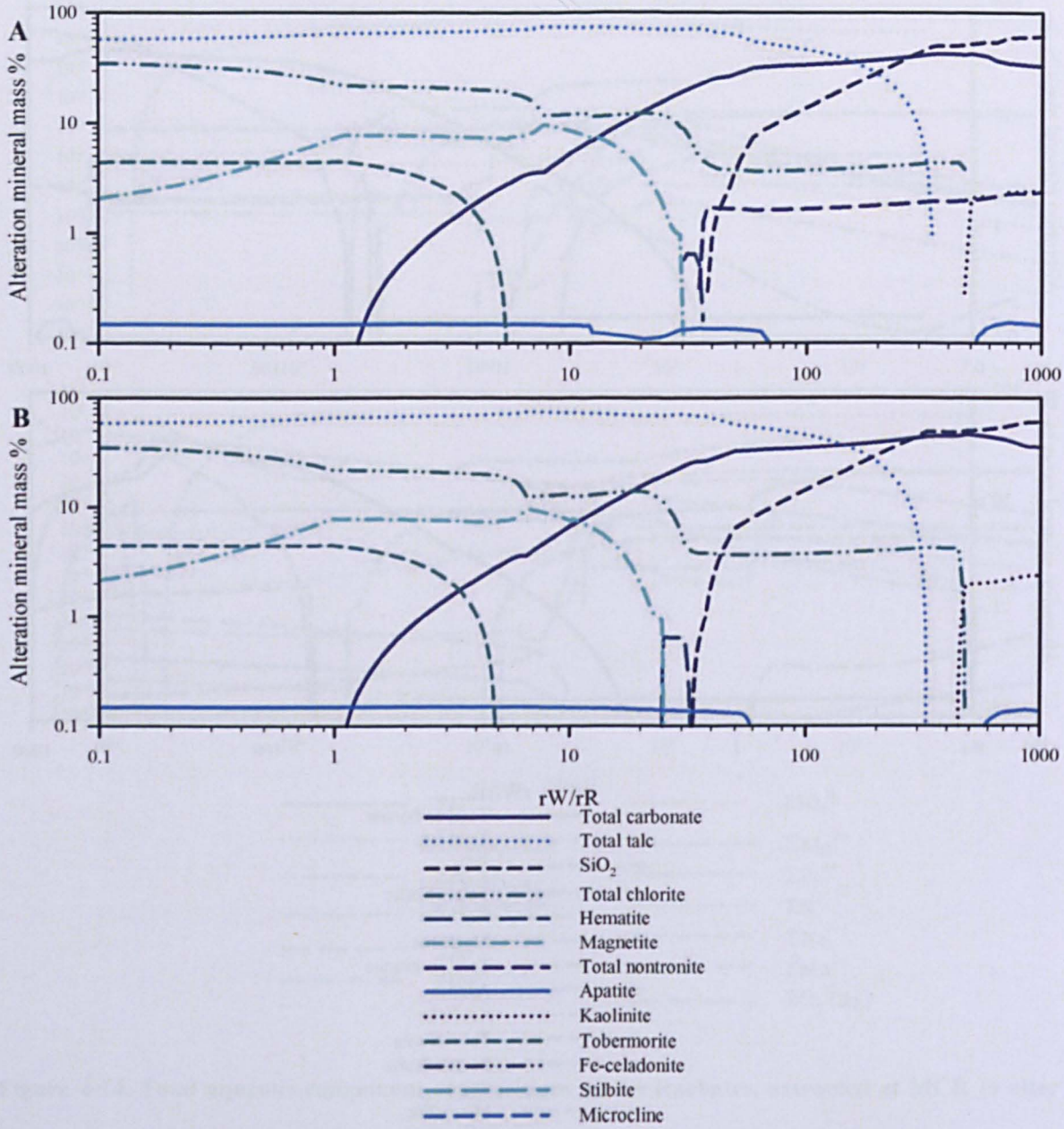

Figure 4-16. Mineral proportions and types of secondary minerals produced by the clay leachates in the host rock of ALH 84001. A) Alteration of ALH 84001 by the nontronite leachate, B) alteration of ALH 84001 by the saponite leachate.

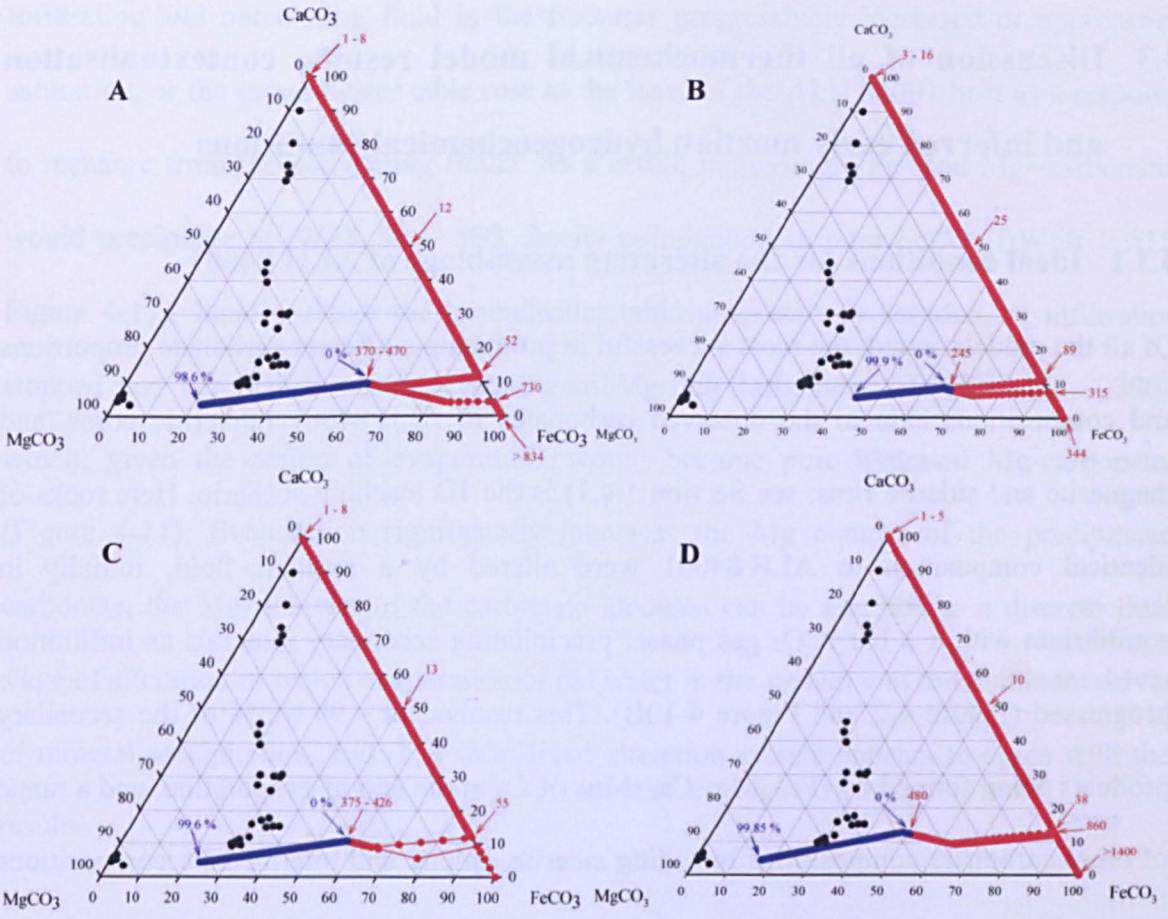

Figure 4-17. Carbonate composition ternaries of the carbonate minerals formed in the ALH 84001 host with the clay leachates, at 20 °C and initial fCO_2 of 1 bar. Carbonate endmembers are in mol % ($MnCO_3$ is ignored here). Black dots are carbonate compositions measured in the meteorite by Corrigan and Harvey (2004). Red numbers are rW/rR. Blue numbers are % of water evaporated. A) Alteration by the celadonite leachate, B) alteration by the clinochlore leachate, C) alteration by the nontronite leachate, and D) alteration by the saponite leachate.

4.3 Discussion of all thermochemical model results, contextualisation and inferred early martian hydrogeochemical conditions

4.3.1 Ideal conditions for the alteration assemblage of ALH 84001

Of all the models tested, the most successful in producing sufficient carbonate proportions and compositions akin to the observed carbonates in ALH 84001 (ankeritic cores, and magnesite and siderite rims; see Section 1.4.1) is the 1D leaching scenario. Here rocks of identical composition to ALH 84001 were altered by a reactant fluid, initially in equilibrium with a 1 bar fCO_2 gas phase, precipitating secondary minerals as infiltration progressed (Figure 4-2 and Figure 4-10B). This resulted in ~ 99 wt. % of the secondary products being formed by $(Fe_{0.2}Mg_{97}Ca_{2.8}Mn_{0.1})CO_3$ at the end of evaporation, and a range of other carbonate compositions including siderite, calcite and intermediate compositions between the three major endmembers, at a range of W/R (Figure 4-11). Moreover, the local equilibrium/1D flow reaction increased the Mg-content in the precipitated carbonate (Figure 4-11) compared to the batch equilibrium reaction (Figure 4-7); low temperature equilibrium conditions inhibit the precipitation of Mg carbonate (e.g., Hänchen et al., 2008; Saldi et al., 2009). While the sequence of precipitated carbonates (starting with $FeCO_3$ at high iW/iR, progressing to Fe-Ca-Mg carbonates at mid-high W/R, and finally calcite at low iW/iR; Figure 4-11) appears to be in a different order to the zonation pattern observed in ALH 84001 (Ca-rich cores with increasing Fe content towards the exterior, followed by siderite and magnesite rims). It is likely then, that the first fluids that arrived at the nucleation sites for the carbonates were relatively low W/R fluids (W/R ≈ 85 – 80; Figure 4-11) that had percolated through the fractures and pores of the dry host rock and the overlying dry rock that was but actively being weathered and with similar composition, and precipitated the first Ca-rich crystals of the cores. Subsequently, either the amount of

infiltrating and percolating fluid in the fractures progressively increased or approached saturation, or the groundwater table rose to the level of the ALH 84001 host as a response to recharge from the percolating fluids. As a result, increasingly Fe- and Mg- carbonates would precipitate at iW/iR 90 – 500, finally culminating in pure $FeCO_3$ (iW/iR > 515; Figure 4-11). Finally, either the groundwater table progressively receded, or infiltration stopped and percolation abated, resulting in Mg-rich carbonates (iW/iR ~455 – 300), which, given the action of evaporation, would become pure hydrated Mg-carbonates (Figure 4-11). Evaporation significantly increases the Mg content of the precipitated carbonate, the Mg-rich rim of the carbonate globules can be ascribed to a discrete final stage of alteration in which evaporation of the water in the system was the dominant driver of mineral precipitation, and so a short-lived alteration system appears to agree with the results.

4.3.2 The roles of hematite and magnetite in gas production

The optimum precipitation of carbonate was achieved in 1D flow conditions where neither hematite nor magnetite was stable (W/R ≈ 455; Figure 4-10B). But carbonate and hematite co-precipitated and were stable if percolation continued (W/R ≈ 340 – 90; Figure 4-10B), and carbonate co-precipitated with magnetite in a small W/R window (W/R ≈ 85 – 80; Figure 4-10B). As such, the hematite grains, observed ubiquitously in the carbonates of ALH 84001 (Steele et al., 2007; and also possibly observed by Raman spectroscopy in this study; Section 3.1.2) were probably co-precipitated with the (Mg-) ankerite cores, but the small window in which carbonates and magnetite were both stable suggests that the magnetite *in the carbonates* may have formed in a separate event, e.g., from the post-impact transformation of siderite into magnetite, as suggested by Brearley (2003). Shock-metamorphism, which almost certainly occurred after the deposition of the carbonates, is

evidenced by fragmentation of the carbonates and emplacement of feldspathic melt glass within them (Treiman, 1998a, 1995). This would also have had the effect of transforming carbonates to macromolecular carbon and graphite (Steele et al., 2012a, 2007), and, relevant to the results presented here, dehydroxylating the hydrated Mg-carbonates to form magnesite (recall that no magnesite was allowed to precipitate; see Section 4.2.1). Conversely, as magnetite *did* precipitate in the 1D flow model, albeit far from the peak in carbonate production (Figure 4-10B, and Equations 4-6 to 4-9), the magnetite crystals in ALH 84001 may have formed by direct secondary precipitation, but do not necessitate transportation into the host rock by allocthonous fluids (Thomas-Keprta et al., 2009). Much work has been carried out to determine the origin of the magnetite crystals in ALH 84001 (Barber and Scott, 2002; Brearley, 2003; Golden et al., 2004; Scott, 1999; Thomas-Keprta et al., 2009, 2000; Treiman and Essene, 2011). Here, an abiogenic, low temperature pathway from the reduction of dissolved FeO and Fe-pyroxene, involving the production of CH_4 and H_2, is able to precipitate magnetite (Figure 4-10B) without direct participation of carbonate minerals in the reaction (Equations 4-6 to 4-9). Incidentally, magnetite that formed in the reduction reaction could further catalyse the reduction of CO_2 to form hydrocarbons (Zolotov and Shock, 1999).

Similar reactions occur in terrestrial weathering of ultramafic rocks at low temperatures (25 °C) which also yield H_2 and CH_4 (Palandri and Reed, 2004). While inorganic CH_4 reaction kinetics are generally inhibited under equilibrium conditions at low temperatures, as modelled in the batch equilibrium scenarios (Section 4.2.3.1), the percolating fluid in the 1D flow model was in chemical disequilibrium with the bulk rock. Equilibrium was only achieved locally (~ 10^{-6} kg unreacted rock/kg leaching fluid) as the fluid percolated the rock, and was immediately in disequilibrium with any precipitates produced. It is worth noting that low temperature abiogenic production of H_2 and CH_4 on Mars has also been

proposed from the serpentinisation of olivine-rich rocks and the reduction of CO_2 (e.g., Oze and Sharma, 2007, 2005), and laboratory evidence shows that CH_4 can be produced from the dissolution of forsterite at 30 °C (Neubeck et al., 2011). Furthermore, the *Curiosity* rover has recently confirmed the presence of extant, variable, CH_4 at Gale Crater (Webster et al., 2015). The possible abiotic production of CH_4 on early Mars has been discussed extensively, particularly in its role and abundance in the atmosphere (e.g., Chassefière and Leblanc, 2011a, 2011b). Similarly, H_2 and CO_2 have been advocated as potential greenhouse agents in the early martian atmosphere which enabled water to stay above the freezing point (e.g., Hirschmann and Withers, 2008; Ramirez et al., 2014).

4.3.3 Hydrated minerals as precursors to the alteration of ALH 84001

Regarding the role of phyllosilicate leachates, producing relatively large quantities of Fe-Ca carbonate compositions in the ALH 84001 host from derived fluids is possible for celadonite, saponite, and nontronite leachates, but pure $MgCO_3$ carbonate was not produced with these leachates (Figure 4-17). Although the Rb/Sr systematics in ALH 84001 point to pre-existing phyllosilicates as the origin of $^{87}Rb/^{86}Sr$ enrichment (Beard et al., 2013), on the basis of the reaction models alone, the hypothetical original phyllosilicate can only be described as Mg-rich and Al-poor, with saponite as the better candidate. Evaporation significantly increased the Mg content of the precipitated carbonate (Figure 4-17), so the Mg-rich rim of the carbonate globules can be ascribed to a discrete final stage of alteration, in which evaporation of the water in the system was the dominant driver of mineral precipitation. Consequently, a short-lived alteration system appears to agree with the results. As it stands, an origin for the carbonates in ALH 84001 from phyllosilicate leachates is not necessary. In fact, the proportion of carbonate and its composition are better explained by a leachate of an ALH 84001-type orthopyroxenite

(Section 4.2.4). The Mg-rich precursor carbonates, huntite and hydromagnesite, are required prior to dehydroxylation and transformation to the observed magnesite, but this may also explain the Sr enrichment observed in the meteorite by Beard et al. (2013). Though the weathering of Mg-silicates may increase Sr/Ca ratios of the leaching fluids, Sr also substitutes readily for Ca in the relatively open-latticed structure of huntite, in comparison to magnesite (Dollase and Reeder, 1986; Stanger and Neal, 1994), and as such, an enriched Sr source may not be required. Unfortunately, recognising whether the Mg-carbonate in ALH 84001 is recrystallized, post-depositionally dehydrated huntite and hydromagnesite difficult. On Earth, huntite occurs as evaporites, near-surface weathering products and as fine-grained diagenetic minerals in dissolution pores of ultramafic rocks (e.g., Akbulut and Kadir, 2003; Kinsman, 1967; Stanger and Neal, 1994), but is metastable (Garrels et al., 1960; Kinsman, 1967), and is replaced in time by magnesite-dolomite or dolomite-calcite, with no diagnostic habits or pseudomorphs preserved (Kinsman, 1967). Hydromagnesite occurs in similar environments, and is also known as a terrestrial alteration product derived from Mg-silicate dissolution in surfaces and fractures of Antarctic meteorites (Velbel et al., 1991), and was also contended to be pre-terrestrial in the martian fall Chassigny (Wentworth and Gooding, 1994). An indication towards the current existence of pre-terrestrial hydromagnesite in ALH 84001 came from H isotope studies. Eiler et al. (2002a) contended that the high δ^2H_{SMOW} in ALH 84001 resided in an indigenous martian salt phase, possibly hydromagnesite. The existence of hydromagnesite currently in the meteorite would imply that the bulk meteorite did not experience the temperature required for the complete dehydroxylation and recrystallisation of hydromagnesite to magnesite (~ 520 °C; Hollingbery and Hull, 2010) since the time the hydromagnesite precipitated. Hydromagnesite has also been predicted from theoretical

modelling to form part of the near-surface evaporitic assemblage of early Mars (Catling, 1999).

4.3.4 Comparison to other geochemical models

Other workers have investigated the distinctive carbonates of ALH 84001 with thermochemical models. Kopp and Humayun (2003) argued that dissolution of the carbonate concretions, subsequent to their deposition on Mars, produced the characteristically zoned siderite-magnesite-siderite rims. They also argued that this process plausibly occurred in Antarctica, during the terrestrial residence time of the meteorite. With the use of a kinetic dissolution-precipitation model, they contended that low amounts of meltwater infiltrating the rock dissolved Mg and Fe from the native carbonates, and subsequent sublimation of the fluids at low fO_2 ($< 10^{-69}$ bar at 25 °C) produced the magnetite crystals and carbonate rims. While a compelling argument, it should be noted that hematite, as computed to co-precipitate with high Mg-carbonates in the 1D flow model here (Figure 4-10B), has also been reported in the carbonate rosettes of ALH 84001 (Steele et al., 2007), signifying that fO_2 conditions may have been different from those described in their model. As far as can be ascertained, no other carbonate-bearing Antarctic meteorite, martian or otherwise, has developed similar magnesite rims around pre-existing carbonate, despite the relative abundance of Antarctic hydrous Mg-carbonates on fusion crusts and cracks of chondrites (e.g., Velbel et al., 1991), which do not occur in ALH 84001. (It is worth noting, however, that the Tatahoiune diogenite does contain terrestrial calcite "rosettes", formed over 60 years of exposure to warm semi-arid conditions; Barrat et al., (1999).) Niles et al. (2005) also offered evidence against an Antarctic origin for the magnesite, based on its high $\delta^{13}C$ values. Finally, Niles et al., (2009) and van Berk et al., (2011) suggested that it was decreasing pCO_2 that caused the carbonates in ALH 84001 to

precipitate. In a broad sense, the 1D flow model carried out here is consistent with theirs, given that the peak of carbonate production (Figure 4-10B) occurred at fCO_2 = 0.12 bar (Table 4-6), compared to the initial reactant fluid with fCO_2 = 1 bar. However, the mechanism described here to remove CO_2 from the system, consisted of progressive alteration by percolating fluids, rather than an externally controlled parameter. Further, the role of leachates of varying compositions, as well as the role of evaporation on the secondary assemblage, have also been considered in the models presented here. Notably, near-neutral pH and relatively low temperatures were required to produce carbonates in all the thermochemical models.

4.3.5 Comparison to terrestrial systems

On Earth, relatively low temperature (~ 17 to 300 °C) silica-carbonate alteration systems produce carbonates of analogous compositions to those observed in ALH 84001 from the CO_2-rich hydrothermal fluid weathering of serpentinites (Ashley, 1997; Barnes et al., 1973). A range of resulting rock compositions are observed in these systems, from nearly pure silica to nearly pure Mg-rich carbonate deposits, often in conjunction with talc and chlorite, similar to the precipitates in the 1D flow model (Figure 4-10B). On the basis of O and C isotope systematics, the source of H_2O in silica-carbonate alteration systems is likely to be both meteoric and metamorphic, whereas the CO_2 is probably metamorphic or magmatic (Ashley, 1997; Barnes et al., 1973). In contrast, in this study, both the H_2O and CO_2 were considered to be meteoric/atmospheric (in line with numerous stable isotope and noble gas observations by other authors and in this study, see Sections 1.4.2.2 and 3.1.3).

4.3.6 Comparison to ancient martian systems

It is useful to discuss previous work on martian aqueous systems and observed alteration assemblages to ascertain the validity of the models and understand the implications of the results of the models. Filiberto and Schwenzer (2013) investigated the potential alteration phases resulting from the alteration of the ancient basalt at Home Plate (Columbia Hills, Gusev Crater). At 13 °C, assemblages were dominated by chlorite or nontronite across all W/R, and only some carbonate (up to ~ 25 wt. % of all secondary products) in fluids with high dissolved initial DIC (or $\sum HCO_3$, approximately one order of magnitude higher than used in these models; Table 4-3). On a first basis, their modelled assemblages appear similar to those modelled here in the batch equilibrium scenarios. Importantly, the Home Plate basalt composition and the reactant water that they used contained Cl, and significantly more S, which probably suppressed higher carbonate production in favour of other secondary phases, which is an unlikely scenario for ALH 84001. Van Berk and Fu (2011), and later, van Berk et al. (2012), carried out 1D diffusive mass transport models on olivine-rich host rocks which effectively reproduced the carbonate assemblages at the Comanche outcrop at Gusev Crater ($Mg_{0.62}Fe_{0.25}Ca_{0.11}Mn_{0.02}CO_3$; Morris et al., 2010), and also the carbonates and stratigraphically lower phyllosilicates at Nili Fossae (Ehlmann et al., 2008). The models presented in this thesis, in which infiltrating fluids first precipitated mainly silica, then carbonates, and finally progressed to phyllosilicates, are broadly consistent with theirs. This indicates that similar pCO_2 and temperature conditions, as well as fluid chemistries, prevailed at the site where ALH 84001 was altered, and also at the Comanche outcrop and Nili Fossae. Their phyllosilicate assemblages (van Berk et al., 2012) differed somewhat from the assemblages calculated here: at Nili Fossae, they computed talc, diaspore, chrysotile, greenalite, prehnite, and minor chlorite precipitation at depth, whereas in this study, talc, chlorite, tobermorite and minor amounts of magnetite,

apatite and ferroceladonite precipitated with further percolation (Figure 4-10B). This difference is probably driven by the different host rock compositions, since ALH 84001 is virtually olivine-free, compared to the olivine-rich host rocks of van Berk and Fu (2011). Another significant difference between their models and the models in this study concerns the progression of carbonate compositions. In this study, the carbonates invariably start at the Fe endmember composition at high W/R, and progress along the Fe-Ca carbonate join with further percolation (via an excursion to higher Mg content; Figure 4-11). The carbonate compositions of van Berk and Fu (2011) progress from Fe- to Mg- carbonate near the Fe-Mg join and then towards the Ca endmember along the Mg-Ca join, signifying that ankerite compositions, as present in the cores of the rosettes in ALH 84001, would be absent. Recent equilibrium thermochemical models of the Comanche outcrop carbonates (Ruff et al., 2014) also suggested that the carbonate formed from the leaching of the nearby olivine-rich Algonquin outcrop. Finally, mineralogical analyses at Yellowknife Bay in Gale crater revealed that mudstones there contained sulfates (basanite and anhydrite) magnetite, hematite, and smectites (possibly saponite) among other components (Vaniman et al., 2014). While hematite and magnetite occur in ALH 84001, and smectite (nontronite) was modelled to form both while carbonates were, and were not, stable (Figure 4-10B), the presence of extensive sulfates at Yellowknife Bay argues against a direct association with carbonate formation. This is further expounded by recent thermochemical models (Bridges et al., 2015) in which low temperature alteration of the unaltered "Portage" soil analysed at Gale crater (Bish et al., 2013) resulted in the detection of mudstone mineralogy (Vaniman et al., 2014), but no carbonates, possibly indicating a low pCO_2 environment.

4.3.7 Final remarks

The results support a low temperature (~ 20 °C) and < 1 bar atmospheric fCO_2 formation of the carbonates in ALH 84001 by relatively local fluids which leached rocks identical in composition to ALH 84001. Mg-enriched carbonate is likely to have precipitated as a consequence of evaporation of the leachates.

While the possibility of a higher temperature for the aqueous alteration cannot be ruled out on the basis of the thermochemical models carried out here alone, the models show that dynamic changes in W/R and a fluid derived from the concurrent alteration of martian crust, coupled with subsequent evaporation are able to replicate the observed carbonate composition. The leaching — followed by evaporation — also matches the observed compositional zoning of carbonate, the presence of hematite and magnetite, and lack of clay minerals or other alteration phases at the peak of carbonate formation. Testing the model in controlled laboratory conditions was considered beneficial, and is explored in the next chapter. Further conclusions, with relation to the other studies carried out and results obtained as part of this thesis are explored in Chapter 6.

5 Characterisation and experimental alteration of ALH 84001 analogues

5.1 Introduction

Following the insights gained from the thermochemical models (Chapter 4) on the geochemical and physical processes governing the formation of secondary carbonates in ALH 84001, experiments were carried out in order to test the results.

To summarise, according to the results of the thermochemical models, a 20 °C fluid initially equilibrated with 1 bar fCO_2 can produce Fe-Ca-Mg carbonates in the orthopyroxenite host, by kinetic dissolution-precipitation reactions, simulating a non-equilibrium reaction flow pathway (leaching by infiltration). Ideally, the initial water to rock ratio (iW/iR, see Section 4.1.2.2 for water to rock ratio definitions) at which the carbonates are produced is ~456 and a resulting or observed W/R (rW/rR) of ~632, so each gram of water must have dissolved and been in contact with ~456 g of host rock while precipitating secondary minerals along the fluid's pathway, until it produced the maximum amount of Mg-carbonates at a rW/rR of ~635.

5.1.1 Purpose

Identifying a terrestrial rock that is geochemically similar to a martian meteorite (i.e.,, a Mars analogue) can help in understanding the chemical and physical processes that lead to the meteorite's formation, especially if the analogue's geological context on Earth is well known. In the case of experimental procedures to form analogues, the physical conditions

are generally controlled and known to a higher degree of certainty than can be inferred from natural systems.

The aim of carrying out aqueous alteration experiments of ALH 84001 host rock analogues was to validate (or understand the limitations of) the results of the ideal carbonate-forming geochemical model illustrated in Chapter 4, and to derive how plausible the model is in supposed early martian conditions.

5.1.2 Previous and related work

Numerous alteration experiments have been carried out by other authors to understand the formation of carbonates on or near the surface of Mars; a summary of the most relevant to ALH 84001 is given in Table 5-1.

Table 5-1. Summary of past alteration experiments under presumed martian conditions. See text for details.

Reference*	Temperature (°C)	pCO_2 (bar)	Host rock†	Time (days)	iW/iR	Fluid	Secondary minerals	
							Carbonates	Other‡
G2000	25	?	None	1 – 3	n/a	Static	Fe-Ca-Mg	Discarded
G2001	150	~ 4.8	Aug	1 – 3	?	Static	Fe-Ca-Mg-Mn	Mt, + discarded
Ba2000	23	1 – 2	SNC	4 – 7	200	Flow	Ca-Fe-Mg	Silica, Qtz
	75	1 – 2	SNC	4 – 7	200	Flow	Ca-Fe-Mg	Silica, Qtz, magh, hem, clay
Bu2004	3	1	SNC	210	n/a	Static	n/a	n/a
	25	1	SNC	210	n/a	Static	n/a	n/a
	35	1	SNC	210	n/a	Static	n/a	n/a
C2004 C2006	15 – 20	0.8	α-Fe	19 – 117	'low'	Gas	Fe	Mt.,goeth
	15 – 20	0.8	Opx	1460	'low'	Gas	No	No
D2012	15 – 20	0.8	Opx + FeS	1460	'low'	Gas	No	Sulf, goeth
	15 – 20	0.8	Ol	1460	'low'	Gas	Mg	No
D2014	45	1.5	Ol	95	10	Static, agitated	No	Mg-smect, silica

*References are: G2001, G2000: Golden et al. (2001, 2000); Ba2000: Baker et al. (2000); Bu2004: Bullock et al. (2004); C2006, C2004: Chevrier et al. (2006, 2004); D2012: Dehouck et al. (2012); D2014: Dehouck et al. (2014).

†Host rock abbreviations are: Aug: augite; SNC: SNC meteorite-like terrestrial analogue rock or mineral assembly; α-Fe: body-centred cubic, "low-T" allotrope of elemental pure iron; Opx: orthopyroxene; FeS: iron sulfide; Ol: olivine.

‡Abbreviations for other secondary minerals are: magnetite (Mt), quartz (qtz), maghemite (magh), hematite (hem), sulfate (sulf), goethite (goeth), Mg-smectites (Mg-smect).

Of these experiments, the studies by Golden et al. (2001, 2000) have specifically addressed the carbonates in ALH 84001. Golden et al. (2000) successfully synthesised zoned carbonate rosettes with CO_2-saturated briny solutions (with varied amounts of $CaCl_2$, $MgCl_2$, $FeCl_2$ and $MnCl_2$) and submicron-sized magnetite crystals in hydrothermal vessels heated to 150 °C for 24 h and then frozen. Their experiment was also tested with augite substrate chips, which revealed that they could indeed form nucleation sites for zoned carbonate rosettes. Here, no phyllosilicates were formed, presumably due to the high pCO_2 inhibiting the dissolution of Si from the augite. Further experiments at 25 °C (and

subsequently frozen) without substrates showed that amorphous, but chemically zoned, carbonates also precipitated.

On a first basis, the experiments of Golden et al. (2001, 2000) explain the carbonate formation very well, with a simple model of precipitation from a CO_2 saturated fluid with dissolved divalent cations, which fractionated as precipitation continued and contributed to the chemical zoning. However, the source of the divalent cations in the experiments was chloride salts, which were intentionally washed away after the heating and freezing procedures. As far as can be ascertained, no extraterrestrial chlorides are found in the meteorite, and so the source of cations is unlikely to be chlorides. (Chlorides are, however, found in the nakhlites, e.g., Bridges and Grady, 2000, 1999.) It is more likely, (as discussed in Chapter 4), that the source of the cations was the host orthopyroxenite rock itself, or surrounding rocks of an identical composition, and so Si and other cations would have been in solution too. There are also issues related to the effects that flash freezing might have had on the chemical zonation and globular morphology of the carbonates, and whether or not a similar process could have occurred near the early martian surface. These include the relatively high temperature or 150 °C, whereas C and O isotope systematics point to lower temperatures (see Section 1.4.2.2 in Chapter 1), and the choice of an augite substrate, because only trace augite is found in ALH84001. However, these problems seem to be acceptable limitations of the experimental setup to approximate a real geological context.

Strictly speaking, the experiments by Golden et al. (2000) could be classed as carbonate precipitation experiments rather than alteration experiments.

Alteration experiments *sensu stricto* were carried out by Baker et al. (2000) on terrestrial basalt from the Columbia River as a host rock analogue to ALH 84001, and to other martian meteorites. However, the basalt had, among other compositional differences, too

much alumina (Al_2O_3 = 12.35 wt. % versus 1.38 wt. %) and too little Mg (MgO = 4.38 wt. % versus 26.1 wt. %) to be an accurate analogue for the ALH 84001 host rock. Nevertheless, the experiments were carried out in flow-through apparatus, with fluid trickling through a vertical cylinder filled with the crushed basalt for seven days. This technique and successfully produced calcite, ankerite, magnesite and opaline silica/cristobalite and quartz in a 1–2 bar pCO_2 atmosphere at 23 °C, and no phyllosilicates. Of particular interest was the distribution of minerals throughout the ~ 12.7 cm length of the basalt column, with calcite, magnesite and opal/cristobalite occurring throughout, but with quartz and siderite only occurring at the bottom. The fluid exiting the column was also analysed with inductively-coupled plasma atomic emission spectroscopy (ICP-AES). The fluid was found to precipitate calcite, magnesite, diaspore and hematite, and was saturated with kaolinite and muscovite, which are phyllosilicates found to be saturated in the disequilibrium leaching models of the ALH 84001 host and clays (see Sections 4.2.4.1 and 4.2.5.1 in Chapter 4).

In a range of experiments designed to constrain the formation of carbonates on early Mars, and to reconcile the apparent paradox of coincident sulfate and carbonate production at the surface, Dehouck et al. (2012) carried out a four-year vapour alteration experiment on orthopyroxene grains under both highly oxidising and relatively reduced closed atmospheres (pCO_2 = 0.8 bar) and at ambient temperature. In addition, they conducted the experiments in the presence and absence of sulfide. No secondary minerals were formed in the samples that contained no sulfides, but various sulfates (jarosite, gypsum, hexahydrite) and goethite (and possibly an Mg-smectite phase; Dehouck et al. (2014)) were produced in the presence of initial sulfide. Carbonates (nesquehonite) were only produced in olivine weathering experiments, and only in the absence of sulfide. In a follow-up study, Dehouck et al. (2014) focused on olivine weathering only, in closed vessels that were regularly

agitated manually (pCO_2 = 1.5 bar), at iW/iR of ~ 10, and higher temperatures (~45 °C) for 95 days. The only appreciable secondary products that formed were a silica-rich phase, and a Mg-smectite.

Various other related alteration experiments have been carried out under simulated martian conditions (e.g., Bullock et al., 2004; Chevrier et al., 2006, 2004; Schröder et al., 2004), but are not directly relevant to the construction of an experimental setup to study the carbonates in ALH 84001. Bullock et al.(2004), although studying the P-T range of interest, focused on the composition of SNC derived alteration fluids (CO_3^{2-} and Cl^- rich), and not mineral precipitates. Chevrier et al. (2006, 2004) found that siderite formed in a 0.8 bar pCO_2 atmosphere on α-Fe (synthetic elemental iron) in the presence of water vapour under ambient temperatures, but this was subsequently replaced by goethite. Schröder et al. (2004) attempted to weather olivine and augite powders under high CO_2 fluxes at 800 °C, but these are physical conditions simply incompatible with surface weathering on early Mars, unless, perhaps, related to impact events or volcanic activity.

5.2 Host rock analogues

5.2.1 Selection of a host rock

Unaltered, olivine-free orthopyroxenite rocks are relatively uncommon on the surface of Earth. Several candidate rocks compositionally that are analogous to ALH 84001 were considered in consultation with the Colleagues from the Department of Mineralogy – Earth Sciences at the Natural History Museum (NHM) in London. Candidates from the mineral collection at the NHM were considered on the basis of petrology and mineralogy (> 90 % volume orthopyroxene viewed in hand specimen) and grade of weathering. The least weathered orthopyroxenite candidates selected are summarised in Table 5-2.

Table 5-2. Least weathered orthopyroxenite samples selected from the NHM.

NHM sample number	Polished thin section number	NHM description	Provenance
BM.1998,P2(2929)	P18428	Hypersthenite	Papua New Guinea
BM.1998,P2(2908)	P18424	Hypersthenite	Papua New Guinea
BM.1970,P20(5)	P18425	Bronzitite	Stillwater Complex

While these candidates were mineralogically and petrologically very similar to ALH 84001 (particularly the Papua New Guinea orthopyroxenites), the information on their actual source, geological context and petrogenesis was lacking, and so their analyses are not relevant to this work and are not included here. Moreover, it was unlikely that enough material of each of the samples would be available for use in the alteration experiments. Consequently, field sampling was required from a known, well studied site. Communication with the mineral curators of the Oxford University Museum of Natural History (M. Price) and the Hunterian Museum (J. Faithfull, University of Glasgow) lead to the identification of two possible localities of near-monomineralic orthopyroxenites in Britain, belonging to the Archaean (2.5 – 4.0 Ga) Lewisian Complex in the NW Scottish highlands, and the Isles of Lewis and Harris in the Outer Hebrides (Figure 5-1). The orthopyroxenite rocks are metamorphic and granulite facies (rather than primary igneous, as ALH 84001) belonging to the Assynt Terrane, with protoliths that are likely to be the oldest rocks in Britain (3030 – 2960 Ma; Jones et al., 2003, pp. 15–18). The metamorphic transformation from igneous protolith to granulite facies occurred ~2490 Ma ago, probably as a consequence of crustal thickening during a collisional orogenic event (Jones et al., 2003).

The locality on the Scottish highlands is near Loch an Daimh Mòr (approximately 58.337° N, −5.148 ° E) in Sutherland, where orthopyroxenites are metamorphic (olivine + SiO_2), equigranular, texturally equilibrated and exhibit triple points (Bowes et al., 1964; and J.

Faithfull, pers. comm.), similar to the 120° triple junctures described between orthopyroxene crystals in ALH 84001 (e.g., Mittlefehldt, 1994). Accessory serpentine and zircons may be found in the outcrops (Bowes et al., 1964; J. Faithfull, pers. comm.). Figure 5-2 is a petrographic microscope image of a thin section of the Loch an Daimh Mòr (LDM) orthopyroxenite.

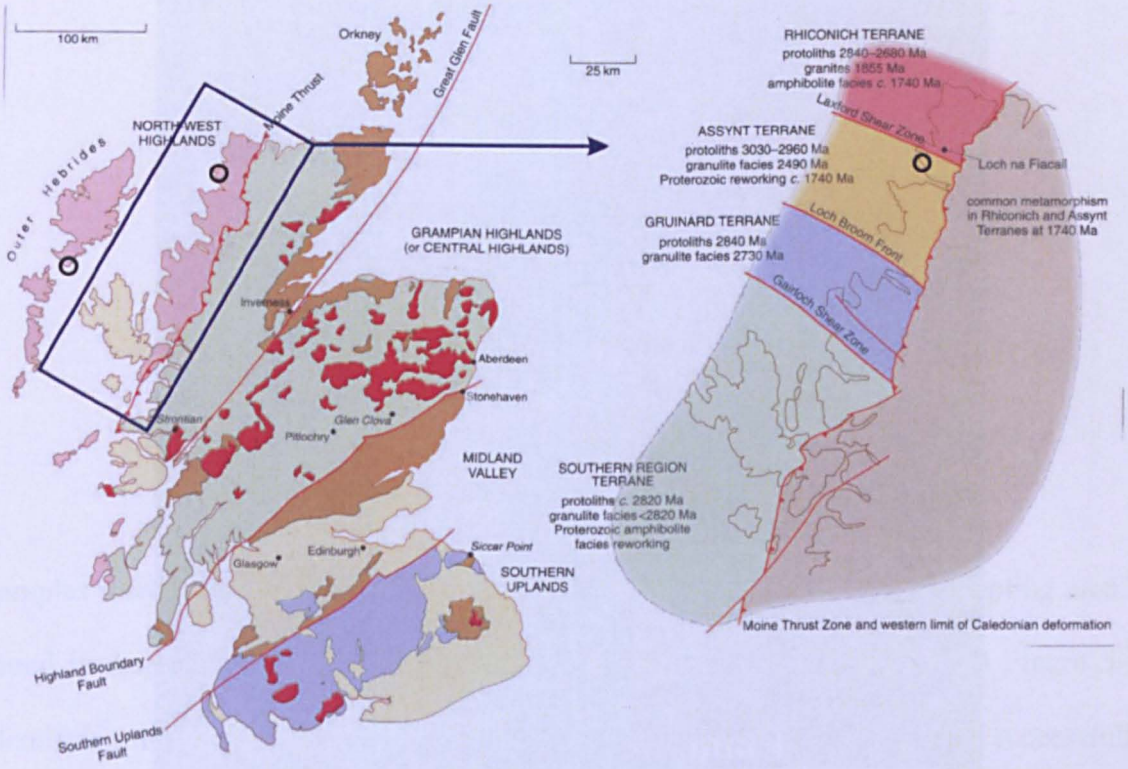

Figure 5-1. Geological map of Northern Scotland, modified from Jones et al. (2003). The map on the right is a close-up of the Loch an Daimh Mòr locality (Sutherland) in geological context. Sampling localities are symbolised by circles: the leftmost one is on Southern Harris.

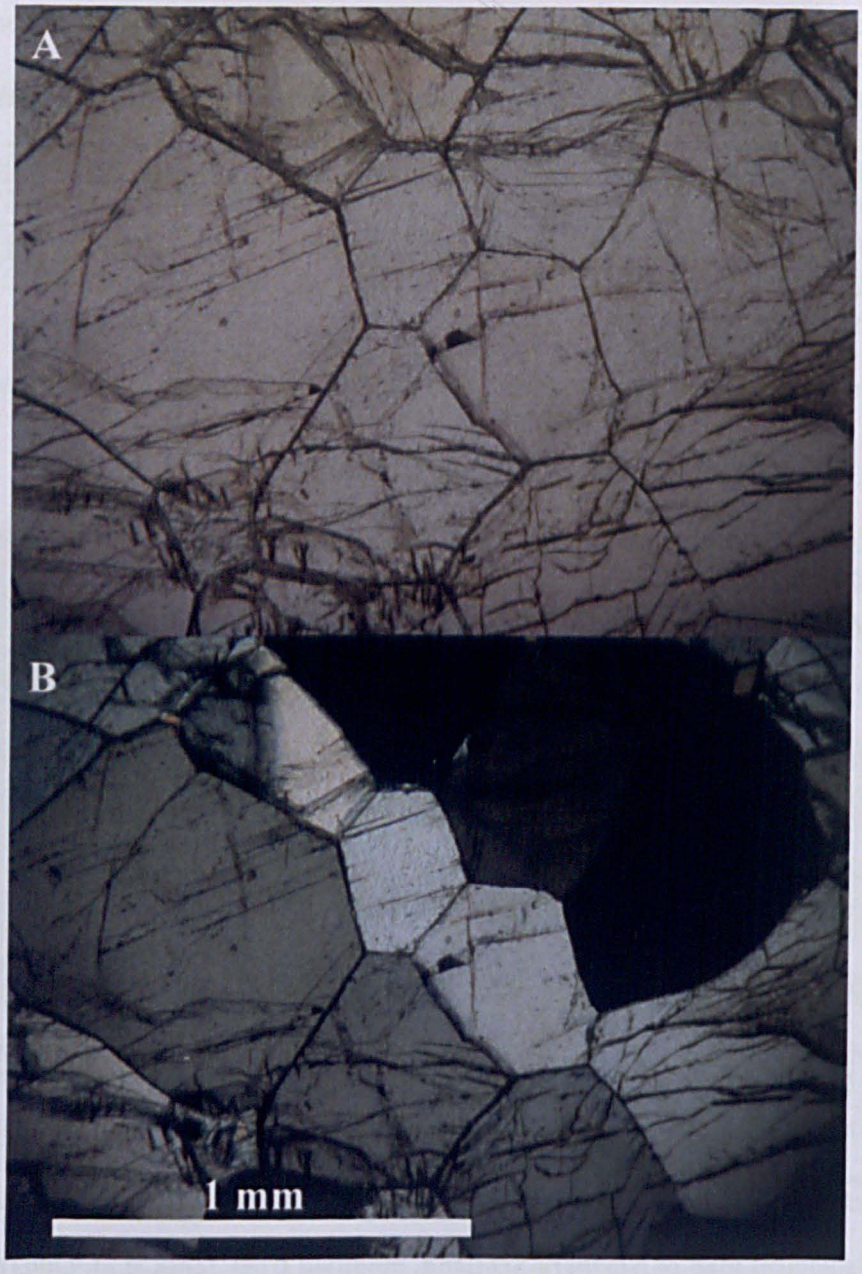

Figure 5-2. Loch an Daimh Mòr orthopyroxenite, thin section. Note the monomineralic, near-euhedral orthopyroxene crystals and triple junctures. A) Plain light. B) Cross-polarised light.

The locality in the Outer Hebrides is near Rodel on the southern coast of the Isle of Harris (approximately 57.742° N, −6.971° E). The orthopyroxenites there are metamorphosed to granulite facies from the Leverburgh Belt, and are possibly metasediments, with 'quite aluminous' chemistry, containing accessory cordierite, phlogopite or kyanite (J. Faithfull, pers. comm.). These are almost certainly the same as the sapphirine-bearing orthopyroxene

granulites described by Baba (1999), a representative analysis of which is given in Table 5-3.

Table 5-3. Orthopyroxene composition of Leverburgh Belt (Isle of Harris) orthopyroxenite and ALH 84001.

	Harris Opx core*	Opx ALH 84001†
SiO_2	53.74	54.0
TiO_2	0.05	0.15
Al_2O_3	5.03	0.64
Cr_2O_3	0.00	0.40
FeO	16.10	17.7
MnO	0.00	0.49
MgO	26.25	25.2
CaO	0.12	1.66
Na_2O	0.03	0.03
K_2O	–	–
Total	101.32	100.24

* Representative microprobe analysis, sample B-16 orthopyroxene core. FeO includes Fe_2O_3 (Baba, 1999).
†Average of 204 analyses (Na_2O based on 130 analyses; Mittlefehldt, 1994).

Samples were collected in August 2013. A geological map of the exact sampling area is found in Appendix B while field photographs are shown in Figure 5-3 and Figure 5-4. Identifying the exact outcrops described in literature was difficult, and when successfully identified, were found to be quite weathered on the surface (both biologically and chemically from rain at LDM and Rodel, and sea spray at Rodel), and in places > 20 cm below the surface, where fluids exploited fractures in the rocks.

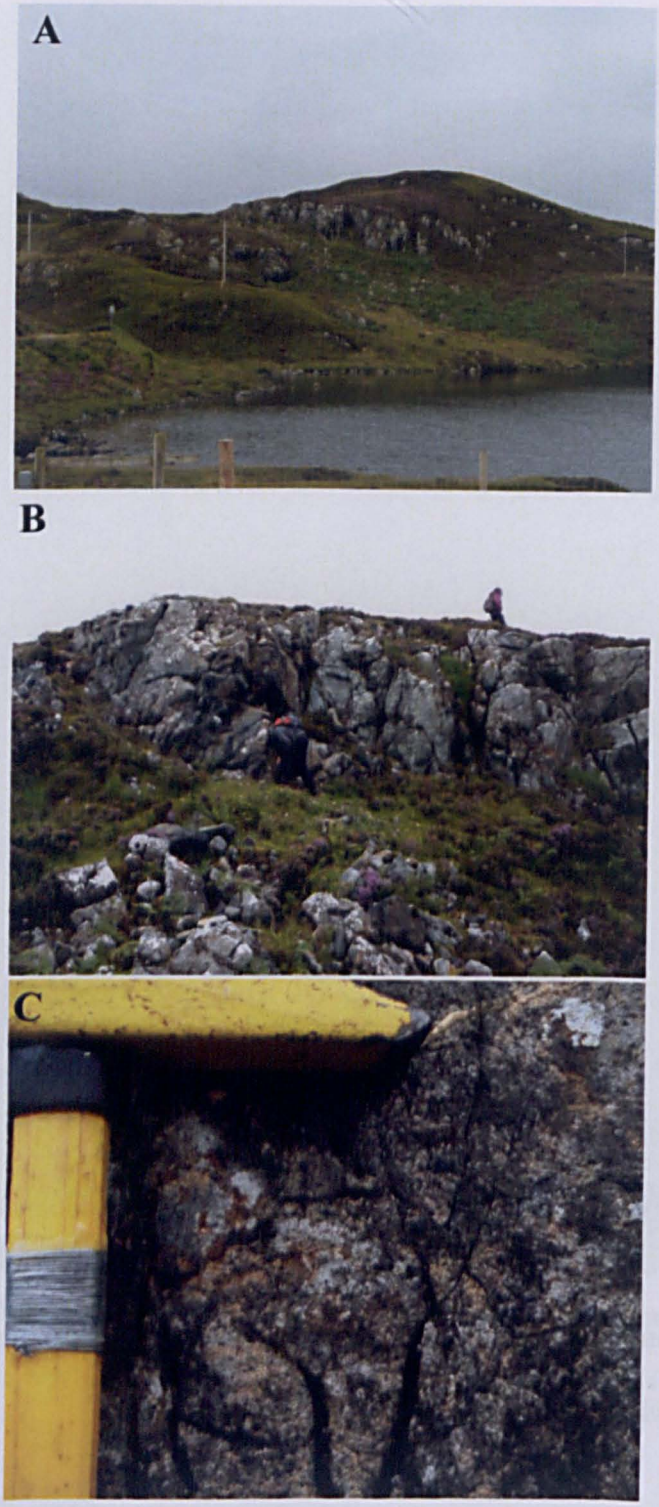

Figure 5-3. Loch an Daimh Mòr (LDM) sampling location A) Context of the orthopyroxenite (Loch in the foreground). B)Close-up of the sampling location. C) Sample in situ. Note the black, near-euhedral orthopyroxene crystals peering through surface alteration. A and B courtesy of J. Snape.

Figure 5-4. South Harris sample locality. A) Outcrop in context. (Sea in the background.) B) Close-up of the weathered orthopyroxenite outcrop. Image credit: J. Snape.

Furthermore, the outcrop at Loch an Daimh Mòr was serpentinised or difficult to distinguish from the serpentinite outcrop adjacent to it, as the serpentinite contained substantial pyroxene visible in hand specimen (Figure 5-5). Microprobe analyses (see Section 2.3 in Chapter 2 for details on the method) of the LDM serpentinite are shown in Table 5-4. Textural relationships between minerals within the serpentinite sample clearly show that the serpentine was formed as a result of olivine replacement (Figure 5-6). Serpentine substitution appears to have affected olivine more than pyroxene (although some relict olivine remains, surrounded by reaction rims of magnetite, Figure 5-6), which caused the relatively unaltered pyroxene grains to be easily distinguishable and to protrude over the rest of the grains, including the weathered exterior (Figure 5-5). As the pyroxene does not appear to be largely involved in the serpentinisation process in the LDM samples, the reaction leading to the formation of serpentine was probably:

$$(Fe,Mg)\text{olivine} + \text{water} \Rightarrow \text{serpentine} + \text{magnetite} + \text{hydrogen} \qquad (5.1)$$

Two parallel paired reactions actually take place mediated by the activity of silica in solution (and therefore temperature and water to rock ratio):

$$3Fe_2SiO_4 + 2H_2O \Rightarrow 3SiO_2(aq) + 2Fe_3O_4 + 2H_2(g) \qquad (5.2)$$

(Fe-olivine + water → aqueous silica + magnetite + hydrogen)

$$3Mg_2SiO_4 + 4H_2O + SiO_2(aq) \Rightarrow 2Mg_3Si_2O_5(OH)_4 \qquad (5.3)$$

(Mg-olivine + water + aqueous silica → serpentine)

The LDM serpentine-pyroxenite appears to be of particular relevance for studying ALH 84001, as some authors (e.g., Harvey and McSween, 1994) have contended that the

carbonates in ALH 84001 were produced from the high temperature (~ 500 °C) replacement of primary (or otherwise existing prior to carbonate precipitation) olivine. At LDM, conditions were probably similar to those purported to occur in ALH 84001 conducive to the formation of the carbonates according to the high-temperature interpretation. However, olivine at LDM was transformed to serpentine and magnetite instead of carbonate (but see Treiman et al. (2002), where hydrothermal alteration of olivine formed zoned carbonate rosettes in Svalbard xenoliths). This implies that carbonates in ALH 84001 did not form as a result of olivine replacement at high temperature because serpentine would have formed instead (and seeing that what little olivine there is in ALH 84001 does not appear to be replaced by any alteration phase. If anything, according to Shearer et al. (1999) and Treiman (1998a), the olivine replaced orthopyroxene and carbonate or a hypothetical serpentine phase, in a post-carbonate heating event, and/or that pCO_2 at LDM was low enough to preclude the precipitation of carbonates in the hydrothermal alteration event that serpentinised the protolith.

Figure 5-5. LDM hand specimen. Relatively resistant orthopyroxenite grains are visible through the weathered exterior (white arrows point to some noticeable dark orthopyroxenite grains). The interior (red arrow) is relatively unaltered at a depth of ~ 4 mm.

Table 5-4. Loch an Daimh Mòr serpentinite EPMA analyses.

	Serpentine		Altered Ol		Magnetite		Phosphate‡‡
	LDM*	Comparison†	High Cr‡	Low Cr§	Ti-Mt**	Mt††	
SiO_2	42.83	43.1	22.22	30.17	2.26	1.36	5.67
TiO_2	0.02	nd	0.27	1.94	47.63	0.01	0.02
Al_2O_3	0.38	0.09	7.50	14.49	0.17	0.10	0.20
Cr_2O_3	bdl	0.01	12.35	0.64	0.41	1.15	bdl
FeO	1.46	1.2	7.93	13.70	35.17	86.98	4.10
MnO	0.02	0.16	1.21	1.54	3.50	0.10	0.04
MgO	41.20	41.9	30.56	24.00	7.78	1.33	5.83
CaO	0.01	nd	0.03	0.06	0.02	0.01	43.61
Na_2O	bdl	nd	0.02	0.01	0.01	0.02	0.02
K_2O	bdl	nd	bdl	bdl	bdl	bdl	bdl
SO_2	0.02	nd	0.06	0.02	bdl	bdl	0.02
P_2O_5	0.03	nd	0.01	0.01	0.01	0.01	35.49
NiO	nd	0.05	nd	nd	nd	0.25	0.09
Cl	nd	nd	nd	nd	nd	0.02	0.36
Total	85.96	87.7	82.17	86.58	97.0	91.92	95.45
H_2O	14.04	13.5	-	-	-	-	-

*Representative analysis of the LDM sample.
†Mesh-textured serpentine analysis (sample 29, probably antigorite) from Dungan (1979) for comparison.
‡Altered olivine, high Cr, mean of 12 analyses.
§Altered olivine, low Cr, mean of three analyses.
**Titanomagnetite, mean of two analyses.
††Magnetite, mean of five analyses (Cl and NiO_2 from only 4 analyses).
‡‡One representative phosphate analysis.
nd: not determined. bdl: below detection limit.

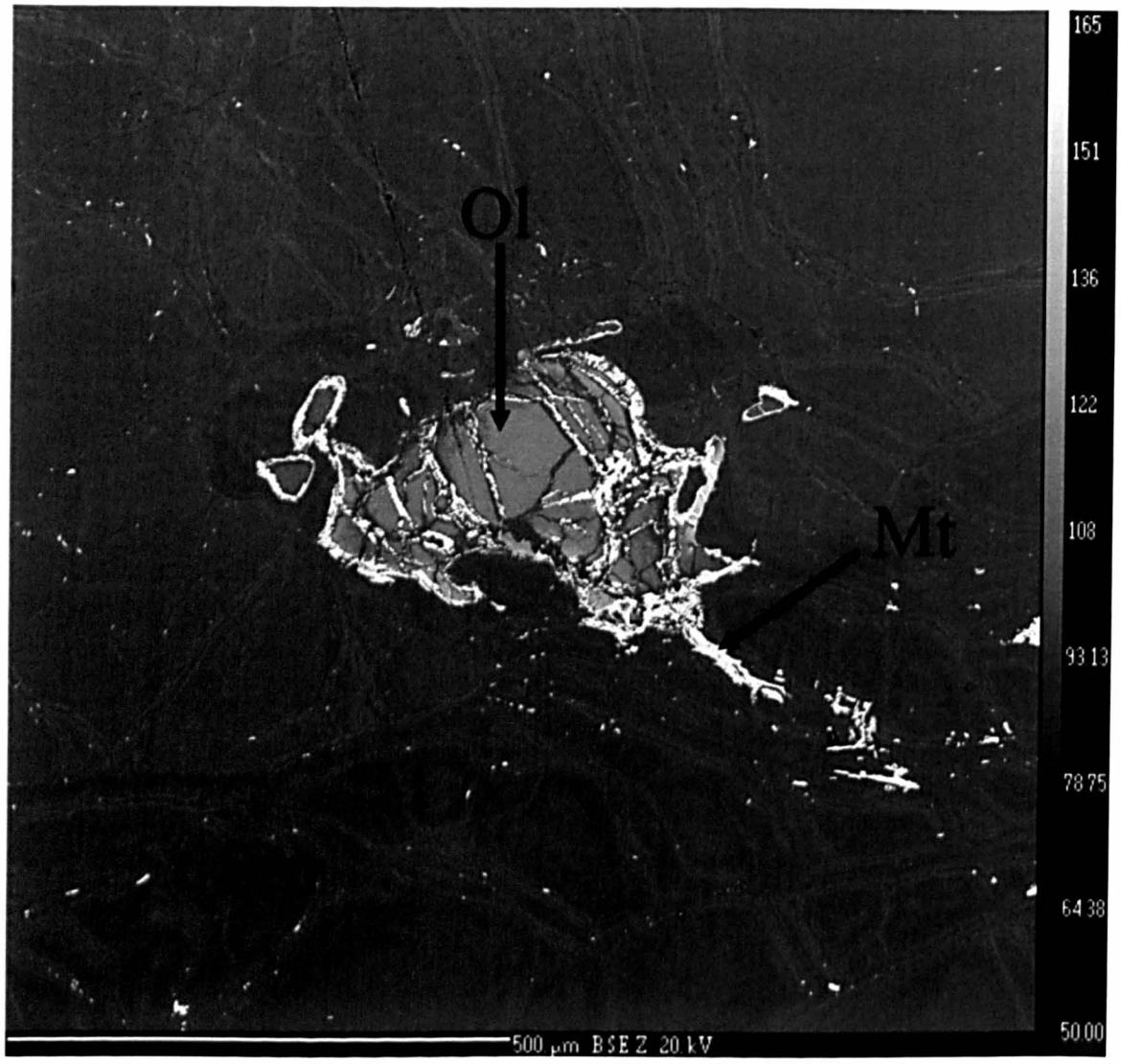

Figure 5-6. EPMA backscattered secondary electron image of serpentine (Srp) and magnetite (Mt) replacement of olivine (Ol) in the Loch an Daimh Mòr serpentinite.

5.2.2 Preparation of the host rock

The LDM samples were sawed into approximately 1 × 1 × 0.5 cm right rectangular cuboids (Figure 5-7) and each face was filed with increasingly finer-grained silicon carbide (SiC) abrasive paper, using isopropanol (IPA) as a lubricant. IPA was chosen to aid the process instead of water to avoid any possible chemical alteration of the samples. The cuboids were then immersed in an ultrasonic bath in IPA at room temperature for 10 minutes to dislodge any loose dust and fragments, and to prevent any possible bacterial

contamination. Finally, the sample cuboids were dried at ~ 40 °C in a vacuum oven, for at least 24 h.

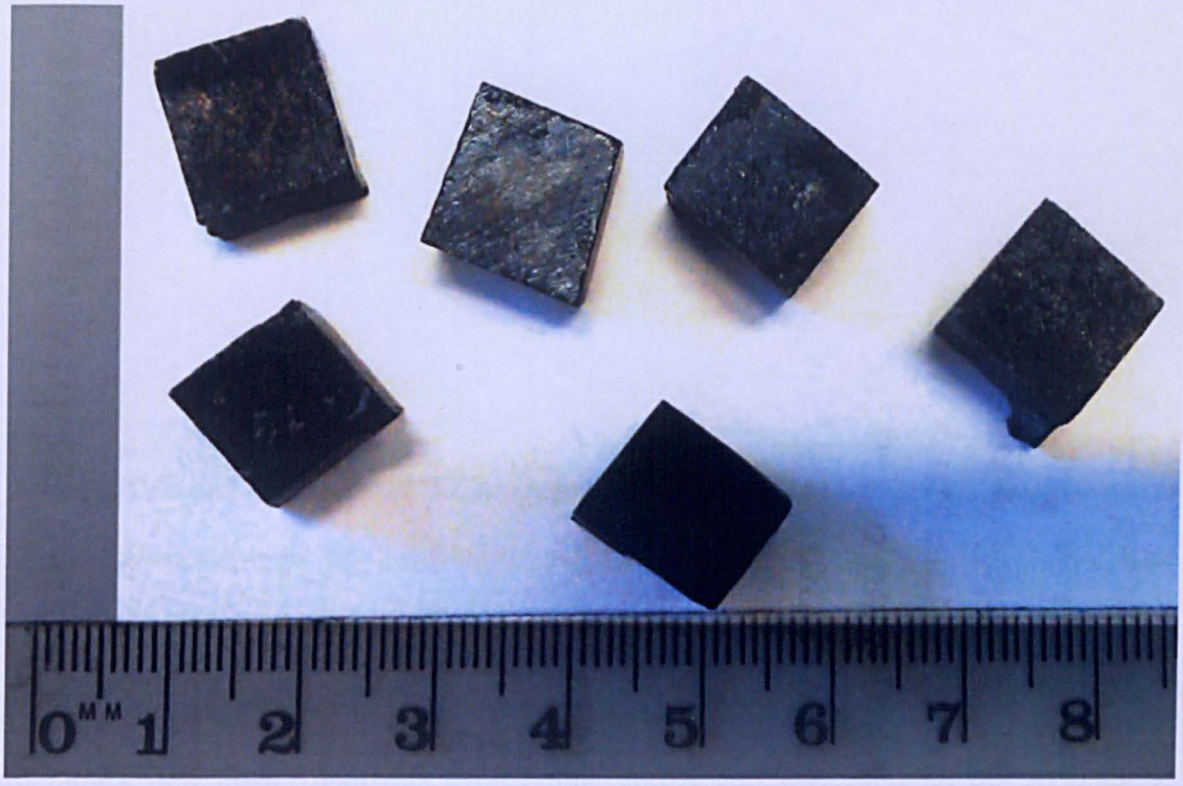

Figure 5-7. LDM samples sawed into ~ 0.5 cm^3 cuboids, prior to filing with the SiC abrasive. Contrast and brightness have been modified to enhance the rotary saw marks and uneven vertices.

The resulting sample cuboids were smooth on each of the faces, but had sharp edges and corners. This ensured that any possible etch pits or changes in the morphology of the cuboids as a result of physical and chemical alteration would be apparent.

Another set of LDM samples were simple 1 – 2 mm irregular chips (Figure 5-8). These were chosen in order to investigate whether irregular surfaces on the host rock were able to catalyse the precipitation of secondary products by providing nucleation sites. The chips were also immersed in IPA in an ultrasonic bath for 15 minutes at ambient temperature to dislodge unconsolidated grains and prevent bacterial growth, and then dried in a vacuum oven for > 24 h at ~ 40 °C.

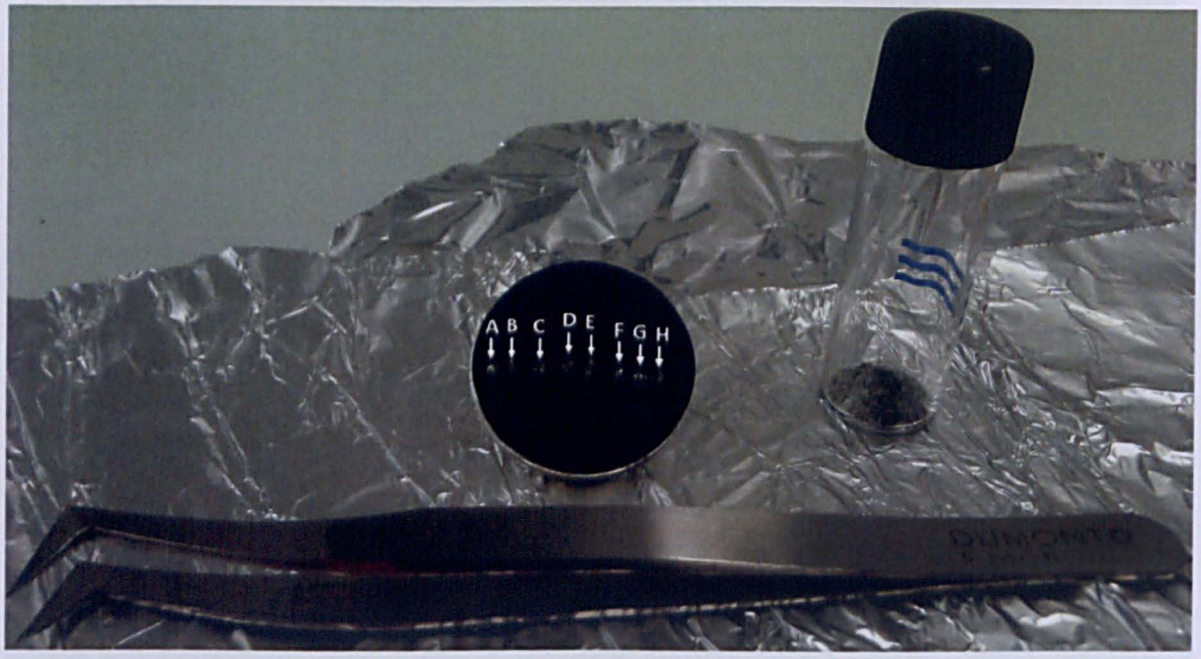

Figure 5-8. LDM host rock chips (A to H on the sample holder) prepared on for observation on the SEM, prior to the alteration experiment. Contrast and brightness have been modified to enhance the chips, attached by carbon tape onto the SEM sample holder. The tweezers are 115 mm in length.

Prior to carrying out the experiments (detailed in Section 5.3), the host rock cuboids and chips were studied (uncoated, to avoid the external introduction of carbon) under the SEM (see Section 2.2 in Chapter 1 for method details) in order to discern the mineralogy and surface morphology of the samples, so as to compare the samples pre- and post-alteration. Given that W/R is a unitless magnitude, the mass of fluid could be adjusted to the individual masses of the rock samples (see Section 5.3 for the W/R chosen). The samples were weighed to the nearest 10^{-5} g using a digital balance.

5.3 Experimental setup and facilities

To simulate the ideal disequilibrium conditions of carbonate formation in ALH 84001, as described in Chapter 4 from the results of the thermochemical models, a system to circulate the alteration fluid would be required. Although a suite of environmental chambers suitable for simulating the martian surface are available at the Department of Physical Sciences at the Open University, none are designed to circulate a fluid automatically in a closely monitored environment, such as a batch reactor, or the 'trickling fluid' system used by Baker et al. (2000). The environmental chambers are akin to closed vessels with controlled gas pressures, similar to the vessels in the experiments by Golden et al., (2001, 2000), with temperature in the laboratory stable at ~ 23.3 °C, although small variations exist (± 0.24 °C), mostly related to day/night cycles, and can be monitored with thermocouples placed on the vessels, which log temperature to a PC. This temperature was considered sufficiently close to the 20 °C geochemical model tested so as not to warrant running a new model with this temperature, and is still very close to the ALH 84001 carbonate formation temperature (18 ± 4 °C; Halevy et al., 2011).

Since it was not possible to run the experiment under flowing conditions, the equilibrium model of carbonate formation (Section 4.2.3 in Chapter 4) was sought to be reproduced. While not producing carbonates with the same efficiency as the non-equilibrium model, approximately 40 % carbonate replacement was still accomplished in the batch equilibrium scenario at iW/iR of 359 (rW/rR ≈ 371) and a maximum $MgCO_3$ content of ~ 25.9 mol % at 20 °C with an initial fCO_2 of 1 bar. It was reasonable to expect some carbonate production in the chamber equilibrium alteration experiments, with some $MgCO_3$ content, given the results of the models (but see Section 5.3.1 for limitations of the experimental procedure).

Figure 5-9 is a schematic of the experimental setup, and Figure 5-10 shows the chamber used for the experiments. Two samples could fit in the chamber at any time: one cuboid and one chip. Cuboids were placed in borosilicate beakers and chips were placed in wide borosilicate test tubes, and these were placed on a custom-made polyacrylate mesh and stainless steel holder (Figure 5-10; a steel mesh holder used previously had rusted heavily in the experiment and was discarded from further use). Purified deionised water (with a resistivity value of 18 MΩ/cm at 25 °C) was used to fill the beaker and test tube until the appropriate iW/iR (~ 359) was reached. The chamber chosen for the alteration experiments had to be able to contain 1 bar of pure CO_2 in the headspace. In practice filled to 1.1 – 1.2 bar total gas pressure, so as to not contaminate the chamber with gas from the exterior were a leak to occur. Immediately after introducing the samples into the sample holder, descending the holder into the chamber and sealing the chamber, the chamber was purged with a flow of high purity CO_2 (Experis® Premier, with 99.995 % purity) for ~ 10 minutes in order to evacuate other gases from the chamber and outgas dissolved gases other than CO_2 from the deionised water.

For each cuboid and chip pair, the experiment was run for 21 days. This time was seen as a compromise between the perceived time needed for the expected chemical reactions to take place and external time constraints. The time also appeared to fit with a realistic, relatively short-lived aqueous event (such as flooding) that may have occurred on the surface of early Mars.

After 21 days, the samples were taken out of their respective holders and dried in a vacuum oven at ~ 40 °C for > 24 h. Finally, the post-altered samples were analysed, uncoated, with the SEM.

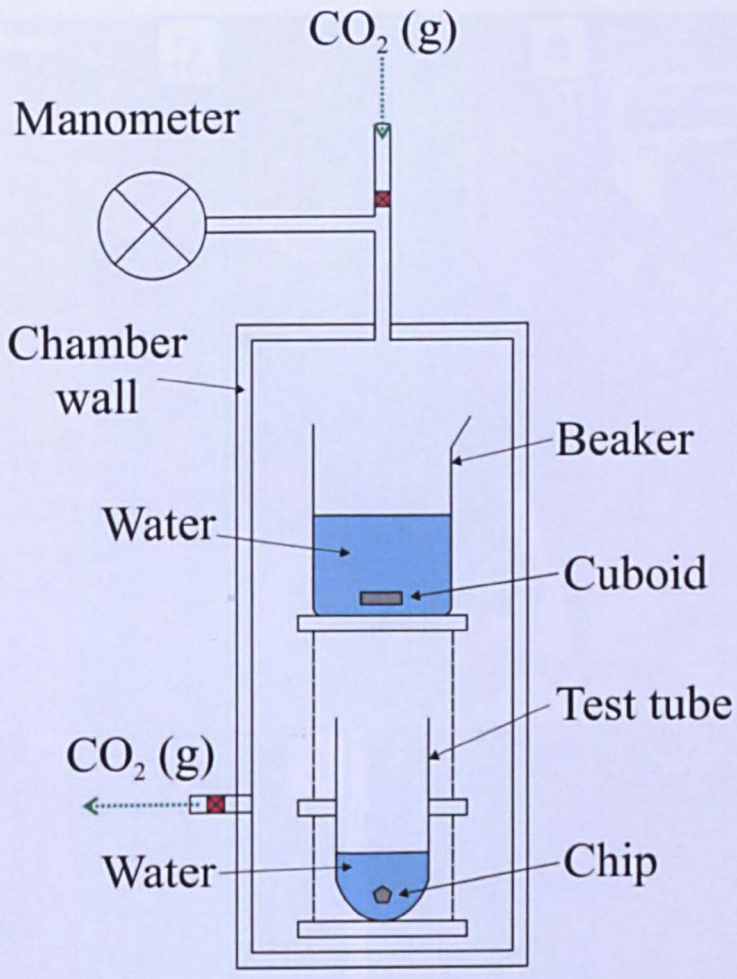

Figure 5-9. Schematic of the chamber and experimental setup. Red boxes are stopper valves for controlling the entrance and exit of CO_2 (g).

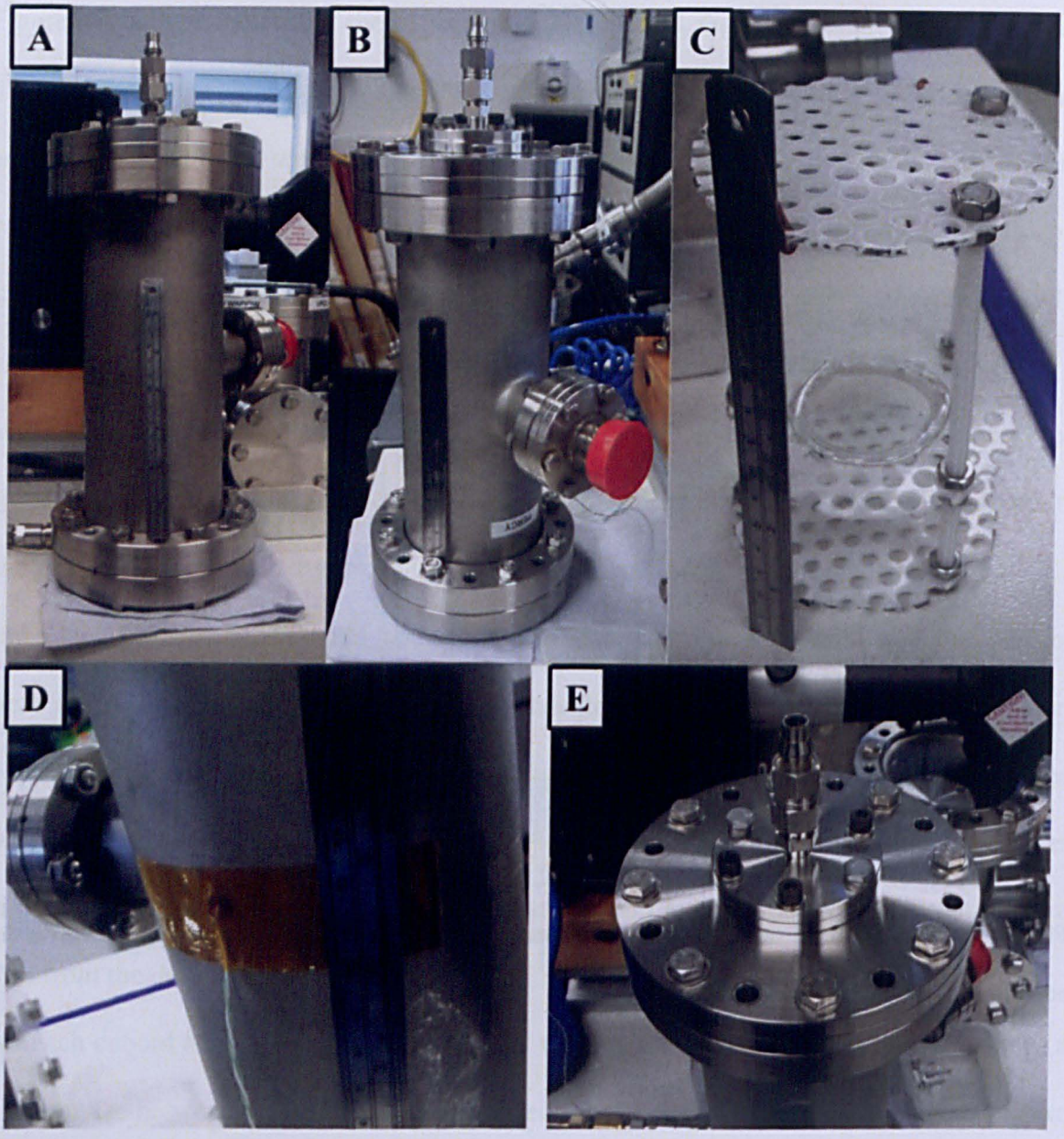

Figure 5-10. Mars environmental chamber used in the alteration experiments. A) and B) chamber, the red cap covers a gas exit which is sealed after purging the chamber; C) sample holder custom made to fit inside the chamber: the top platform is flat to accommodate a beaker, the middle platform contains a hole to accommodate a wide test tube; D) detail of the wired thermocouple on the surface of the chamber; E) valve allowing the input of CO_2, and monitoring of gas pressure.

5.3.1 Limitations of the experiments

The most important limitation of the experimental setup was the imposed time constraint. Ascertaining the progression of the alteration was difficult, given the known slow reaction times of silicate dissolution and mineral precipitation at the low temperatures tested, and the inability to subsample any precipitated minerals, or indeed, observe the marks of any reactions occurring (such as etching).

Other limitations related to the experimental setup, the samples, and the analyses were:

a) The host rock samples were not pure orthopyroxenites, but rather, had a large serpentine content, and so were probably not mineralogically representative of ALH 84001. However, their MgO content was higher than that of the meteorite, and potentially conducive to the precipitation of high Mg-carbonate.

   Furthermore, the heterogeneity of the sample meant that any particularly undesired phases possibly existing in them prior to experimental alteration (e.g., carbonates) could not be seen in their interior and could skew the results.

b) Since the alteration fluid could not be flowed (mimicking infiltration and dynamic, non-equilibrium reactions), Mg-carbonate precipitation could be extremely slow and perhaps unobservable, even in a magnesite-supersaturated fluid. Related to this, in the absence of flowing fluid, the samples could develop a Si-rich phase acting as a "passivating layer" on the surfaces of the host rock samples, which could act as a barrier between the unaltered host rock and the fluid to prevent further reactions from occurring. The absence of carbonate precipitates in low temperature olivine alteration experiments was attributed to a possible Si-rich passivating layer by Dehouck et al. (2014).

c) While the irregular chips of host rock could provide surfaces for mineral nucleation, the chips were quite frail, and tended to disaggregate when handled to be imaged and analysed with the SEM, prior to experimentation. This signified that post-alteration disaggregation of the chips would be impossible to ascribe solely to chemical alteration during experimentation.

d) The initial W/R in the experiments was an approximation, taking account the bulk mass of water and rock in the samples. In practice, W/R was extremely variable, given that the samples were not crushed: at the start of the experiments, the surfaces of the cuboids were subjected to high W/R, whereas their interiors were at W/R = 0. Similarly, the surfaces of the samples that were in contact with the bases of the beaker or test tube, were subject to low initial W/R. The expectation was that W/R would gradually increase towards the interior of the host rocks as the experiment progressed, and that possible secondary products could be precipitated with increased infiltration into the sample, their composition reflecting the change in W/R.

e) Gas compositions could not be sampled from the headspace, so any gas alteration products (e.g., the H_2 predicted in the model, Section 4.2.3.1, Chapter 4) could not be ascertained.

f) Pre- and post-alteration samples were analysed by SEM. While the high spatial resolution gained from using the SEM was considered an advantage, the 2D analyses precluded observations of internal fractures and pits in which secondary mineral precipitation could be favoured. Furthermore, in the absence of a carbon coat quantifying element abundances was restricted and inaccurate.

g) While the post-alteration sample drying process (in a vacuum oven) could be seen as a proxy for evaporation, the thermochemical models presented in Chapter 4 considered the evaporation of all the fluid in the system, so solutes in the fluid were precipitated. In the experiments, only the solid rock samples were dried, and the fluid was discarded.

5.4 Results

Despite three separate repeat experiments for 21 days each, under a 1.1 – 1.2 bar pCO_2 and an ideal (bulk) iW/iR of ~ 359, the results, were inconclusive, which could be anticipated given the limitations described in Section 5.3.1. A further complication arose from IT problems concerning the temperature-logging PC, resulting in the loss of data from one cuboid – chip sample.

No alteration products were identified by SEM, and no etch pits in the samples could be ascribed to the experimental conditions. Similarly, any particles disaggregated from the irregular chips were suspected to have been dislodged during handling due to the samples' relative weakness.

Pre-alteration SEM images of one of the chips (Chip H, weighing 55.83 mg) are presented in Figure 5-11. Post-alteration SEM analyses of the chips are indistinguishable apart from the minor fragmenting due to handling (not shown here). Differences between pre- and post-altered states in the cuboids are even less apparent as they did not fragment during sample handling and the surface morphologies (flat surfaces and sharp vertices) remained the same.

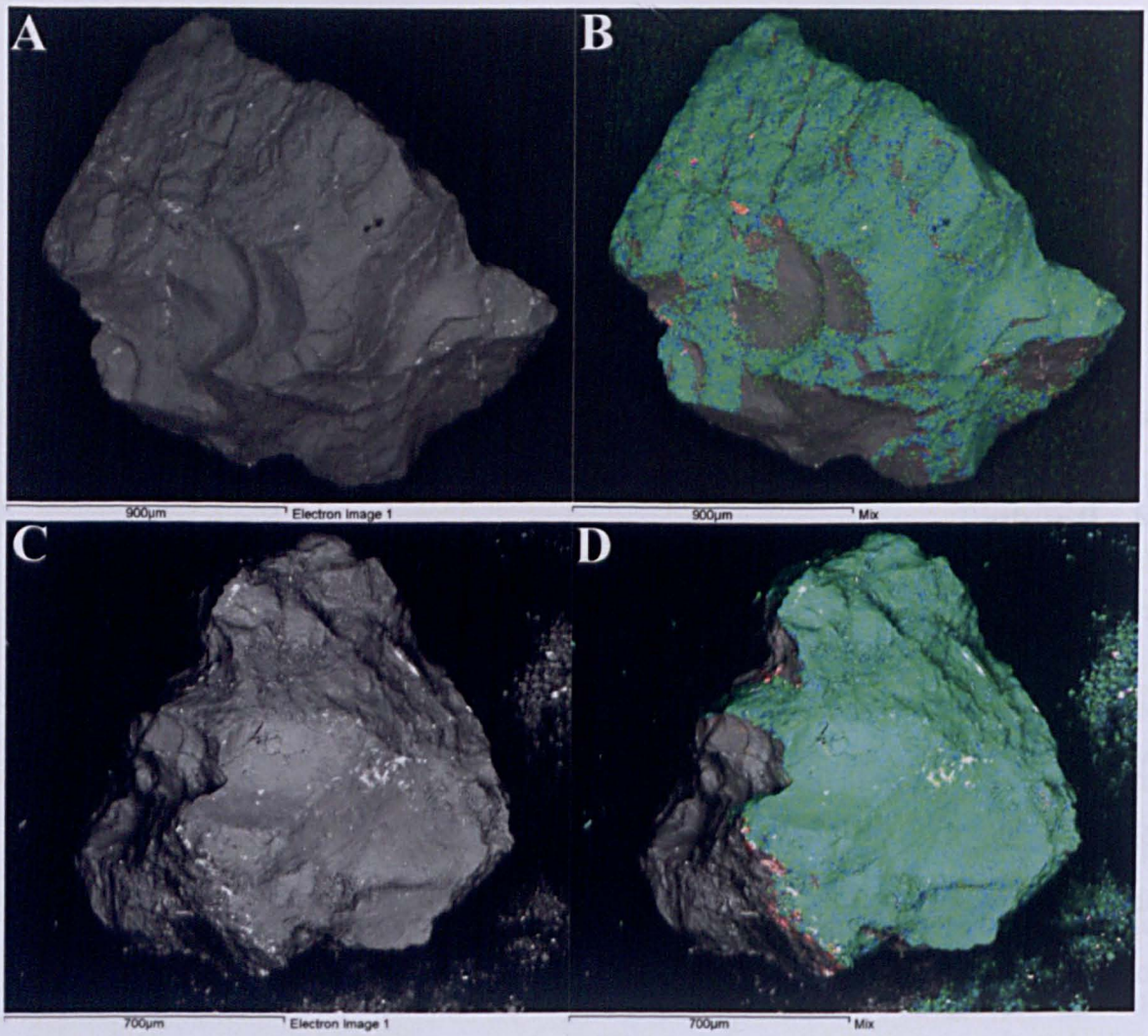

Figure 5-11. SEM images of Chip H, prior to the experiment. A and C: Secondary electron images of the sample from different angles. B and D: RGB colour composites where red = Fe, green = Mg and blue = Si. Note the fragmentation in C and D as a result of turning the sample over for SEM analyses from a different angle.

5.5 Discussion and suggestions for future work

The inconclusive results highlight the importance of experimental design. In this case, the experiment suffered from a number of design flaws (detailed in Section 5.3.1), which probably affected the results. Consequently the results do not reflect the carbonate formation processes in ALH 84001.

In future, the limitations identified in these experiments should be taken into account, particularly sourcing better (unaltered) geochemical analogues. Catalysing the carbonation reaction by activating (crushing) the orthopyroxenite would test the feasibility of the experiment in reasonable timescales (weeks), however, analyses of the samples would not be possible by SEM. Infrared or Raman spectra, or X-ray diffraction would be more suited to determining the mineralogy of a powdered sample, but information on the contextual and spatial relationships of the minerals would be lost. Progressing to large samples (such as chips) should only take place after proving that the calculated reactions do take place in the experimental conditions. Finally, the interiors of the samples should also be mineralogically characterised, a process that could be possible with analytical techniques like X-ray computed tomography.

A variety of techniques could have been used to monitor the progress of reactions inside the chamber. Hydrothermal atomic force microscopy is a technique that may be used to observe the mineral/fluid interface, and calculate mineral growth and dissolution rates (e.g., magnesite, Saldi et al. (2009)). Unfortunately, this technique was not available, but other methods could have been used to that effect: gas chromatography – mass spectrometry during the experiment could monitor the uptake of CO_2 from the headspace by the reaction, and could check the saturation state of carbonates and other minerals in the liquid. The liquid, which was discarded in the experiments, should also be evaporated at the end of the alteration experiment, to investigate whether any precipitates form (as they do in the 1D flow and leaching geochemical models; Sections 4.2.4 and 4.2.5, Chapter 4).

Given the described problems with the experimental setup, the framework for experimental alteration of orthopyroxenites, and carbonate formation akin to the model predicted to have occurred in ALH 84001 can be significantly improved.

6 Conclusions

Over 30 years since its recovery from Antarctica, and over 20 since it was recognised as a martian meteorite, ALH 84001 continues to reveal a wealth of information about the hydrological and geochemical conditions of early Mars. Here I have seen evidence from a wide variety of techniques — from compositional analyses to experimental studies — which have revealed the conditions under which the alteration minerals precipitated. This study has also shed light on the composition of the early martian fluids that altered the host rock, and the alteration mineralogy of the rocks in the vicinity of ALH 84001, when it was emplaced near the surface of Mars.

6.1 Insights into geochemical conditions from the composition

The compositional analyses explored in Chapter 3 confirmed that the primary mineralogy (orthopyroxene, maskelynite, chromite and phosphates) of the ALH 84001 aliquot studied is similar to published data, but also, that the primary mineralogy is affected by the fluids. Some of the orthopyroxene crystals contain a relative excess of silica (~ 0.02 atoms per formula unit in excess (Section 3.1.1.1) that, as far as I am aware, has not been reported previously), which, as seen in the 1D flow, aqueous alteration of ALH 84001 in Chapter 4 (Section 4.2.4.1), would have been the result of aqueous alteration while the carbonates were being precipitated. Most likely, this effect was caused the leaching of cations (viz. Mg^{2+}, Fe^{2+}, Mn^{2+} and Ca^{2+}) by percolating fluids.

Raman spectroscopy, whilst relatively imprecise because of the carbon coat from SEM analyses also showed possible traces of hematite and graphite. Both of these minerals have been detected by Raman spectroscopy in previous studies (Steele et al., 2012a, 2007), and

have profound implications for the early martian fluids and the processes that affected the martian surface. Detection of any hematite in the carbonates implies that conditions were more oxidising than the presence of magnetite, well known to be present in ALH 84001, would suggest. Hematite was formed while the carbonates precipitated in the low temperature geochemical models presented in Chapter 4, and virtually stopped forming when CH_4 and magnetite became stable. From these results, it would seem that ALH 84001 experienced changing redox conditions during its alteration, from relatively oxidising, to reducing conditions. Most likely, this was brought on by a decrease in the partial pressure of CO_2, as it was taken up by the carbonation process. This is likely to occur if CO_2 was limiting in the system, possibly because ALH 84001 was in poor contact with the martian palaeoatmosphere. Conditions that are increasingly reducing are in opposition to alteration conditions purported to have occurred in the nakhlites, where the alteration fluids progressively formed more oxidised phases, probably due to the progressive cooling of the fluid (Bridges and Schwenzer, 2012; Hicks et al., 2014).

The formation of secondary products, such as phyllosilicates and carbonates stratigraphically above the host rock (as computed in the 1D flow local equilibrium geochemical model of Chapter 4) may have aided in blocking pores and reducing overall permeability, since carbonates and phyllosilicates are less dense than pyroxene (measured density values of e.g., enstatite, ankerite and nontronite are 3.2 – 3.9, 2.93 – 3.10 and 2.2 – 2.3 g/cm^3, respectively (Anthony et al., 2003)). Graphite, on the other hand, is representative of reduced conditions. If the graphite is primary, then it is indicative of reducing conditions of the magma that crystallised into (mainly) orthopyroxene. However, the high $\delta^{13}C$ measured at the combustion temperature of graphite (700 – 900 °C; Chapter 3), indicates that the source of the carbon was likely to be (at least in part) the martian atmosphere, and so an origin from the carbonates, thermally decomposed and shocked as a

result of an impact, is plausible. Further, the extensive textural evidence for shock processes having affected the carbonates post-deposition, is well documented (e.g., Treiman, 1998).

6.2 Carbon, nitrogen and noble gases: sampling the atmosphere, parental magma, space... And Earth

The suite of gases analysed in stepped combustion mass spectrometry in Chapter 3 demonstrates that a variety of components from different sources were represented in ALH 84001. From most ancient to most modern, the signatures consist of:

1. A primordial neon component ($^{20}Ne/^{22}Ne$ = +11.39 ± 0.75, $^{21}Ne/^{22}Ne$ = +0.16 ± 0.03), approaching the Solar value ($^{20}Ne/^{22}Ne \approx$ +13.80, $^{21}Ne/^{22}Ne \approx$ +0.03; Lupton et al., 2012), released from the primary, magmatic orthopyroxene at 1400 °C. Very likely, this was incorporated from the Solar nebula as Mars accreted. This signature may have stayed relatively unchanged while ALH 84001 crystallised shortly after the planetary differentiation of Mars 4.5 – 4.1 Ga ago (Lapen et al., 2010; Nyquist et al., 2001; Nyquist and Shih, 2013). This solar component has hitherto been unreported in the literature for ALH 84001.

2. An ancient martian magmatic signature. Carbon released from the bulk ALH 84001 sample at temperatures above the decrepitation of the carbonate (> 700 °C) appear to have the value near to that ascribed to the ancient martian mantle ($\delta^{13}C \approx$ +3.90 ‰, cf. +0.8 ‰ by Grady et al. (1994)), but appreciably different so as to suggest that another component from a reservoir with a different signature may be released at the same time, probably from the ancient martian atmosphere (see next point). From the data gathered in this work, a magmatic nitrogen component was

unclear. Helium measured was mostly radiogenic, although specific isotope ratios could not be calculated.

3. The palaeoatmosphere of Mars, with a relatively heavy $\delta^{13}C$ (+39.91 ± 0.36 ‰), very clearly sampled from the decomposition of the carbonates. The high $\delta^{13}C$ of the carbonates is compelling evidence for their origin distinct from the Earth's atmosphere (the Earth's atmosphere has a current $\delta^{13}C \approx -7.8$ ‰ far from anthropogenic sources, but has decreased ~ 1.2 ‰ over the past 130 years, mostly as a result of fossil fuel burning and deforestation (Boutton, 1991)). Other signatures from the early atmosphere are less clear, including from the possible graphite derived from shock heating the carbonates ($\delta^{13}C = +19.01 \pm 0.31$ ‰, and $\delta^{15}N = 127.78 \pm 27.20$ ‰ at 700 – 750 °C), nitrogen released at the height of carbonate decomposition ($\delta^{15}N = 4.74 \pm 0.35$ ‰ at 450 – 500 °C), and possible shock-implanted nitrogen released from maskelynite and (maybe even) graphite ($\delta^{15}N \approx 128.21$ ‰ between 700 and 900 °C). The presence of nitrates, which presumably formed near the martian surface and are sampled at < 250 °C (Grady et al., 1998, 1995), remains speculative, since terrestrial components are released at the same temperature range.

4. Cosmogenic components, trapped in transit from Mars to Earth. An exposure age of 17.52 Ma was calculated here from the cosmogenic neon measured in the bulk sample, which is on the higher end of the estimates given by several authors (see Chapter 3). Above 1200 °C, all carbon and nitrogen released was spallogenic (negative $\delta^{13}C$, and very high $\delta^{15}N$), implanted by cosmic rays into the lattices of the primary orthopyroxene, and released from these silicates as they began to melt.

5. Finally, components of the Earth, acquired during the residence of ALH 84001 in Antarctica (and since its recovery) are plenty: all components released, at least below 300 °C were considered to be 'contaminated' by terrestrial signatures. The very negative $\delta^{13}C$ at < 400 °C, and negative $\delta^{15}N$ at < 250 °C, corroborates this, as well as the low abundances of noble gases (see Chapter 3).

6.3 Hydrogeological clues, atmospheric pressures, aqueous chemistry and alteration minerals derived from geochemical modelling

Geochemical modelling showed that a low temperature (~20 °C) percolating fluid, initially in equilibrium with the martian atmosphere (here constrained to be at a maximum partial pressure of 1 bar CO_2), best describes the first fluids that altered the host rock of ALH 84001 on Mars. The model called for varying compositions of carbonate to precipitate, mostly with silica at the height of carbonate production, as well as changing water to rock ratios and CO_2 pressures. This could be as an effect of changing amounts of water percolating from the surface (Hypothesis 1), or, from a rising and falling water table (Hypothesis 2), all while evaporation of the fluids was taking place (Figure 6-1). As a consequence, copious and varied phyllosilicates (mainly nontronite, chlorite and talc) were required to precipitate, though not at the peak of carbonate production. This appears to be in line with the mineralogy of ALH 84001, where phyllosilicates are rare, but if the computed model is correct, the other minerals should be observed at or near the oldest surfaces of Mars. Nontronite and chlorite have been observed at the Mawrth Vallis region (Bishop et al., 2013, 2008; McKeown et al., 2009; Poulet et al., 2005) and at the Nili Fossae region (Ehlmann et al., 2009; Mangold et al., 2007; Michalski et al., 2010; Mustard et al., 2007; Viviano et al., 2013), and talc is probably present near Nili Fossae (Viviano et

al., 2013), although interpreted as a higher temperature hydrothermal product. However, on Earth and in laboratory studies, talc is stable and able to form at low temperature (see Chapter 4).

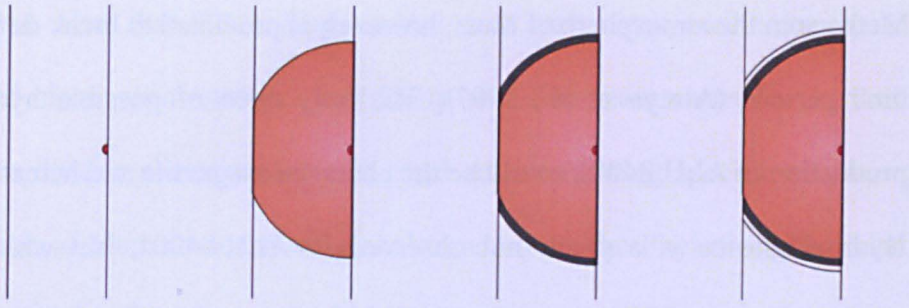

Hypothesis 1	Wetting front arrives	Percolation increased	Percolation maximum	Percolation steady state
Hypothesis 2	Wetting front arrives	Percolation increased	Water table rises	Water table recedes
iW/iR	< 85	85 - 500	> 500	~ 455
Carbonates	Ca > Fe >> Mg	Ca → Fe > Mg	Fe >> Ca +Mg	Mg >> Ca > Fe
Other phases	Talc, chlorite, mt.	SiO_2 + hematite	SiO_2	SiO_2

Figure 6-1. Sequence of the carbonate formation in ALH 84001, from left to right: nucleation of the Ca-rich carbonates on a mineral surface within a fracture, growth of the carbonates and progression to Fe-rich carbonates with increasing W/R, and finally Mg-rich carbonates form when W/R decreases and evaporation dominates in the system.

The reactions that formed magnetite, hematite, methane and hydrogen are important. Hematite formed while carbonates formed in the models, but hematite has also been observed in the carbonates of ALH 84001 (Steele et al., 2007). The work here contains (as far as I am aware) the only detailed computation for hematite precipitation in ALH 84001, as opposed to goethite (Niles et al., 2009), which has not been observed in the meteorite. Magnetite and methane formed at low water to rock ratios, i.e., from percolation past the peak in carbonate production (which occurred when $pCO_2 \approx 0.12$ bar). This reaction prevented further carbonates from forming, as it consumed the CO_2 in the system, marking

a change in redox conditions from the simultaneous precipitation of hematite and carbonate. With the recent detection of methane at Gale crater (Webster et al., 2015), the possibility that methane was formed in low temperature aqueous reactions and locked in the martian subsurface (perhaps as clathrates) is intriguing, especially if the methane is ancient. Methane in the atmosphere of Mars, however, is predicted to break down or escape in short time periods (Atreya et al., 2007). The only trace of possible hydrogen and methane production in ALH 84001 would be the observed magnetite and hematite.

Hydromagnesite is a phase not observed in ALH 84001, but which was predicted to precipitate in the flowing geochemical alteration model, as a consequence of evaporation of the alteration fluids in ALH 84001, after reaction at relatively high W/R (W/R = 455 – 300) with neighbouring rocks of ALH 84001 composition (probably stratigraphically higher). Evaporation was necessary to produce the final Mg-carbonate rims in the carbonate assemblage. Most likely, evaporation was relatively constant throughout the formation of the carbonates, driving the carbonates to more Mg-rich compositions from core to rim as they grew. With this result in mind, hydromagnesite precluded magnesite formation – the latter formed from the dehydration and dehydroxylation of the former with raised temperatures. Eiler et al. (2002a) offered further evidence in favour of hydromagnesite existing in ALH 84001 with hydrogen isotopes, as they contended that the high δD they measured in the meteorite came from martian hydrous salts such as hydromagnesite.

Leachate fluids produced from the alteration of some detected phyllosilicate compositions on Mars (celadonite, chlorite, montmorillonite, nontronite and saponite) did not form enough carbonates in the host rock of ALH 84001, or the range in carbonate compositions observed, so the fluids could not have travelled from extensively weathered terrains to

ALH 84001. Most likely, the alteration fluids weathered rocks of similar composition to ALH 84001, and so were likely to have been relatively local.

The variety of alteration minerals identified by the modelling shows that early Mars was phyllosilicate-rich, but also that Fe-(oxihydr)oxides and carbonates could coexist in relatively similar and close environments. It is likely that fine scale variations in fluid chemistry has lead to diverse alteration minerals, and so, interpreting specific alteration minerals on the surface of Mars as tracers of global trends (e.g., the Phylosian, Theiikian and Siderikian proposed by Bibring et al., 2006) is an oversimplification. Hence, the conditions that ALH 84001 experienced at a particular location near the surface of Mars ~3.9 Ga ago may not have been representative of conditions elsewhere on Mars. Nevertheless, from this work, it can be inferred that even though liquid water was only available (in the system, but perhaps on the surface of Mars) while it had not evaporated, the production of aqueous alteration minerals was extensive. This indicates that perhaps aqueous alteration on early Mars was transient. Atmospheric pressures were low ($pCO_2 < 1$ bar, and likely, < 0.5 bar) liquid water may have been available in limited settings, and yet, aqueous alteration minerals were diverse and abundant, as observed on ancient surfaces. Carbonates would be more the exception than the norm, and would mostly form a small percentage of the alteration assemblage, unless the physicochemical conditions (as in ALH 84001) were especially conducive. Ca-carbonates would form in low W/R environments, and Mg-carbonates under evaporative ones. Excursions to high Fe-carbonate compositions could signify particularly water-rich alteration.

If biological activity ever took place on Mars, the relatively safeguarded formation environment (below the subsurface, formed with higher infiltration) of the carbonates and some of the clays shown to form here, would have been ideal for the purposes of

habitability of simple organisms. The near-neutral waters that formed the carbonates, and the protection from UV and cosmic irradiation of the overlying altered rocks may have aided the establishment of life, but that is not to say that the alteration in ALH 84001 was mediated or in any way affected by biological activity; a suitable abiogenic formation is explained in this thesis.

Current and future missions can benefit from the findings in this work. ExoMars 2018, especially, with its drill, offers the exciting propect of possibly finding organisms beneath the surface. Whether martian organisms are extant, extinct or simply inexistent, the work here has direct relevance for finding suitable target areas for drilling: ancient terrains with phyllosilicates may be ideal, but ancient altered mafic rocks could verify this thesis: silica-rich mafic rocks should grade to carbonate-rich and finally phyllosilicate-rich rocks with depth.

Of course, rovers and mobile science laboratories pave the way to sample return missions, where samples from near the surface of Mars may be studied back on Earth with the precision allowed by the scientific community, much like how meteorites are studied currently. Most importantly though, the crucial, missing aspect of ALH 84001 is its precise geological context on Mars (the hydrogeochemical conditions of which were elucidated in this thesis): the study of ancient Mars would benefit enormously from human exploration.

6.4 Limitations, and observations, in experimental work

While experimental work carried out to produce carbonates analogous to the ones in ALH 84001 had the potential to test, and perhaps even validate the modelled scenarios from Chapter 4, a significantly different setup would have been required. Starting from the selection of host rock samples, and on to the monitoring of the reactions occurring in the

environmental chamber, a number of improvements could be made (detailed in Chapter 5). A particular positive, valuable insight could be gained from the experience: the host rock, while different in bulk rock composition to ALH 84001, was interesting because the magnetite forming reaction ascertained in Chapter 4 (Equations 4-6 to 4-9) could be seen, albeit forming from olivine instead of orthopyroxene. Very fine crystals of magnetite were spread throughout the sample (Figure 5-6), as remnants of the reaction. This, coupled with the high serpentine content and chlorite content, showed that ALH 84001 would have tended to this type of composition had reactions progressed for longer, at further depth and with increasing temperature. The models in Chapter 4 show that with further percolation, talc would have been a major resulting secondary mineral, whereas in the Loch an Daimh Mòr (LDM) serpentinised pyroxenite, the most important alteration mineral was of course, serpentine. But talc (monoclinic or triclinic, $Mg_3Si_4O_{10}(OH)_2$) and serpentine (Mg-antigorite, monoclinic, $Mg_3Si_2O_5(OH)_4$), are compositionally and structurally very similar. The serpentinised pyroxenite appears to be a likely lithology found on Mars, maybe even below to where ALH 84001 originated. Serpentine has been detected from orbit near Nili Fossae, associated with impact craters in Noachian terrains and in olivine-rich strata at the Isidis basin, probably having formed simultaneously with H_2 and magnetite (Ehlmann et al., 2010).

From this, the LDM orthopyroxenite is perhaps still a good analogue to martian mineralogy, and exemplifies the diversity of martian alteration minerals. There is reason to be optimistic about the study of altered analogues and the experimental alteration of analogues, given the variability in martian alteration minerals.

7 Further work

The alteration assemblage in ALH 84001 is almost certainly of a low-temperature, near-surface nature, as demonstrated in this thesis and in work by numerous other authors mentioned throughout this document. However, relatively high temperature thermochemical models have been limited, and remain relatively unexplored. High-temperature (~300 °C) aqueous models can verify the viability of an early martian hydrothermal system capable of forming the carbonates in ALH 84001. The problem with such models would be that most of the evidence (mainly isotopic) points to a low temperature process. Nevertheless, the effects of high temperatures should be explored.

Based on this thesis, further improvements could obviously be made to the experimental work. The insights gained from the laboratory experiments could be the groundwork for experiments simulating the formation of carbonates similar to the ones in ALH 84001. Given the right starting compositions, a flow-reactor setup, and the lessons learnt from the attempts here, an attempt could be made to synthesise the carbonates.

The solar neon isotopic signature obtained in this work is unique. No other martian meteorite appears to contain this primordial signature. A confirmation from a different technique would make this work more robust. The Open University has a unique set of instruments to measure the volatile budgets of small samples – Finesse, the step-combustion system equipped with various mass spectrometers used in this project will soon be equipped to study heavy noble gases (which have not been measured in this work) and Kr/Xe ratios with high accuracy and precision, but the noble gas laboratory in the

Earth, Environment and Ecosystems Department at the Open University would have the benefit of offering spatial resolution to sample individual mineral phases.

Work on the NWA 6234 shergottite is still in progress with the consortium. The exciting results presented in Section 3.2 show that a distinct new phase in a shock-melt vein is likely to be an alteration phase, but further spatially resolved work needs to be carried out to understand the origin and nature of the phases.

The methane and hydrogen producing reactions studied here in ALH 84001 have implications for beyond Mars. Wherever water-rock reactions may take place and CO_2-H_2O reactions can be catalysed to produce methane and hydrogen by iron in rocks, the potential for methane and hydrogen to accumulate may exist. Terrestrial exoplanets enveloped by thick atmospheres and icy moons are places where these reactions could potentially take place. It is no coincidence that they are targeted for the study of potential habitability.

Appendix A

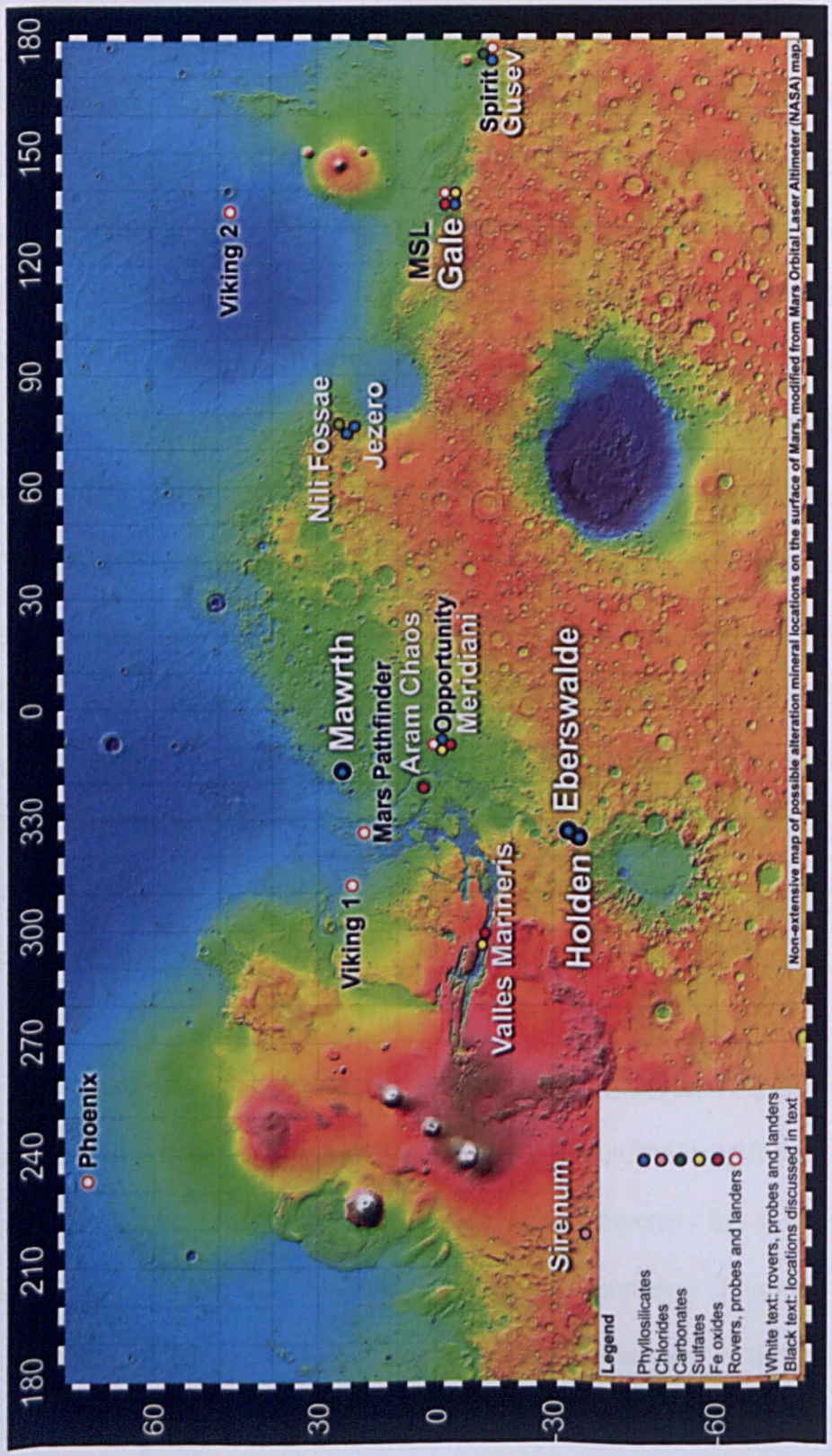
180
210
240
270
300
330
0
30
60
90
120
150
180
60
30
0
-30
-60
Phoenix
Viking 1
Viking 2
Mawrth
Mars Pathfinder
Aram Chaos
Opportunity
Meridiani
Nili Fossae
Jezero
MSL
Gale
Spirit
Gusev
Valles Marineris
Holden
Eberswalde
Sirenum
Legend
Phyllosilicates
Chlorides
Carbonates
Sulfates
Fe oxides
Rovers, probes and landers
White text: rovers, probes and landers
Black text: locations discussed in text
Non-extensive map of possible alteration mineral locations on the surface of Mars, modified from Mars Orbital Laser Altimeter (NASA) map.

Appendix B

Appendix A: Loch an Daimh Mòr sampling locality

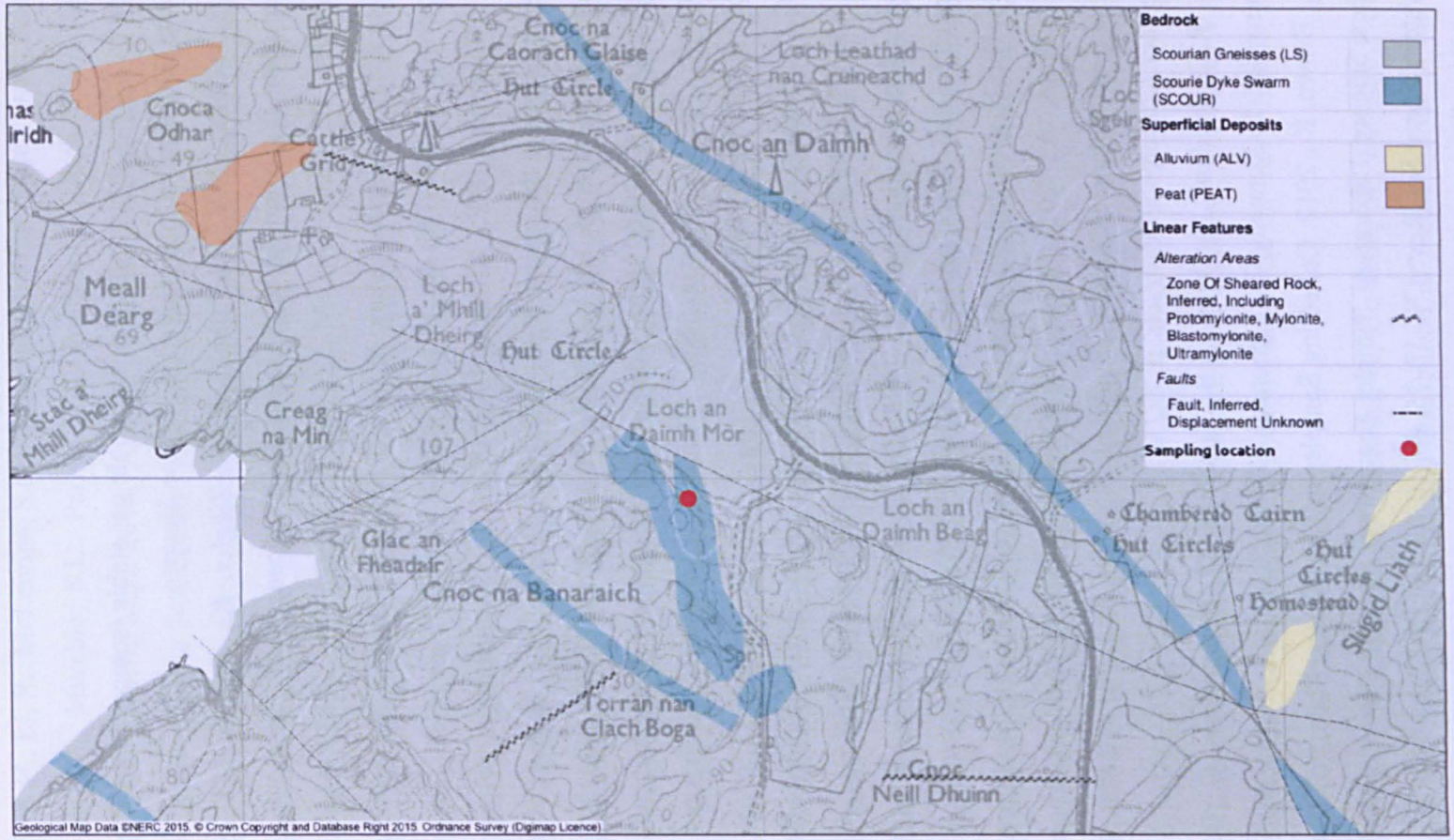

Scale 1:10000

0 100 200 300 400 500 600 700 800 900 1000 m

Digimap

Mohit Melwani Daswani
The Open University

Bibliography

Abernethy, F., 2014. Carbon, nitrogen, and noble gas stable isotopes in angrites, Mars, and Vesta (Doctoral). Open University, Milton Keynes.

Agee, C.B., Wilson, N.V., McCubbin, F.M., Ziegler, K., Polyak, V.J., Sharp, Z.D., Asmerom, Y., Nunn, M.H., Shaheen, R., Thiemens, M.H., Steele, A., Fogel, M.L., Bowden, R., Glamoclija, M., Zhang, Z., Elardo, S.M., 2013. Unique Meteorite from Early Amazonian Mars: Water-Rich Basaltic Breccia Northwest Africa 7034. Science 339, 780–785. doi:10.1126/science.1228858

Aja, S.U., Rosenberg, P.E., Kittrick, J.A., 1991. Illite equilibria in solutions: I. Phase relationships in the system K_2O-Al_2O_3-SiO_2-H_2O between 25 and 250°C. Geochim. Cosmochim. Acta 55, 1353–1364. doi:10.1016/0016-7037(91)90313-T

Akbulut, A., Kadir, S., 2003. Huntite deposits in the neogene lacustrine sediments of the Cameli basin, Denizli, SW Turkey. Carbonates Evaporites 18, 1–9. doi:10.1007/BF03178382

Allègre, C.J., Manhès, G., Göpel, C., 2008. The major differentiation of the Earth at ~ 4.45 Ga. Earth Planet. Sci. Lett. 267, 386–398. doi:10.1016/j.epsl.2007.11.056

Allègre, C.J., Manhès, G., Göpel, C., 1995. The age of the Earth. Geochim. Cosmochim. Acta 59, 1445–1456. doi:10.1016/0016-7037(95)00054-4

Amundsen, H.E.F., Benning, L., Blake, D.F., Fogel, M., Ming, D., Skidmore, M., Steele, A., Team, A., 2011. Cryogenic Origin for Mars Analog Carbonates in the Bockfjord Volcanic Complex, Svalbard (Norway), in: Lunar and Planetary Institute Science Conference Abstracts. p. 2223.

Anderson, R.C., Jandura, L., Okon, A.B., Sunshine, D., Roumeliotis, C., Beegle, L.W., Hurowitz, J., Kennedy, B., Limonadi, D., McCloskey, S., Robinson, M., Seybold, C., Brown, K., 2012. Collecting Samples in Gale Crater, Mars; an Overview of the Mars Science Laboratory Sample Acquisition, Sample Processing and Handling System. Space Sci. Rev. 170, 57–75. doi:10.1007/s11214-012-9898-9

Anthony, J.W., Bideaux, R.A., Bladh, K.W., Nichols, M.C., 2003. Handbook of Mineralogy. Mineralogical Society of America, Chantilly, VA 20151-1110, USA.

Arvidson, R.E., Squyres, S.W., Bell, J.F., Catalano, J.G., Clark, B.C., Crumpler, L.S., de Souza, P.A., Fairén, A.G., Farrand, W.H., Fox, V.K., Gellert, R., Ghosh, A., Golombek, M.P., Grotzinger, J.P., Guinness, E.A., Herkenhoff, K.E., Jolliff, B.L., Knoll, A.H., Li, R., McLennan, S.M., Ming, D.W., Mittlefehldt, D.W., Moore, J.M., Morris, R.V., Murchie, S.L., Parker, T.J., Paulsen, G., Rice, J.W., Ruff, S.W., Smith, M.D., Wolff, M.J., 2014. Ancient Aqueous Environments at Endeavour Crater, Mars. Science 343. doi:10.1126/science.1248097

Arvidson, R.S., Mackenzie, F.T., 1999. The dolomite problem; control of precipitation kinetics by temperature and saturation state. Am. J. Sci. 299, 257–288. doi:10.2475/ajs.299.4.257

Ashley, P.M., 1997. Silica-carbonate alteration zones and gold mineralisation in the Great Serpentinite Belt, New England Orogen, New South Wales. Geol. Soc. Aust. Spec. Publ. 19, 212–225.

Asimow, P.D., Ghiorso, M.S., 1998. Algorithmic modifications extending MELTS to calculate subsolidus phase relations. Am. Mineral. 83, 1127–1132.

Atreya, S.K., Mahaffy, P.R., Wong, A.-S., 2007. Methane and related trace species on Mars: Origin, loss, implications for life, and habitability. Planet. Space Sci. 55, 358–369. doi:10.1016/j.pss.2006.02.005

Baba, S., 1999. Sapphirine-bearing orthopyroxene-kyanite/sillimanite granulites from South Harris, NW Scotland: evidence for Proterozoic UHT metamorphism in the Lewisian. Contrib. Mineral. Petrol. 136, 33–47. doi:10.1007/s004100050522

Baker, L.L., Agenbroad, D.J., Wood, S.A., 2000. Experimental hydrothermal alteration of a martian analog basalt: Implications for martian meteorites. Meteorit. Planet. Sci. 35, 31–38. doi:10.1111/j.1945-5100.2000.tb01971.x

Baker, V.R., 2001. Water and the martian landscape. Nature 412, 228–236. doi:10.1038/35084172

Baker, V.R., Strom, R.G., Gulick, V.C., Kargel, J.S., Komatsu, G., Kale, V.S., 1991. Ancient oceans, ice sheets and the hydrological cycle on Mars. Nature 352, 589–594. doi:10.1038/352589a0

Balme, M., Mangold, N., Baratoux, D., Costard, F., Gosselin, M., Masson, P., Pinet, P., Neukum, G., 2006. Orientation and distribution of recent gullies in the southern hemisphere of Mars: Observations from High Resolution Stereo Camera/Mars Express (HRSC/MEX) and Mars Orbiter Camera/Mars Global Surveyor (MOC/MGS) data. J Geophys Res 111, E05001. doi:10.1029/2005JE002607

Barber, D.J., Scott, E.R.D., 2002. Origin of supposedly biogenic magnetite in the Martian meteorite Allan Hills 84001. Proc. Natl. Acad. Sci. 99, 6556–6561.

Barnes, I., O'Neill, J.R., Rapp, J.B., White, D.E., 1973. Silica-carbonate alteration of serpentine; wall rock alteration in mercury deposits of the California Coast Ranges. Econ. Geol. 68, 388–398.

Barnes, J.J., Franchi, I.A., Anand, M., Tartèse, R., Starkey, N.A., Koike, M., Sano, Y., Russell, S.S., 2013. Accurate and precise measurements of the D/H ratio and hydroxyl content in lunar apatites using NanoSIMS. Chem. Geol. 337–338, 48–55. doi:10.1016/j.chemgeo.2012.11.015

Barrat, J.A., Gillet, P., Lesourd, M., Blichert-Toft, J., Poupeau, G.R., 1999. The Tatahouine diogenite: Mineralogical and chemical effects of sixty-three years of terrestrial residence. Meteorit. Planet. Sci. 34, 91–97. doi:10.1111/j.1945-5100.1999.tb01734.x

Baxter, E.F., 2010. Diffusion of Noble Gases in Minerals. Rev. Mineral. Geochem. 72, 509–557. doi:10.2138/rmg.2010.72.11

Beard, B.L., Ludois, J.M., Lapen, T.J., Johnson, C.M., 2013. Pre-4.0 billion year weathering on Mars constrained by Rb–Sr geochronology on meteorite ALH84001. Earth Planet. Sci. Lett. 361, 173–182. doi:10.1016/j.epsl.2012.10.021

Berkley, J.L., Boynton, N.J., 1992. Minor/major element variation within and among diogenite and howardite orthopyroxenite groups. Meteoritics 27, 387–394. doi:10.1111/j.1945-5100.1992.tb00220.x

Berman, D.C., Hartmann, W.K., 2002. Recent Fluvial, Volcanic, and Tectonic Activity on the Cerberus Plains of Mars. Icarus 159, 1–17. doi:10.1006/icar.2002.6920

Bethke, C.M., Yeakel, S., 2014. GWB Essentials Guide, The Geochemist's Workbench. Aqueous Solutions LLC, Champaign, Illinois.

Bibring, J.-P., Langevin, Y., Mustard, J.F., Poulet, F., Arvidson, R., Gendrin, A., Gondet, B., Mangold, N., Pinet, P., Forget, F., the OMEGA team, Berthé, M., Bibring, J.-P., Gendrin, A., Gomez, C., Gondet, B., Jouglet, D., Poulet, F., Soufflot, A., Vincendon, M., Combes, M., Drossart, P., Encrenaz, T., Fouchet, T., Merchiorri, R., Belluci, G., Altieri, F., Formisano, V., Capaccioni, F., Cerroni, P., Coradini, A., Fonti, S., Korablev, O., Kottsov, V., Ignatiev, N., Moroz, V., Titov, D., Zasova, L., Loiseau, D., Mangold, N., Pinet, P., Douté, S., Schmitt, B., Sotin, C., Hauber, E., Hoffmann, H., Jaumann, R., Keller, U., Arvidson, R., Mustard, J.F., Duxbury, T.,

Forget, F., Neukum, G., 2006. Global Mineralogical and Aqueous Mars History Derived from OMEGA/Mars Express Data. Science 312, 400 –404. doi:10.1126/science.1122659

Bibring, J.-P., Soufflot, A., Berthé, M., Langevin, Y., Gondet, B., Drossart, P., Bouyé, M., Combes, M., Puget, P., Semery, A., 2004. OMEGA: Observatoire pour la Minéralogie, l'Eau, les Glaces et l'Activité, in: Mars Express: The Scientific Payload. pp. 37–49.

Bird, D.K., Schiffman, P., Elders, W.A., Williams, A.E., McDowell, S.D., 1984. Calc-silicate mineralization in active geothermal systems. Econ. Geol. 79, 671–695. doi:10.2113/gsecongeo.79.4.671

Bish, D.L., Blake, D.F., Vaniman, D.T., Chipera, S.J., Morris, R.V., Ming, D.W., Treiman, A.H., Sarrazin, P., Morrison, S.M., Downs, R.T., Achilles, C.N., Yen, A.S., Bristow, T.F., Crisp, J.A., Morookian, J.M., Farmer, J.D., Rampe, E.B., Stolper, E.M., Spanovich, N., Team, M.S., 2013. X-ray Diffraction Results from Mars Science Laboratory: Mineralogy of Rocknest at Gale Crater. Science 341. doi:10.1126/science.1238932

Bishop, J.L., Dobrea, E.Z.N., McKeown, N.K., Parente, M., Ehlmann, B.L., Michalski, J.R., Milliken, R.E., Poulet, F., Swayze, G.A., Mustard, J.F., Murchie, S.L., Bibring, J.-P., 2008. Phyllosilicate Diversity and Past Aqueous Activity Revealed at Mawrth Vallis, Mars. Science 321, 830–833. doi:10.1126/science.1159699

Bishop, J.L., Loizeau, D., McKeown, N.K., Saper, L., Dyar, M.D., Des Marais, D.J., Parente, M., Murchie, S.L., 2013. What the ancient phyllosilicates at Mawrth Vallis can tell us about possible habitability on early Mars. Planet. Space Sci. 86, 130–149. doi:10.1016/j.pss.2013.05.006

Bloch, E., Ganguly, J., 2014. ^{176}Lu–^{176}Hf and ^{147}Sm–^{143}Nd ages of the Martian shergottites: Evaluation of the shock-resetting hypothesis through diffusion kinetic experiments and modeling, and petrological observations. Earth Planet. Sci. Lett. 395, 173–183. doi:10.1016/j.epsl.2014.03.037

Boctor, N.Z., Wang, J., Alexander, C.O.A., Hauri, E., Bertka, C.M., Fei, Y., Humayun, M., 1998. Petrology and hydrogen and sulfur isotope studies of mineral phases in Martian meteorite ALH 84001, in: Lunar and Planetary Institute Science Conference Abstracts. p. 1787.

Bogard, D.D., 1997. A reappraisal of the Martian ^{36} Ar/ ^{38} Ar ratio. J. Geophys. Res. 102, 1653. doi:10.1029/96JE02796

Boutton, T.W., 1991. Stable carbon isotope ratios of natural materials: II. Atmospheric, terrestrial, marine, and freshwater environments. Carbon Isot. Tech. 173–185.

Bouvier, A., Blichert-Toft, J., Albarède, F., 2009. Martian meteorite chronology and the evolution of the interior of Mars. Earth Planet. Sci. Lett. 280, 285–295. doi:10.1016/j.epsl.2009.01.042

Bouvier, A., Blichert-Toft, J., Vervoort, J.D., Albarède, F., 2005. The age of SNC meteorites and the antiquity of the Martian surface. Earth Planet. Sci. Lett. 240, 221–233. doi:10.1016/j.epsl.2005.09.007

Bowes, D.R., Wright, A.E., Park, R.G., 1964. Layered intrusive rocks in the Lewisian of the North-West Highlands of Scotland. Q. J. Geol. Soc. 120, 153–192. doi:10.1144/gsjgs.120.1.0153

Boyd, S.R., Wright, I.P., Franchi, I.A., Pillinger, C.T., 1988. Preparation of sub-nanomole quantities of nitrogen gas for stable isotopic analysis. J. Phys. [E] 21, 876–885. doi:10.1088/0022-3735/21/9/012

Bradley, J.P., Harvey, R.P., McSween Jr., H.Y., 1996. Magnetite whiskers and platelets in the ALH84001 Martian meteorite: Evidence of vapor phase growth. Geochim. Cosmochim. Acta 60, 5149–5155. doi:10.1016/S0016-7037(96)00383-3

Brady, J., Perkins, D., 2012. Mineral Formulae Recalculation [WWW Document]. Miner. Formulae Recalculation. URL http://serc.carleton.edu/18592 (accessed 11.21.14).

Brearley, A.J., 2003. Magnetite in ALH 84001: An origin by shock-induced thermal decomposition of iron carbonate. Meteorit. Planet. Sci. 38, 849–870. doi:10.1111/j.1945-5100.2003.tb00283.x

Brearley, A.J., 2000. Hydrous phases in ALH84001: Further evidence for preterrestrial alteration and a shock-induced thermal overprint, in: Lunar and Planetary Institute Science Conference Abstracts. p. 1203.

Bricker, O.P., Nesbitt, H.W., Gunter, W.D., 1973. Stability of talc. Am. Mineral. 58, 64–72.

Bridges, J.C., Catling, D.C., Saxton, J.M., Swindle, T.D., Lyon, I.C., Grady, M.M., 2001. Alteration Assemblages in Martian Meteorites: Implications for Near-Surface Processes, in: Kallenbach, R., Geiss, J., Hartmann, W. (Eds.), Chronology and Evolution of Mars, Space Sciences Series of ISSI. Springer Netherlands, pp. 365–392.

Bridges, J.C., Grady, M.M., 2000. Evaporite mineral assemblages in the nakhlite (martian) meteorites. Earth Planet. Sci. Lett. 176, 267–279. doi:10.1016/S0012-821X(00)00019-4

Bridges, J.C., Grady, M.M., 1999. A halite-siderite-anhydrite-chlorapatite assemblage in Nakhla: Mineralogical evidence for evaporites on Mars. Meteorit. Planet. Sci. 34, 407–415. doi:10.1111/j.1945-5100.1999.tb01349.x

Bridges, J.C., Schwenzer, S.P., 2012. The nakhlite hydrothermal brine on Mars. Earth Planet. Sci. Lett. 359, 117–123.

Bridges, J.C., Schwenzer, S.P., Leveille, R., Westall, F., Wiens, R.C., Mangold, N., Bristow, T., Edwards, P., Berger, G., 2015. Diagenesis and clay mineral formation at Gale Crater, Mars: Gale Crater Diagenesis. J. Geophys. Res. Planets 120, 1–19. doi:10.1002/2014JE004757

Bridges, J.C., Warren, P.H., 2006. The SNC meteorites: basaltic igneous processes on Mars. J. Geol. Soc. 163, 229–251. doi:10.1144/0016-764904-501

Bullock, M.A., Moore, J.M., Mellon, M.T., 2004. Laboratory simulations of Mars aqueous geochemistry. Icarus 170, 404–423. doi:10.1016/j.icarus.2004.03.016

Carr, M.H., Head, J.W., 2010. Geologic history of Mars. Earth Planet. Sci. Lett. 294, 185–203. doi:doi: DOI: 10.1016/j.epsl.2009.06.042

Carr, M.H., Wänke, H., 1992. Earth and Mars: Water inventories as clues to accretional histories. Icarus 98, 61–71. doi:10.1016/0019-1035(92)90207-N

Cassata, W.S., Shuster, D.L., Renne, P.R., Weiss, B.P., 2012. Trapped Ar isotopes in meteorite ALH 84001 indicate Mars did not have a thick ancient atmosphere. Icarus 221, 461–465. doi:10.1016/j.icarus.2012.05.005

Catling, D.C., 1999. A chemical model for evaporites on early Mars: Possible sedimentary tracers of the early climate and implications for exploration. J. Geophys. Res. 104, 16453. doi:10.1029/1998JE001020

Changela, H.G., Bridges, J.C., 2010. Alteration assemblages in the nakhlites: Variation with depth on Mars. Meteorit. Planet. Sci. 45, 1847–1867. doi:10.1111/j.1945-5100.2010.01123.x

Chassefière, E., Leblanc, F., 2011a. Constraining methane release due to serpentinization by the observed D/H ratio on Mars. Earth Planet. Sci. Lett. 310, 262–271. doi:10.1016/j.epsl.2011.08.013

Chassefière, E., Leblanc, F., 2011b. Methane release and the carbon cycle on Mars. Planet. Space Sci. 59, 207–217. doi:10.1016/j.pss.2010.09.004

Chen, M., El Goresy, A., 2000. The nature of maskelynite in shocked meteorites: not diaplectic glass but a glass quenched from shock-induced dense melt at high pressures. Earth Planet. Sci. Lett. 179, 489–502. doi:10.1016/S0012-821X(00)00130-8

Chevrier, V.F., Rivera-Valentin, E.G., 2012. Formation of recurring slope lineae by liquid brines on present-day Mars. Geophys. Res. Lett. 39, L21202. doi:10.1029/2012GL054119

Chevrier, V., Mathé, P.-E., Rochette, P., Grauby, O., Bourrié, G., Trolard, F., 2006. Iron weathering products in a CO_2 + (H_2O or H_2O_2) atmosphere: Implications for weathering processes on the surface of Mars. Geochim. Cosmochim. Acta 70, 4295–4317. doi:10.1016/j.gca.2006.06.1368

Chevrier, V., Rochette, P., Mathé, P.-E., Grauby, O., 2004. Weathering of iron-rich phases in simulated Martian atmospheres. Geology 32, 1033–1036. doi:10.1130/G21078.1

Chicarro, A., Martin, P., Trautner, R., 2004. The Mars Express mission: an overview. Mars Express Sci. Payload 3–13.

Christensen, P., Jakosky, B., Kieffer, H., Malin, M., McSween, H., Jr., Nealson, K., Mehall, G., Silverman, S., Ferry, S., Caplinger, M., Ravine, M., 2004. The Thermal Emission Imaging System (THEMIS) for the Mars 2001 Odyssey Mission. Space Sci. Rev. 110, 85–130. doi:10.1023/B:SPAC.0000021008.16305.94

Christensen, P.R., 2006. Water at the Poles and in Permafrost Regions of Mars. Elements 2, 151–155.

Christensen, P.R., Bandfield, J.L., Hamilton, V.E., Ruff, S.W., Kieffer, H.H., Titus, T.N., Malin, M.C., Morris, R.V., Lane, M.D., Clark, R.L., Jakosky, B.M., Mellon, M.T., Pearl, J.C., Conrath, B.J., Smith, M.D., Clancy, R.T., Kuzmin, R.O., Roush, T., Mehall, G.L., Gorelick, N., Bender, K., Murray, K., Dason, S., Greene, E., Silverman, S., Greenfield, M., 2001. Mars Global Surveyor Thermal Emission Spectrometer experiment: Investigation description and surface science results. J. Geophys. Res. Planets 106, 23823–23871. doi:10.1029/2000JE001370

Clark, B.C., Arvidson, R.E., Gellert, R., Morris, R.V., Ming, D.W., Richter, L., Ruff, S.W., Michalski, J.R., Farrand, W.H., Yen, A., Herkenhoff, K.E., Li, R., Squyres, S.W., Schröder, C., Klingelhöfer, G., Bell, J.F., 2007. Evidence for montmorillonite or its compositional equivalent in Columbia Hills, Mars. J. Geophys. Res. Planets 112, E06S01. doi:10.1029/2006JE002756

Clifford, S.M., Parker, T.J., 2001. The Evolution of the Martian Hydrosphere: Implications for the Fate of a Primordial Ocean and the Current State of the Northern Plains. Icarus 154, 40–79. doi:10.1006/icar.2001.6671

Corrigan, C.M., Harvey, R.P., 2004. Multi-generational carbonate assemblages in martian meteorite Allan Hills 84001: Implications for nucleation, growth, and alteration. Meteorit. Planet. Sci. 39, 17–30. doi:10.1111/j.1945-5100.2004.tb00047.x

Craddock, R.A., Howard, A.D., 2002. The case for rainfall on a warm, wet early Mars. J. Geophys. Res. Planets 107, 5111. doi:10.1029/2001JE001505

Dauphas, N., Pourmand, A., 2011. Hf-W-Th evidence for rapid growth of Mars and its status as a planetary embryo. Nature 473, 489–492. doi:10.1038/nature10077

Debaille, V., Yin, Q.-Z., Brandon, A.D., Jacobsen, B., 2008. Martian mantle mineralogy investigated by the 176Lu–176Hf and 147Sm–143Nd systematics of shergottites. Earth Planet. Sci. Lett. 269, 186–199. doi:10.1016/j.epsl.2008.02.008

Decarreau, A., Petit, S., Viellard, P., Dabert, N., 2004. Hydrothermal synthesis of aegirine at 200°C. Eur. J. Mineral. 16, 85–90. doi:10.1127/0935-1221/2004/0016-0085

Deer, W.A., Howie, R.A., Zussman, J., 2013. An introduction to the rock-forming minerals, 3rd ed. The Mineralogical Society, London.

Deer, W.A., Howie, R.A., Zussman, J., 1992. An Introduction to the Rock-Forming Minerals, 2nd ed. Prentice Hall, Essex, England.

Dehouck, E., Chevrier, V., Gaudin, A., Mangold, N., Mathé, P.-E., Rochette, P., 2012. Evaluating the role of sulfide-weathering in the formation of sulfates or carbonates on Mars. Geochim. Cosmochim. Acta 90, 47–63. doi:10.1016/j.gca.2012.04.057

Dehouck, E., Gaudin, A., Mangold, N., Lajaunie, L., Dauzères, A., Grauby, O., Le Menn, E., 2014. Weathering of olivine under CO_2 atmosphere: A martian perspective. Geochim. Cosmochim. Acta 135, 170–189. doi:10.1016/j.gca.2014.03.032

De Ros, L.F., Anjos, S.M.C., Morad, S., 1994. Authigenesis of amphibole and its relationship to the diagenetic evolution of lower cretaceous sandstones of the Potiguar rift basin, northeastern Brazil. Sediment. Geol. 88, 253–266. doi:10.1016/0037-0738(94)90065-5

Di Achille, G., Hynek, B.M., 2010. Ancient ocean on Mars supported by global distribution of deltas and valleys. Nat. Geosci 3, 459–463. doi:10.1038/ngeo891

Diniega, S., Hansen, C.J., McElwaine, J.N., Hugenholtz, C.H., Dundas, C.M., McEwen, A.S., Bourke, M.C., 2013. A new dry hypothesis for the formation of martian linear gullies. Icarus 225, 526–537. doi:10.1016/j.icarus.2013.04.006

DoITPoMS - TLP Library Raman Spectroscopy - Raman scattering [WWW Document], 2007. . Raman Spectrosc. URL http://www.doitpoms.ac.uk/tlplib/raman/raman_scattering.php (accessed 11.10.14).

Dollase, W.A., Reeder, R.J., 1986. Crystal structure refinement of huntite, $CaMg_3(CO_3)_4$, with X-ray powder data. Am. Mineral. 71, 163–166.

Dos Santos, M.C., Alvarez, F., 1998. Nitrogen substitution of carbon in graphite: Structure evolution toward molecular forms. Phys. Rev. B 58, 13918–13924.

Dungan, M.A., 1979. A microprobe study of antigorite and some serpentine pseudomorphs. Can. Mineral. 17, 771–784.

Easton, A.J., Hamilton, D., Kempe, D.R.C., Sheppard, S.M.F., Agrell, S.O., 1977. Low-Temperature Metasomatic Garnets in Marine Sediments [and Discussion]. Philos. Trans. R. Soc. Lond. Ser. Math. Phys. Sci. 286, 253–271. doi:10.2307/74717

Ehlmann, B.L., Mustard, J.F., Murchie, S.L., 2010. Geologic setting of serpentine deposits on Mars. Geophys. Res. Lett. 37, L06201. doi:10.1029/2010GL042596

Ehlmann, B.L., Mustard, J.F., Murchie, S.L., Poulet, F., Bishop, J.L., Brown, A.J., Calvin, W.M., Clark, R.N., Des Marais, D.J., Milliken, R.E., Roach, L.H., Roush, T.L., Swayze, G.A., Wray, J.J., 2008. Orbital Identification of Carbonate-Bearing Rocks on Mars. Science 322, 1828 – 1832. doi:10.1126/science.1164759

Ehlmann, B.L., Mustard, J.F., Swayze, G.A., Clark, R.N., Bishop, J.L., Poulet, F., Des Marais, D.J., Roach, L.H., Milliken, R.E., Wray, J.J., Barnouin-Jha, O., Murchie, S.L., 2009. Identification of hydrated silicate minerals on Mars using MRO-CRISM: Geologic context near Nili Fossae and implications for aqueous alteration. J. Geophys. Res. Planets 114, E00D08. doi:10.1029/2009JE003339

Eiler, J.M., Kitchen, N., Leshin, L., Strausberg, M., 2002a. Hosts of hydrogen in Allan Hills 84001: Evidence for hydrous martian salts in the oldest martian meteorite? Meteorit. Planet. Sci. 37, 395–405. doi:10.1111/j.1945-5100.2002.tb00823.x

Eiler, J.M., Valley, J.W., Graham, C.M., Fournelle, J., 2002b. Two populations of carbonate in ALH84001: geochemical evidence for discrimination and genesis. Geochim. Cosmochim. Acta 66, 1285–1303. doi:10.1016/S0016-7037(01)00847-X

El Goresy, A., Gillet, P., Miyahara, M., Ohtani, E., Ozawa, S., Beck, P., Montagnac, G., 2013. Shock-induced deformation of Shergottites: Shock-pressures and perturbations of magmatic ages on Mars. Geochim. Cosmochim. Acta 101, 233–262. doi:10.1016/j.gca.2012.10.002

Elliott, J.C., 1994. Structure and Chemistry of the Apatites and Other Calcium Orthophosphates. Stud. Inorg. Chem. 18, ALL.

Ernst, W.G., 1962. Synthesis, stability relations, and occurrence of riebeckite and riebeckite-arfvedsonite solid solutions. J. Geol. 689–736.

Eugster, O., 1994. Orthopyroxenite ALH 84001: Ejection from Mars (?) 15 Ma. Meteoritics 29, 464.

Eugster, O., Michel, T., 1995. Common asteroid break-up events of eucrites, diogenites, and howardites and cosmic-ray production rates for noble gases in achondrites. Geochim. Cosmochim. Acta 59, 177–199. doi:10.1016/0016-7037(94)00327-I

Eugster, O., Weigel, A., Polnau, E., 1997. Ejection times of Martian meteorites. Geochim. Cosmochim. Acta 61, 2749–2757. doi:10.1016/S0016-7037(97)00115-4

Evans, B.W., 2004. The Serpentinite Multisystem Revisited: Chrysotile Is Metastable. Int. Geol. Rev. 46, 479–506. doi:10.2747/0020-6814.46.6.479

Farley, K.A., Malespin, C., Mahaffy, P., Grotzinger, J.P., Vasconcelos, P.M., Milliken, R.E., Malin, M., Edgett, K.S., Pavlov, A.A., Hurowitz, J.A., Grant, J.A., Miller, H.B., Arvidson, R., Beegle, L., Calef, F., Conrad, P.G., Dietrich, W.E., Eigenbrode, J., Gellert, R., Gupta, S., Hamilton, V., Hassler, D.M., Lewis, K.W., McLennan, S.M., Ming, D., Navarro-González, R., Schwenzer, S.P., Steele, A., Stolper, E.M., Sumner, D.Y., Vaniman, D., Vasavada, A., Williford, K., Wimmer-Schweingruber, R.F., the MSL Science Team, 2014. In Situ Radiometric and Exposure Age Dating of the Martian Surface. Science 343. doi:10.1126/science.1247166

Fassett, C.I., Head, J.W., 2011. Sequence and timing of conditions on early Mars. Icarus 211, 1204–1214. doi:10.1016/j.icarus.2010.11.014

Fassett, C.I., Head, J.W., 2008. The timing of martian valley network activity: Constraints from buffered crater counting. Icarus 195, 61–89. doi:10.1016/j.icarus.2007.12.009

Filiberto, J., Abernethy, F., Butler, I.B., Cartwright, J., Chin, E.J., Day, J.M., Goodrich, C., Grady, M., Gross, J., Franchi, I., Herd, C.D., Kelley, S.P., Ott, U., Penniston-Dorland, S.C., Schwenzer, S.P., Treiman, A.H., 2011. Maximizing the science return from 3.3 g of martian meteorite: A consortium study of olivine-phyric shergottite NorthWest Africa 6234. AGU Fall Meet. Abstr. B3.

Filiberto, J., Chin, E., Day, J.M.D., Franchi, I.A., Greenwood, R.C., Gross, J., Penniston-Dorland, S.C., Schwenzer, S.P., Treiman, A.H., 2012: Geochemistry of intermediate olivine-phyric shergottite Northwest Africa 6234, with similarities to basaltic shergottite Northwest Africa 480 and olivine-phyric shergottite Northwest

Africa 2990. Meteorit. Planet. Sci. 47, 1256–1273. doi:10.1111/j.1945-5100.2012.01382.x

Filiberto, J., Goodrich, C.A., Treiman, A.H., Gross, J., Giesting, P.A., 2014. Evidence for Magmatic-Hydrothermal Activity on Mars from Cl-Rich Scapolite in Nakhla, in: Lunar and Planetary Institute Science Conference Abstracts. p. 1620.

Filiberto, J., Schwenzer, S.P., 2013. Alteration mineralogy of Home Plate and Columbia Hills—Formation conditions in context to impact, volcanism, and fluvial activity. Meteorit. Planet. Sci. 48, 1937–1957. doi:10.1111/maps.12207

Fireman, E.L., Norris, T.L., 1982. Ages and composition of gas trapped in Allan Hills and Byrd core ice. Earth Planet. Sci. Lett. 60, 339–350.

Forbes, W.C., 1977. Stability relations of grunerite, $Fe_7Si_8O_{22}(OH)_2$. Am. J. Sci. 277, 735–749. doi:10.2475/ajs.277.6.735

Forget, F., Wordsworth, R., Millour, E., Madeleine, J.-B., Kerber, L., Leconte, J., Marcq, E., Haberle, R.M., 2013. 3D modelling of the early martian climate under a denser CO_2 atmosphere: Temperatures and CO_2 ice clouds. Icarus 222, 81–99. doi:10.1016/j.icarus.2012.10.019

Foster, M.D., Washing, D.C., 1967. Tetrasilicic dioctahedral micas–celadonite from near Reno, Nevada. US Geol. Surv. Prof. Pap. 17–22.

French, B.M., 1973. Mineral Assemblages in Diagenetic and Low-Grade Metamorphic Iron-Formation. Econ. Geol. 68, 1063–1074. doi:10.2113/gsecongeo.68.7.1063

Fridriksson, T., Neuhoff, P.S., Arnórsson, S., Bird, D.K., 2001. Geological constraints on the thermodynamic properties of the stilbite—stellerite solid solution in low-grade metabasalts. Geochim. Cosmochim. Acta 65, 3993–4008. doi:10.1016/S0016-7037(01)00629-9

Gaffney, A.M., Borg, L.E., Asmerom, Y., Shearer, C.K., Burger, P.V., 2011. Disturbance of isotope systematics during experimental shock and thermal metamorphism of a lunar basalt with implications for Martian meteorite chronology. Meteorit. Planet. Sci. 46, 35–52. doi:10.1111/j.1945-5100.2010.01137.x

Garrels, R.M., Thompson, M.E., Siever, R., 1960. Stability of some carbonates at 25 degrees C and one atmosphere total pressure. Am. J. Sci. 258, 402–418. doi:10.2475/ajs.258.6.402

Garrison, D.H., Bogard, D.D., 1998. Isotopic composition of trapped and cosmogenic noble gases in several Martian meteorites. Meteorit. Planet. Sci. 33, 721–736. doi:10.1111/j.1945-5100.1998.tb01678.x

Garrison, D.H., Rao, M.N., Bogard, D.D., 1995. Solar-proton-produced neon in shergottite meteorites and implications for their origin. Meteoritics 30, 738–747. doi:10.1111/j.1945-5100.1995.tb01172.x

Gat, J.R., Mook, W.G., Meijer, H.A., 2001. Environmental isotopes in the hydrological cycle. Princ. Appl. UNESCOIAEA Ser. 2, 63–67.

Ghiorso, M.S., Hirschmann, M.M., Reiners, P.W., Kress, V.C., 2002. The pMELTS: A revision of MELTS for improved calculation of phase relations and major element partitioning related to partial melting of the mantle to 3 GPa. Geochem. Geophys. Geosystems 3, 1–35. doi:10.1029/2001GC000217

Ghiorso, M.S., Sack, R.O., 1995. Chemical mass transfer in magmatic processes IV. A revised and internally consistent thermodynamic model for the interpolation and extrapolation of liquid-solid equilibria in magmatic systems at elevated temperatures and pressures. Contrib. Mineral. Petrol. 119, 197–212. doi:10.1007/BF00307281

Gleason, J.D., Kring, D.A., Hill, D.H., Boynton, W.V., 1997. Petrography and bulk chemistry of Martian orthopyroxenite ALH84001: Implications for the origin of secondary carbonates. Geochim. Cosmochim. Acta 61, 3503–3512. doi:10.1016/S0016-7037(97)00173-7

Golden, D.C., Ming, D.W., Morris, R.V., Brearley, A.J., Lauer, H.V., Treiman, A.H., Zolensky, M.E., Schwandt, C.S., Lofgren, G.E., McKay, G.A., 2004. Evidence for exclusively inorganic formation of magnetite in Martian meteorite ALH84001. Am. Mineral. 89, 681–695.

Golden, D.C., Ming, D.W., Schwandt, C.S., Lauer, H.V., Socki, R.A., Morris, R.V., Lofgren, G.E., McKay, G.A., 2001. A simple inorganic process for formation of carbonates, magnetite, and sulfides in Martian meteorite ALH84001. Am. Mineral. 86, 370–375.

Golden, D.C., Ming, D.W., Schwandt, C.S., Morris, R.V., Yang, S.V., Lofgren, G.E., 2000. An experimental study on kinetically-driven precipitation of calcium-magnesium-iron carbonates from solution: Implications for the low-temperature formation of carbonates in martian meteorite Allan Hills 84001. Meteorit. Planet. Sci. 35, 457–465. doi:10.1111/j.1945-5100.2000.tb01428.x

Gooding, J.L., 1992. Soil mineralogy and chemistry on Mars: Possible clues from salts and clays in SNC meteorites. Icarus 99, 28–41. doi:10.1016/0019-1035(92)90168-7

Gooding, J.L., Wentworth, S.J., Zolensky, M.E., 1988. Calcium carbonate and sulfate of possible extraterrestrial origin in the EETA 79001 meteorite. Geochim. Cosmochim. Acta 52, 909–915. doi:10.1016/0016-7037(88)90361-4

Goodrich, C.A., 2002. Olivine-phyric martian basalts: A new type of shergottite. Meteorit. Planet. Sci. 37, B31–B34. doi:10.1111/j.1945-5100.2002.tb00901.x

Grady, M.M., Gibson, E.K., Wright, I.P., Pillinger, C.T., 1989. The formation of weathering products on the LEW 85320 ordinary chondrite: Evidence from carbon and oxygen stable isotope compositions and implications for carbonates in SNC meteorites. Meteoritics 24, 1–7. doi:10.1111/j.1945-5100.1989.tb00934.x

Grady, M.M., Verchovsky, A.B., Franchi, I.A., Wright, I.P., Pillinger, C.T., 2002. Light dement geochemistry of the Tagish Lake CI2 chondrite: Comparison with CI1 and CM2 meteorites. Meteorit. Planet. Sci. 37, 713–735. doi:10.1111/j.1945-5100.2002.tb00851.x

Grady, M.M., Verchovsky, A.B., Wright, I.P., 2004. Magmatic carbon in Martian meteorites: Attempts to constrain the carbon cycle on Mars. Int. J. Astrobiol. 3, 117–124.

Grady, M.M., Wright, I.P., 2003. Elemental and isotopic abundances of carbon and nitrogen in meteorites. Space Sci. Rev. 106, 231–248.

Grady, M.M., Wright, I.P., Douglas, C., Pillinger, C.T., 1994. Carbon and nitrogen in ALH84001. Meteoritics 29, 469.

Grady, M.M., Wright, I.P., Pillinger, C.T., 1998. A nitrogen and argon stable isotope study of Allan Hills 84001: Implications for the evolution of the Martian atmosphere. Meteorit. Planet. Sci. 33, 795–802. doi:10.1111/j.1945-5100.1998.tb01686.x

Grady, M.M., Wright, I.P., Pillinger, C.T., 1995. A search for nitrates in Martian meteorites. J. Geophys. Res. Planets 100, 5449–5455. doi:10.1029/94JE02803

Greenwood, J.P., Blake, R.E., Coath, C.D., 2003. Ion microprobe measurements of $^{18}O/^{16}O$ ratios of phosphate minerals in the Martian meteorites ALH84001 and Los Angeles. Geochim. Cosmochim. Acta 67, 2289–2298. doi:10.1016/S0016-7037(03)00130-3

Greenwood, J.P., McSween, Jr., H.Y., 2001. Petrogenesis of Allan Hills 84001: Constraints from impact-melted feldspathic and silica glasses. Meteorit. Planet. Sci. 36, 43–62. doi:10.1111/j.1945-5100.2001.tb01809.x

Greenwood, J.P., Mojzsis, S.J., Coath, C.D., 2000. Sulfur isotopic compositions of individual sulfides in Martian meteorites ALH84001 and Nakhla: implications for crust–regolith exchange on Mars. Earth Planet. Sci. Lett. 184, 23–35. doi:10.1016/S0012-821X(00)00301-0

Greenwood, J.P., Riciputi, L.R., McSween Jr., H.Y., 1997. Sulfide isotopic compositions in shergottites and ALH84001, and possible implications for life on Mars. Geochim. Cosmochim. Acta 61, 4449–4453. doi:10.1016/S0016-7037(97)00246-9

Grimm, R.E., Harrison, K.P., Stillman, D.E., 2014. Water budgets of martian recurring slope lineae. Icarus 233, 316–327. doi:10.1016/j.icarus.2013.11.013

Gross, J., Filiberto, J., Herd, C.D.K., Melwani Daswani, M., Schwenzer, S.P., Treiman, A.H., 2013. Petrography, mineral chemistry, and crystallization history of olivine-phyric shergottite NWA 6234: A new melt composition. Meteorit. Planet. Sci. 48, 854–871. doi:10.1111/maps.12092

Gross, J., Filiberto, J., Treiman, A.H., Herd, C.D.K., Melwani Daswani, M., Schwenzer, S.P., 2012. Petrography, Mineral Chemistry, and Crystallization History of Olivine-Phyric Shergottite NWA6234: A New Intermediate Melt Composition, in: Lunar and Planetary Institute Science Conference Abstracts, Lunar and Planetary Inst. Technical Report. p. 2693.

Grotzinger, J.P., Sumner, D.Y., Kah, L.C., Stack, K., Gupta, S., Edgar, L., Rubin, D., Lewis, K., Schieber, J., Mangold, N., Milliken, R., Conrad, P.G., DesMarais, D., Farmer, J., Siebach, K., Calef, F., Hurowitz, J., McLennan, S.M., Ming, D., Vaniman, D., Crisp, J., Vasavada, A., Edgett, K.S., Malin, M., Blake, D., Gellert, R., Mahaffy, P., Wiens, R.C., Maurice, S., Grant, J.A., Wilson, S., Anderson, R.C., Beegle, L., Arvidson, R., Hallet, B., Sletten, R.S., Rice, M., Bell, J., Griffes, J., Ehlmann, B., Anderson, R.B., Bristow, T.F., Dietrich, W.E., Dromart, G., Eigenbrode, J., Fraeman, A., Hardgrove, C., Herkenhoff, K., Jandura, L., Kocurek, G., Lee, S., Leshin, L.A., Leveille, R., Limonadi, D., Maki, J., McCloskey, S., Meyer, M., Minitti, M., Newsom, H., Oehler, D., Okon, A., Palucis, M., Parker, T., Rowland, S., Schmidt, M., Squyres, S., Steele, A., Stolper, E., Summons, R., Treiman, A., Williams, R., Yingst, A., Team, M.S., 2014. A Habitable Fluvio-Lacustrine Environment at Yellowknife Bay, Gale Crater, Mars. Science 343. doi:10.1126/science.1242777

Haas, H., Banewiez, Jj., 1980. Radiocarbon Dating of Boise Apatite Using Thermal Release of CO_2. Radiocarbon 22, 537–544.

Haas, H., Holdaway, M.J., 1973. Equilibria in the system Al_2O_3-SiO_2-H_2O involving the stability limits of pyrophyllite, and thermodynamic data of pyrophyllite. Am. J. Sci. 273, 449–464.

Halevy, I., Fischer, W.W., Eiler, J.M., 2011. Carbonates in the Martian meteorite Allan Hills 84001 formed at 18 ± 4 °C in a near-surface aqueous environment. Proc. Natl. Acad. Sci. 108, 16895–16899. doi:10.1073/pnas.1109444108

Halevy, I., Zuber, M.T., Schrag, D.P., 2007. A Sulfur Dioxide Climate Feedback on Early Mars. Science 318, 1903–1907. doi:10.1126/science.1147039

Hänchen, M., Prigiobbe, V., Baciocchi, R., Mazzotti, M., 2008. Precipitation in the Mg-carbonate system—effects of temperature and CO_2 pressure. Chem. Eng. Sci. 63, 1012–1028. doi:10.1016/j.ces.2007.09.052

Hartley, A., Flint, S., Turner, P., 1991. Analcime: A characteristic authigenic phase of andean alluvium, northern chile. Geol. J. 26, 189–202. doi:10.1002/gj.3350260302

Harvey, R.P., McSween, H.Y., 1996. A possible high-temperature origin for the carbonates in the martian meteorite ALH84001. Nature 382, 49–51. doi:10.1038/382049a0

Hemley, J.J., Montoya, J.W., Shaw, D.R., Luce, R.W., 1977. Mineral equilibria in the MgO-SiO_2-H_2O system; II, Talc-antigorite-forsterite-anthophyllite-enstatite stability relations and some geologic implications in the system. Am. J. Sci. 277, 353–383. doi:10.2475/ajs.277.4.353

Herd, C.D.., Borg, L.E., Jones, J.H., Papike, J.J., 2002. Oxygen fugacity and geochemical variations in the martian basalts: implications for martian basalt petrogenesis and the oxidation state of the upper mantle of Mars. Geochim. Cosmochim. Acta 66, 2025–2036. doi:10.1016/S0016-7037(02)00828-1

Herd, C.D.K., 2003. The oxygen fugacity of olivine-phyric martian basalts and the components within the mantle and crust of Mars. Meteorit. Planet. Sci. 38, 1793–1805. doi:10.1111/j.1945-5100.2003.tb00015.x

Hicks, L.J., Bridges, J.C., Gurman, S.J., 2014. Ferric saponite and serpentine in the nakhlite martian meteorites. Geochim. Cosmochim. Acta 136, 194–210. doi:10.1016/j.gca.2014.04.010

Hirschmann, M.M., Withers, A.C., 2008. Ventilation of CO_2 from a reduced mantle and consequences for the early Martian greenhouse. Earth Planet. Sci. Lett. 270, 147–155. doi:10.1016/j.epsl.2008.03.034

Hoefs, J., 2009. Stable isotope geochemistry, Sixth edition. ed. Springer, Berlin.

Holland, T.J.B., Powell, R., 1998. An internally consistent thermodynamic data set for phases of petrological interest. J. Metamorph. Geol. 16, 309–343.

Hollingbery, L.A., Hull, T.R., 2010. The thermal decomposition of huntite and hydromagnesite—A review. Thermochim. Acta 509, 1–11. doi:10.1016/j.tca.2010.06.012

Hoppe, P., Amari, S., Zinner, E., Lewis, R.S., 1995. Isotopic compositions of C, N, O, Mg, and Si, trace element abundances, and morphologies of single circumstellar graphite grains in four density fractions from the Murchison meteorite. Geochim. Cosmochim. Acta 59, 4029–4056. doi:10.1016/0016-7037(95)00280-D

Huang, W., Rubenach, M., 1995. Structural controls on syntectonic metasomatic tremolite and tremolite-plagioclase pods in the Molanite Valley, Mt. Isa, Australia. J. Struct. Geol. 17, 83–94.

Humayun, M., Nemchin, A., Zanda, B., Hewins, R.H., Grange, M., Kennedy, A., Lorand, J.-P., Gopel, C., Fieni, C., Pont, S., Deldicque, D., 2013. Origin and age of the earliest Martian crust from meteorite NWA[thinsp]7533. Nature 503, 513–516.

Imahashi, M., Takamatsu, N., 1976. The Dissolution of Titanium Minerals in Hydrochloric and Sulfuric Acids. Bull. Chem. Soc. Jpn. 49, 1549–1553. doi:10.1246/bcsj.49.1549

Irving, A.J., Herd, C.D.K., Gellissen, M., Kuehner, S.M., Bunch, T.E., 2011. Paired Fine Grained, Permafic Olivine-Phyric Shergottites Northwest Africa 2990/5960/6234/6710: Trace Element Evidence for a New Type of Martian Mantle Source or Complex Lithospheric Assimilation Processes. Meteorit. Planet. Sci. Suppl. 74, 5232.

Jakosky, B.M., Phillips, R.J., 2001. Mars' volatile and climate history. nature 412, 237–244.

Jenkins, D.M., Bozhilov, K.N., 2003. Stability and thermodynamic properties of ferro-actinolite: A re-investigation. Am. J. Sci. 303, 723–752. doi:10.2475/ajs.303.8.723

Johannes, W., 1969. An experimental investigation of the system MgO-SiO_2-H_2O-CO_2. Am. J. Sci. 267, 1083–1104. doi:10.2475/ajs.267.9.1083

Johnson, J.W., Oelkers, E.H., Helgeson, H.C., 1992. SUPCRT92: A software package for calculating the standard molal thermodynamic properties of minerals, gases, aqueous species, and reactions from 1 to 5000 bar and 0 to 1000°C. Comput. Geosci. 18, 899–947. doi:10.1016/0098-3004(92)90029-Q

Jones, K., Blake, S., Open University, 2003. Mountain building in Scotland. The Open University, Milton Keynes.

Jull, A.J.T., Courtney, C., Jeffrey, D.A., Beck, J.W., 1998. Isotopic Evidence for a Terrestrial Source of Organic Compounds Found in Martian Meteorites Allan Hills 84001 and Elephant Moraine 79001. Science 279, 366–369. doi:10.1126/science.279.5349.366

Jull, A.J.T., Eastoe, C.J., Cloudt, S., 1997. Isotopic composition of carbonates in the SNC meteorites, Allan Hills 84001 and Zagami. J. Geophys. Res. Planets 1991–2012 102, 1663–1669.

Jull, A.J.T., Eastoe, C.J., Xue, S., Herzog, G.F., 1995. Isotopic composition of carbonates in the SNC meteorites Allan Hills 84001 and Nakhla. Meteoritics 30, 311–318. doi:10.1111/j.1945-5100.1995.tb01129.x

Kanaris-Sotiriou, R., Angus, N.S., 1979. Metasomatic reaction between acid pegmatite and orthopyroxenite at Currywongaun, Connemara, Ireland. Mineral. Mag. 43, 473–478.

Kazmierczak, J., Kempe, S., 2003. Modern terrestrial analogues for the carbonate globules in Martian meteorite ALH84001. Naturwissenschaften 90, 167–172. doi:10.1007/s00114-003-0411-x

Kempe, S., Kazmierczak, J., 1997. A terrestrial model for an alkaline martian hydrosphere. Planet. Space Sci. 45, 1493–1499. doi:10.1016/S0032-0633(97)00116-5

Kent, A.J.R., Hutcheon, I.D., Ryerson, F.J., Phinney, D.L., 2001. The temperature of formation of carbonate in martian meteorite ALH84001: constraints from cation diffusion. Geochim. Cosmochim. Acta 65, 311–321. doi:10.1016/S0016-7037(00)00528-7

Kinsman, D.J.J., 1967. Huntite from a carbonate-evaporite environment. Am. Mineral. 52, 1332.

Kite, E.S., Williams, J.-P., Lucas, A., Aharonson, O., 2014. Low palaeopressure of the martian atmosphere estimated from the size distribution of ancient craters. Nat. Geosci. 7, 335–339. doi:10.1038/ngeo2137

Klingsberg, C., Roy, R., 1959. Stability and interconvertibility of phases in the system Mn-O-OH. Am. Mineral. 44, 819–838.

Koeberl, C., Reimold, W.U., Blum, J.D., Chamberlain, C.P., 1998. Petrology and geochemistry of target rocks from the Bosumtwi impact structure, Ghana, and

comparison with Ivory Coast tektites. Geochim. Cosmochim. Acta 62, 2179–2196. doi:10.1016/S0016-7037(98)00137-9

Kopp, R.E., Humayun, M., 2003. Kinetic model of carbonate dissolution in Martian meteorite ALH84001. Geochim. Cosmochim. Acta 67, 3247–3256. doi:10.1016/S0016-7037(02)01114-6

Kounaves, S.P., Carrier, B.L., O'Neil, G.D., Stroble, S.T., Claire, M.W., 2014. Evidence of martian perchlorate, chlorate, and nitrate in Mars meteorite EETA79001: Implications for oxidants and organics. Icarus 229, 206–213. doi:10.1016/j.icarus.2013.11.012

Koziol, A.M., 2004. Experimental determination of siderite stability and application to Martian Meteorite ALH84001. Am. Mineral. 89, 294–300.

Krasnopolsky, V.A., Gladstone, G.R., 1996. Helium on Mars: EUVE and PHOBOS data and implications for Mars' evolution. J. Geophys. Res. 101, 15765. doi:10.1029/96JA01080

Krasnopolsky, V., Gladstone, G., 2005. Helium on Mars and Venus: EUVE observations and modeling. Icarus 176, 395–407. doi:10.1016/j.icarus.2005.02.005

Kring, D., Swindle, T., Gleason, J., Grier, J., 1998. Formation and relative ages of maskelynite and carbonate in ALH84001. Geochim. Cosmochim. Acta 62, 2155–2166. doi:10.1016/S0016-7037(98)00133-1

Lapen, T.J., Righter, M., Brandon, A.D., Debaille, V., Beard, B.L., Shafer, J.T., Peslier, A.H., 2010. A Younger Age for ALH84001 and Its Geochemical Link to Shergottite Sources in Mars. Science 328, 347 –351. doi:10.1126/science.1185395

Larkin, P., 2011a. Chapter 1 - Introduction: Infrared and Raman Spectroscopy, in: Larkin, P. (Ed.), Infrared and Raman Spectroscopy. Elsevier, Oxford, pp. 1–5.

Larkin, P., 2011b. Chapter 2 - Basic Principles, in: Larkin, P. (Ed.), Infrared and Raman Spectroscopy. Elsevier, Oxford, pp. 7–25.

Laverne, C., 1987. Unusual occurrences of aegirine-augite, fassaite and melanite in oceanic basalts (DSDP Hole 504B). Lithos 20, 135–151. doi:10.1016/0024-4937(87)90003-X

Lécuyer, C., Gillet, P., Robert, F., 1998. The hydrogen isotope composition of seawater and the global water cycle. Chem. Geol. 145, 249–261. doi:10.1016/S0009-2541(97)00146-0

Lodders, K., 1998. A survey of shergottite, nakhlite and chassigny meteorites whole-rock compositions. Meteorit. Planet. Sci. 33, A183–A190. doi:10.1111/j.1945-5100.1998.tb01331.x

Lunine, J.I., Chambers, J., Morbidelli, A., Leshin, L.A., 2003. The origin of water on Mars. Icarus 165, 1–8. doi:10.1016/S0019-1035(03)00172-6

Lupton, J.E., Arculus, R.J., Evans, L.J., Graham, D.W., 2012. Mantle hotspot neon in basalts from the Northwest Lau Back-arc Basin. Geophys. Res. Lett. 39, L08308. doi:10.1029/2012GL051201

Mahaffy, P.R., Webster, C.R., Atreya, S.K., Franz, H., Wong, M., Conrad, P.G., Harpold, D., Jones, J.J., Leshin, L.A., Manning, H., Owen, T., Pepin, R.O., Squyres, S., Trainer, M., MSL Science Team, 2013. Abundance and Isotopic Composition of Gases in the Martian Atmosphere from the Curiosity Rover. Science 341, 263–266. doi:10.1126/science.1237966

Malin, M.C., Bell, J.F., Cantor, B.A., Caplinger, M.A., Calvin, W.M., Clancy, R.T., Edgett, K.S., Edwards, L., Haberle, R.M., James, P.B., 2007. Context camera investigation on board the Mars Reconnaissance Orbiter. J. Geophys. Res. Planets 1991–2012 112.

Malin, M.C., Edgett, K.S., 2001. Mars Global Surveyor Mars Orbiter Camera: Interplanetary cruise through primary mission. J. Geophys. Res. Planets 106, 23429–23570. doi:10.1029/2000JE001455

Malin, M.C., Edgett, K.S., Posiolova, L.V., McColley, S.M., Dobrea, E.Z.N., 2006. Present-Day Impact Cratering Rate and Contemporary Gully Activity on Mars. Science 314, 1573–1577. doi:10.1126/science.1135156

Mangold, N., Mangeney, A., Migeon, V., Ansan, V., Lucas, A., Baratoux, D., Bouchut, F., 2010. Sinuous gullies on Mars: Frequency, distribution, and implications for flow properties. J. Geophys. Res. Planets 115, E11001. doi:10.1029/2009JE003540

Mangold, N., Poulet, F., Mustard, J.F., Bibring, J.-P., Gondet, B., Langevin, Y., Ansan, V., Masson, P., Fasset, C., Head III, J.W., Hoffmann, H., Neukum, G., 2007. Mineralogy of the Nili Fossae region with OMEGA/Mars Express data: 2. Aqueous alteration of the crust. J. Geophys. Res. 112. doi:10.1029/2006JE002835

Marion, G.M., Mironenko, M.V., Roberts, M.W., 2010. FREZCHEM: A geochemical model for cold aqueous solutions. Comput. Geosci. 36, 10–15. doi:10.1016/j.cageo.2009.06.004

Marti, K., Mathew, K.J., 2000. Ancient Martian nitrogen. Geophys. Res. Lett. 27, 1463–1466. doi:10.1029/1999GL011064

Marty, B., 2012. The origins and concentrations of water, carbon, nitrogen and noble gases on Earth. Earth Planet. Sci. Lett. 313–314, 56–66. doi:10.1016/j.epsl.2011.10.040

Marumo, K., 1989. Genesis of kaolin minerals and pyrophyllite in Kuroko deposits of Japan: Implications for the origins of the hydrothermal fluids from mineralogical and stable isotope data. Geochim. Cosmochim. Acta 53, 2915–2924. doi:10.1016/0016-7037(89)90168-3

Maruyama, S., Liou, J.G., 1988. Petrology of Franciscan Metabasites Along the Jadeite-Glaucophane Type Facies Series, Cazadero, California. J. Petrol. 29, 1–37. doi:10.1093/petrology/29.1.1

Mathew, K.J., Marti, K., 2001. Early evolution of Martian volatiles: Nitrogen and noble gas components in ALH84001 and Chassigny. J. Geophys. Res. 106, 1401. doi:10.1029/2000JE001255

McCubbin, F.M., Hauri, E.H., Elardo, S.M., Vander Kaaden, K.E., Wang, J., Shearer, C.K., 2012. Hydrous melting of the martian mantle produced both depleted and enriched shergottites. Geology 40, 683–686. doi:10.1130/G33242.1

McEwen, A.S., Dundas, C.M., Mattson, S.S., Toigo, A.D., Ojha, L., Wray, J.J., Chojnacki, M., Byrne, S., Murchie, S.L., Thomas, N., 2014. Recurring slope lineae in equatorial regions of Mars. Nat. Geosci 7, 53–58.

McEwen, A.S., Eliason, E.M., Bergstrom, J.W., Bridges, N.T., Hansen, C.J., Delamere, W.A., Grant, J.A., Gulick, V.C., Herkenhoff, K.E., Keszthelyi, L., 2007. Mars reconnaissance orbiter's high resolution imaging science experiment (HiRISE). J. Geophys. Res. Planets 1991–2012 112.

McEwen, A.S., Ojha, L., Dundas, C.M., Mattson, S.S., Byrne, S., Wray, J.J., Cull, S.C., Murchie, S.L., Thomas, N., Gulick, V.C., 2011. Seasonal Flows on Warm Martian Slopes. Science 333, 740–743. doi:10.1126/science.1204816

McKay, D.S., Gibson, E.K., Thomas-Keprta, K.L., Vali, H., Romanek, C.S., Clemett, S.J., Chillier, X.D.F., Maechling, C.R., Zare, R.N., 1996. Search for Past Life on Mars: Possible Relic Biogenic Activity in Martian Meteorite ALH84001. Science 273, 924–930.

McKeown, N.K., Bishop, J.L., Noe Dobrea, E.Z., Ehlmann, B.L., Parente, M., Mustard, J.F., Murchie, S.L., Swayze, G.A., Bibring, J.-P., Silver, E.A., 2009. Characterization of phyllosilicates observed in the central Mawrth Vallis region,

Mars, their potential formational processes, and implications for past climate. J. Geophys. Res. Planets 114, E00D10. doi:10.1029/2008JE003301

McLennan, S.M., Bell III, J.F., Calvin, W.M., Christensen, P.R., Clark, B.C., de Souza, P.A., Farmer, J., Farrand, W.H., Fike, D.A., Gellert, R., Ghosh, A., Glotch, T.D., Grotzinger, J.P., Hahn, B., Herkenhoff, K.E., Hurowitz, J.A., Johnson, J.R., Johnson, S.S., Jolliff, B., Klingelhöfer, G., Knoll, A.H., Learner, Z., Malin, M.C., McSween Jr., H.Y., Pocock, J., Ruff, S.W., Soderblom, L.A., Squyres, S.W., Tosca, N.J., Watters, W.A., Wyatt, M.B., Yen, A., 2005. Provenance and diagenesis of the evaporite-bearing Burns formation, Meridiani Planum, Mars. Sediment. Geol. Meridiani Planum Mars 240, 95–121. doi:10.1016/j.epsl.2005.09.041

McSween, H.Y., 1994. What we have learned about Mars from SNC meteorites. Meteoritics 29, 757–779. doi:10.1111/j.1945-5100.1994.tb01092.x

McSween, H.Y., Harvey, R.P., 1998. An Evaporation Model for Formation of Carbonates in the ALH84001 Martian Meteorite. Int. Geol. Rev. 40, 774–783. doi:10.1080/00206819809465238

Melwani Daswani, M., Schwenzer, S.P., Reed, M.H., Wright, I.P., Grady, M.M., 2014. Carbonate Precipitation Driven by Clay Leachates on Early Mars, in: 45th Lunar and Planetary Science Conference. Lunar and Planetary Institute, Houston, p. Abstract #1280.

Melwani Daswani, M., Schwenzer, S.P., Reed, M.H., Wright, I.P., Grady, M.M., in prep. Alteration minerals and fluids on early Mars: Predictions from 1D flow geochemical modelling of mineral assemblages in meteorite ALH 84001.

Melwani Daswani, M., Schwenzer, S.P., Wright, I.P., Grady, M.M., 2013. Low Temperature Near-Surface Thermochemical Modelling of the Alteration Assemblage in Martian Meteorite ALH 84001. Presented at the 44th Lunar and Planetary Science Conference, Lunar and Planetary Institute, Houston, p. Abstract #2712.

Michalski, J., Poulet, F., Bibring, J.-P., Mangold, N., 2010. Analysis of phyllosilicate deposits in the Nili Fossae region of Mars: Comparison of TES and OMEGA data. Icarus 206, 269–289. doi:doi: DOI: 10.1016/j.icarus.2009.09.006

Mikhail, S., 2011. Stable isotope fractionation during diamond growth and the Earth's deep carbon cycle (Doctoral). University College London, London.

Mittlefehldt, D.W., 1994. ALH84001, a cumulate orthopyroxenite member of the Martian meteorite clan. Meteoritics 29, 214–221.

Miura, Y.N., Nagao, K., Sugiura, N., Sagawa, H., Matsubara, K., 1995. Orthopyroxenite ALH84001 and shergottite ALH77005: Additional evidence for a martian origin from noble gases. Geochim. Cosmochim. Acta 59, 2105–2113. doi:10.1016/0016-7037(95)00130-1

Miura, Y.N., Sugiura, N., 2000. Martian atmosphere-like nitrogen in the orthopyroxenite ALH84001. Geochim. Cosmochim. Acta 64, 559–572. doi:10.1016/S0016-7037(99)00297-5

Miyano, T., Beukes, N.J., 1987. Physicochemical environments for the formation of quartz-free manganese oxide ores from the early Proterozoic Hotazel Formation, Kalahari manganese field, South Africa. Econ. Geol. 82, 706–718.

Mohapatra, R.K., Schwenzer, S.P., Ott, U., 2003. Trapped Neon in the Martian Meteorite SaU 005. Meteorit. Planet. Sci. Suppl. 38, 5206.

Morbidelli, A., Chambers, J., Lunine, J.I., Petit, J.M., Robert, F., Valsecchi, G.B., Cyr, K.E., 2000. Source regions and timescales for the delivery of water to the Earth. Meteorit. Planet. Sci. 35, 1309–1320. doi:10.1111/j.1945-5100.2000.tb01518.x

Morimoto, N., 1988. Nomenclature of Pyroxenes. Mineral. Petrol. 39, 55–76. doi:10.1007/BF01226262

Morris, R.V., Ruff, S.W., Gellert, R., Ming, D.W., Arvidson, R.E., Clark, B.C., Golden, D.C., Siebach, K., Klingelhöfer, G., Schröder, C., Fleischer, I., Yen, A.S., Squyres, S.W., 2010. Identification of Carbonate-Rich Outcrops on Mars by the Spirit Rover. Science 329, 421–424. doi:10.1126/science.1189667

Mortimer, J., Verchovsky, A.B., Anand, M., Gilmour, I., Pillinger, C.T., 2014. Simultaneous analysis of abundance and isotopic composition of nitrogen, carbon, and noble gases in lunar basalts: insights into interior and surface processes on the Moon. Icarus.

Murchie, S., Arvidson, R., Bedini, P., Beisser, K., Bibring, J.-P., Bishop, J., Boldt, J., Cavender, P., Choo, T., Clancy, R.T., Darlington, E.H., Des Marais, D., Espiritu, R., Fort, D., Green, R., Guinness, E., Hayes, J., Hash, C., Heffernan, K., Hemmler, J., Heyler, G., Humm, D., Hutcheson, J., Izenberg, N., Lee, R., Lees, J., Lohr, D., Malaret, E., Martin, T., McGovern, J.A., McGuire, P., Morris, R., Mustard, J., Pelkey, S., Rhodes, E., Robinson, M., Roush, T., Schaefer, E., Seagrave, G., Seelos, F., Silverglate, P., Slavney, S., Smith, M., Shyong, W.-J., Strohbehn, K., Taylor, H.,

Thompson, P., Tossman, B., Wirzburger, M., Wolff, M., 2007. Compact Reconnaissance Imaging Spectrometer for Mars (CRISM) on Mars Reconnaissance Orbiter (MRO). J. Geophys. Res. Planets 112, E05S03. doi:10.1029/2006JE002682

Murty, S.V.S., Mohapatra, R.K., 1997. Nitrogen and heavy noble gases in ALH 84001: Signatures of ancient Martian atmosphere. Geochim. Cosmochim. Acta 61, 5417–5428. doi:10.1016/S0016-7037(97)00315-3

Mustard, J.F., Murchie, S.L., Pelkey, S.M., Ehlmann, B.L., Milliken, R.E., Grant, J.A., Bibring, J.-P., Poulet, F., Bishop, J., Dobrea, E.N., Roach, L., Seelos, F., Arvidson, R.E., Wiseman, S., Green, R., Hash, C., Humm, D., Malaret, E., McGovern, J.A., Seelos, K., Clancy, T., Clark, R., Marais, D.D., Izenberg, N., Knudson, A., Langevin, Y., Martin, T., McGuire, P., Morris, R., Robinson, M., Roush, T., Smith, M., Swayze, G., Taylor, H., Titus, T., Wolff, M., 2008. Hydrated silicate minerals on Mars observed by the Mars Reconnaissance Orbiter CRISM instrument. Nature 454, 305–309. doi:10.1038/nature07097

Mustard, J.F., Poulet, F., Head, J.W., Mangold, N., Bibring, J.-P., Pelkey, S.M., Fasset, C.I., Langevin, Y., Neukum, G., 2007. Mineralogy of the Nili Fossae region with OMEGA/Mars Express data: 1. Ancient impact melt in the Isidis Basin and implications for the transition from the Noachian to Hesperian. J. Geophys. Res. 112. doi:10.1029/2006JE002834

Nadeau, S.L., Epstein, S., Stolper, E., 1999. Hydrogen and carbon abundances and isotopic ratios in apatite from alkaline intrusive complexes, with a focus on carbonatites. Geochim. Cosmochim. Acta 63, 1837–1851.

Neubeck, A., Duc, N., Bastviken, D., Crill, P., Holm, N.G., 2011. Formation of H_2 and CH_4 by weathering of olivine at temperatures between 30 and 70°C. Geochem. Trans. 12, 6. doi:10.1186/1467-4866-12-6

Neukum, G., Jaumann, R., 2004. HRSC: The high resolution stereo camera of Mars Express, in: Mars Express: The Scientific Payload. pp. 17–35.

Niles, P.B., Leshin, L.A., Guan, Y., 2005. Microscale carbon isotope variability in ALH84001 carbonates and a discussion of possible formation environments. Geochim. Cosmochim. Acta 69, 2931–2944. doi:10.1016/j.gca.2004.12.012

Niles, P.B., Zolotov, M.Y., Leshin, L.A., 2009. Insights into the formation of Fe- and Mg-rich aqueous solutions on early Mars provided by the ALH 84001 carbonates. Earth Planet. Sci. Lett. 286, 122–130. doi:10.1016/j.epsl.2009.06.039

Nimmo, F., Kleine, T., 2007. How rapidly did Mars accrete? Uncertainties in the Hf–W timing of core formation. Icarus 191, 497–504. doi:10.1016/j.icarus.2007.05.002

Nyquist, L.E., Bogard, D.D., Shih, C.Y., Greshake, A., Stöffler, D., Eugster, O., 2001. Ages and geologic histories of Martian meteorites. Space Sci. Rev. 96, 105–164.

Nyquist, L.E., Shih, C.-Y., 2013. Peering Through a Martian Veil: ALHA 84001 Sm-Nd Age Revisited. LPI Contrib. 1719, 2182.

O'Brien, D.P., Morbidelli, A., Levison, H.F., 2006. Terrestrial planet formation with strong dynamical friction. Icarus 184, 39–58. doi:10.1016/j.icarus.2006.04.005

Ostwald, J., 1992. Mineralogy, paragenesis and genesis of the braunite deposits of the Mary Valley Manganese Belt, Queensland, Australia. Miner. Deposita 27, 326–335. doi:10.1007/BF00193403

Ott, U., Lohr, H.P., 1992. Noble Gases in the New Shergottite LEW 88516. Meteoritics 27, 271.

Owen, T., Biemann, K., 1976. Composition of the Atmosphere at the Surface of Mars: Detection of Argon-36 and Preliminary Analysis. Science 193, 801–803. doi:10.1126/science.193.4255.801

Owen, T., Biemann, K., Rushneck, D.R., Biller, J.E., Howarth, D.W., Lafleur, A.L., 1977. The composition of the atmosphere at the surface of Mars. J. Geophys. Res. 82, 4635–4639. doi:10.1029/JS082i028p04635

Ozawa, S., Ohtani, E., Miyahara, M., Suzuki, A., Kimura, M., Ito, Y., 2009. Transformation textures, mechanisms of formation of high-pressure minerals in shock melt veins of L6 chondrites, and pressure-temperature conditions of the shock events. Meteorit. Planet. Sci. 44, 1771–1786. doi:10.1111/j.1945-5100.2009.tb01206.x

Oze, C., Sharma, M., 2007. Serpentinization and the inorganic synthesis of H2 in planetary surfaces. Icarus 186, 557–561. doi:10.1016/j.icarus.2006.09.012

Oze, C., Sharma, M., 2005. Have olivine, will gas: Serpentinization and the abiogenic production of methane on Mars. Geophys. Res. Lett. 32, L10203. doi:10.1029/2005GL022691

Palandri, J.L., Reed, M.H., 2004. Geochemical models of metasomatism in ultramafic systems: serpentinization, rodingitization, and sea floor carbonate chimney precipitation. Geochim. Cosmochim. Acta 68, 1115–1133. doi:10.1016/j.gca.2003.08.006

Palandri, J.L., Reed, M.H., 2001. Reconstruction of in situ composition of sedimentary formation waters. Geochim. Cosmochim. Acta 65, 1741–1767. doi:10.1016/S0016-7037(01)00555-5

Parker, T.J., Grant, J.A., Franklin, B.J., 2010. 9 - The northern plains: A Martian oceanic basin?, in: Nathalie A. Cabrol, Edmond A. Grin (Eds.), Lakes on Mars. Elsevier, Amsterdam, pp. 249–273.

Parkhurst, D.L., Appelo, C.A.J., 2013. Description of Input and Examples for PHREEQC Version 3—A Computer Program for Speciation, Batch-Reaction, One-Dimensional Transport, and Inverse Geochemical Calculations, in: Modeling Techniques, USGS Techniques and Methods. U.S. Geological Survey, Denver, Colorado, p. 497.

Peck, W.H., Tumpane, K.P., 2007. Low carbon isotope ratios in apatite: An unreliable biomarker in igneous and metamorphic rocks. Chem. Geol. 245, 305–314. doi:10.1016/j.chemgeo.2007.08.012

Pepin, R.O., 1991. On the origin and early evolution of terrestrial planet atmospheres and meteoritic volatiles. Icarus 92, 2–79. doi:10.1016/0019-1035(91)90036-S

Perkins, D., Essene, E.J., Westrum, E.F., Wall, V.J., 1979. New thermodynamic data for diaspore and their application to the system Al_2O_3-SiO_2-H_2O. Am. Mineral. 64, 1080–1090.

Peters, T., Trommsdorff, V., Sommerauer, J., 1978. Manganese pyroxenoids and carbonates: Critical phase relations in metamorphic assemblages from the Alps. Contrib. Mineral. Petrol. 66, 383–388. doi:10.1007/BF00403423

Picardi, G., Biccari, D., Seu, R., Plaut, J., Johnson, W.T.K., Jordan, R.L., Safaeinili, A., Gurnett, D.A., Huff, R., Orosei, R., 2004. MARSIS: Mars advanced radar for subsurface and ionosphere sounding. Mars Express Sci. Payload 51–69.

Pollack, J.B., Kasting, J.F., Richardson, S.M., Poliakoff, K., 1987. The case for a wet, warm climate on early Mars. Icarus 71, 203–224. doi:10.1016/0019-1035(87)90147-3

Poulet, F., Bibring, J.-P., Mustard, J.F., Gendrin, A., Mangold, N., Langevin, Y., Arvidson, R.E., Gondet, B., Gomez, C., 2005. Phyllosilicates on Mars and implications for early martian climate. Nature 438, 623–627. doi:10.1038/nature04274

Ramirez, R.M., Kopparapu, R., Zugger, M.E., Robinson, T.D., Freedman, R., Kasting, J.F., 2014. Warming early Mars with CO2 and H2. Nat. Geosci 7, 59–63.

Raymond, S.N., O'Brien, D.P., Morbidelli, A., Kaib, N.A., 2009. Building the terrestrial planets: Constrained accretion in the inner Solar System. Icarus 203, 644–662. doi:10.1016/j.icarus.2009.05.016

Raymond, S.N., Quinn, T., Lunine, J.I., 2007. High-resolution simulations of the final assembly of Earth-like planets. 2. Water delivery and planetary habitability. Astrobiology 7, 66–84.

Raymond, S.N., Quinn, T., Lunine, J.I., 2006. High-resolution simulations of the final assembly of Earth-like planets I. Terrestrial accretion and dynamics. Icarus 183, 265–282. doi:10.1016/j.icarus.2006.03.011

Redhammer, G.J., Amthauer, G., Lottermorser, W., Treutmann, W., 2000. Synthesis and structural properties of clinopyroxenes of the hedenbergite $CaFe_2$+Si_2O_6 – aegirine $NaFe_3$+Si_2O_6 solid-solution series. Eur. J. Mineral. 12, 105–120. doi:10.1127/0935-1221/2000/0012-0105

Reed, M.H., 1998. Calculation of simultaneous chemical equilibria in aqueous-mineral-gas systems and its application to modeling hydrothermal processes, in: Techniques in Hydrothermal Ore Deposits Geology, Reviews in Economic Geology. pp. 109–124.

Reed, M.H., 1983. Seawater-basalt reaction and the origin of greenstones and related ore deposits. Econ. Geol. 78, 466–485. doi:10.2113/gsecongeo.78.3.466

Reed, M.H., 1982. Calculation of multicomponent chemical equilibria and reaction processes in systems involving minerals, gases and an aqueous phase. Geochim. Cosmochim. Acta 46, 513–528. doi:10.1016/0016-7037(82)90155-7

Reed, M., Spycher, N., Palandri, J., 2012. Users Guide for CHIM-XPT: A Program for Computing Reaction Processes in Aqueous- Mineral-Gas Systems and MINTAB Guide.Ver. 2.43.

Reimold, W.U., Barr, J.M., Grieve, R.A.F., Durrheim, R.J., 1990a. Geochemistry of the melt and country rocks of the Lake St. Martin impact structure, Manitoba, Canada. Geochim. Cosmochim. Acta 54, 2093–2111. doi:10.1016/0016-7037(90)90273-N

Reimold, W.U., Durrheim, R.J., Horsch, H., 1990b. The "bronzite"-granophyre from the Vredefort structure - A detailed analytical study and reflections on the genesis of one of Vredefort's enigmas, in: Sharpton, V.L., Ryder, G. (Eds.), Lunar and Planetary Science Conference Proceedings, Lunar and Planetary Science Conference Proceedings. pp. 433–450.

Reiss, D., Erkeling, G., Bauch, K.E., Hiesinger, H., 2010. Evidence for present day gully activity on the Russell crater dune field, Mars. Geophys. Res. Lett. 37, n/a–n/a. doi:10.1029/2009GL042192

Retallack, G.J., 2014. Paleosols and paleoenvironments of early Mars. Geology 42, 755–758. doi:10.1130/G35912.1

Richard, F.C., Bourg, A.C.M., 1991. Aqueous geochemistry of chromium: A review. Water Res. 25, 807–816. doi:10.1016/0043-1354(91)90160-R

Rodriguez, J.A.P., Sasaki, S., Kuzmin, R.O., Dohm, J.M., Tanaka, K.L., Miyamoto, H., Kurita, K., Komatsu, G., Fairén, A.G., Ferris, J.C., 2005. Outflow channel sources, reactivation, and chaos formation, Xanthe Terra, Mars. Icarus 175, 36–57. doi:10.1016/j.icarus.2004.10.025

Romanek, C.S., Grady, M.M., Wright, I.P., Mittlefehldt, D.W., Socki, R.A., Pillinger, C.T., Gibson, E.K., 1994a. Record of fluid-rock interactions on Mars from the meteorite ALH84001. Nature 372, 655–657. doi:10.1038/372655a0

Romanek, C.S., Jiménez-López, C., Navarro, A.R., Sánchez-Román, M., Sahai, N., Coleman, M., 2009. Inorganic synthesis of Fe–Ca–Mg carbonates at low temperature. Geochim. Cosmochim. Acta 73, 5361–5376. doi:10.1016/j.gca.2009.05.065

Romanek, C.S., Mittlefehldt, D.W., Gibson, Jr., E.K., Socki, R.A., 1994b. Martian carbonates in ALH 84001: Textural, elemental, and stable isotopic compositional evidence on their formation. Meteoritics 29, 523.

Ruff, S.W., Niles, P.B., Alfano, F., Clarke, A.B., 2014. Evidence for a Noachian-aged ephemeral lake in Gusev crater, Mars. Geology 42, 359–362. doi:10.1130/G35508.1

Saldi, G.D., Jordan, G., Schott, J., Oelkers, E.H., 2009. Magnesite growth rates as a function of temperature and saturation state. Geochim. Cosmochim. Acta 73, 5646–5657. doi:10.1016/j.gca.2009.06.035

Sandiford, M., n.d. Pyroxene [WWW Document]. Mike Sandifords Sci. Pages. URL http://jaeger.earthsci.unimelb.edu.au/msandifo/Teaching/Minerals/pyroxene.html (accessed 11.21.14).

Schröder, C., Klingelhöfer, G., Tremel, W., 2004. Weathering of Fe-bearing minerals under Martian conditions, investigated by Mössbauer spectroscopy. Planet Mars

Spons. Cent. Natl. Etudes Spatiales CNES Cent. Natl. Rech. Sci. CNRS Obs. Paris 52, 997–1010. doi:10.1016/j.pss.2004.07.018

Schultz, L., Franke, L., 2004. Helium, neon, and argon in meteorites: A data collection. Meteorit. Planet. Sci. 39, 1889–1890. doi:10.1111/j.1945-5100.2004.tb00083.x

Schwenzer, S.P., Fritz, J., Stöffler, D., Trieloff, M., Amini, M., Greshake, A., Herrmann, S., Herwig, K., Jochum, K.P., Mohapatra, R.K., Stoll, B., Ott, U., 2008. Helium loss from Martian meteorites mainly induced by shock metamorphism: Evidence from new data and a literature compilation. Meteorit. Planet. Sci. 43, 1841–1859. doi:10.1111/j.1945-5100.2008.tb00647.x

Schwenzer, S.P., Herrmann, S., Mohapatra, R.K., Ott, U., 2007. Noble gases in mineral separates from three shergottites: Shergotty, Zagami, and EETA79001. Meteorit. Planet. Sci. 42, 387–412. doi:10.1111/j.1945-5100.2007.tb00241.x

Schwenzer, S.P., Kring, D.A., 2013. Alteration minerals in impact-generated hydrothermal systems – Exploring host rock variability. Icarus 226, 487–496. doi:10.1016/j.icarus.2013.06.003

Schwenzer, S.P., Kring, D.A., 2009. Impact-generated hydrothermal systems capable of forming phyllosilicates on Noachian Mars. Geology 37, 1091–1094. doi:10.1130/G30340A.1

Scott, E.R.D., 1999. Origin of carbonate-magnetite-sulfide assemblages in Martian meteorite ALH84001. J. Geophys. Res. 104, 3803. doi:10.1029/1998JE900034

Scott, E.R.D., Yamaguchi, A., Krot, A.N., 1997. Petrological evidence for shock melting of carbonates in the martian meteorite ALH84001. Nature 387, 377–379. doi:10.1038/387377a0

Shatkay, M., Magaritz, M., 1987. Dolomitization and sulfate reduction in the mixing zone between brine and meteoric water in the newly exposed shores of the Dead Sea. Geochim. Cosmochim. Acta 51, 1135–1141.

Shearer, C.K., Layne, G.D., Papike, J.J., Spilde, M.N., 1996. Sulfur isotopic systematics in alteration assemblages in martian meteorite Allan Hills 84001. Geochim. Cosmochim. Acta 60, 2921–2926. doi:10.1016/0016-7037(96)00165-2

Shearer, C.K., Leshin, L.A., Adcock, C.T., 1999. Olivine in Martian meteorite ALH 84001: Evidence for a high-temperature origin and implications for signs of life. Meteorit. Planet. Sci. 34, 331–339. doi:10.1111/j.1945-5100.1999.tb01343.x

Shelkov, D.A., 1997. N and C isotopic composition of different varieties of terrestrial diamonds and carbonado., Open University Thesis Collection. n.p., 1997.

Sheppard, S.F., Schwarcz, H., 1970. Fractionation of carbon and oxygen isotopes and magnesium between coexisting metamorphic calcite and dolomite. Contrib. Mineral. Petrol. 26, 161–198. doi:10.1007/BF00373200

Sparks, D.L., 2003. Environmental soil chemistry. Academic Press, Amsterdam; Boston.

Spycher, N.F., Reed, M.H., 1988. Fugacity coefficients of H_2, CO_2, CH_4, H_2O and of H_2O-CO_2-CH_4 mixtures: A virial equation treatment for moderate pressures and temperatures applicable to calculations of hydrothermal boiling. Geochim. Cosmochim. Acta 52, 739–749. doi:10.1016/0016-7037(88)90334-1

Squyres, S.W., Arvidson, R.E., Baumgartner, E.T., Bell, J.F., Christensen, P.R., Gorevan, S., Herkenhoff, K.E., Klingelhöfer, G., Madsen, M.B., Morris, R.V., Rieder, R., Romero, R.A., 2003. Athena Mars rover science investigation. J. Geophys. Res. Planets 108, 8062. doi:10.1029/2003JE002121

Squyres, S.W., Arvidson, R.E., Bell, J.F., Calef, F., Clark, B.C., Cohen, B.A., Crumpler, L.A., de Souza, P.A., Farrand, W.H., Gellert, R., Grant, J., Herkenhoff, K.E., Hurowitz, J.A., Johnson, J.R., Jolliff, B.L., Knoll, A.H., Li, R., McLennan, S.M., Ming, D.W., Mittlefehldt, D.W., Parker, T.J., Paulsen, G., Rice, M.S., Ruff, S.W., Schröder, C., Yen, A.S., Zacny, K., 2012. Ancient Impact and Aqueous Processes at Endeavour Crater, Mars. Science 336, 570–576. doi:10.1126/science.1220476

Stanger, G., Neal, C., 1994. The occurrence and chemistry of huntite from Oman. Chem. Geol. 112, 247–254. doi:10.1016/0009-2541(94)90027-2

Steele, A., Fries, M.D., Amundsen, H.E.F., Mysen, B.O., Fogel, M.L., Schweizer, M., Boctor, N.Z., 2007. Comprehensive imaging and Raman spectroscopy of carbonate globules from Martian meteorite ALH 84001 and a terrestrial analogue from Svalbard. Meteorit. Planet. Sci. 42, 1549–1566. doi:10.1111/j.1945-5100.2007.tb00590.x

Steele, A., McCubbin, F.M., Fries, M.D., Golden, D.C., Ming, D.W., Benning, L.G., 2012a. Graphite in the martian meteorite Allan Hills 84001. Am. Mineral. 97, 1256–1259.

Steele, A., McCubbin, F.M., Fries, M., Kater, L., Boctor, N.Z., Fogel, M.L., Conrad, P.G., Glamoclija, M., Spencer, M., Morrow, A.L., Hammond, M.R., Zare, R.N., Vicenzi, E.P., Siljeström, S., Bowden, R., Herd, C.D.K., Mysen, B.O., Shirey, S.B., Amundsen, H.E.F., Treiman, A.H., Bullock, E.S., Jull, A.J.T., 2012b. A Reduced Organic Carbon Component in Martian Basalts. Science 337, 212–215. doi:10.1126/science.1220715

Stöckelmann, D., Reimold, W.U., 1989. The HMX mixing calculation program. Math. Geol. 21, 853–860.

Stumm, W., 1996. Aquatic chemistry: chemical equilibria and rates in natural waters, 3rd ed. ed, Environmental science and technology. Wiley, New York.

Swindle, T.D., 2002. Martian Noble Gases. Rev. Mineral. Geochem. 47, 171–190. doi:10.2138/rmg.2002.47.6

Swindle, T.D., Grier, J.A., Burkland, M.K., 1995. Noble gases in orthopyroxenite ALH84001: A different kind of martian meteorite with an atmospheric signature. Geochim. Cosmochim. Acta 59, 793–801. doi:10.1016/0016-7037(94)00359-T

Tanger, J.C., Helgeson, H.C., 1988. Calculation of the thermodynamic and transport properties of aqueous species at high pressures and temperatures; revised equations of state for the standard partial molal properties of ions and electrolytes. Am. J. Sci. 288, 19–98. doi:10.2475/ajs.288.1.19

The Geochemist's Workbench, 2014. , The Geochemist's Workbench. Aqueous Solutions LLC, Champaign, Illinois.

Theis, K.J., Lyon, I., Burgess, R., Turner, G., 2008. Iron Isotope Composition of Zoned Carbonates from ALH 84001. Meteorit. Planet. Sci. Suppl. 43, 5218.

Theye, T., Chopin, C., Grevel, K.-D., Ockenga, E., 1997. The assemblage diaspore+quartz in metamorphic rocks: a petrological, experimental and thermodynamic study. J. Metamorph. Geol. 15, 17–28. doi:10.1111/j.1525-1314.1997.1501050.x

Thomas-Keprta, K.L., Bazylinski, D.A., Kirschvink, J.L., Clemett, S.J., McKay, D.S., Wentworth, S.J., Vali, H., Gibson Jr., E.K., Romanek, C.S., 2000. Elongated prismatic magnetite crystals in ALH84001 carbonate globules:: Potential Martian magnetofossils. Geochim. Cosmochim. Acta 64, 4049–4081. doi:10.1016/S0016-7037(00)00481-6

Thomas-Keprta, K.L., Clemett, S.J., Bazylinski, D.A., Kirschvink, J.L., McKay, D.S., Wentworth, S.J., Vali, H., Gibson, E.K., Romanek, C.S., 2002. Magnetofossils from Ancient Mars: a Robust Biosignature in the Martian Meteorite ALH84001. Appl. Environ. Microbiol. 68, 3663–3672. doi:10.1128/AEM.68.8.3663-3672.2002

Thomas-Keprta, K.L., Clemett, S.J., McKay, D.S., Gibson, E.K., Wentworth, S.J., 2009. Origins of magnetite nanocrystals in Martian meteorite ALH84001. Geochim. Cosmochim. Acta 73, 6631–6677. doi:10.1016/j.gca.2009.05.064

Tosca, N.J., Macdonald, F.A., Strauss, J.V., Johnston, D.T., Knoll, A.H., 2011. Sedimentary talc in Neoproterozoic carbonate successions. Earth Planet. Sci. Lett. 306, 11–22. doi:10.1016/j.epsl.2011.03.041

Treiman, A.H., 2005. The nakhlite meteorites: Augite-rich igneous rocks from Mars. Chem. Erde - Geochem. 65, 203–270. doi:10.1016/j.chemer.2005.01.004

Treiman, A.H., 1998a. The history of Allan Hills 84001 revised: Multiple shock events. Meteorit. Planet. Sci. 33, 753–764. doi:10.1111/j.1945-5100.1998.tb01681.x

Treiman, A.H., 1998b. Amphiboles in More Martian Meteorites: Elephant Moraine 79001 B, Elephant Moraine 79001 X, and Lewis Cliff 88516. Meteorit. Planet. Sci. Suppl. 33, 156.

Treiman, A.H., 1995. A petrographic history of martian meteorite ALH84001: Two shocks and an ancient age. Meteoritics 30, 294.

Treiman, A.H., 1985. Amphibole and hercynite spinel in Shergotty and Zagami: Magmatic water, depth of Crystallisation, and metasomatism. Meteoritics 20, 229–243. doi:10.1111/j.1945-5100.1985.tb00862.x

Treiman, A.H., Amundsen, H.E.., Blake, D.F., Bunch, T., 2002. Hydrothermal origin for carbonate globules in Martian meteorite ALH84001: a terrestrial analogue from Spitsbergen (Norway). Earth Planet. Sci. Lett. 204, 323–332. doi:10.1016/S0012-821X(02)00998-6

Treiman, A.H., Barrett, R.A., Gooding, J.L., 1993. Preterrestrial aqueous alteration of the Lafayette (SNC) meteorite. Meteoritics 28, 86–97. doi:10.1111/j.1945-5100.1993.tb00251.x

Treiman, A.H., Essene, E.J., 2011. Chemical composition of magnetite in Martian meteorite ALH 84001: Revised appraisal from thermochemistry of phases in Fe–Mg–C–O. Geochim. Cosmochim. Acta 75, 5324–5335. doi:10.1016/j.gca.2011.06.038

Turner, G., Knott, S.F., Ash, R.D., Gilmour, J.D., 1997. Ar-Ar chronology of the Martian meteorite ALH84001: Evidence for the timing of the early bombardment of Mars. Geochim. Cosmochim. Acta 61, 3835–3850. doi:10.1016/S0016-7037(97)00285-8

Valley, J.W., Eiler, J.M., Graham, C.M., Gibson, E.K., Romanek, C.S., Stolper, E.M., 1997. Low-Temperature Carbonate Concretions in the Martian Meteorite ALH84001: Evidence from Stable Isotopes and Mineralogy. Science 275, 1633–1638. doi:10.1126/science.275.5306.1633

Van Berk, W., Fu, Y., 2011. Reproducing hydrogeochemical conditions triggering the formation of carbonate and phyllosilicate alteration mineral assemblages on Mars (Nili Fossae region). J. Geophys. Res. 116. doi:10.1029/2011JE003886

Van Berk, W., Fu, Y., Ilger, J.-M., 2012. Reproducing early Martian atmospheric carbon dioxide partial pressure by modeling the formation of Mg-Fe-Ca carbonate identified in the Comanche rock outcrops on Mars. J. Geophys. Res. 117. doi:10.1029/2012JE004173

Van Berk, W., Ilger, J.-M., Fu, Y., Hansen, C., 2011. Decreasing CO_2 partial pressure triggered Mg–Fe–Ca carbonate formation in ancient Martian crust preserved in the ALH84001 Meteorite. Geofluids 11, 6–17. doi:10.1111/j.1468-8123.2010.00296.x

Vaniman, D.T., Bish, D.L., Ming, D.W., Bristow, T.F., Morris, R.V., Blake, D.F., Chipera, S.J., Morrison, S.M., Treiman, A.H., Rampe, E.B., Rice, M., Achilles, C.N., Grotzinger, J.P., McLennan, S.M., Williams, J., Bell, J.F., Newsom, H.E., Downs, R.T., Maurice, S., Sarrazin, P., Yen, A.S., Morookian, J.M., Farmer, J.D., Stack, K., Milliken, R.E., Ehlmann, B.L., Sumner, D.Y., Berger, G., Crisp, J.A., Hurowitz, J.A., Anderson, R., Des Marais, D.J., Stolper, E.M., Edgett, K.S., Gupta, S., Spanovich, N., MSL Science Team, 2014. Mineralogy of a Mudstone at Yellowknife Bay, Gale Crater, Mars. Science 343. doi:10.1126/science.1243480

Velbel, M.A., Long, D.T., Gooding, J.L., 1991. Terrestrial weathering of Antarctic stone meteorites: Formation of Mg-carbonates on ordinary chondrites. Geochim. Cosmochim. Acta 55, 67–76. doi:10.1016/0016-7037(91)90400-Y

Vidal, O., 1997. Experimental study of the thermal stability of pyrophyllite, paragonite, and clays in a thermal gradient. Eur. J. Mineral. 9, 123–140.

Vidal, O., Dubacq, B., 2009. Thermodynamic modelling of clay dehydration, stability and compositional evolution with temperature, pressure and H_2O activity. Geochim. Cosmochim. Acta 73, 6544–6564. doi:10.1016/j.gca.2009.07.035

Vidal, O., Goffé, B., Theye, T., 1992. Experimental study of the stability of sudoite and magnesiocarpholite and calculation of a new petrogenetic grid for the system FeO–MgO–Al_2O_3–SiO_2–H_2O. J. Metamorph. Geol. 10, 603–614. doi:10.1111/j.1525-1314.1992.tb00109.x

Viviano, C.E., Moersch, J.E., McSween, H.Y., 2013. Implications for early hydrothermal environments on Mars through the spectral evidence for carbonation and chloritization reactions in the Nili Fossae region: Hydrothermal environments in Nili Fossae. J. Geophys. Res. Planets 1858–1872. doi:10.1002/jgre.20141

Walsh, K.J., Morbidelli, A., Raymond, S.N., O'Brien, D.P., Mandell, A.M., 2012. Populating the asteroid belt from two parent source regions due to the migration of giant planets—"The Grand Tack." Meteorit. Planet. Sci. 47, 1941–1947. doi:10.1111/j.1945-5100.2012.01418.x

Walsh, K.J., Morbidelli, A., Raymond, S.N., O'Brien, D.P., Mandell, A.M., 2011. A low mass for Mars from Jupiter's early gas-driven migration. Nature 475, 206–209. doi:10.1038/nature10201

Warren, P.H., 1998. Petrologic evidence for low-temperature, possibly flood evaporitic origin of carbonates in the ALH84001 meteorite. J. Geophys. Res. Planets 103, 16759–16773. doi:10.1029/98JE01544

Watters, T.R., McGovern, P.J., Irwin Iii, R.P., 2007. Hemispheres apart: The crustal dichotomy on Mars. Annu Rev Earth Planet Sci 35, 621–652.

Webster, C.R., Mahaffy, P.R., Atreya, S.K., Flesch, G.J., Mischna, M.A., Meslin, P.-Y., Farley, K.A., Conrad, P.G., Christensen, L.E., Pavlov, A.A., Martín-Torres, J., Zorzano, M.-P., McConnochie, T.H., Owen, T., Eigenbrode, J.L., Glavin, D.P., Steele, A., Malespin, C.A., Archer, P.D., Sutter, B., Coll, P., Freissinet, C., McKay, C.P., Moores, J.E., Schwenzer, S.P., Bridges, J.C., Navarro-Gonzalez, R., Gellert, R., Lemmon, M.T., Team, the M.S., 2015. Mars methane detection and variability at Gale crater. Science 347, 415–417.

Wedepohl, K.H., 1969. Manganese Abundance in Rock-Forming Minerals, Phase Equilibria, Manganese Minerals, in: Handbook of Geochemistry. Springer-Verlag, Berlin.

Weiss, B.P., Kirschvink, J.L., Baudenbacher, F.J., Vali, H., Peters, N.T., Macdonald, F.A., Wikswo, J.P., 2000. A low temperature transfer of ALH84001 from Mars to Earth. Science 290, 791–795.

Wentworth, S.J., Gibson, E.K., Velbel, M.A., McKay, D.S., 2005. Antarctic Dry Valleys and indigenous weathering in Mars meteorites: Implications for water and life on Mars. Icarus 174, 383–395. doi:10.1016/j.icarus.2004.08.026

Wentworth, S.J., Gooding, J.L., 1995. Carbonates in the Martian meteorite, ALH 84001: water-borne but not like the SNCs, in: Lunar and Planetary Institute Science Conference Abstracts. p. 1489.

Wentworth, S.J., Gooding, J.L., 1994. Carbonates and sulfates in the Chassigny meteorite: Further evidence for aqueous chemistry on the SNC parent planet. Meteoritics 29, 860–863. doi:10.1111/j.1945-5100.1994.tb01100.x

Wentworth, S.J., Thomas-Keprta, K.L., McKay, D.S., 2000. Weathering and Secondary Minerals in the Martian Meteorite Shergotty, in: Lunar and Planetary Science Conference, Lunar and Planetary Science Conference. p. 1888.

Wentworth, S.J., Thomas-Keprta, K.L., McKay, D.S., 1998. Alteration Products and Secondary Minerals in Martian Meteorite Allan Hills 84001, in: Martian Meteorites: Where Do We Stand and Where Are We Going? Abstracts from a Workshop. p. 59.

Williams, R.M.E., Grotzinger, J.P., Dietrich, W.E., Gupta, S., Sumner, D.Y., Wiens, R.C., Mangold, N., Malin, M.C., Edgett, K.S., Maurice, S., Forni, O., Gasnault, O., Ollila, A., Newsom, H.E., Dromart, G., Palucis, M.C., Yingst, R.A., Anderson, R.B., Herkenhoff, K.E., Le Mouélic, S., Goetz, W., Madsen, M.B., Koefoed, A., Jensen, J.K., Bridges, J.C., Schwenzer, S.P., Lewis, K.W., Stack, K.M., Rubin, D., Kah, L.C., Bell, J.F., Farmer, J.D., Sullivan, R., Van Beek, T., Blaney, D.L., Pariser, O., Deen, R.G., MSL Science Team, 2013. Martian Fluvial Conglomerates at Gale Crater. Science 340, 1068–1072. doi:10.1126/science.1237317

Wones, D.R., Eugster, H.P., 1965. Stability of biotite-experiment theory and application. Am. Mineral. 50, 1228–&.

Wordsworth, R., Forget, F., Millour, E., Head, J.W., Madeleine, J.-B., Charnay, B., 2013. Global modelling of the early martian climate under a denser CO_2 atmosphere: Water cycle and ice evolution. Icarus 222, 1–19. doi:10.1016/j.icarus.2012.09.036

Wray, J.J., Squyres, S.W., Roach, L.H., Bishop, J.L., Mustard, J.F., Noe Dobrea, E.Z., 2010. Identification of the Ca-sulfate bassanite in Mawrth Vallis, Mars. Icarus 209, 416–421. doi:10.1016/j.icarus.2010.06.001

Wright, I.P., Boyd, S.R., Franchi, I.A., Pillinger, C.T., 1988. High-precision determination of nitrogen stable isotope ratios at the sub-nanomole level. J. Phys. [E] 21, 865–875. doi:10.1088/0022-3735/21/9/011

Yi, H., Balan, E., Gervais, C., Segalen, L., Fayon, F., Roche, D., Person, A., Morin, G., Guillaumet, M., Blanchard, M., Lazzeri, M., Babonneau, F., 2013. A carbonate-fluoride defect model for carbonate-rich fluorapatite. Am. Minéral. 98, 1066–1069. doi:10.2138/am.2013.4445

Yin, Q., Jacobsen, S.B., Yamashita, K., Blichert-Toft, J., Telouk, P., Albarede, F., 2002. A short timescale for terrestrial planet formation from Hf-W chronometry of meteorites. Nature 418, 949–952. doi:10.1038/nature00995

Zegers, T.E., Oosthoek, J.H.P., Rossi, A.P., Blom, J.K., Schumacher, S., 2010. Melt and collapse of buried water ice: An alternative hypothesis for the formation of chaotic terrains on Mars. Earth Planet. Sci. Lett. 297, 496–504. doi:10.1016/j.epsl.2010.06.049

Zolotov, M., Shock, E., 1999. Abiotic synthesis of polycyclic aromatic hydrocarbons on Mars. J. Geophys. Res. Planets 104, 14033–14049. doi:10.1029/1998JE000627